Summer 2011

A Wind Tunnel Technique for the Identification of Ship Airwake/ Rotor Downwash Coupling

Stargel R. Doane
Old Dominion University

A WIND TUNNEL TECHNIQUE FOR THE IDENTIFICATION OF SHIP AIRWAKE/ROTOR DOWNWASH COUPLING

by

Stargel R. Doane
B.S. May 2006, Old Dominion University

A Dissertation Submitted to the Faculty of
Old Dominion University in Partial Fulfillment of the
Requirement for the Degree of

DOCTOR OF PHILOSOPHY

AEROSPACE ENGINEERING

OLD DOMINION UNIVERSITY
August 2011

Approved by:

Drew Landman (Director)

Colin Britcher (Member)

Ali Beskok (Member)

Tony Dean (Member)

A WIND TUNNEL TECHNIQUE FOR THE IDENTIFICATION OF SHIP AIRWAKE/ROTOR DOWNWASH COUPLING

Stargel R. Doane
Old Dominion University, 2011
Director: Dr. Drew Landman

A wind tunnel study is performed to analyze the interaction between ship airwakes and helicopter rotor downwash. This interaction is of interest to naval aviators and researchers as this phenomenon is thought to limit helicopter flight envelopes and increase the overall difficulty of maritime rotorcraft operations. In this study, a $1/50^{th}$ scale simplified naval frigate model and appropriately scaled rotor model are used for all experimental work. A rotor thrust survey was conducted in the immediate vicinity of the landing deck. Two dimensional and stereo particle image velocimetry surveys and rotor thrust measurements with various rotor and ship configurations were conducted. Finally, a velocity based coupling analysis technique was developed and applied. In addition, extensive systems were developed to control wind tunnel conditions, accurately position wind tunnel models, manage data, and ultimately facilitate an efficient experimental process. The developed coupling technique quantifies aerodynamic coupling by examining the component-wise velocity discrepancies between the experimentally observed flowfield and the flowfield generated by superposition. Significant aerodynamic coupling was found below a rotor-over-deck height of Z/D=1.2 for a wind tunnel speed of 5 m/s and zero wind-over-deck angle.

ACKNOWLEDGMENTS

I would like to express my sincere thanks to my advisor, Dr. Drew Landman, for all of his help and support over the years. Dr. Landman is one of the finest engineers I have ever met. I would also like to thank Dr. Colin Britcher, Dr. Ali Beskok, and Dr. Tony Dean for their valuable insight that helped improve this work. I extend my sincere thanks to Tom Galloway and Kevin Colvin for fabricating numerous devices used in this work and other projects. Finally, I would like to thank my family for their constant encouragement and love over the years.

NOMENCLATURE

X	Longitudinal Rotor Position
Y	Lateral Rotor Position
Z	Vertical Rotor Position
D	Rotor Diameter
X/D	Non-dimensionalized Longitudinal Rotor Position
Y/D	Non-dimensionalized Lateral Rotor Position
Z/D	Non-dimensionalized Vertical Rotor Position
AR	Advance Ratio
ANOVA	Analysis of Variance
b	Least Squares Estimator of Regression Coefficients
β	Regression Coefficients
y	Response Matrix
X_M	Model Matrix
SS	Sum of Squares
H_0	Null Hypothesis
H_1	Alternate Hypothesis
MS	Mean Square
σ^2	Error Variance
$\hat{\sigma}^2$	Estimated Error Variance
F_0	F-Test Statistic
$F_{critical}$	Critical F-value
n	Sample Size

k	Number of Regression Coefficients
α	Significance Level
P	P-Value
e_i	Residual
r	Studentized Residual
H	Hat Matrix Defined as$X_M(X_M^T X_M)^{-1} X_M^T$
h_{ii}	Diagonal Elements of the Hat Matrix H
R^2	Coefficient of Determination
R^2_{adj}	Adjusted Coefficient of Determination
R^2_{pred}	Coefficient of Determination for Prediction
PRESS	Prediction Error Sum of Squares
p	Number of Model Parameters Including the Mean
m	Number of Factor Levels
n_{terms}	Number of terms being tested
t	T-Statistic
C_{ii}	Diagonal Elements of $(X_M^T X_M)^{-1}$
x_0	Design Point
F_{Thrust}	Rotor Thrust (N)
C_T	Rotor Thrust Coefficient
P_{atm}	Atmospheric Pressure (Pa)
R_{air}	Gas Constant for Air (J/(Kg·K))
T	Wind Tunnel Fluid Temperature (K)
Ω	Rotor Rotation Rate (Rad./Sec)

r_{rotor}	Radius of Rotor (m)
A	Area of Rotor Disk (m2)
PIV	Particle Image Velocimetry
PTV	Particle Tracking Velocimetry
θ	Camera Angle (deg.)
d_0	Object Distance (m)
d_i	Image Distance (m)
Δt	Time Delay (sec)
U	U-Component of Velocity (m/s)
V	V-Component of Velocity
W	W-Component of Velocity
$H.P.$	Horse Power
q	Dynamic Pressure (Pa)
ΔP	Wind Tunnel Static Pressure Differential
e_T	Combined Error
e_b	Bias Error
e_p	Precision Error
S	Sample Standard Deviation
N	Number of Individual Observations
E_T	Total Error
e_{bc}	Bias Error Component
$e_{b_{W_i}}$	Bias Error Associated with Individual Variables
I	Image Intensity

I_0	Particle Image Intensity
x_p	Particle Location
y_p	Particle location
x_{img}	Image Location
y_{img}	Image Location
z_p	Particle Location
d_τ	Particle Image Diameter
q	Particle Light Scattering Efficiency
ΔZ_L	Thickness of Laser Light Sheet

TABLE OF CONTENTS

LIST OF TABLES

LIST OF FIGURES

Figure Page

Figure Page

Figure Page

Figure Page

Figure Page

Figure Page

Figure Page

Figure Page

Figure Page

Figure Page

Figure Page

Figure Page

Figure Page

Figure Page

Figure Page

Figure Page

Figure Page

1. INTRODUCTION

1.1 Overview

The operation of aircraft from naval vessels constitutes a significant portion of all maritime based military operations. A large subset of these operations rely on helicopters and other rotorcraft such as the V22 Osprey to carry out important tasks such as moving men and machines from one location to another. Maritime flight operations carry substantial risk; however, this risk is magnified for rotorcraft operations due to numerous factors. Thus, ship based helicopter operations present a significant challenge for pilots and flight crew[1]. Aside from direct enemy threats, these operational risks peak during so called "terminal" operations, that is, take-off and landing configurations as shown in Figure 1.

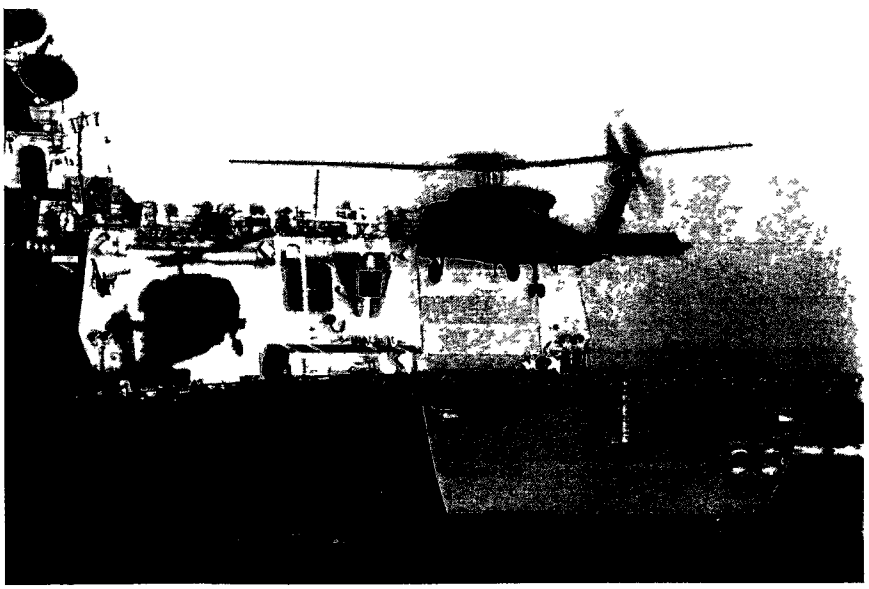

Figure 1: Helicopter landing on the deck of a naval frigate[2]

For instance, it was observed on serveral occasions that the V-22 experienced uncommanded rolls while landing on LHA ships due to the aerodynamic interactions with the ship and other landing helicopters[3]. Considerable interest and resources have been devoted to the academic study of rotorcraft operations in close proximity to ships[4]. Ship airwake/rotor downwash coupling has been identified by numerous research groups as a significant contributor to increased flight operation complexity[5,6].

The majority of ships, whether considered aviation or non-aviation, have poor aerodynamic qualities, common to bluff-bodies, that have a significant impact on helicopter handling. However, the operation of helicopters from non-aviation ships is considered to be more challenging when compared to flight operations from aviation ships[5]. Marine vessels such as aircraft carriers and amphibious assault ships (LHA) are considered "aviation" ships and characteristically have large flat landing surfaces with limited ship superstructure (islands, towers, antenna, etc.) as shown in Figure 2.

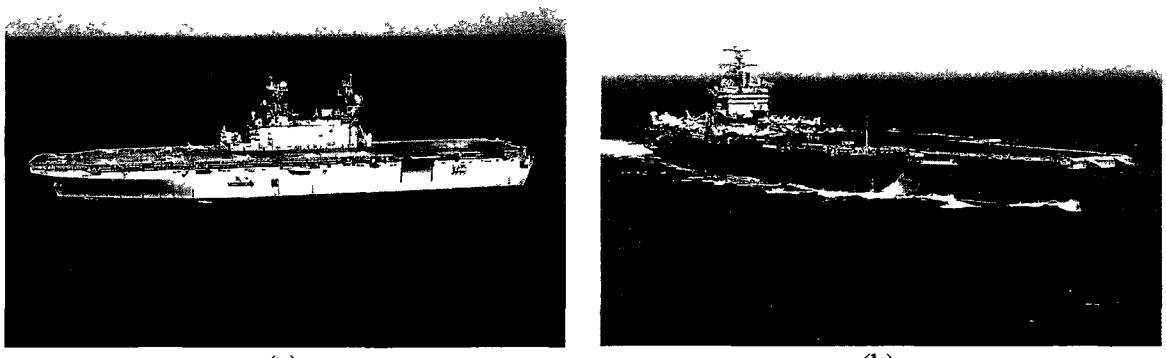

(a) (b)

Figure 2: Typical naval "aviation" vessels (a) *USS Peleliu*[7] (b) *USS Enterprise*[8]

The configuration of "aviation" ships limits the effects of airwakes on aircraft operations, though not completely, as shown in a study by Polsky and Naylor[9]. However, non-aviation ships have only a small portion of deck space reserved for flight operations as shown in Figure 3. Often, the flight deck of non-aviation ships is the same dimension as the helicopter rotor. Complicating matters, sharp-edged hangars are typically placed immediately forward of the flight deck for helicopter storage[5]. The sharp edges of the hangar and ship cause a significant airwake to be generated in the vicinity of the flight deck.

(a) (b)

Figure 3: Examples of typical "non-aviation" ships (a) *USS Mason*[10] (b) *USNS Amelia Earhart*[11]

In general, the interactions between a ship's airwake and rotor downwash are recognized by aviators and aerodynamicists as the cause for sudden changes in flight dynamics[6,12,13]. This phenomenon is responsible for increased pilot workload and increased risk to man and machine. The increase in risk and workload often leads to accidents as shown in Figure 4. In addition, this configuration has been found to cause blade strikes in which the rotor blades impact the fuselage of the helicopter[5].

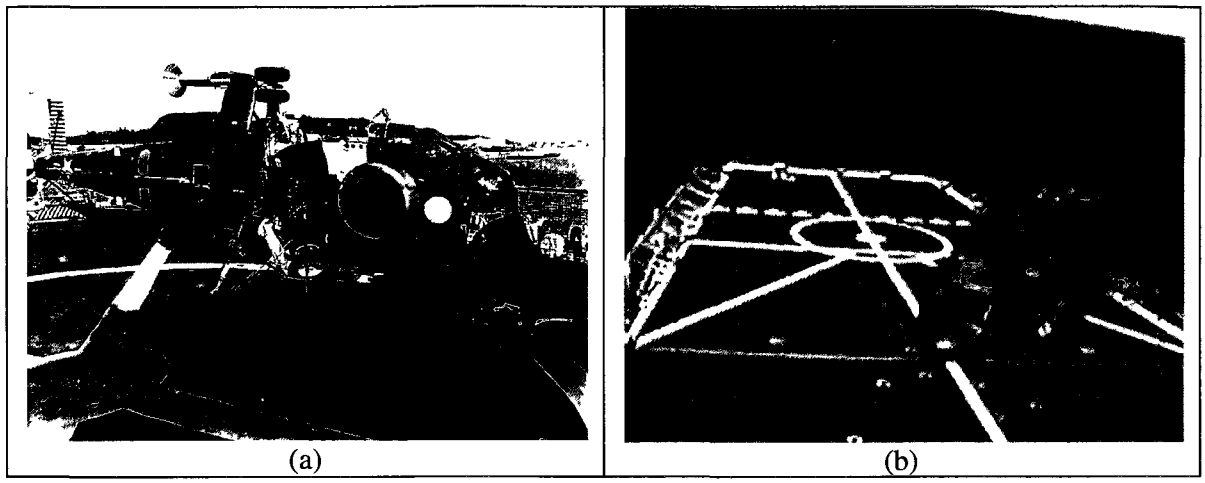

(a) (b)

Figure 4: Naval helicopter crashes during landing (a) *USS Trippe* 1978[14] (b) *USNS Arctic* 2009[15]

The ship airwake has been found to contain a wide spectrum of turbulent length scales. The effect of this turbulence ranges from the pilot feeling small vibrations to large variations in the helicopter's handling[16]. In general, ship airwakes are complex flow fields emanating from intricate ship structures such as antennas, towers, exhaust stacks, and hangars[17]. This flowfield contains strong velocity gradients and turbulence[6,16,18]. Flow separation, routinely found in the study of bluff body aerodynamics, is also a major contributor in the rotor downwash/ship airwake interaction and acts to futher complicate the flowfield. When the rotor downwash and ship airwake are considered in a combined fashion, representing a landing or takeoff configuration, the flowfield is considered to be coupled[18]. Coupling, as defined by Naval Air Systems Command(NAVAIR)computational fluid dynamics (CFD) modelers, is a condition in which the rotor wake has a significant impact on the inflow at the rotor and superposition fails to accurately predict the flowfield. In this case, superposition refers to the modeling of a complex flowfield (e.g. combined rotor downwash and ship airwake) by

mathematical addition or subtraction of fundamental flowfield components (e.g. isolated ship airwake, isolated rotor, isolated freestream). In general, the ship airwake/rotor downwash interaction forms a complex flowfield that pushes the limits of man, machine, and current computational abilities[19].

In all cases, operational limits must be developed to guide pilots and crew in the safe operation of aircraft[5]. Figure 5 shows an example operational envelope for a helicopter as presented in Wilkinson et al.[20] In Figure 5, radial lines indicate the relative wind direction with respect to the helicopter, circumferential lines indicate wind speed, and the shaded area represents safe operating conditions. Operational envelopes are developed through at-sea trials (dynamic interface testing) and require considerable time and resources[5]. Even after testing is complete, the outcome of the tests are not guaranteed due to variability in weather and other factors[5]. Therefore, the development of simulation capabilities (both CFD and real-time flight simulation) is of great interest to the naval aviation community[1,5].

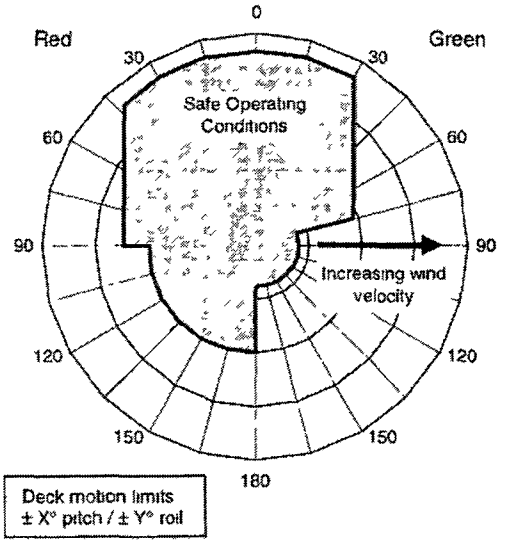

Figure 5: Example of helicopter flight envelope[20]

The development of accurate computational fluid dynamics simulations allows for pre-production design improvments and investigations, saving time and money[12]. Similarly, the development of high fidelity flight simulations allows for improvements to be made in pilot training by allowing the trainee to experience the ship environment before attempting actual operations[12].

The development of accurate flight simulations requires high-fidelity models of the near-ship environment and the inclusions of coupling effects between ship airwake and rotor downwash[12]. The unsteady turbulent flow of the ship's airwake is considered difficult to predict. Adding to this technical challenge is the coupled interaction between the helicopter and ship airwake. Researchers have observed that the flowfield induced by rotor downwash significantly influences the upstream flow[12]. At the present time, flight simulators are able to incorporate an airwake effect using superposition techniques[12]. However, the superposition technique considers only the influence of the airwake on the helicopter with no inclusion of the coupling effect between the rotor and airwake[12]. This approach therefore limits the realism of current piloted flight simulations. In addition, real-time CFD based flight simulations incorporating the airwake and rotor downwash interaction are computationally intensive and not possible with today's technology[12].

Due to the computational issues related to the integration of real-time CFD simulations of the airwake/downwash interaction in piloted flight simulators, a hybrid approach has been proposed by NAVAIR. It is hypothesized that by incorporating an airwake/downwash interaction model, generated from offline CFD simulations, for regions where coupling is significant and switching to standard superposition techniques

in regions where coupling is not significant, the fidelity of piloted flight simulations can be improved.

1.2 Problem Statement and Objective

Current helicopter flight simulations rely on superposition techniques to model the effects of wind gust or ship airwake on helicopter handling. Unfortunately, this superposition technique is inadequate for accurate modeling of the aerodynamic coupling associated with a helicopter operating in close proximity to a ship. NAVAIR defines coupling as the region where rotor downwash has a significant impact on the rotor inlet and superposition fails to accurately predict the flowfield. The superposition technique adds velocity perturbations to an isolated helicopter rotor configuration in the form of a gust as shown in Figure 6. The velocity perturbations are computed from independent airwake and freestream components with no incorporation of the coupling phenomenon.

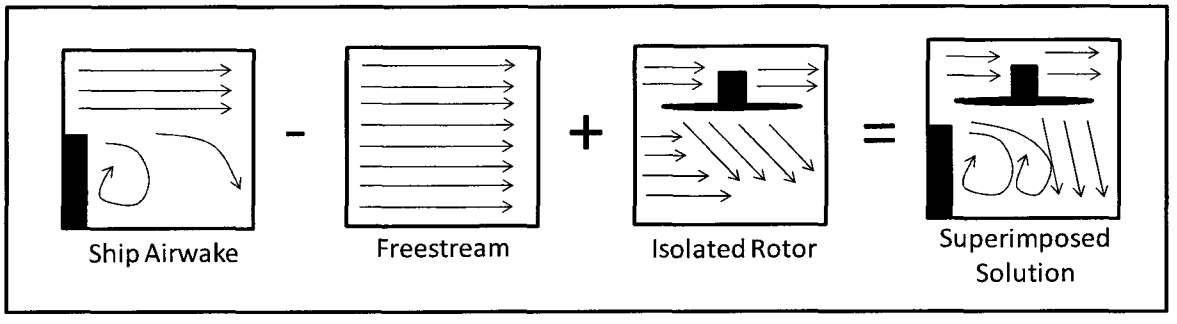

Figure 6: Illustration of the superposition technique used in real-time flight simulations

CFD has shown progress towards the accurate modeling of the coupling phenomenon. However, incorporation of CFD into real-time flight simulations is not yet

feasible due to computational limitations. Based on discussions with NAVAIR researchers, it is believed that a series of "off-line" CFD simulations of close-in ship/helicopter configurations could be used to develop an appropriate airwake model that could be preloaded into flight simulations. The key problem in the application of this technique is the large computational resources required to model the entire ship/helicopter flowfield. Therefore, it is desired to reduce the size of the computational domain to focus only on the region where superposition fails to accurately model the flowfield.

Based on the computational problem given above, the objective of this study is to develop wind tunnel measurement techniques capable of quantifying the degree of aerodynamic coupling between a rotor and ship airwake. The developed technique can then be used to identify regions above the frigate's landing deck where aerodynamic coupling is significant. The defined region can then be used to guide computational fluid dynamics (CFD) and flight simulations.

2. LITERATURE REVIEW

2.1 Overview of Wind Tunnel Investigations

Wind tunnel and full scale experimental studies have been performed by various research groups to investigate the aerodynamic coupling of ships and aircraft. Wind tunnel tests are useful in identifying the underlying aerodynamic interactions responsible for the coupling phenomena and are ideally suited to investigate worst case configurations[3]. In addition, wind tunnel studies provide much needed validation data for CFD simulations[4]. The majority of the work performed has focused on ship airwake/rotor downwash coupling, however some studies have examined the interaction between ships and fixed wing aircraft[9]. As with any investigative technique (wind tunnel, CFD, or full scale testing), limitations exist which must be considered during the experiment planning and design phase. In the case of scaled wind tunnel studies, ideally the proper matching of similarity parameters to ensure accurate representation of the relevant physics is highly desirable. In most cases, Reynolds number (Re) is used to ensure dynamic similitude. However, due to the large scale of naval ships, wind tunnel speed limitations prohibit the matching of Reynolds number[3]. Thus, for the ship airwake problem, a different approach must be taken to ensure similitude. Rotor advance ratio (AR) and thrust coefficient (C_T) were determined to be the key similarity parameters required to best reproduce the full-scale configuration[3]. Thus, by matching only thrust coefficient and advance ratio, the constraint on model scale is sufficiently relaxed[3].

2.2 Experimental and Computational Modeling of Ship Geometries

Model geometries of varying complexities have been used in the study of ship airwakes and ship airwake/rotor downwash interactions. Past studies (both experimental and computational) have relied on simple ship models that are based on a backward facing step (see Figure 7) with the addition of a simplified rectangular tower (Figure 8) or exhast stack[6, 17, 20, 21, 22, 23] and triangular bow (Figure 9)[16, 24].

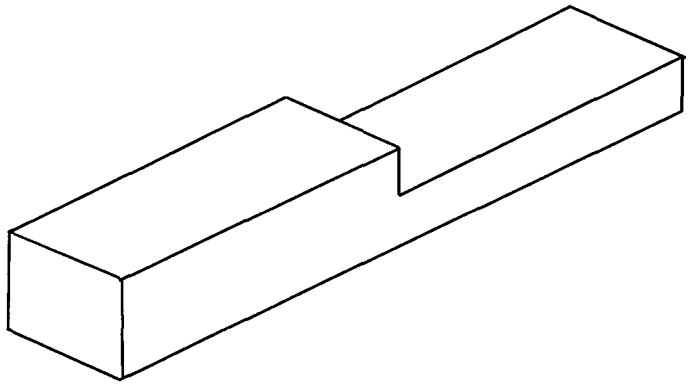

Figure 7: Backward facing step geometry

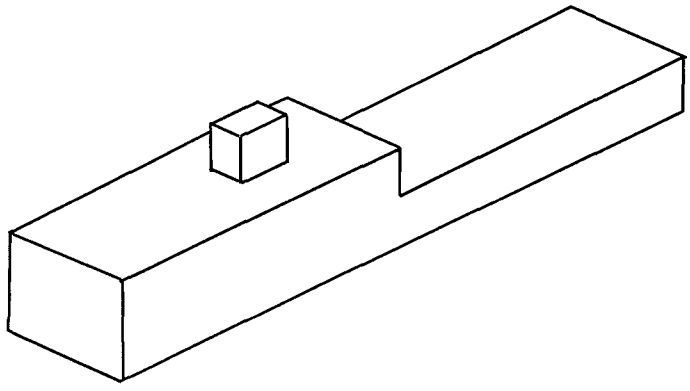

Figure 8: Simple frigate shape (SFS) with exhaust stack[20]

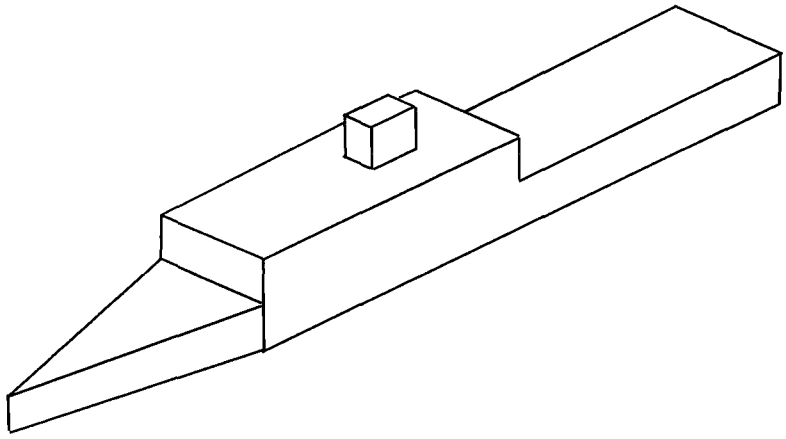

Figure 9: Simple frigate shape (SFS) with exhaust stack and triangular bow[16]

These simplified geometries, commonly refered to by the acronym SFS (simple frigate shape), were developed through an international collaboration between the United States, Canada, Australia, and the United Kingdom[20, 22]. The nominal dimensions of the geometries are scaled to match a typical naval frigate. In addition, the sharp edges of the simplified geometry make the model relatively insensitive to mismatched Reynolds numbers. This permits a fundamental study of the ship airwake/rotor downwash problem. Other studies have utilized higher fidelity ship models, like those shown in Figures 10 and 11, that include exhaust stacks, antenna towers, and hangar doors to better model the more intricate factors affecting ship airwakes[3, 18, 25, 26, 27, 28, 29, 30].

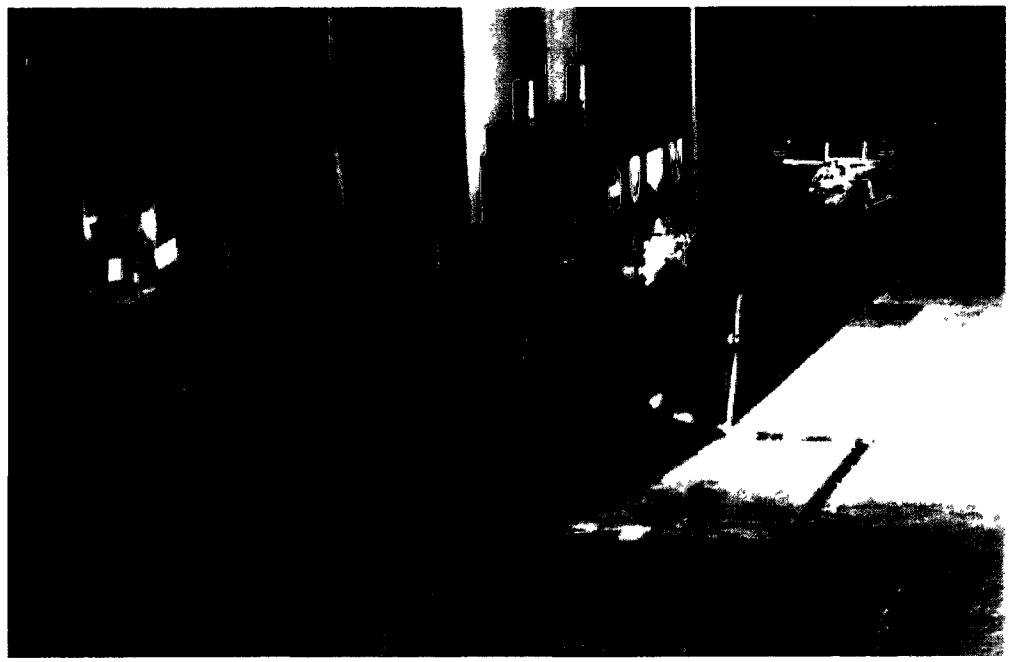

Figure 10: LHA ship model for helicopter/tiltrotor interaction wind tunnel investigation[3]

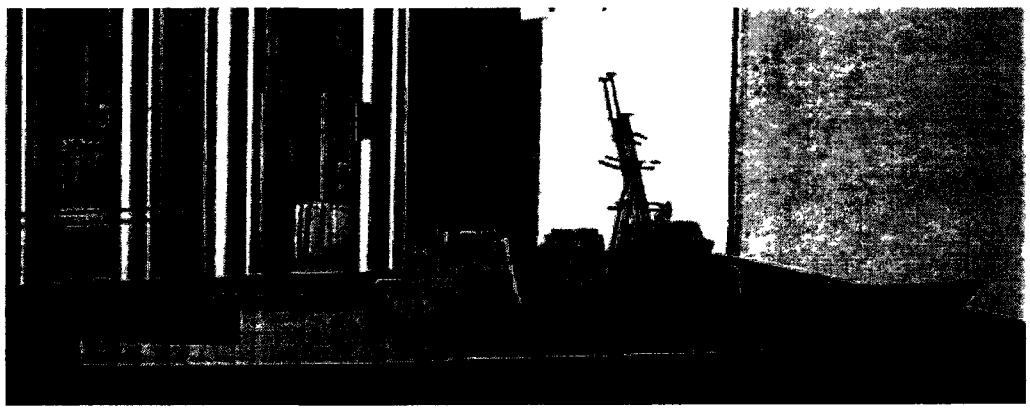

Figure 11: 1/144th scale wind tunnel model of the *USS Winston S. Churchill* (DDG-81)[29]

2.3 Experimental and Computational Modeling of Helicopter and Rotor Geometries

Like the variety of scaled ship models mentioned in the previous section, scaled helicopter and rotor models are also found with various levels of detail. Reported model designs ranged from simplistic fixed pitch rotors with no fuselage to highly detailed rotor hubs and variable pitch blades with fuselage. Zan[31] utilized a fixed pitch rotor with no collective, teetering, flapping, or lead/lag capabilities. This was due to the relatively small scales involved in the problem and the difficulty in fabricating such models. A small 500W DC electric motor was used in this study to drive the rotor. A constant voltage was applied to the motor ensuring a constant rotor rotation rate.

In studies by Silva et al.[3] and Wadcock et al.[32] the so-called "Roll On-Deck" phenomena of the V-22 rotorcraft was examined. In these studies highly detailed helicopter and rotor models were constructed using off-the-shelf (RC) components and included a fuselage as shown in Figures 12-14.

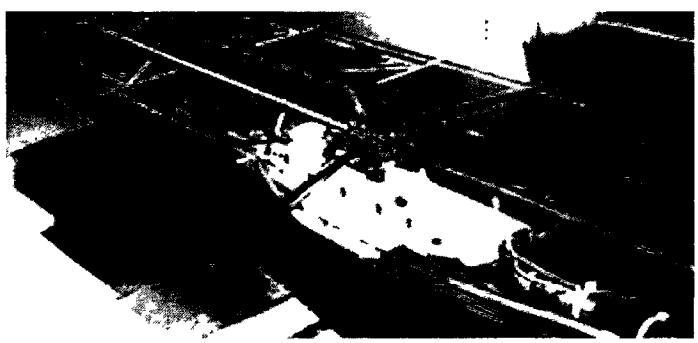

Figure 12: 1/48th scale model of a CH-53E helicopter[3]

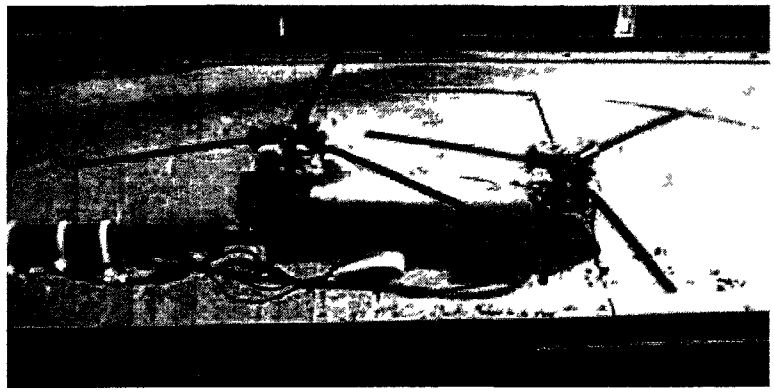

Figure 13: 1/48th scale model of a CH-46 tandem-rotor helicopter[3]

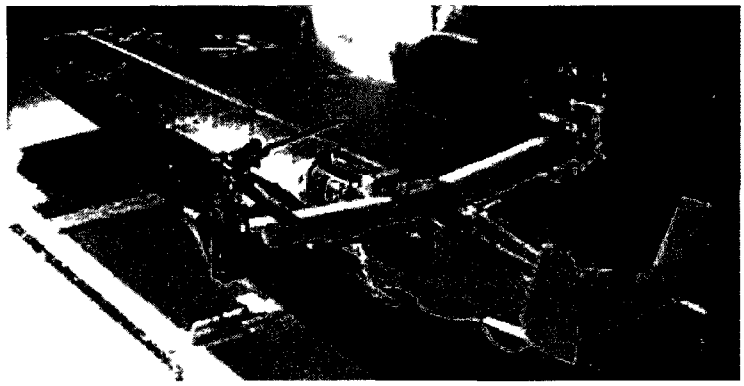

Figure 14: 1/48th scale model of a V-22 tiltrotor[3]

2.4 Summary of Past Wind Tunnel Research

For experimental work, model scales typically ranged from 1/48th scale such as in a V-22/LHA study by Silva et al.[3] to 1/144th scale as in a DDG airwake study by Woodson and Ghee[29]. In the study by Silva et al.[3] the wind tunnel test section measured 7ft high by 10ft wide by 15ft in length, and wind speeds ranged between 13 and 26 ft/s (3.96- 7.92 m/s)[3]. The ship model was mounted on the floor of the wind tunnel as shown in Figure 15.

Figure 15: 1/48th scale LHA model installed in the Army 7x10 ft. wind tunnel[3]

In the study by Woodson and Ghee[29] CFD airwake simulations were verified using scaled wind tunnel tests. The wind tunnel tests used a 1/144th scale DDG model that was mounted eight inches above the tunnel floor (Figure 16) on a raised ground board that measured 62 inches in length and 46.5 inches in width. The wind tunnel test section measured 4 x4 ft. The tunnel wind speed during testing was set to 75 ft/s.

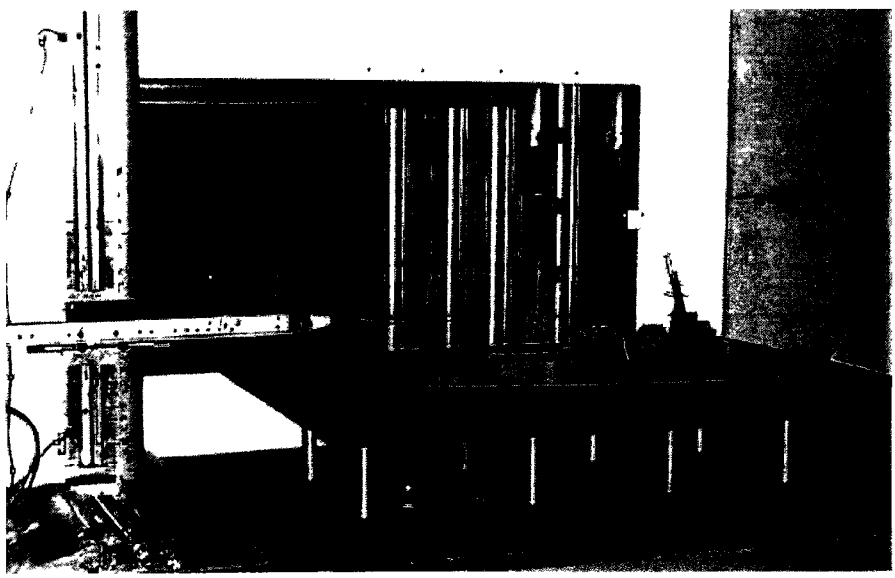

Figure 16: 1/144th scale DDG model mounted on a raised groundboard[29]

Thermal anemometry was used to capture the velocity and turbulence intensity in the wake of the DDG model. A two-axis traversing system was used to position the hot-film probe. The probe was positioned at various locations (forming a grid pattern within measurement planes) as shown in Figures 17 and 18.

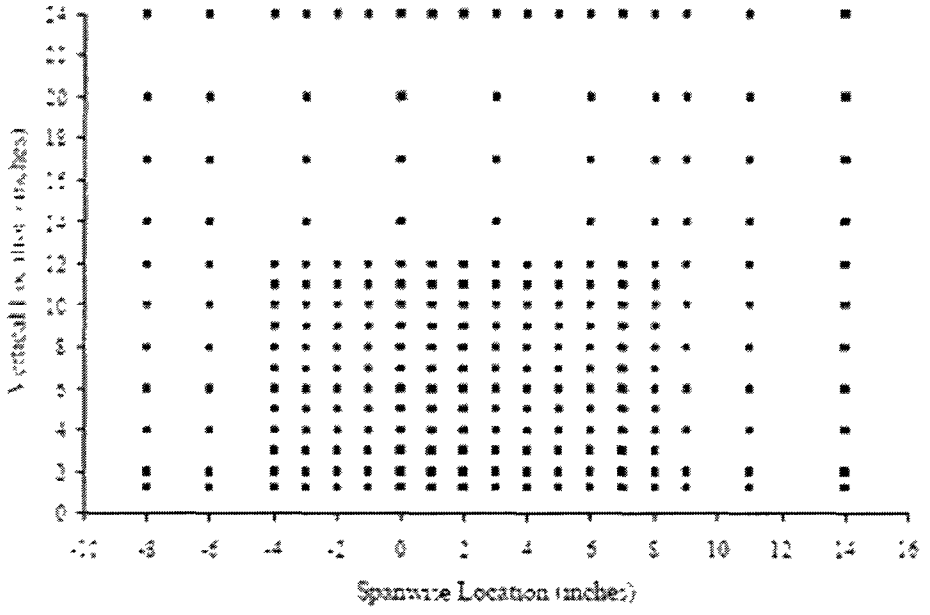

Figure 17: Vertical and spanwise location of hot-film measurements[29]

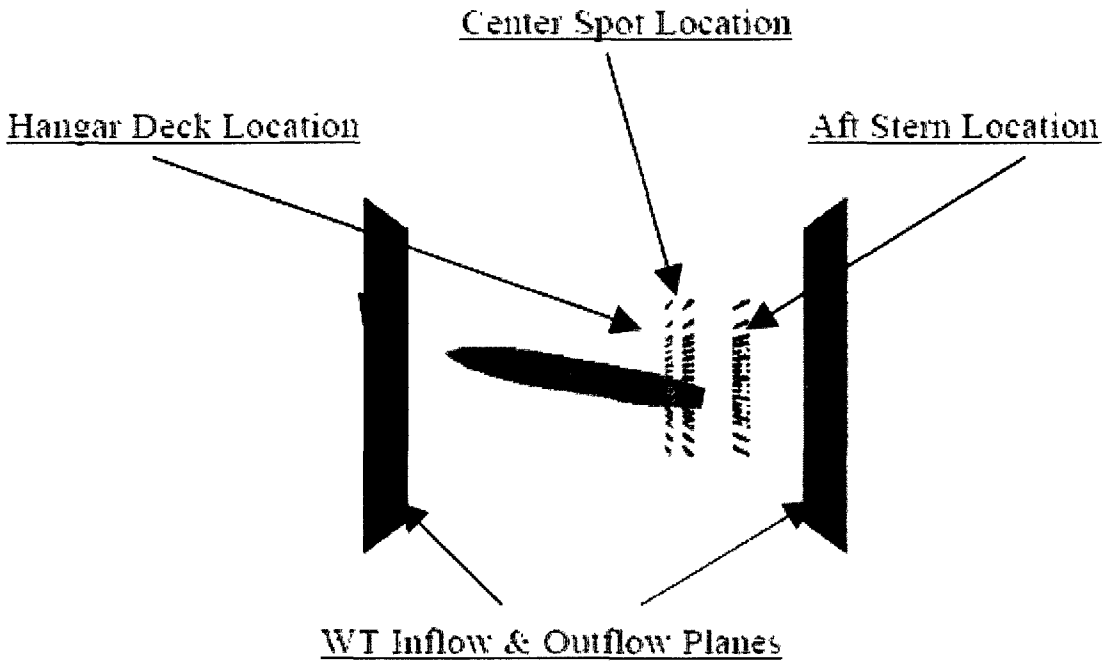

Figure 18: Location of hot-film measurement planes[29]

The results of the wind tunnel study for a 10 deg. starboard yaw as shown in Figure 18 are presented as contours (Figures 19-21) of the velocity field as measured by the single-film probe (a) and CFD simulation (b). The units of the velocity contours are ft/s. A comparison between the wind tunnel measurements and the CFD simulations reveals that CFD is able to predict the ships airwake with reasonable accuracy. The magnitude of the airwake velocity gradients is seen to decrease as the measurement plane moves aft.

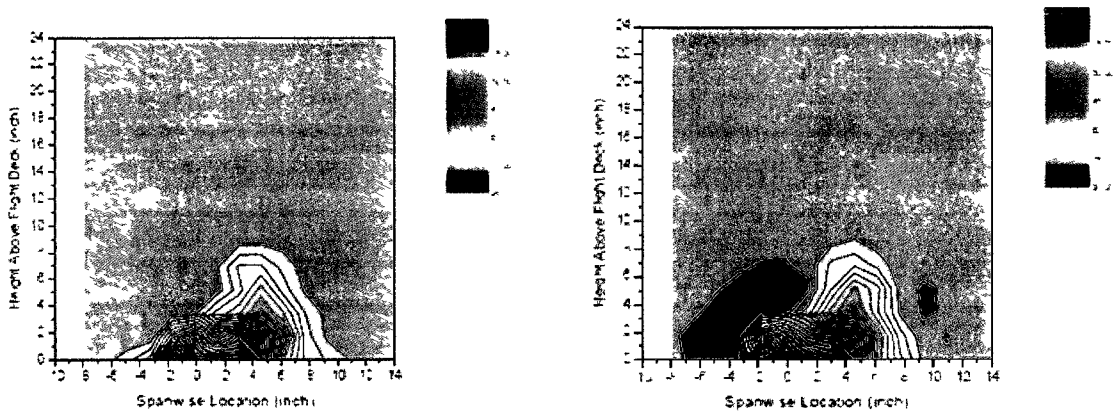

(a) Wind Tunnel **(b) CFD**

Figure 19: Forward most hot-film velocity survey[29]

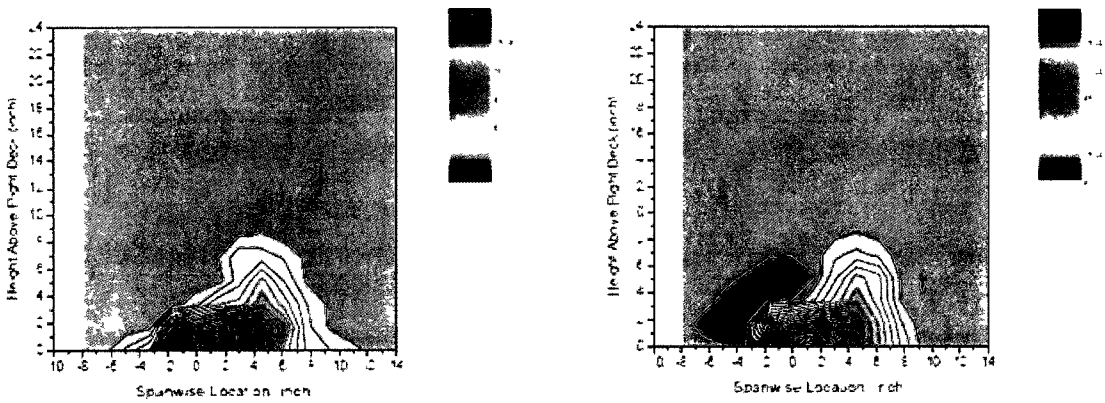

(a) Wind Tunnel (b) CFD

Figure 20: Hot-film velocity survey for center measurement plane[29]

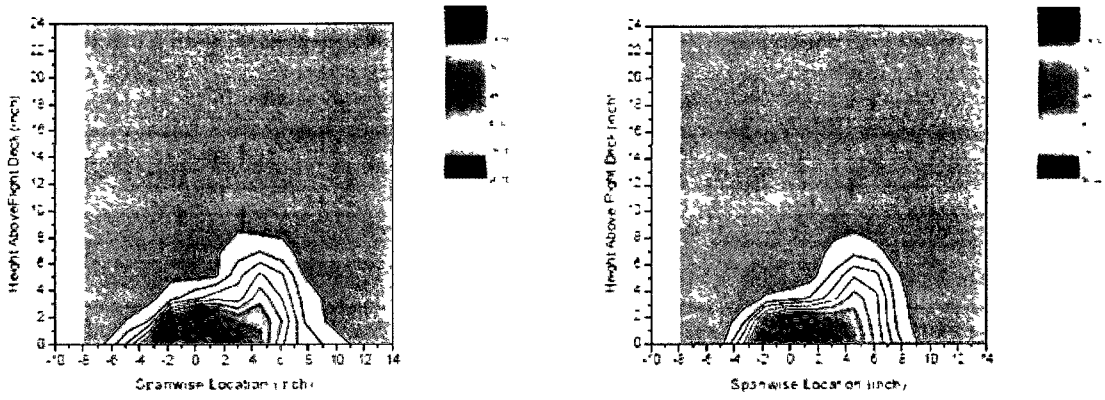

(a) Wind Tunnel (b) CFD

Figure 21: Rear most hot-film velocity survey[29]

While experimental studies examining both rotor downwash and ship airwake are limited, as most experimental studies focus solely on ship airwakes, studies by Zan[31] and Silva et al.[3] utilized both rotor and ship models for experimental investigation.

In a study by Zan[31] an experimental wind tunnel investigation was performed in which the variation of rotor thrust over the landing deck of two different simplified Canadian patrol frigate geometries (Figure 22) was examined.

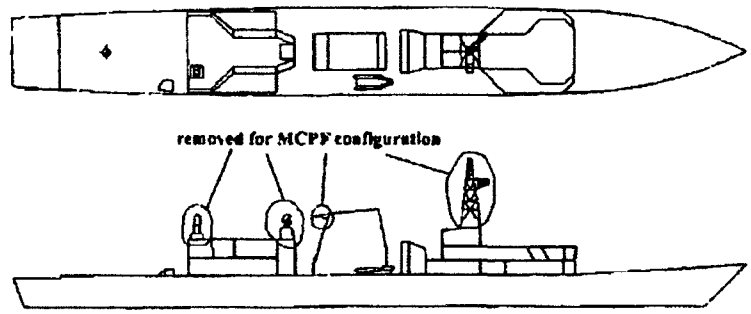

Figure 22: 1/50th scale simplified Canadian patrol frigate model[31]

In general the purpose of this study was not to consider absolute values of rotor thrust but instead to examine rotor thrust gradients in the ship airwake. No helicopter fuselage was included in this study. The observed rotor thrust variations, reported in terms of a rotor thrust coefficient along lateral planes for a wind-over-deck angle (WOD) of zero degrees, are shown in Figures 23-25.

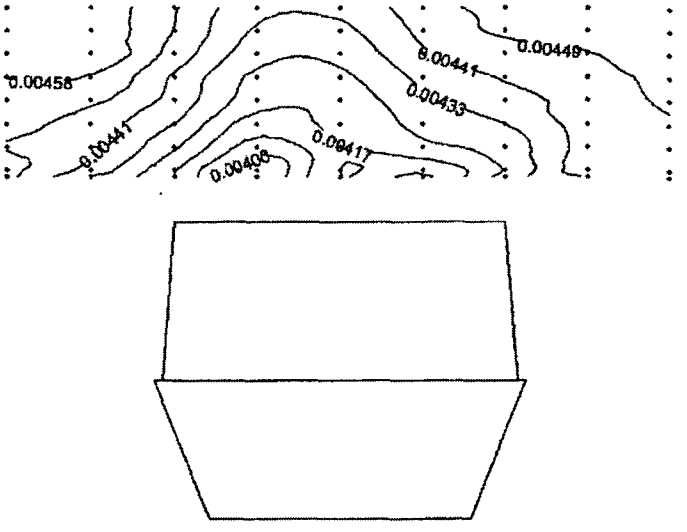

Figure 23: Thrust coefficient contours shown for lateral plane x=-3.6m using the Canadian patrol frigate geometry, for a tunnel speed of V=19 m/s, and a WOD=0 deg.[31]

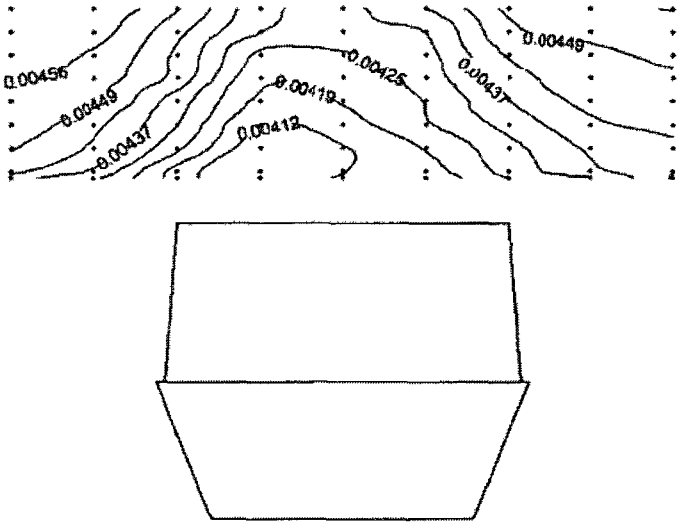

Figure 24: Thrust coefficient contours shown for lateral plane x=6 m using the Canadian patrol frigate geometry, a tunnel speed of V=19 m/s, and a WOD=0 deg.[31]

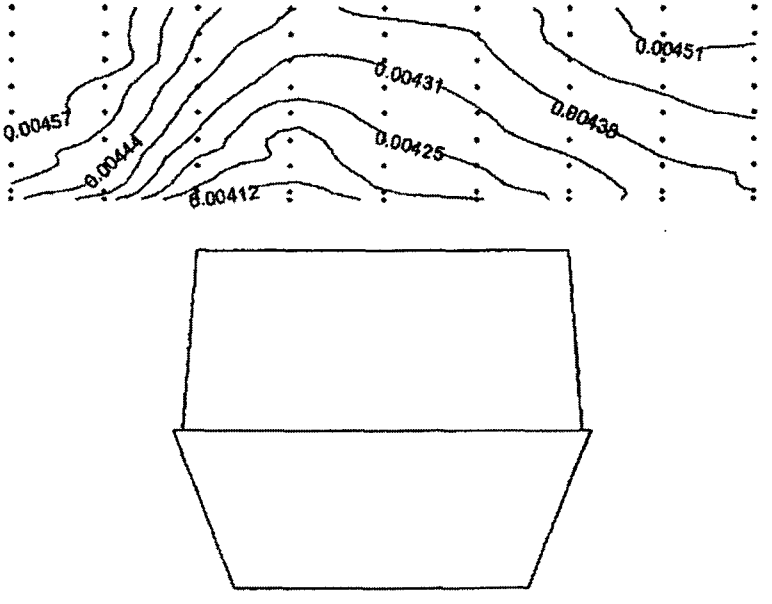

Figure 25: Thrust coefficient contours shown for lateral plane x=19 m using the Canadian patrol frigate geometry, a tunnel speed of V=19 m/s, and a WOD=0 deg.[31]

Results indicate that as the rotor is moved aft, rotor thrust increases. Zan[31] notes that this phenomenon is caused by the increase in streamwise velocity flow that is seen by the rotor as it moves aft. Figure 26 reports the observed rotor thrust variations for a longitudinal plane corresponding to the centerline of the ship landing deck. Results indicate a significant gradient in the vertical direction with rotor thrust decreasing as the rotor nears the landing deck. Only a small gradient was observed in the forward-aft direction.

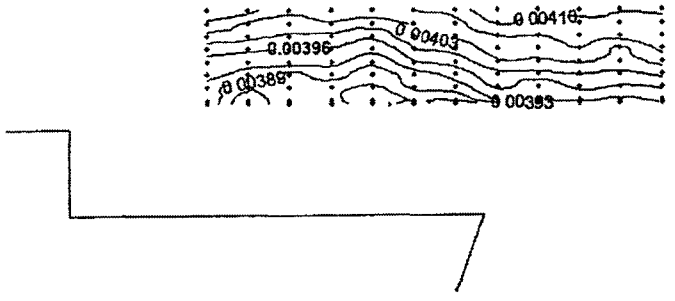

Figure 26: Thrust coefficient contours shown for longitudinal plane y=0 m using the Canadian patrol frigate geometry, a tunnel speed of V=19 m/s, and a WOD=0 deg.[31]

The effect of ship superstructure on rotor thrust variations was examined by comparing contours of rotor thrust coefficient for the Canadian patrol frigate geometry (Figures 27-29) and the modified Canadian patrol frigate geometry (Figures 30-32). Recall that the modified Canadian patrol frigate geometry is the same as the original geometry with the antennas and towers removed. The results indicate that superstructure has a significant effect on the observed rotor thrust.

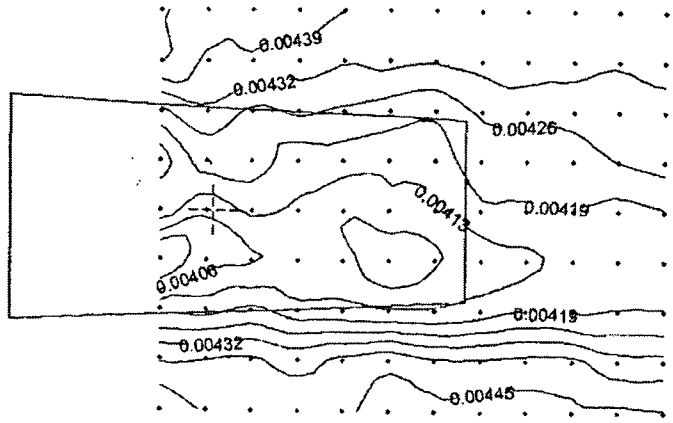

Figure 27: Thrust coefficient contours shown for elevation plane z=9 m using the Canadian patrol frigate geometry, a tunnel speed of V=19 m/s, and a WOD=0 deg.[31]

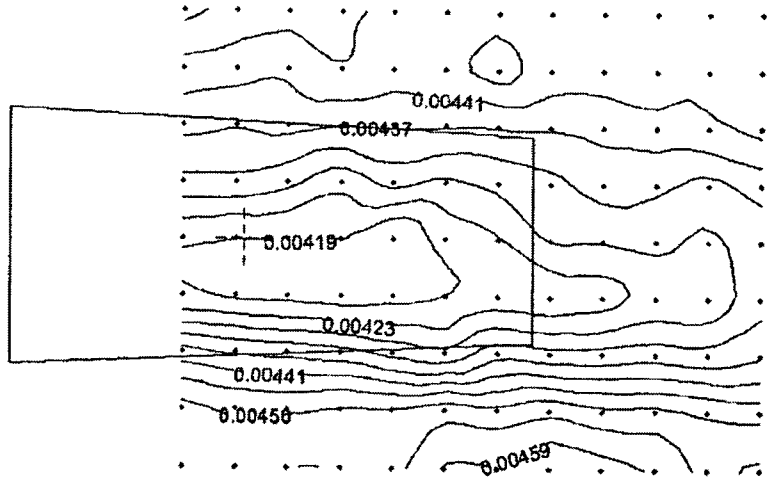

Figure 28: Thrust coefficient contours shown for elevation plane z=12 m using the Canadian patrol frigate geometry, a tunnel speed of V=19 m/s, and a WOD=0 deg.[31]

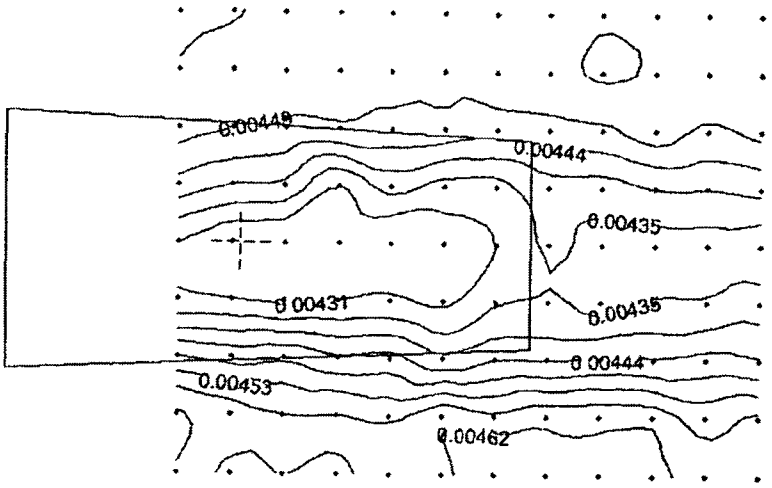

Figure 29: Thrust coefficient contours shown for elevation plane z=15 m using the Canadian patrol frigate geometry, a tunnel speed of V=19 m/s, and a WOD=0 deg.[31]

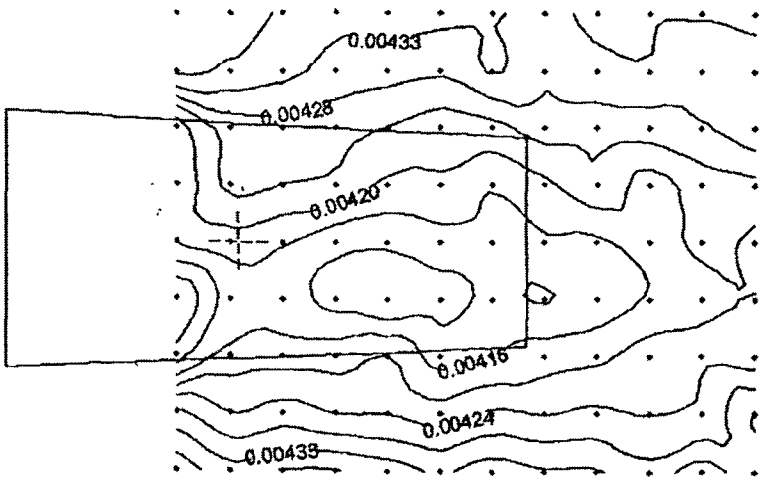

Figure 30: Thrust coefficient contours shown for elevation plane z=9 m using the modified Canadian patrol frigate geometry, a tunnel speed of V=19 m/s, and a WOD=0 deg.[31]

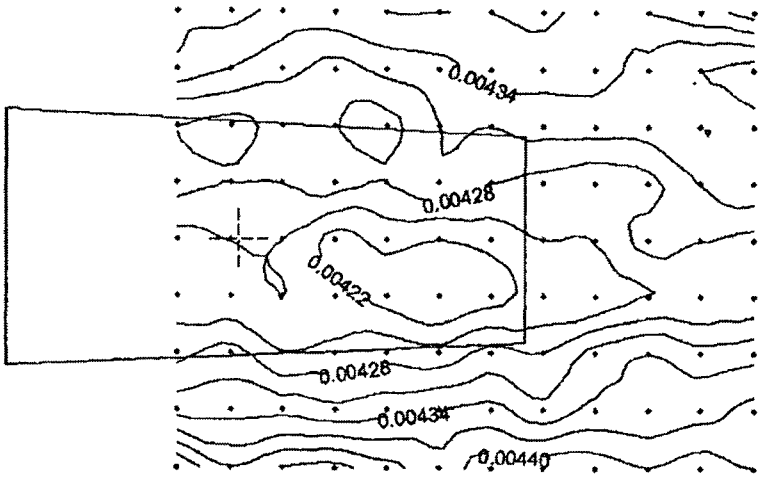

Figure 31: Thrust coefficient contours shown for elevation plane z=12 m using the modified Canadian patrol frigate geometry, a tunnel speed of V=19 m/s, and a WOD=0 deg.[31]

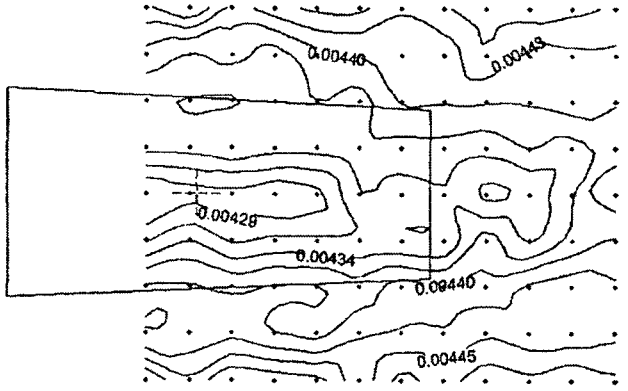

Figure 32: Thrust coefficient contours shown for elevation plane z=15 m using the modified Canadian patrol frigate geometry, a tunnel speed of V=19 m/s, and a WOD=0 deg.[31]

Additional investigations were performed at a reduced tunnel wind speed (7.2 ms/) to examine the effect of freestream wind conditions on the rotor/airwake interaction. The observed rotor thrust variations (reported as rotor thrust coefficient) are shown below in Figures 33-35.

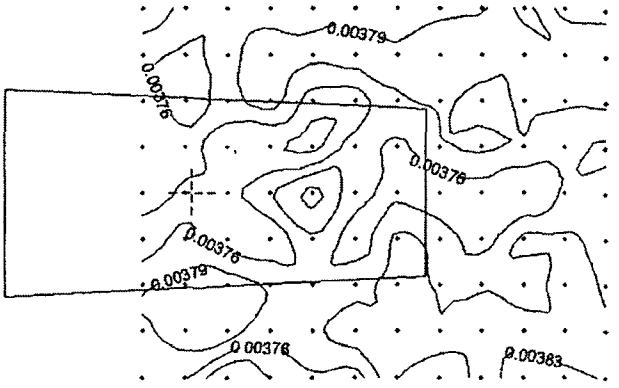

Figure 33: Thrust coefficient contours shown for elevation plane z=9 m using the modified Canadian patrol frigate geometry, a tunnel speed of V=7.2 m/s, and a WOD=0 deg.[31]

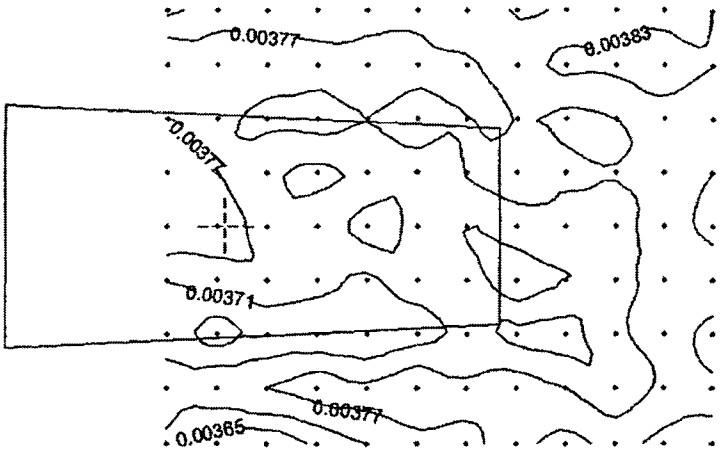

Figure 34: Thrust coefficient contours shown for elevation plane z=12 m using the modified Canadian patrol frigate geometry, a tunnel speed of V=7.2 m/s, and a WOD=0 deg.[31]

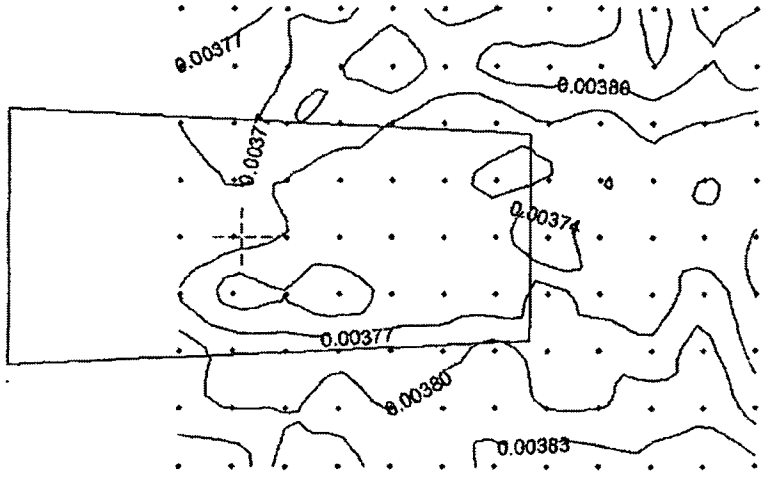

Figure 35: Thrust coefficient contours shown for elevation plane z=15 m using the modified Canadian patrol frigate geometry, a tunnel speed of V=7.2 m/s, and a WOD=0 deg.[31]

Results indicate that for the lower tunnel speed, the effect of the ship airwake has been significantly reduced. Researchers note that in this configuration, the overall degree of coupling has been reduced since rotor downwash overpowers the coupling phenomenon. It is also mentioned that even though rotor thrust variations are minimal, pilot workload may still remain high since the reported rotor loadings are averages. Averaging does not reveal the potentially strong unsteady flow that exists in the ship airwake.

In a study by Silva et al.[3] an experimental investigation was conducted to examine the aerodynamic interactions between helicopters (CH-46 and CH-53) and tiltrotors (V-22) while in landing configuration on an aviation ship (LHA). The study measured the flowfield in the vicinity of the V-22 and the force and moments of the V-22 tiltrotor at various locations and aircraft configurations. This study examined isolated ship, isolated rotorcraft, and combined rotorcraft and ship configurations[3].

Silva et al.[3] utilized stereo Particle Image Velocimetry (PIV) techniques to obtain three-component velocity measurements of the flowfield associated with various ship/helicopter/tiltrotor configurations (isolated aircraft, isolated ship, and ship with on-deck V-22 and upwind aircraft). PIV surveys were conducted at several lateral planes as shown in Figure 36. PIV results were comprised of 50 to 100 instantaneous frames collected at a frame capture rate of 2Hz[3]. A diagram of the overall experimental setup of the PIV system obtained from Silva et al.[3] is shown in Figure 37.

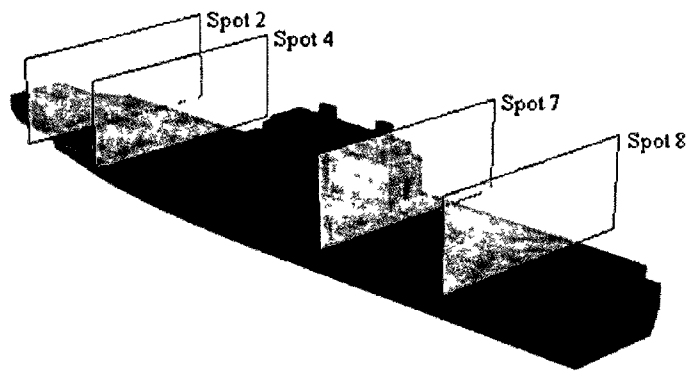

Figure 36: Measurement planes for ship airwake PIV survey[3]

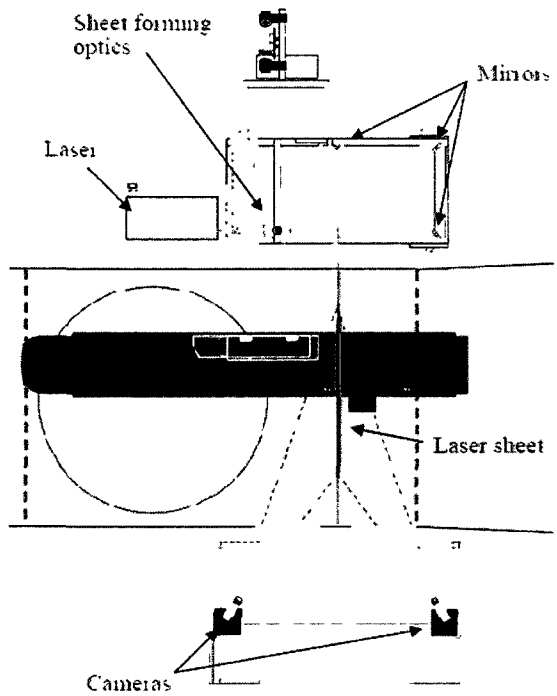

Figure 37: Stereo PIV setup for helicopter/tiltrotor interaction study[3]

An initial investigation examined the isolated ship airwake at measurement planes (spot) 2, 4, 7, and 8 for a WOD angle of 0 and 135 deg. Results from the airwake study as reported by have been included as Figure 38 and Figure 39. Significant findings in the airwake study include the deck edge vorticies seen in Figure 38 at spot 2 and 4 and the strong effect of wind-over-deck angle WOD on ship airwake structure as seen by comparing spot 7 in Figures 39 and 40.

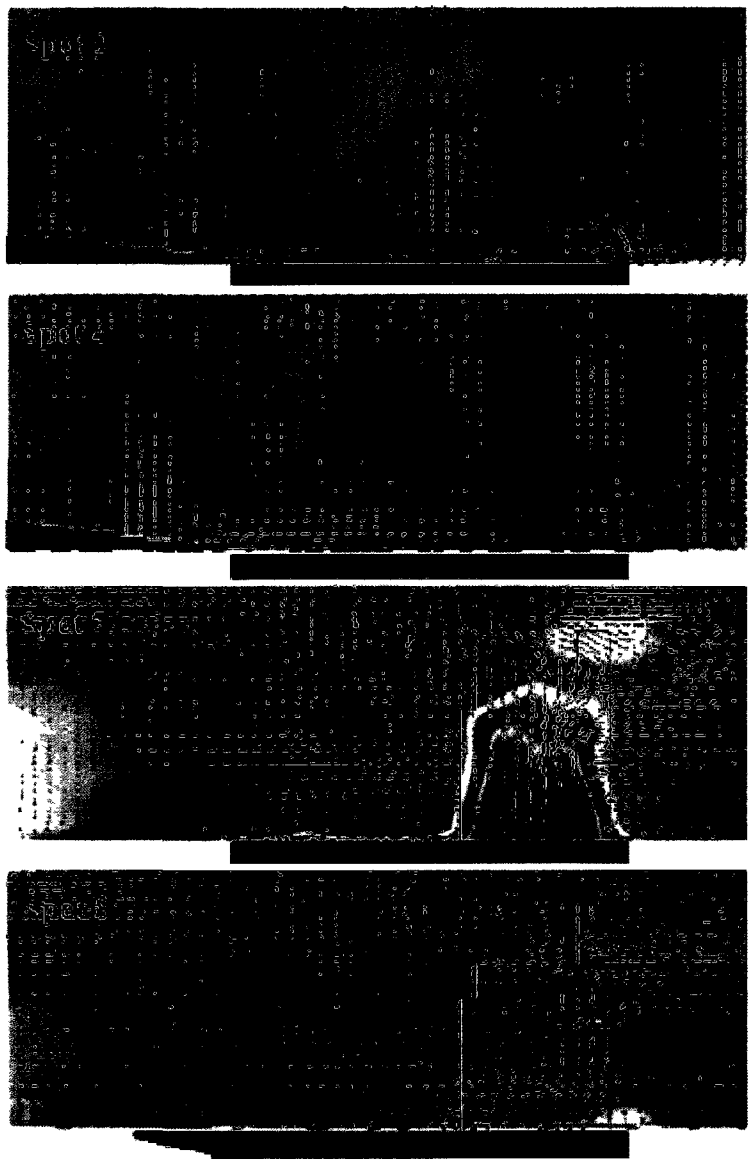

Figure 38: Results from a model scale ship airwake PIV survey with WOD=0 and wind speed of 40 kts.[3]

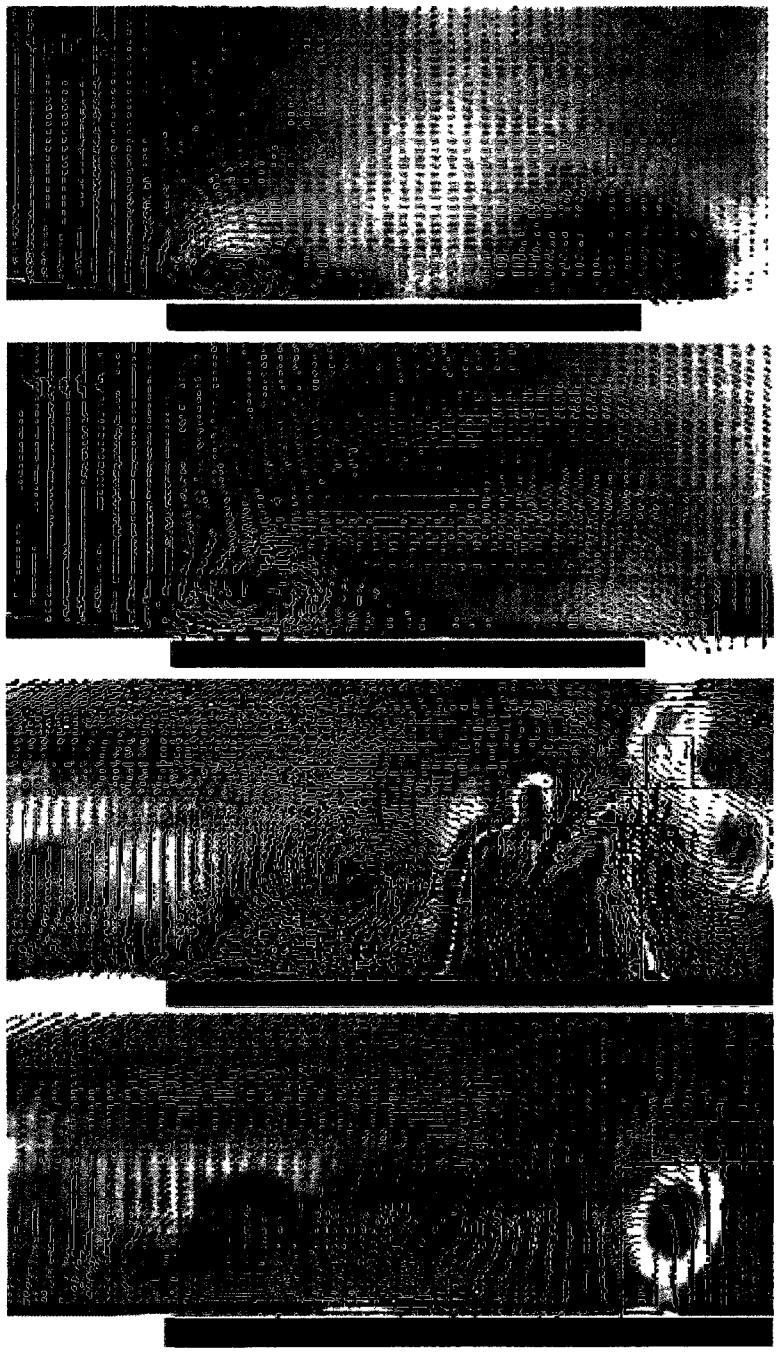

Figure 39: Results from a model scale ship airwake PIV survey with WOD=135 deg. and wind speed of 40 kts.[3]

In addition to the airwake survey, the rotor downwash of an isolated V-22 tiltrotor was examined. The results of this survey (shown in Figure 40) indicate strong recirculation regions at the edge of the rotor disk.

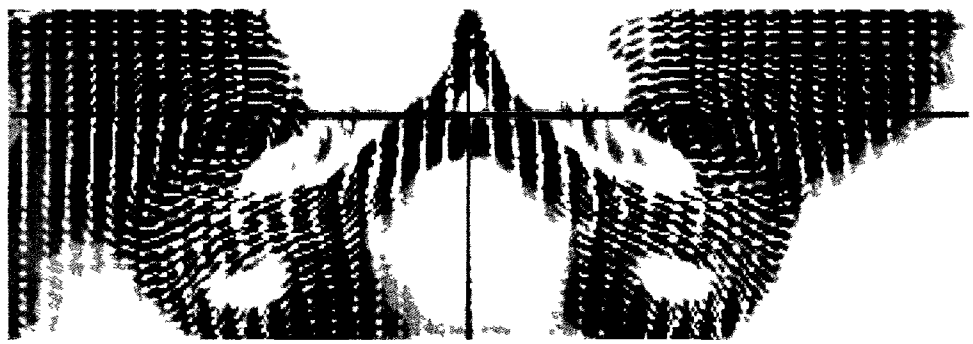

Figure 40: Results from a PIV survey of an isolated model scale V-22[3]

A typical operational configuration (Figure 41) involving an on-deck V22 and hovering CH-46 was investigated using PIV surveys. The time averaged results (from 100 instantaneous surveys) have been included below from Silva et al.[3] as Figure 42. This configuration was chosen due to the peak left rolling moment obtained in the force and moment study. The results detail the highly complex flowfield associated with maritime rotorcraft operations. The two tip vortices from the forward and aft rotors of the CH-46 helicopter have combined to form two large vortices ahead of the V-22 tiltrotor[3]. This aerodynamic configuration is associated with a peak left rolling moment for the on-deck V-22.

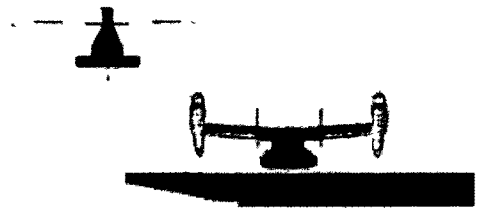

Figure 41: Aircraft configuration for combined ship airwake, on-deck V-22, and hovering helicopter[3]

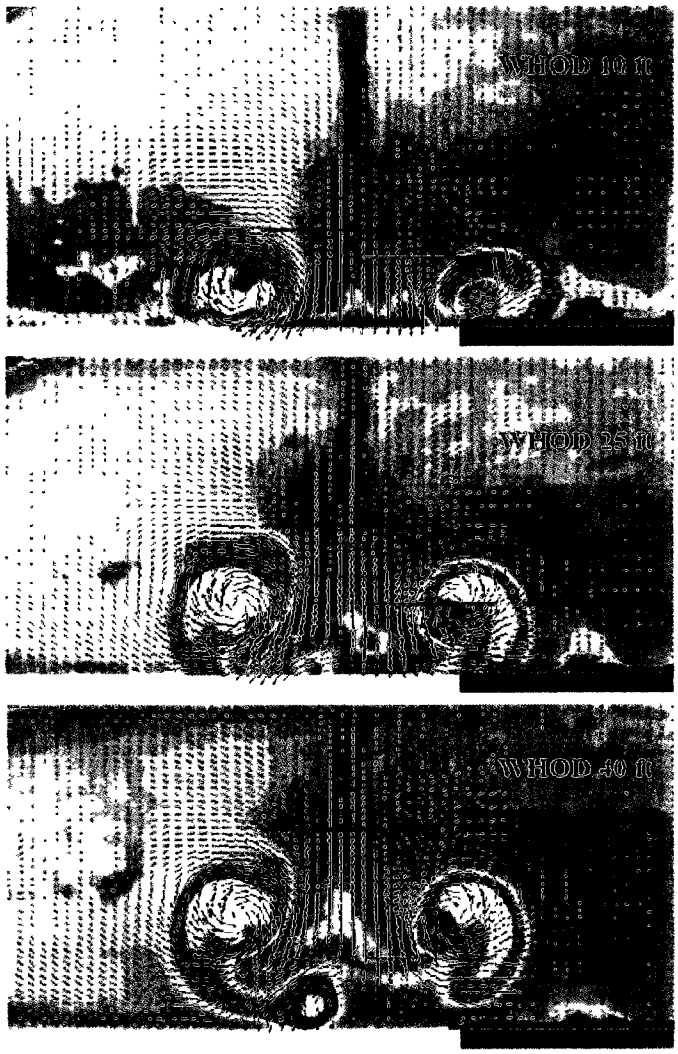

Figure 42: Results from PIV survey for a combined ship airwake, on-deck V-22, and hovering helicopter configuration[3]

2.5 Full Scale Experimental Studies

Full scale tests are useful since no scaling or simplifications are required (i.e. actual helicopter and ship are used). However, the inherent difficulties in making accurate full-scale measurements aboard operational ships presents a significant challenge to researchers. Variability in wind conditions, atmospheric boundary layers, and ship motion all limit the feasibility of full-scale measurement and support the use of

wind tunnel studies[32]. In a study by Polsky and Wilkinson[12] a full scale flight test was conducted in which a helicopter was hovered in front of a vertical face (large airport hangar) as shown in Figure 43 (experiment) and Figure 44 (computational model).

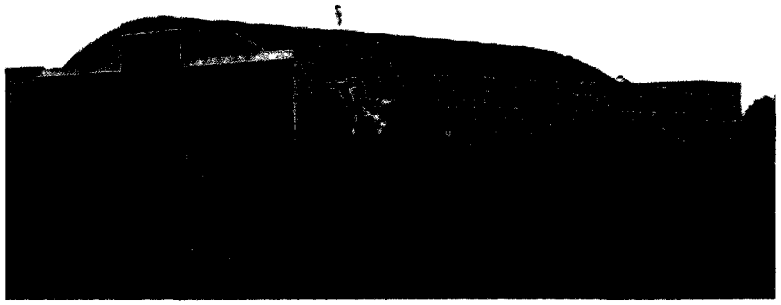

Figure 43: Airport hangar used in full scale aerodynamic interaction study[12]

Figure 44: Computational model of airport hangar used in full scale aerodynamic interaction study[12]

This study used ultrasonic anemometers to collect point velocity data in the downwash of a hovering helicopter. The layout of ultrasonic anemometers in addition to approximate wind direction for the full scale study is shown in Figure 45.

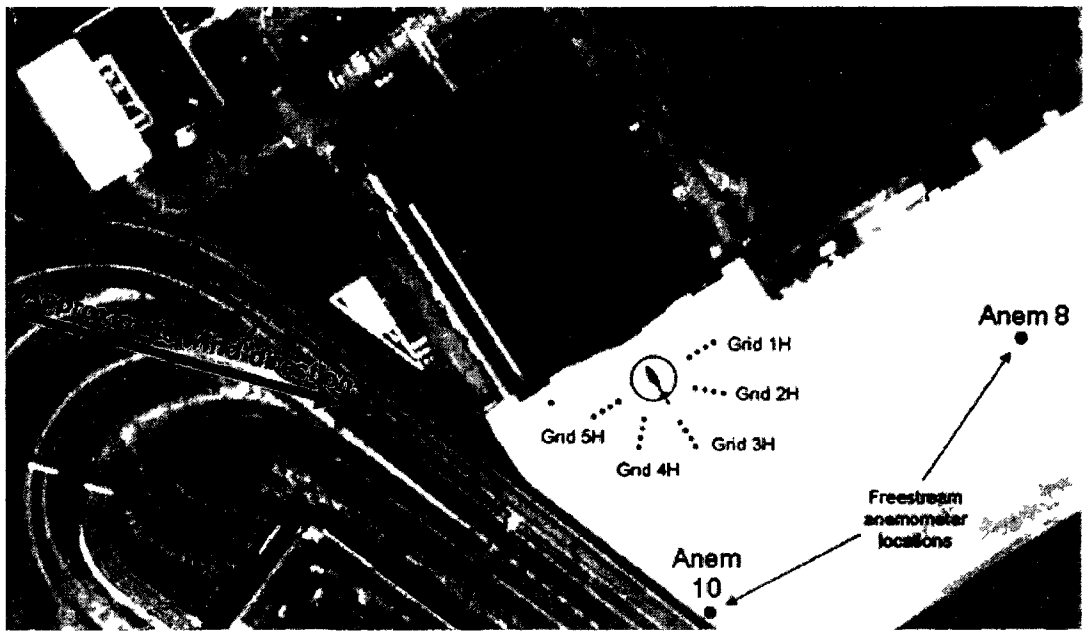

Figure 45: Layout of anemometer measurement stations as reported by[12]

This study presented a unique oportunity to validate CFD simulation results using a configuration that could be modeled both experimentally and computationally. Mixed results were obtained in this study. At some measurement locations good agreement was found between experimental and computational results as shown in Figure 46. However, at other measurement locations significant disagreement between rotor experimental and computaitonal results were found as shown in Figure 47. The dependancy of CFD simulations on mesh size, turbulence model, and boundary conditions are cited as the main technical challenge in accurately modeling the interactive flowfield[12].

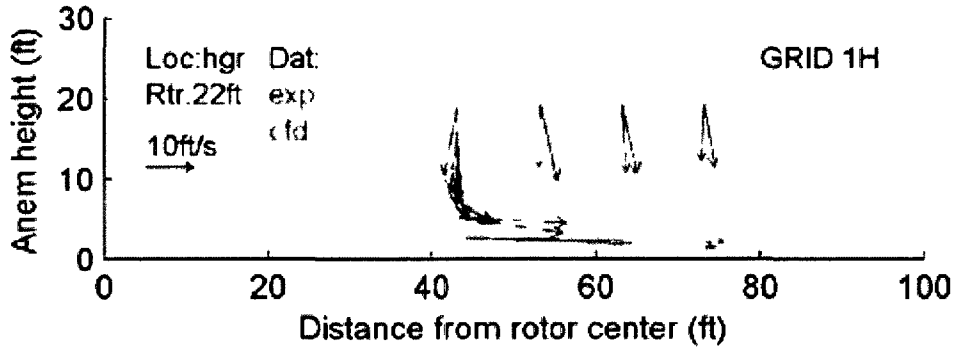

Figure 46: Comparison of experimental and CFD results for grid location 1H[12]

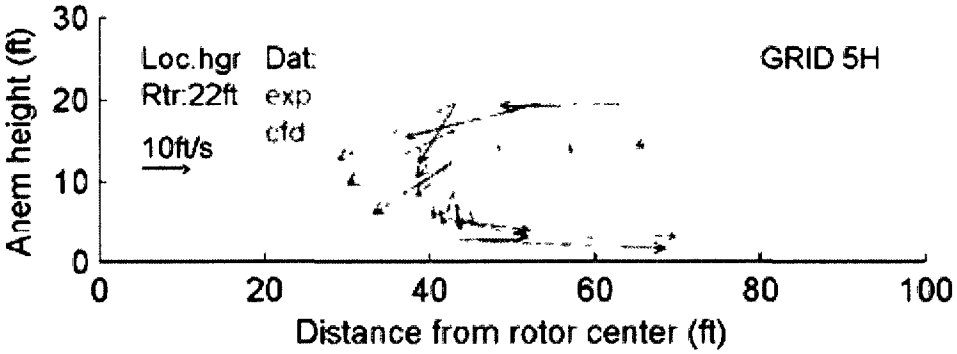

Figure 47: Comparison of experimental and CFD results for grid location 5H[12]

2.6 Ship Airwake/Rotor Downwash Simulation

While this research study is focused on the use of experimental wind tunnel techniques to investigate ship airwake/rotor downwash coupling, the intended outcome of this work is to support flight simulation development. The developed experimental technique, which will be discussed in greater detail later, parallels helicopter flight simulation techniques. Current flight simulations rely on superposition to incorporate the effects of ship airwake on rotor loading. Unfortunately, the superposition method does

not accurately model the coupling associated with the ship's airwake and rotor downwash. Thus, fully coupled simulations must be developed to accurately incorporate this effect. CFD provides the best avenue, though still challenging, to investigate this coupled flow regime. However, CFD is considered to be too computationally intensive for real-time flight simulation, and thus airwake models must be constructed using offline CFD simulations. The experimental technique developed in this research study will help to reduce the size of the computational domain and reduce the size of the dataset required for input into flight simulators. This will allow for a more efficient incorporation of the coupling effect into real-time flight simulations.

Numerous research bodies have identified the modeling of the ship airwake/rotor downwash interaction as one of the most significant technical challenges for modern computational fluid dynamics[20,33]. Naval Air Systems Command (NAVAIR) reports actively pursuing ship-aircraft modeling technology for use in various applications[12]. In general, researchers cite the importance of developing accurate airwake models and dynamic interface models, noting this would improve pilot training and technological development[9,34].

Area experts believe computational fluid dynamics provides the best avenue to develop airwake models for simulation of the ship airwake/rotor downwash interaction. The development of accurate fully coupled computational fluid dynamics (CFD) simulations of the ship airwake/rotor downwash interaction are viewed as the first step in producing accurate piloted flight simulations. It is important to note that the development of simulations that incorporate aerodynamic interactions apply not just to helicopter and ship interface modeling but also apply to a wide variety of other applications. For

instance, some research studies are focused on developing simulations to predict the aerodynamic interactions between an F/A-18 aircraft and CVN class aircraft carrier[9,33]. Figure 48 shows significant regions of vorticity (the so-called"burble") experience by landing aircraft.

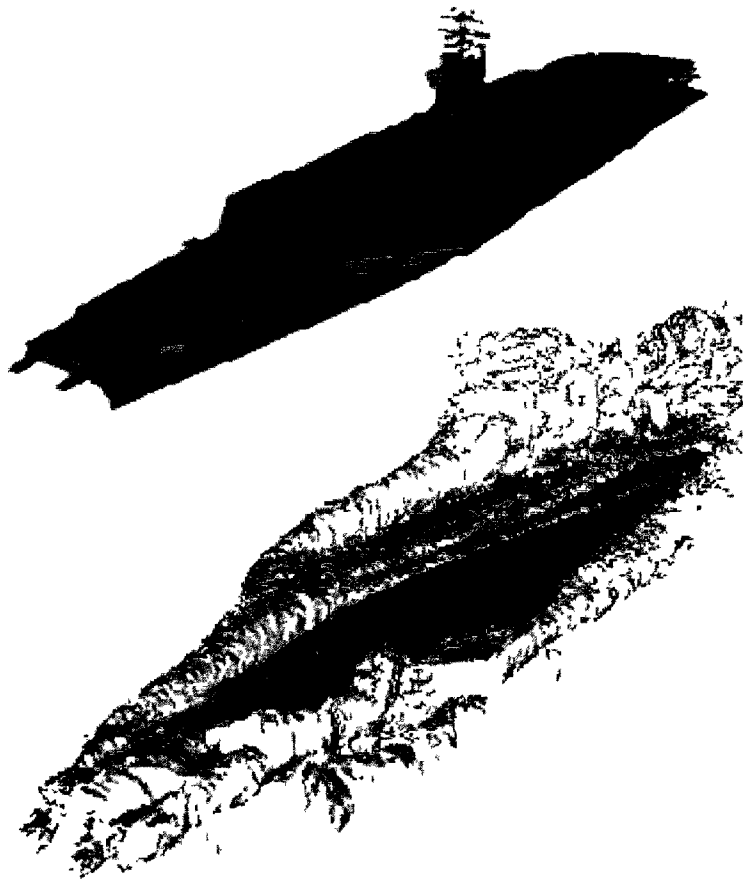

Figure 48: Carrier model and reported iso-surface of vorticity for starboard winds[9]

In these studies, researchers are focused on the simulation of F-18 carrier landings that include a so-called "virtual burble"[9]. Results (Figures 49-51) indicate that CFD simulations agreed reasonably well with time-averaged wind tunnel data.

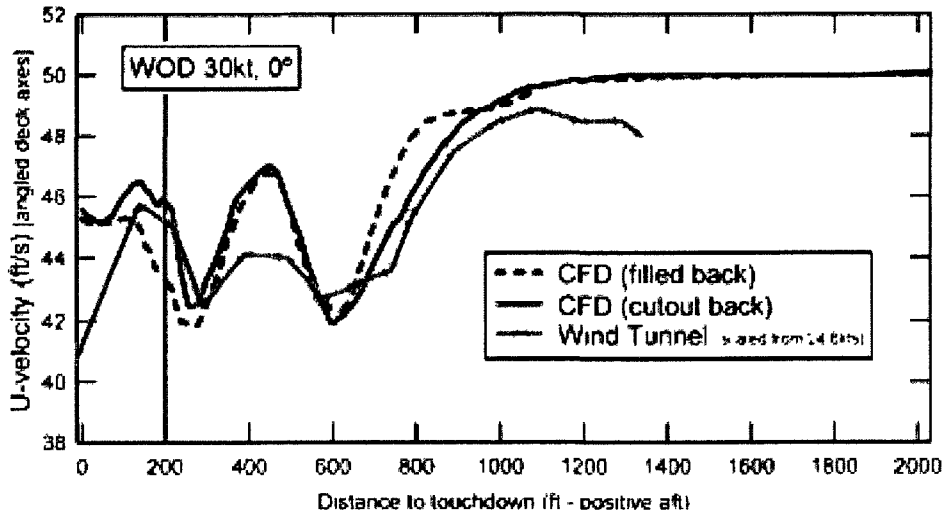

Figure 49: Head wind velocity component along approach path for two CFD model configurations (filled and cutout aft ends) and wind tunnel measurements[9]

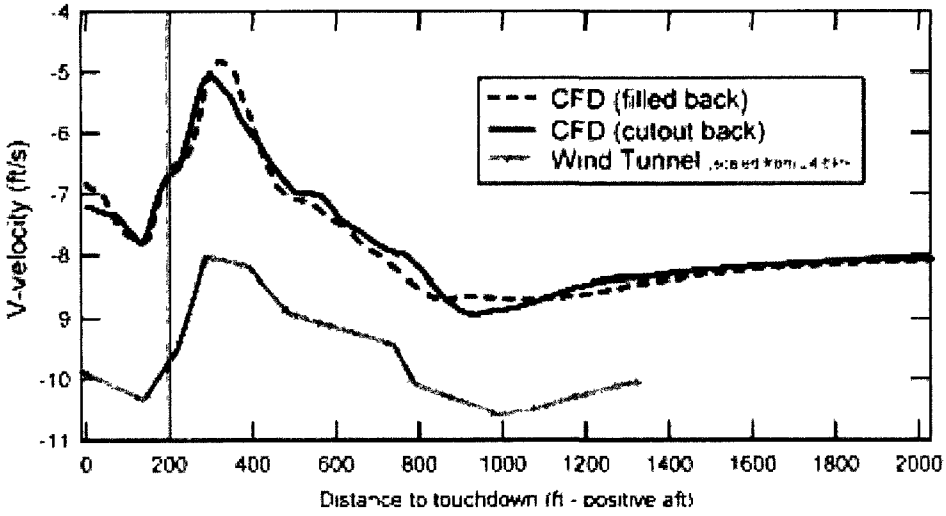

Figure 50: Cross flow velocity component along approach path for two CFD model configurations (filled and cutout aft ends) and wind tunnel measurements[9]

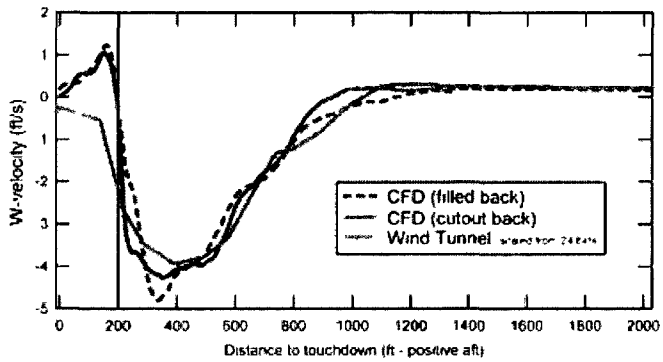

Figure 51: Vertical velocity component along approach path for two CFD model configurations (filled and cutout aft ends) and wind tunnel measurements[9]

Similarly, the standard deviation of the U-velocity component was examined to quantify the ability of CFD simulations to predict the unsteadiness (turbulence) associated with the carrier burble. Comparison of the CFD simulation results with wind tunnel data as shown in Figure 52 again reveals reasonable agreement between experiment and computational simulation.

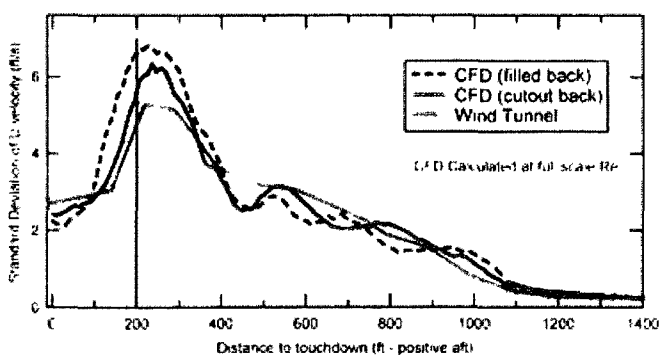

Figure 52: Standard Deviation of U-velocity component along approach path for two CFD model configurations (filled and cutout aft ends) and wind tunnel measurements[9]

In addition to ship airwake/aircraft coupling, aircraft/aircraft coupling has been studied. Research efforts in this area have focused on the development of simulation

capabilities to study the aerodynamic coupling between a KC-135 tanker (Figure 53) and an unmanned aircraft[34]. In this study, researchers note the significance of both steady-state and the dynamic interactions between the tanker aircraft, refueling boom, and the aircraft being refueled[34].

Figure 53: KC-135 tanker with refueling boom extended[34]

Like the experimental investigations, the scope of the computational modeling efforts varies greatly throughout the literature. Some computational efforts have focused exclusively on the modeling of only the ship airwake and did not consider an immersed rotor. This is considered the first step in accurately modeling the interaction between rotor downwash and ship airwakes. In the airwake studies, basic information about the rotor's operating environment was gained providing insight into the structure of ship airwakes. In a study by Syms[16], both the mean and fluctuating components of the ship airwake were captured using a lattice-Boltzmann method and compared with wind tunnel measurements. Results (Figures 54 and 55) show reasonable agreement in airwake structure for stream-wise velocity and RMS velocity.

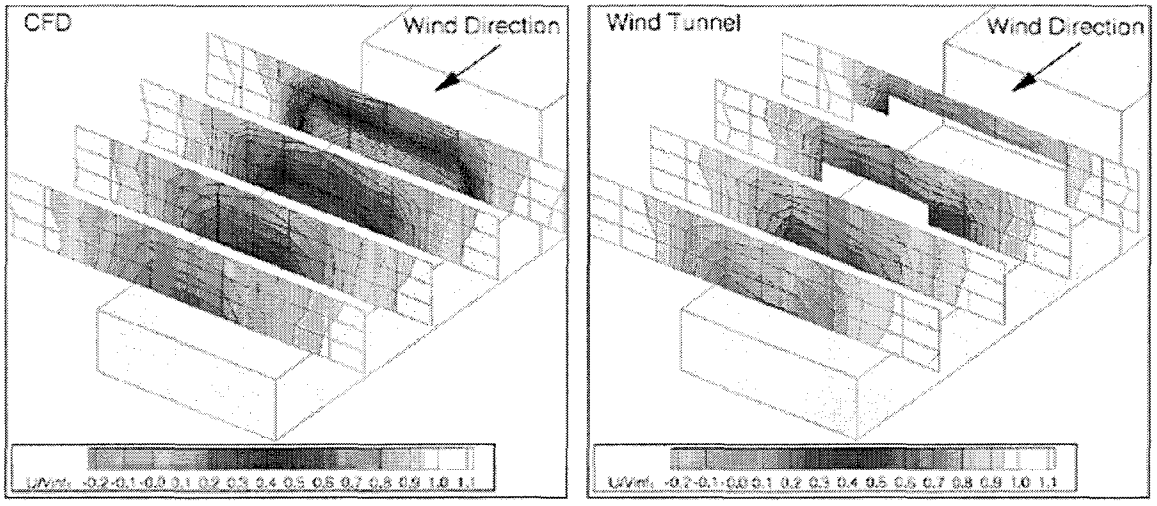

Figure 54: Contours of stream-wise velocity over the landing deck of a simple frigate shape with triangular bow for CFD and wind tunnel studies[16]

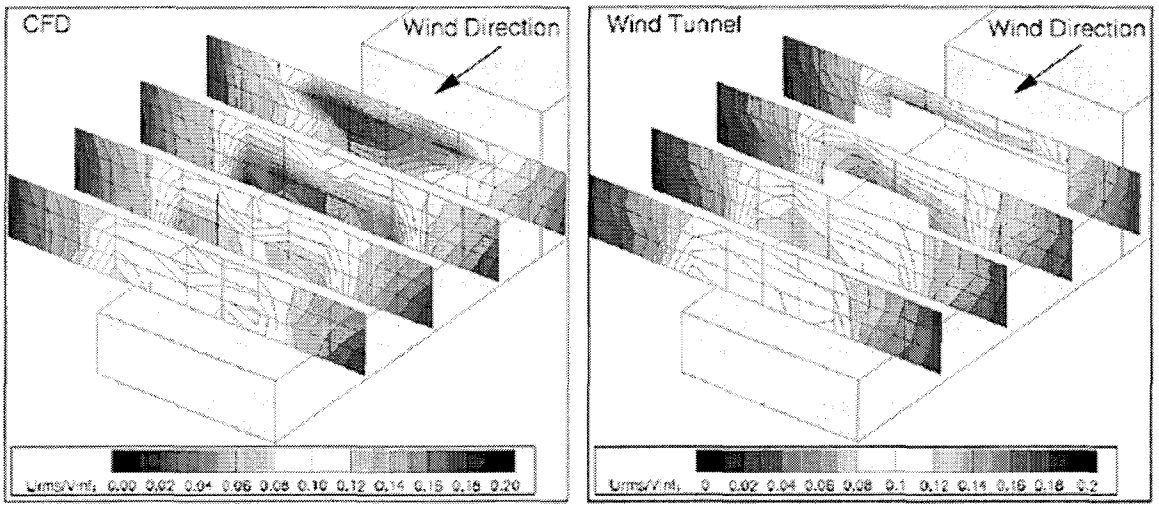

Figure 55: Contours of RMS velocity over the landing deck of a simple frigate shape with triangular bowfor CFD and wind tunnel studies[16]

More recent efforts have focused on the combined case of rotor and ship airwake. In a study by Lee and Silva[13] the loading of the hangar doors on a non-aviation ship was examined. This analysis provided insight into the interaction between ship airwakes and

rotor downwash and the resulting pressure loading on hangar doors. This study investigated several rotor configurations: isolated, hover, hover in ground effect, and rotor above ship deck. The computational domain including ship, main rotor, and tail rotor is shown in Figure 56.

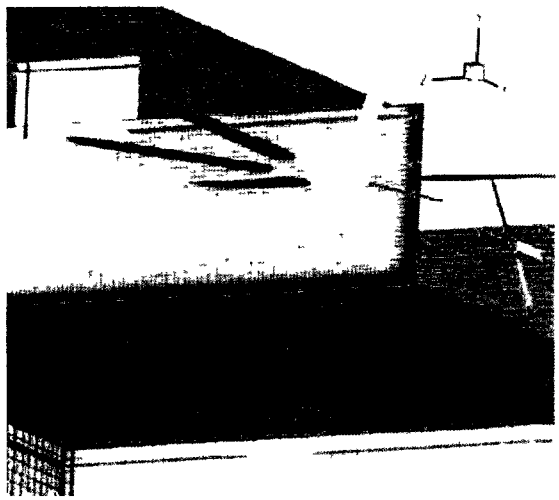

Figure 56: Computational modeling of ship, helicopter main rotor, and tail rotor[13]

One of the interesting results of this study was the observed asymmetric flow (Figure 57) in the rotor downwash[13]. Recirculation was observed in the region of the landing deck and hangar door and shown in Figure 58[13]. In this study, the helicopter fuselage was not modeled in an effort to simplify the computational problem.

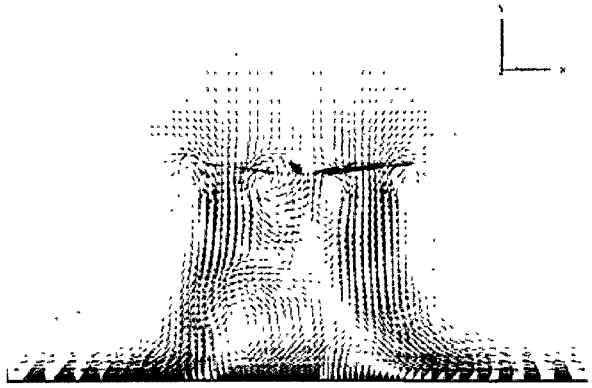

Figure 57: Asymmetric rotor outwash[13]

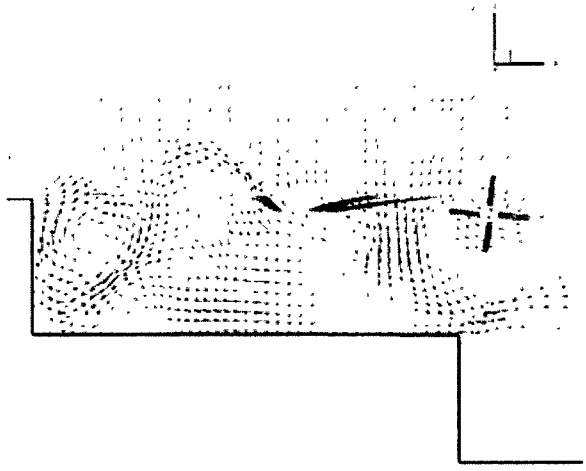

Figure 58: Recirculation in flowfield[13]

2.6.1 CFD Solution Techniques

Direct numerical simulation (DNS), large eddy simulation (LES), and Reynolds-averaged Navier-Stokes (RANS) simulations are common numerical solution techniques used in the prediction of ship airwakes[16]. As cited earlier (Syms[16]), Lattice-Boltzmann simulations have also been used successfully in ship airwake simulations but this

technqiue is not applied as often as LES and RANS. In addition, a hybrid technique called detached eddy simulation (DES), which is a combination of LES and RANS, has been developed to reduce computational requirements[35]. In a study by Dietiker and Hoffman[35], the unsteady flowfield behind a backward facing step was examined using DES. In this study the meanwall pressure, skin-friction coefficient, velocity, and turbulent kinetic energy were accurately calculated as shown in Figures 59-62[35].

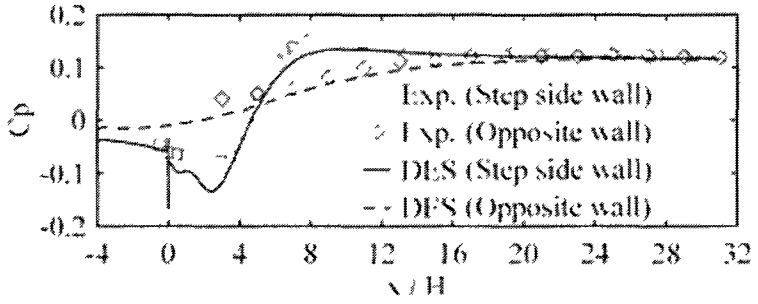

Figure 59: Comparison of measured and calculated wall pressure coefficients[35]

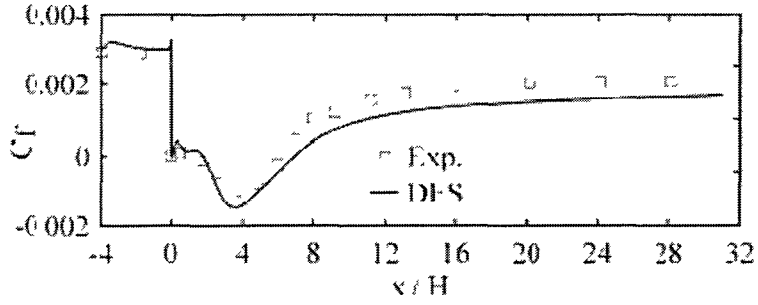

Figure 60: Comparison of measured and calculated skin-friction coefficients[35]

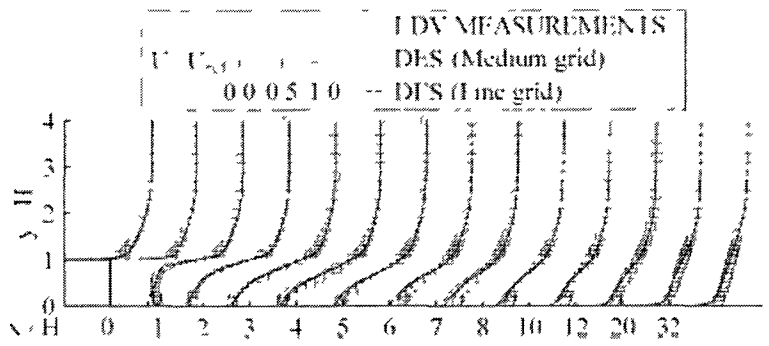

Figure 61: Comparison of measured and calculated velocity profiles[35]

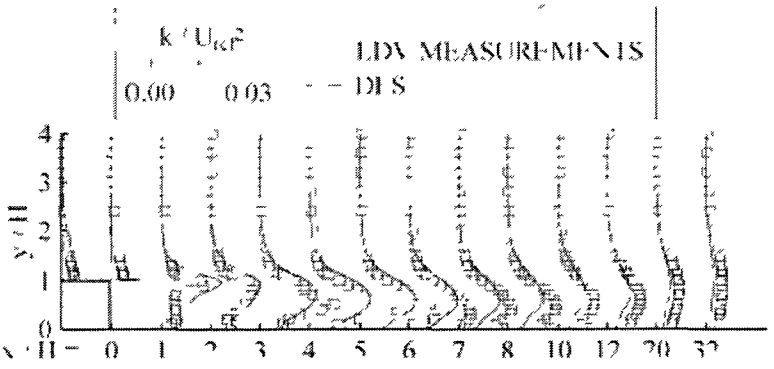

Figure 62: Comparison of measured and calculated turbulent kinetic energy[35]

In addition to the accurate modeling of ship airwakes, current CFD research has focused on improving the accuracy of rotor models. Until recently, rotor blades were typically modeled as an actuator disk with no individual blades. In this case, the rotor is modeled by adding extra terms to the governing equations in the rotor disk region, thus producing a downward force on the fluid. In this technique, the lift force is independent of the flow around the rotor. This technique fails to accurately model the viscous effects and other phenomena associated with rotor aerodynamics[13]. In more recent studies,

researchers have been moving away from the less-accurate rotor disk superposition technique and are instead relying on blade element models[13].

2.6.2 Current Limitations of CFD

Results from recent advancements in turbulence modeling technology have shown promise but results are susceptible to boundary conditions and grid generation issues[12]. In addition, variations in wind speed and direction were found to have a significant impact on the relative magnitudes of the ship/aircraft aerodynamic interaction adding to the technical challenge of accurately modeling this phenomenon[9]. Finally, the computational requirements to carry out fully coupled simulations make real-time application of the technology in flight simulations impractical.

2.7 Summary

In summary, the wind tunnel studies performed by Silva et al.[3] and Zan[31] provide oportunities for continued research. Specifically, the development of a coupling analysis technique capable of providing a quantifiable estimation of the degree of coupling would aid in the investigation of rotorcraft/ship aerodynamic interaction. The findings of Silva et al.[3] identified regions of interaction between neighboring helicopters in landing configuration. No attempt to quantify the degree of coupling was presented, only a raw examination of the velocity field. In addition, the wind tunnel study by Zan[31] examined the variations of rotor thrust coefficient over the deck of a naval frigate model. While thrust coefficient was reported in this work, no consideration of measurement uncertainty was reported nor any consideration of correlation with the velocity field. The reporting of measurement uncertainty is required to make results statistically defensible. Finally,

comments by NAVAIR and in the literature by Czerwiec and Polsky[4] indicate the need for validation of CFD simulation results.

3. METHODOLOGY

3.1 Overview

A wind tunnel measurement and analysis technique was developed at Old Dominion University with the guidance of NAVAIR's Applied Aerodynamics and Store Separation Branch (4.3.2.1) for the identification of ship airwake/rotor downwash coupling. Rotor thrust measurements and particle image velocimetry measurements were collected to study the variations in rotor thrust, the velocity field, and for use in a quantitative coupling analysis technique. In all cases, a single rotor advance ratio ($AR = 0.075$) was used to ensure proper dynamic scaling. As recommended by Silva et al.[3] this similarity parameter is used instead of Reynold's number (Re) since rotor downwash velocity and the freestream velocity are the primary physical components of the problem. Length scales (i.e. ship size and rotor diameter) are not the dominant factor in this case, hence it is not required to match Reynolds number (Re) in this case. Rotor advance ratio is defined as the ratio of the freestream velocity to the rotor tip velocity as shown below in equation (1).

$$AR = \frac{V_{freestream}}{V_{rotor\ tip}} \tag{1}$$

This work required extensive software and hardware development to minimize the variance associated with experimental measurements. The developed analysis technique parallels current flight simulation technology by investigating the validity of superposition for prediction of the velocity field in the immediate vicinity of the rotor.

3.2 Design of Experiments

Design of experiments methodology was used extensively in this study to ensure proper experimental technique and data analysis. The principles and recommended best practices from design of experiments are applied to both the investigation of rotor thrust variations over the frigate's landing deck and the velocity coupling investigation.

3.2.1 Application of Design of Experiments

Following the outline of Montgomery[36] the recommended steps for designing an experiment can be summarized as follows.

1. Problem Statement
2. Selection of factors and response variables
3. Selection of factor levels
4. Selection of experimental design
5. Performing the experiment
6. Statistical analysis of the data
7. Conclusion

While this procedure is very useful, experience has shown that proper planning requires at least an iterative approach and at most a simultaneous approach to experiment planning. The first step in any experiment is to formulate a problem statement. This step may seem somewhat intuitive, however depending on the problem this is not always straightforward. In this study, the ultimate motive was to identify ship airwake/rotor downwash coupling. Rotor thrust coefficient was identified as the response variable in this case and rotor-over-deck position was selected as one possible factor affecting rotor thrust. To determine factor levels, experimental feasibility and the desired response model had to be considered. Using insight gained from the previous work of Nacakli[37,45]

it was determined that at a minimum a cubic model for thrust would be required to properly model the interaction. However, the ability to fit higher order models was also desired. In addition, a newly developed automated experiment control system was available, allowing for efficient data collection. This system permitted an increase in the number of factor levels that would have otherwise not been feasible. Thus factor levels were chosen permitting a sixth-order response surface if deemed necessary. Specifically, seven X/D, 13 Y/D, and seven Z/D unique levels were chosen. Ultimately, it is up to the experimenter to think ahead and determine what the expected outcome of a given experiment might be, what resources are available, and what is required in terms of analysis to achieve the goal defined in the problem statement.

Given the available data, a general factorial design with complete replication was chosen for the rotor thrust variation investigation. This approach allowed for flexibility in fitting methods including non-parametric modeling. The experiment was performed in random order. In the study of rotor thrust variations, an analysis of variance (ANOVA) was performed to identify significant factors affecting rotor thrust and to guide the development of an appropriate response surface. In the velocity coupling investigation, an ANOVA was not required; however, the design of experiments methodology was still applied through randomization and replication of experimental observations.

In both studies experimental runs were randomized to account for any extraneous effects that would otherwise influence the experimental observations. Past experience has shown that randomization is an essential component in any experimental design. In the case of wind tunnel studies numerous extraneous lurking factors may or may not be present. The closed-circuit atmospheric pressure tunnel used in this study is subject to

fluid temperature and atmospheric pressure variations during run-time. While these variations are monitored and accounted for using wind tunnel software, randomization provides an extra layer of protection by identifying trends[36]. In addition, all observations in both studies were replicated in random order. Replicates allow for an estimate to be made of the overall model-independent experimental error and also provide important information required to determine if observations are statistically significant[38].

3.2.2 Overview of Analysis of Variance (ANOVA) and Regression Modeling

In this study, rotor thrust measurements are made for three factors X/D, Y/D, and Z/D with seven X/D levels, 13 Y/D levels, and seven Z/D levels. Two replicates were made at each measurement location and a regression model was developed to describe the data. Since there was no guarantee that the model chosen would accurately predict the system's response to factor inputs, an objective, statistically defensible analysis of the model was desired. Thus an analysis of variance (ANOVA) was used in this study and found to be the ideal tool to evaluate model significance and error. This analysis technique also tested for the significance of individual model terms and allowed for model reduction.

In general, multiple linear regression is used to fit a model to a given set of data[38]. For instance, a second order response surface in three variables would assume the following form.

$$y = \beta_o + \beta_1 x_1 + \beta_2 x_2 + \beta_3 x_3 + \beta_{12} x_1 x_2 + \beta_{13} x_1 x_3 + \beta_{23} x_2 x_3 + \beta_{11} {x_1}^2 + \beta_{22} {x_2}^2 + \beta_{33} {x_3}^2 + \varepsilon \quad \textbf{(2)}$$

The regression model is typically a polynomial of order equal to the number of factor levels minus one. Hence in this study, the minimum number of factor levels is seven; thus, a regression model of order six or less can be developed.

The regression model is developed by computing the least squares estimator (b) of regression coefficients (β) given the model matrix (X_M) and response matrix (y) as shown in equation (3)[38].

$$b = (X_M^T X_M)^{-1} X_M^T y \tag{3}$$

Hence for the second order response surface given in equation (2) the fitted model becomes:

$$\hat{y} = b_o + b_1 x_1 + b x_2 + b x_3 + b x_1 x_2 + b_{13} x_1 x_3 + b_{23} x_2 x_3 + b_{11} {x_1}^2 + b_{22} {x_2}^2 + b_{33} {x_3}^2 + \varepsilon \tag{4}$$

If a linear relationship exists between the response variable and a subset of the regressor variables then the model can be considered significant. An ANOVA is used to determine if this linear relationship exists through statistical hypothesis testing[36]. The hypothesis in this case is as follows.

$$H_0: \beta_1 = \beta_2 = \cdots = \beta_k = 0$$
$$H_1: \beta_j \neq 0 \; for \; at \; least \; one \; j \tag{5}$$

If the null hypothesis H_0 can be rejected then at least one regressor contributes significantly to the model.

The ANOVA test procedure partitions the total variability in the observations, which is computed in terms of a sum of squares (SS_T), into the variability associated with the regression model (SS_R) and the variability associated with the residual error (SS_E) as shown in equation (6)[36].

$$SS_T = SS_R + SS_E \quad \textbf{(6)}$$

Following the procedure detailed in Montgomery[36], the total corrected sum of squares (SS_T) is measured by computing the overall variability in the observations as shown in equation (7).

$$SS_T = \sum_{i=1}^{n} (y_i - \bar{y})^2 = y^T y - \frac{(\sum_{i=1}^{n} y_i)^2}{n} \quad \textbf{(7)}$$

Similarly, the error sum of squares (SS_E) measures the variability due to the combination of pure (experimental) error and lack-of-fit. This quantity is estimated by computing total disagreement between the observed response and estimated (model) response as shown in equation (8).

$$SS_E = y^T y - b^T X_M^T y \quad \textbf{(8)}$$

The variability associated with the individual factors or treatments can then be determined by subtraction.

$$SS_R = SS_T - SS_E \quad \textbf{(9)}$$

The overall variance observed within each factor's levels and between factors can be estimated by computing mean square quantities[36]. Equations (10) and (11) show the mean square estimates for the variance within factor levels and between factors, respectively.

$$MS_E = \frac{SS_E}{n - k - 1} \quad \textbf{(10)}$$

$$MS_R = \frac{SS_E}{k} \tag{11}$$

In the above equations, n is the total number of observations and k is the total number of regression variables included in the model. It should be noted that the error variance (σ^2) can be estimated from the mean square for error as follows.

$$\hat{\sigma}^2 = MS_E \tag{12}$$

The F_0test statistic is used to accept or reject the null hypothesis. The F_0 statistic is computed from MS_E and MS_R as follows.

$$F_0 = \frac{MS_R}{MS_E} \tag{13}$$

To reject H_0 (meaning that the model is significant) F_0 must be greater than $F_{critical}$. The critical F value is based on a specified confidence level (i.e. for 95% confidence, $\alpha = 0.05$) and the degrees of freedom associated with the regression (k) and the error ($n - k - 1$). Thus if the inequality expressed in equation (14) is true, the model is considered significant.

$$F_0 > F_{\alpha,k,n-k-1} \tag{14}$$

The F test determines significance in a strict sense, however, no indication is given as to how significant any given model or term might be. It is possible to have terms that are only marginally significant while others are very significant. Hence, a P-value approach to hypothesis testing is often used. This is especially true in the case of statistical software packages like Design Expert. The P-value reports the value of α for which the model or term becomes significant. Therefore, for 95% confidence, any value

P-value less than $\alpha = 0.05$ would be considered significant. P=0.0001 would be considered very significant, while P=0.049 would be considered only marginally significant.

3.2.3 Lack of Fit and Pure Error

The total error term SS_E can be further decomposed provided that the experiment has been replicated (true replicates). This decomposition provides additional useful information with regards to model fit and experimental error (5). Specifically, the total error SS_E is a combination of error due to lack of fit (SS_{LOF}) and pure error (SS_{PE}). Lack of fit refers to how well the regression model fits the experimental observations. Thus, lack of fit is considered a model dependent measure. Pure error refers to the errors present in repeated experimental measurements. Unlike lack of fit, pure error is a model independent measure. As detailed in Myers et al.[38], lack of fit (SS_{LOF}) is computed by subtracting the sum of squares for pure error (SS_{PE}) from the sum of squares for total error (SS_E) as shown in equation (15)

$$SS_{LOF} = SS_E - SS_{PE} \tag{15}$$

In general, a replicated design will have several observations (n_{rep}) at the same factor level (m). The sum of squares for pure error is calculated from the available replicated observations as shown in equation (16)

$$SS_{PE} = \sum_{i=1}^{m} \sum_{j=1}^{n_{rep}} \left(y_{ij} - \bar{y}_i\right)^2 \tag{16}$$

Similar to the model significance test, mean squares can be calculated to test for a significant lack of fit based on (SS_{LOF}) and (SS_{PE}) as shown in equation (17) and (18).

$$MS_{LOF} = \frac{SS_{LOF}}{(m-p)} \tag{17}$$

$$MS_{PE} = \frac{SS_{PE}}{(n-m)} \tag{18}$$

Note that there are $m-p$ degrees of freedom associated with SS_{LOF} where p is the number of model parameters (including the mean). Similarly, there are $n-m$ degrees of freedom for SS_{PE}. A test statistic for lack of fit can then be calculated as follows.

$$F_0 = \frac{MS_{LOF}}{MS_{PE}} \tag{19}$$

Lack of fit would be considered significant if the test statistic was larger than the critical F value as shown in equation (20). A significant lack of fit is generally not desired.

$$F_0 > F_{\alpha,m-p,n-m} \tag{20}$$

There are some situations, like that found in this study, where pure error (experimental error) is very small (common to wind tunnel applications) and a large number of replicated observations have been made. In this case lack of fit will be significant, but the model is significant and fit is acceptable. Thus, other fit statistics such as R^2 must be consulted before any definite conclusions can be made regarding goodness of fit.

3.2.4 Residual Diagnostics

Residual diagnostics are used to ensure that the normality, independence, and constant variance assumptions used in the development of the ANOVA are valid for a given set of observations[36]. The residuals (e) are computed by comparing the observed response (y) with the predicted response ($\hat{y}$).

$$e = y - \hat{y} \tag{21}$$

In many instances, it is helpful to scale the residuals to form a so-called studentized residual (r_i) as shown in equation (22)[36]. This accounts for the variance of the residuals associated with where in the design space the residual lies (i.e. variance due to design) and scales the residual accordingly.

$$r_i = \frac{e_i}{\sqrt{\sigma^2(1 - h_{ii})}} \tag{22}$$

The normality assumption is checked using a normal probability plot of the residuals. If the residuals appear to fall along a straight line the normality assumption is valid. Additionally, the independence assumption is verified by plotting the residuals versus time. If the residuals appear to oscillate in a random fashion with no trends visible then the independence assumption is verified. Finally, by plotting residuals versus predicted response the constant variance assumption can be checked. If the residuals appear to be randomly scattered about the plot with no barreling or coning the constant variance assumption is valid.

3.2.5 Model Adequacy

Several statistics are available to assess the ability of a model to describe an observed response[36]. The most familiar of these statistics is the coefficient of multiple determination (R^2). $R^2$is a measure of the amount of reduction in the variability of the response due to the inclusion of model parameters and is defined as follows[38].

$$R^2 = \frac{SS_R}{SS_T} = 1 - \frac{SS_E}{SS_T} \tag{23}$$

The value of R^2 will range between zero and one, with one being the ideal case in which the model describes 100% of the variability in the observed response y. It should be noted that large R^2 (i.e. $R^2 = 0.98$) does not imply that the given model is capable of making good predictions of the response but rather that it fits the observed data (i.e. data used to generate the model) well[38]. In general, R^2 can be increased by adding additional model terms, regardless of significance, to the regression model[36]. Thus, an additional statistic is available that considers model size. The adjusted R^2 or R^2_{adj} is shown in equation (24).The value of R^2_{adj}will often decrease when insignificant terms are included in a model yielding a better estimate of the model's ability to explain the variability associated with the observed response[36].

$$R^2_{adj} = 1 - \frac{n-1}{n-p}(1 - R^2) \tag{24}$$

While the previous statistics help to quantify how well a given model fits the data, additional information can be gained by examining the model's ability to predict future observations. A prediction error sum of squares (PRESS) can be used to examine each observation's influence on the developed model and incorporate this information into a quantifiable model adequacy statistic[38]. The end result of the PRESS residual provides an estimate of how well the model predicts future observations. Computation of the PRESS statistic involves considering all possible subsets of $n - 1$ obervations, and fitting a model to each reduced data set ($n$models total). Next n new models are used to predict the response and the residual error (e) for the omitted observations. Finally, the sum of all the residual errors is computed yielding the PRESS statistic. This statistic can be

efficiently calculated by first mapping the vector of observed values into a vector of fitted values using the so-called hat matrix H as shown in equation (25)[38].

$$H = X_M(X_M^T X_M)^{-1} X_M^T \tag{25}$$

Next, the residual vector from the original fitted model is calculated.

$$e = y - X_M b \tag{26}$$

Finally, the PRESS residual is computed by weighting the ordinary residual e according to the diagonal elements of the hat matrix (h_{ii}) as shown in equation (27).

$$PRESS = \sum_{i=1}^{n} \left(\frac{e_i}{1 - h_{ii}}\right)^2 \tag{27}$$

The PRESS statistic can be used to compute an approximate R^2 that gives some indication of the predictive capability of the regression model.

$$R^2_{pred} = 1 - \frac{PRESS}{SS_T} \tag{28}$$

Expected values for R^2_{pred} will range between zero and one with one being the ideal case. A$R^2_{pred} = 1$ would mean that the model is expected to explain 100% of the variability in predicting new observations.

3.2.6 Model Reduction

In the previous section, the use of ANOVA was described for the purpose of determining if a regression model was statistically significant. No tests were shown to examine the significance of individual model terms. It is desired however, to reduce the model to include only statistically significant model terms. This reduction reduces the

model degrees of freedom, adding to the degrees of freedom available for estimation of error. Also, from a practical standpoint, it is far less cumbersome to deal with reduced models (model parsimony). The significance of any given model term can be determined through a procedure called the extra sum of squares method using a partial F-test[38]. The hypothesis to test in this case is as follows:

$$\begin{matrix} H_0: \beta_i = 0 \\ H_1: \beta_i \neq 0 \end{matrix} \quad \textbf{(29)}$$

where β_i refers to any single model term.

Following the extra sum of squares method detailed in Myers et al.[38], the partial sum of squares for each model term is calculated by first computing the sum of squares for the original regression model (SS_R). Next a reduced model is created that is essentially the same as the original model minus the term in question. Finally, the sum of squares for the reduced regression model ($SS_{Reduced}$) is calculated and subtracted from the original regression sum of squares. For a first order model in two factors with the $\beta_1$being the term of interest, this would be expressed mathematically as follows.

$$SS_R(\beta_1|\beta_0, \beta_2) = SS_R(\beta_1, \beta_2|\beta_0) - SS_R(\beta_2|\beta_0) \quad \textbf{(30)}$$

In the above relation $SS_R\left(\beta_1, \beta_2|\beta_0\right)$ is the regression sum of squares for the original model and $SS_R(\beta_2|\beta_0)$ is the regression sum of square for the reduced model with the β_1 term removed. The partial sum of squares for the β_1 term would then be given by $SS_R(\beta_1|\beta_0, \beta_2)$. Noting that the single term of interest has one degree of freedom, the mean square based on the partial sum of squares for the term of interest can be obtained as follows:

$$MS_{partial} = \frac{SS_{Reduced}}{1} \tag{31}$$

or for the case of the first order example this would be expressed mathematically as shown below.

$$MS_{partial} = \frac{SS_R(\beta_1|\beta_0, \beta_2)}{1} \tag{32}$$

The test statistic F_0 is then computed based on the partial mean squares for the term of interest ($MS_{partial}$) and the mean square for error (MS_E) of the original regression model as shown in equation (33)[38].

$$F_0 = \frac{MS_{partial}}{MS_E} \tag{33}$$

F_0 is then compared to the critical F-value ($F_{\alpha,n_{terms},n-p}$) where $\alpha = 1 - confidence$, n_{terms} is the number of terms being tested (there could be more than one), n is the total number of observations, and p is the number of model parameters including the mean. If F_0 is greater than the critical F-value the null hypothesis H_0 can be rejected, meaning that the term in question (β_i) is significant and should be included in the regression model. As before, the P-value can be used to determine level of significance.

Since most models will have more than one term, a backwards elimination procedure is used to reduce the model. In this procedure, terms are tested for significance and eliminated (if not significant) one at a time starting with the highest order term and ending with the lowest order term. Once complete, the model is reduced to include only significant terms.

3.2.7 Confidence Intervals

Noting that there is a certain degree of uncertainty associated with any estimated parameter, it is often useful to quantify this uncertainty in the form of a range or confidence interval ($C.I.$). In the case of a regression model, uncertainty is associated with the individual regression coefficients, mean response at a particular point, and prediction of future responses[38]. As detailed in Myers et al.[38], the $100(1-\alpha)\%$ confidence interval for the individual regression coefficients is shown below.

$$b_i - t_{\frac{\alpha}{2},n-p}\sqrt{\hat{\sigma}^2 C_{ii}} \leq \beta_i \leq b_i + t_{\frac{\alpha}{2},n-p}\sqrt{\hat{\sigma}^2 C_{ii}} \tag{34}$$

where β_i is the actual regression coefficient, b_i is the estimated regression coefficient, C_{ii} is the diagonal element of the matrix $(X_M^T X_M)^{-1}$, α is the confidence level, n is the number of observations, $t_{\frac{\alpha}{2},n-p}$ is the t-statistic, $\hat{\sigma}^2$ is the error variance, and p is the number of model parameters including the mean.

Similarly, as defined by Myers et al.[38] the $100(1-\alpha)\%$ confidence interval for the mean response is given as shown in (35).

$$\begin{aligned} \hat{y}(x_0) - t_{\frac{\alpha}{2},n-p}\sqrt{\hat{\sigma}^2 x_0^T (X_M^T X_M)^{-1} x_0} &\leq \mu_{\hat{y}(x_0)} \\ &\leq \hat{y}(x_0) + t_{\frac{\alpha}{2},n-p}\sqrt{\hat{\sigma}^2 x_0^T (X_M^T X_M)^{-1} x_0} \end{aligned} \tag{35}$$

where $\mu_{\hat{y}(x_0)}$ is the actual mean response, $\hat{y}(x_0)$ is the estimated mean response at the design point x_0, X_M is the model matrix, α is the confidence level, n is the number of observations, $t_{\frac{\alpha}{2},n-p}$ is the t-statistic, $\hat{\sigma}^2$ is the error variance, and p is the number of model parameters including the mean.

Finally, from Myers et al.[38] the $100(1-\alpha)\%$ confidence interval for the prediction of future observations is given as follows.

$$\hat{y}(x_0) - t_{\frac{\alpha}{2},n-p}\sqrt{\hat{\sigma}^2(1+x_0^T(X_M^TX_M)^{-1}x_0)} \leq y \leq \hat{y}(x_0) + t_{\frac{\alpha}{2},n-p}\sqrt{\hat{\sigma}^2(1+x_0^T(X_M^TX_M)^{-1}x_0)} \quad (36)$$

where y is the actual future response, $\hat{y}(x_0)$ is the predicted future response at the design point x_0, X_M is the model matrix, α is the confidence level, n is the number of observations, $t_{\frac{\alpha}{2},n-p}$ is the t-statistic, $\hat{\sigma}^2$ is the error variance, and p is the number of model parameters including the mean.

3.3 Rotor Thrust Measurement

An investigation of rotor thrust variations in the vicinity of the ship landing deck was used to examine the effect of ship airwake/rotor downwash interactions on rotor loads. Rotor thrust measurements were collected using a single component (thrust) beam-type load cell. All thrust measurements were non-dimensionalized according to equation (37).

$$C_T = \frac{F_{Thrust}}{\frac{P_{atm}}{R_{air}T}(\Omega r_{rotor})^2 A} \quad (37)$$

A regression model was fitted to map the variation of thrust coefficient over a volume enclosing a region above the frigate's landing deck as shown in Figure 63. The measurement region extends vertically 0.85 rotor diameters as shown in Figure 64. A total of 637 unique measurement locations were chosen for the rotor thrust investigation.

The run order was randomized within each measurement region according to design of experiments recommended best practices.

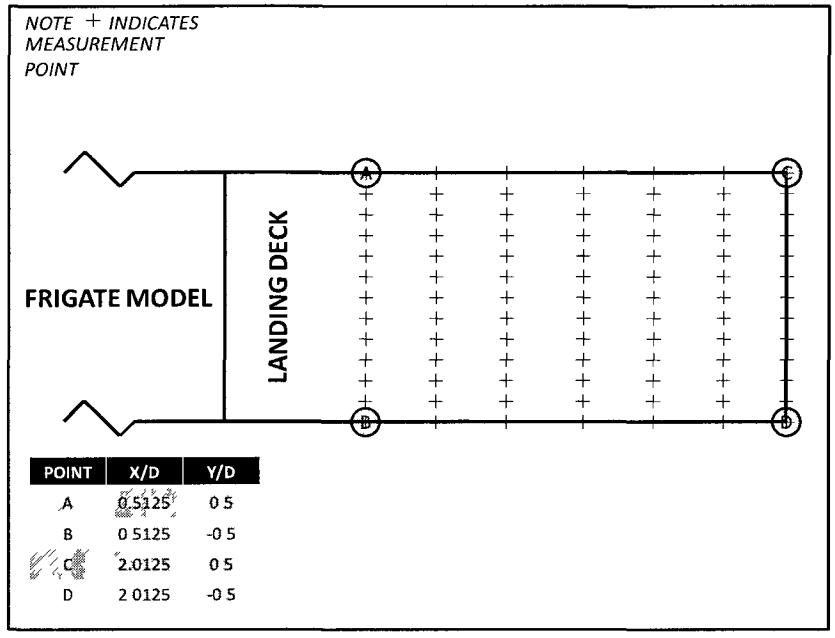

Figure 63: Top view of frigate model showing x-y thrust measurement locations

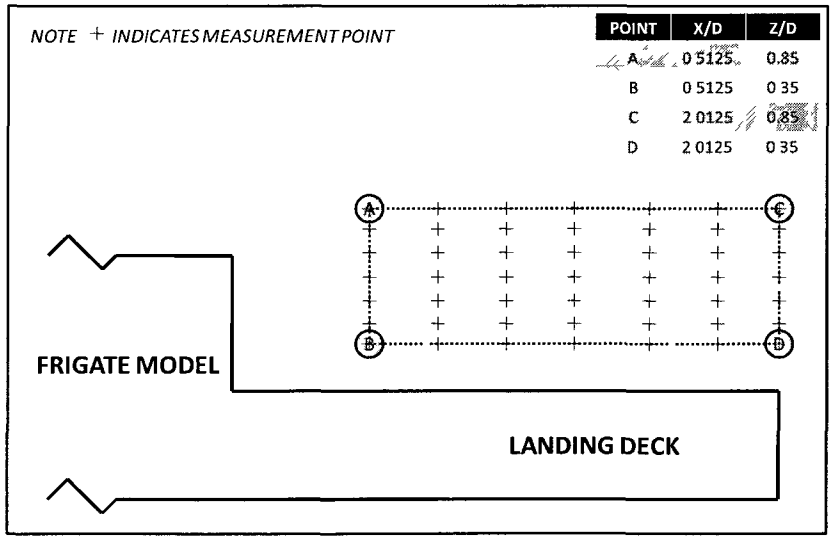

Figure 64: Side view of frigate model showing x-z thrust measurement locations

3.4 Particle Image Velocimetry

Particle image velocimetry (PIV) is an optical technique for global velocity measurement that relies on particle displacements to determine fluid velocity. Unlike particle tracking velocimetry (PTV), which measures individual particle displacements, PIV considers the displacements of groups of particles for estimation of fluid velocity. Basic particle image velocimetry systems consist of one (2-D) or two (stereo) cameras, lasers, synchronization hardware, and processing software. The optical arrangements for two dimensional and stereo PIV systems are shown in Figures 65 and 66, respectively.

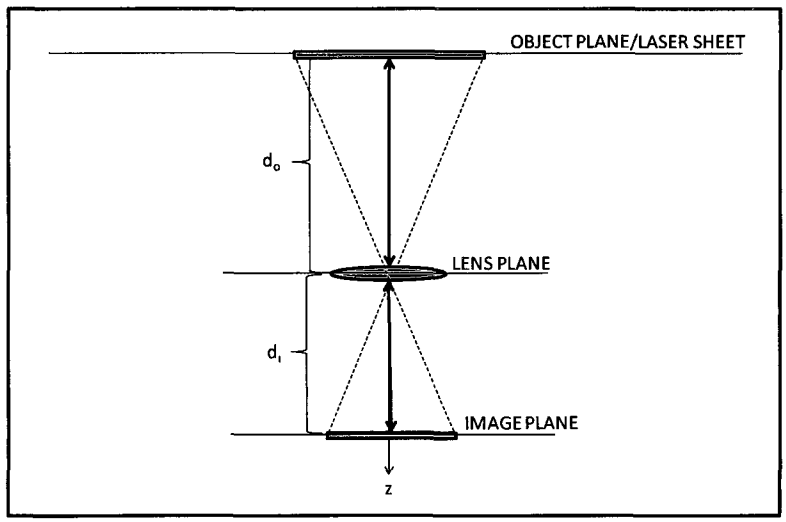

Figure 65: Optical arrangement for two dimensional particle image velocimetry

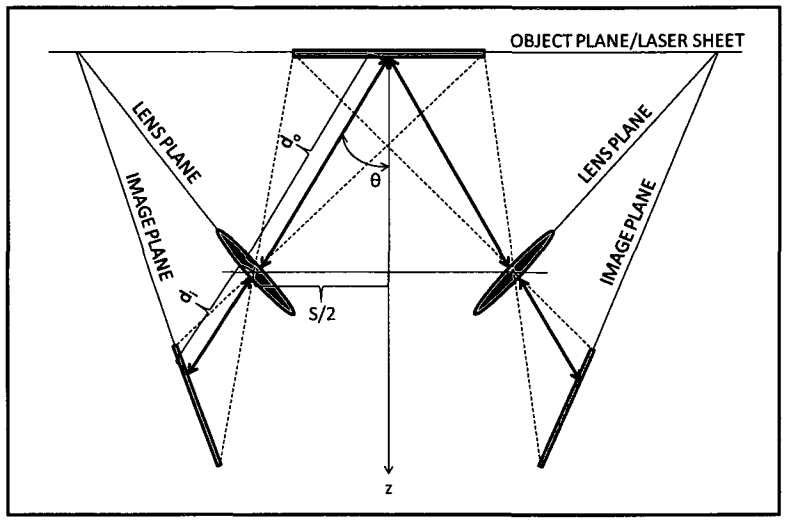

Figure 66: Optical arrangement for three dimensional particle image velocimetry[39]

For wind tunnel experiments and most other applications, seeding particles must be added to the flow of interest[40]. In this study, a mineral oil based vaporizer was used to generate the seeding particles. In a typical measurement scenario, a laser is used to illuminate a planar region of the flow and cameras are used to record particle locations as shown in Figure 67.

Figure 67: Typical stereo PIV application showing laser, cameras, and seeded flow

Several image capture techniques can be used to record particle displacements. In this experiment, two frames per camera are captured independently with each frame separated by a short time delay (Δt). Due to limitations associated with CCD cameras, frame straddling is used to reduce the minimum allowable Δt between frame captures[40]. When frame straddling is used, a laser pulse is generated at the end of the image capture in the first frame and at the beginning of the image capture of the second frame as shown in Figure 68.

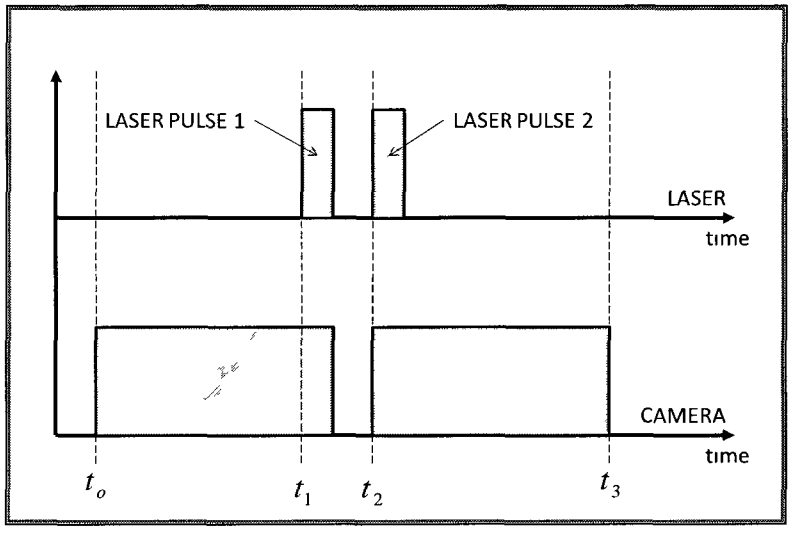

Figure 68: Timing of camera exposures and laser pulses for frame straddling

After image capture, the full image is divided into a series of image spots. In this study a typical image spot was 64x64 pixels in size. For each image spot in both exposures, a two-dimensional Fast-Fourier Transform (FFT) is calculated[40]. Next the results of the two-dimensional FFT are multiplied together and the inverse FFT is calculated. The result from the last step contains a correlation peak corresponding to the

total particle displacement. For added accuracy sub-pixel interpolation is used to better estimate particle displacements. The result is a particle displacement estimate for each spot image. By calibrating the PIV system, particle pixel displacements are mapped into real physical dimensions. The velocity can be determined by dividing the displacement by time. It should be noted that the calculated displacement is not for a single particle but rather a group or "cloud" of particles in the image spot. Therefore, displacement estimates constitute an average particle displacement within the image spot. To maximize the signal to noise ratio, thus improving the chance of successful correlation (displacement estimates), maximum particle image shift is limited to a quarter of the spot image size. This maximum displacement is adjusted by varying Δt. After processing, the velocity estimates are assembled, yielding an easily viewed measured velocity vector field.

3.5 Coupling Analysis Technique

The developed coupling analysis technique allows for the identification of ship airwake/rotor downwash coupling. For this analysis, coupled flow is considered to be a flow that deviates from a theoretical flowfield generated from superposition. Laser particle image velocity is used to measure the velocity fields of the experimentally observed ship/rotor configuration and the velocity fields required to generate the superimposed flowfield.

3.5.1 Computation of the Average Velocity Field

The time averaged velocity field is computed from 200 instantaneous PIV measurements captured at a frame rate of 1.75Hz for stereo PIV or 3Hz for two-dimensional PIV. Velocity measurements are made of the combined rotor and ship

airwake ($V_{observed}$), combined rotor and freestream ($V_{combined}$), isolated airwake ($V_{airwake}$), and isolated freestream ($V_{freestream}$) with two replicates of each configuration. Velocity components are extracted from a rectangular analysis region (Figure 69) under the rotor for each of the average velocity fields mentioned above. This region extends 0.3 non-dimensional (rotor) units from the left of the rotor hub to 0.3 non-dimensional units to the right of the rotor hub and 0.1 non-dimensional units below the rotor hub to 0.25 non-dimensional units below the rotor hub. The variance associated with each averaged velocity field is computed by summing the square of the difference between respective velocity components as shown in equation (38).

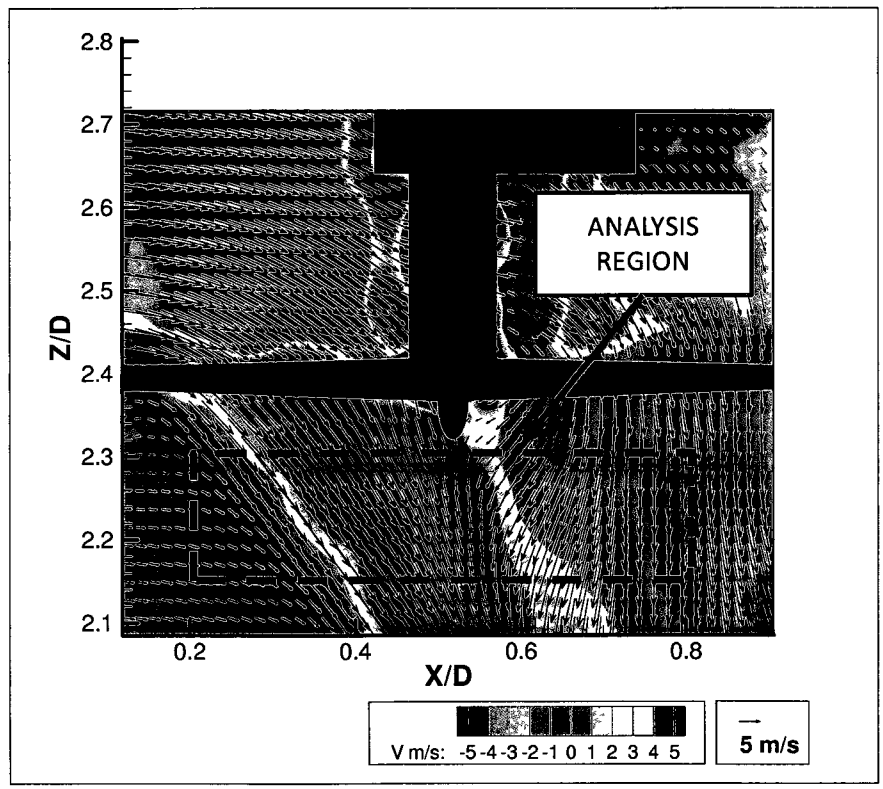

Figure 69: Typical PIV measurement result showing velocity vectors and contours

$$\sigma_V^2 = \frac{1}{nm-1}\sum_{i=1}^{n}\sum_{j=1}^{m}\left(V_{Rep1}(i,j) - V_{Rep2}(i,j)\right)^2 \quad (38)$$

In equation (38) $V_{Rep1}$and V_{Rep2} are replicated averaged velocity fields. The indices i and j correspond to individual velocity vectors within a given vector field and n and m are the number of i and j vector indices, respectively.

3.5.2 Generation of the Superimposed Velocity Field

The superimposed velocity field is generated by subtracting the corresponding velocity components of the averaged freestream velocity field from the averaged isolated airwake velocity field and adding the corresponding velocity components of the averaged combined rotor and freestream velocity field as shown in equation (39) and Figure 70.

$$\begin{aligned} V_{superimposed}(i,j) \\ &= V_{airwake}(i,j) - V_{freestream}(i,j) \\ &+ V_{combined}(i,j) \end{aligned} \quad (39)$$

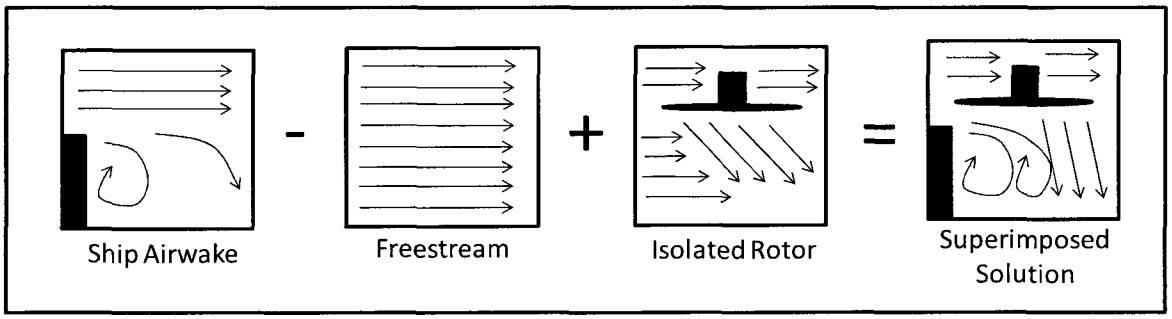

Figure 70: Computation of superimposed velocity field

The variance associated with the superimposed velocity field is computed by summing the contribution of each individual variance from the previous step as shown in equation (40).

$$\sigma^2_{V_{superimposed}} = \sigma^2_{V_{airwake}} + \sigma^2_{V_{combined}} + \sigma^2_{V_{freestream}} \quad \textbf{(40)}$$

3.5.3 Computation of the Velocity Discrepancy

The average magnitude of velocity discrepancies between the superimposed and the experimentally observed flowfield is computed to quantify the level of coupling associated with a particular ship/rotor configuration. The average component wise velocity discrepancy is computed as shown in equation (41).

$$V_{DIFF} = \frac{1}{nm}\sum_{i=1}^{n}\sum_{j=1}^{m}\left|V_{observed}(i,j) - V_{superimposed}(i,j)\right| \quad \textbf{(41)}$$

The total variance associated with the average velocity discrepancy is computed by summing the variances associated with the experimentally observed, superimposed, and the variance between individual velocity discrepancies as shown in equation (42). A computational flowchart has been included in Figure 71 summarizing the coupling analysis technique. The computational algorithm for the extraction of regional velocity components has been included in Appendix A. The algorithm for velocity based coupling analysis has been included in Appendix B.

$$\sigma^2_{\overline{V_{DIFF}}} = \sigma^2_{V_{observed}} + \sigma^2_{V_{superimposed}} + \sigma^2_{V_{DIFF}} \quad \textbf{(42)}$$

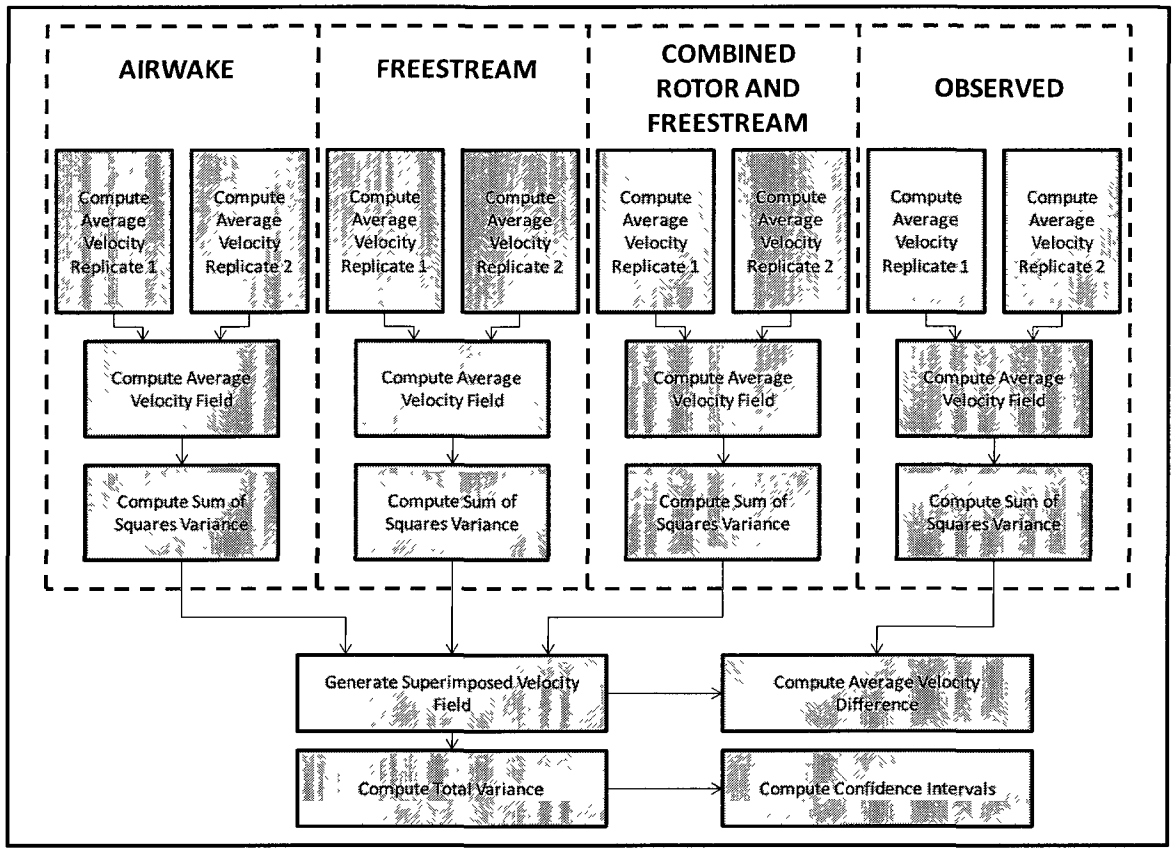

Figure 71: Computation flowchart of coupling analysis

4. EXPERIMENTAL SETUP

This section details the experimental setup used for the ship airwake/rotor downwash coupling investigation. Basic information regarding models, test facilities, instrument systems, and measurement uncertainties are described.

4.1 Overall Experimental Setup

The overall experimental setup including model and PIV laser traversing systems are shown in Figures 72 and 73. The frigate model is placed on a raised ground-board to reduce boundary layer effects on the frigate and rotor model. The position of the primary components (laser and cameras) is also documented in Figure 72.

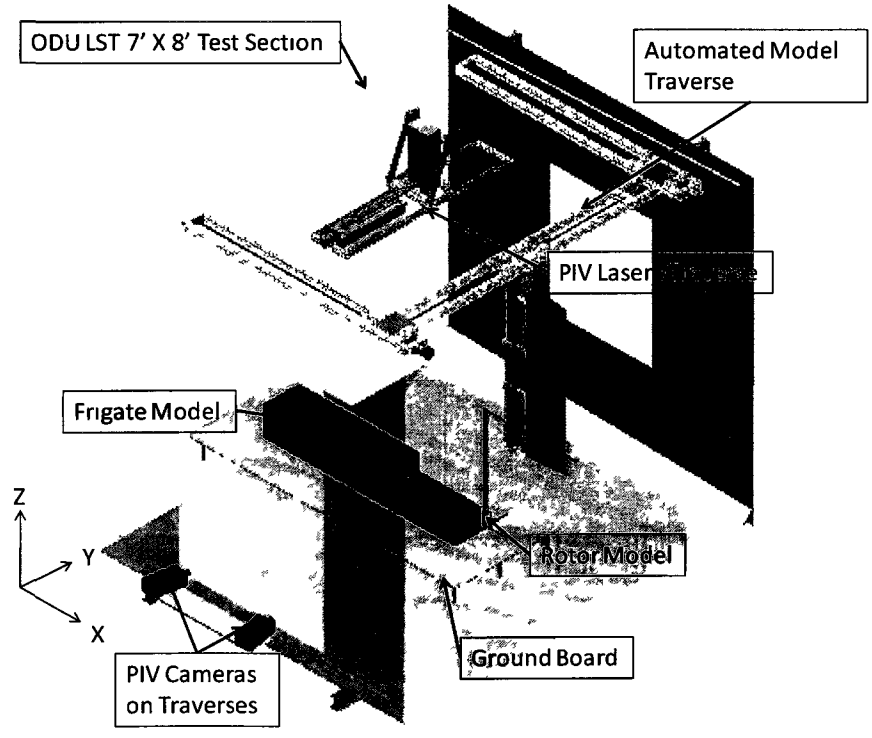

Figure 72: CAD model of the overall experimental setup

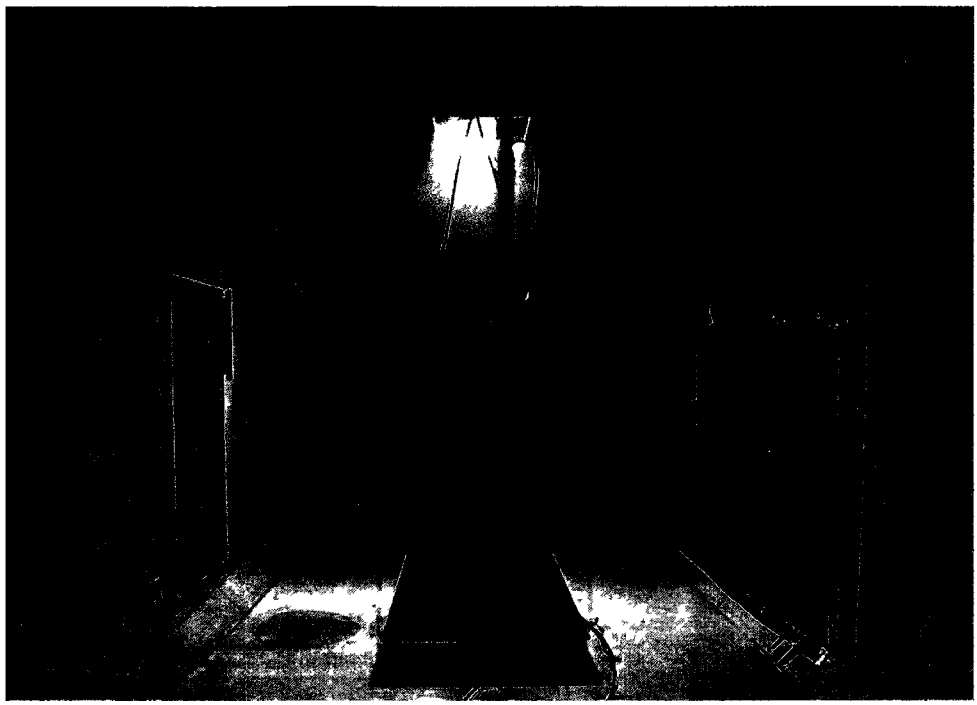

Figure 73: Tunnel test section with model traverse, frigate model, and rotor

4.2 Model Geometries

In wind tunnel studies (and most other experimental studies), proper model selection is an important component of the overall planning process. Models must be selected to capture the important details of the original full scale geometry. For intricate model shapes, such as ships, secondary components (e.g. antennas, towers, and other superstructures) are often omitted. In this study, the basic effects and interactions of ship airwakes and rotor downwash are of interest. Thus, as detailed in Figure 74, a1/50 scale simplified ship geometry, as found in the literature (Wilkinson et al.[20]) and recommended by NAVAIR, was used to model the frigate. As detailed in Figure 75, a four-bladed Advanced Precision Composites off-the-shelf rotor was used to model the helicopter rotor. The rotor measured 10 inches in diameter with a pitch of 6 inches. According to

the manufacturer's website, the rotor blades may have arbitrary shape defined by either tabular data with splined cubic fits or analytical functions typically used for NACA airfoils. The primary airfoil shapes used in this propeller are the NACA 4412 and Clark-Y airfoils[41]. The rotor was powered using an Astro Flight Cobalt 40 DC brushed motor and Sorensen DCS 55-55E model 3kW DC power supply. In this case, no fuselage was included when modeling the helicopter, as this is considered a second order effect with the primary effect being the rotor downwash.

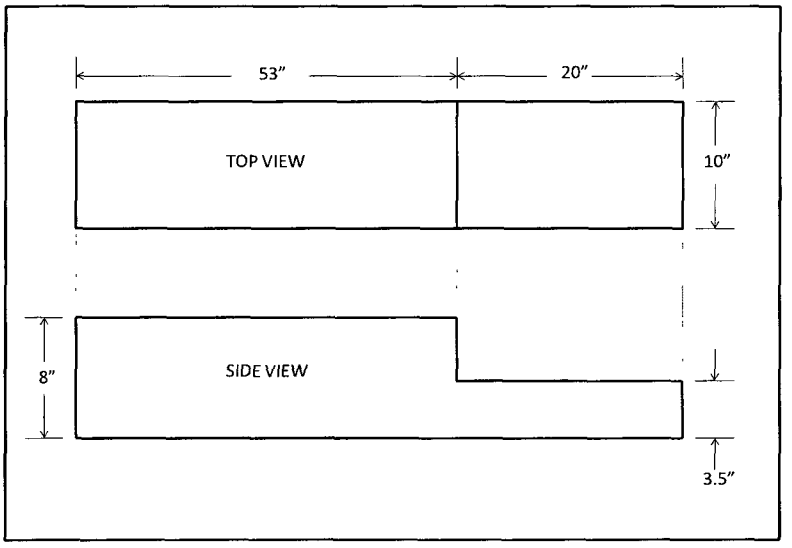

Figure 74: Simple frigate model dimensions

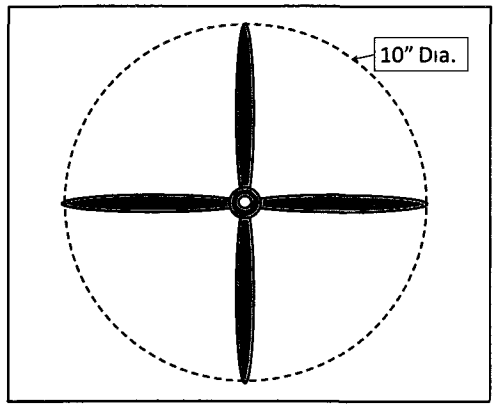

Figure 75: Dimensions of model rotor

4.3 Rotor Thrust Measurements

As part of the research objective, rotor thrust variations over the landing deck of the frigate model are of interest. Thus a rotor thrust measurement system was developed using a beam type load cell (OMEGA LCAE-3KG). To allow for non-dimensionalization to a thrust coefficient, this system also monitors rotor RPM using an optical interrupter. The complete rotor assembly showing load cell and RPM sensor is shown below as Figure 76.

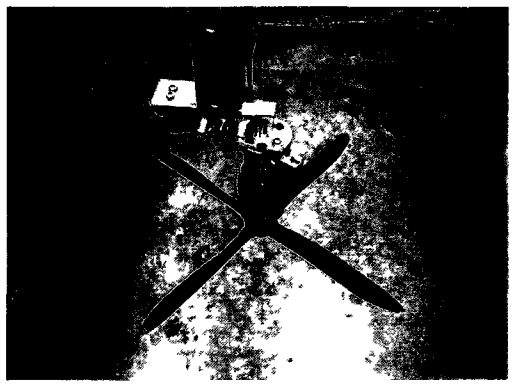

Figure 76: Rotor assembly

4.4 Optical Measurement of the Velocity Field

To study the interaction of rotor downwash and ship airwake, it is necessary to capture velocity field information. Two dimensional and stereo particle image velocimetry systems were used to measure the velocity field for a given plane of interest. A positioning system, utilizing a VELMEX NF-90 stepping motor controller and VELMEX MA25 linear motion traverse assemblies, was developed for the efficient measurement of the velocity field. Two linear traverses are used to move the PIV cameras and a third is used to move the laser in unison. This system is computer controlled using specially developed LabVIEW programs. The PIV camera and laser traversing hardware are shown in Figures 77 and 78, respectively.

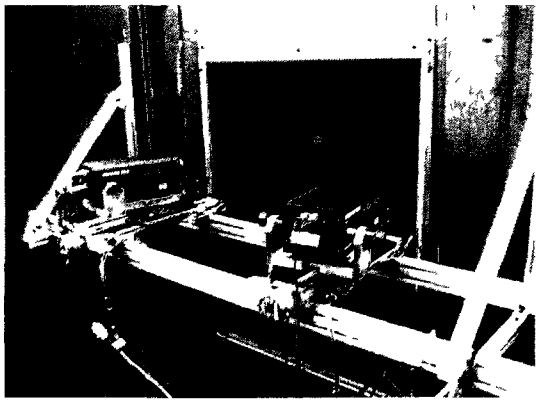

Figure 77: Stereo PIV cameras and traverse

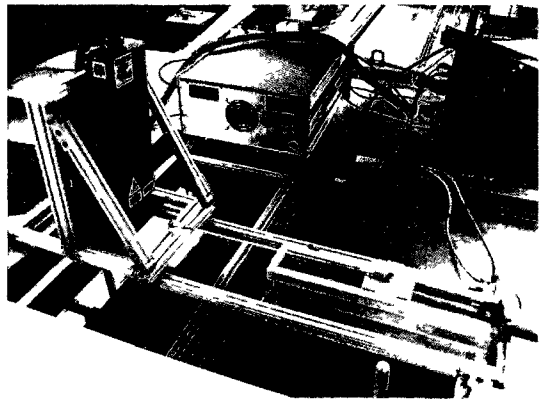

Figure 78: PIV laser and traverse

4.5 Overview of Wind Tunnel Facilities and Systems

The low speed wind tunnel (ODULSWT) at Old Dominion University is an atmospheric closed loop tunnel equipped with a 125 H.P. drive motor and frequency

controller. The tunnel has high speed and low speed test sections measuring 3x4 feet and 7x8 feet, respectively, as shown in Figure 79. The 3x4 foot test section is 8 feet long and has a top speed of 55 m/s (123 mph). The 7x8 foot test section is 7 feet in length and has a top speed of 12m/s (26 mph). The tunnel is computer controlled with compensation for temperature rise and barometric pressure change. In addition, a three axis model traversing system was developed in this study that facilitates automated model positioning and data collection in the 7 X 8 ft. section. The model positioning system is computer controlled using LabVIEW software and is networked with the wind tunnel control system for real-time logging of wind tunnel conditions. Screenshots of all software that was developed for this study has been included in Appendix C for reference. Figures 80 and 81 give the connections of the various wind tunnel control and experiment management systems available in the ODULSWT.

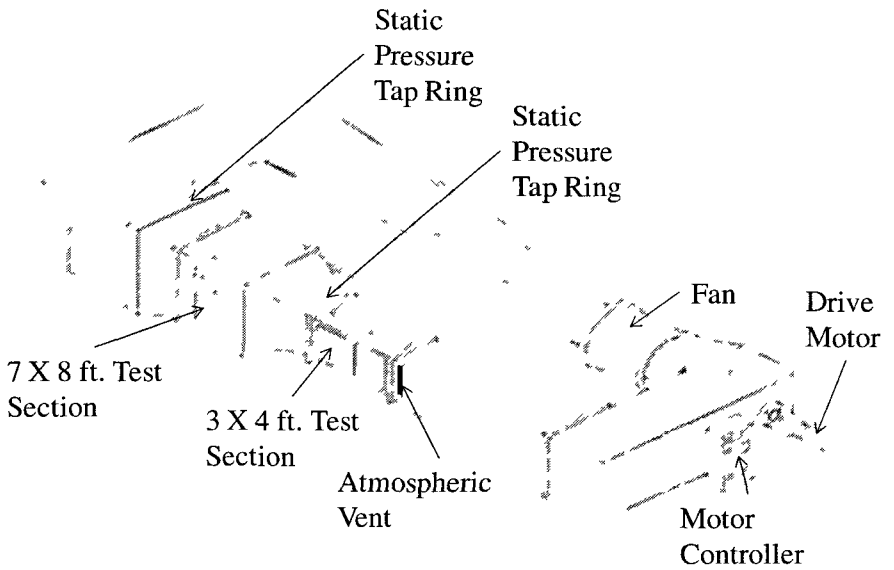

Figure 79: Old Dominion University Low Speed Wind Tunnel

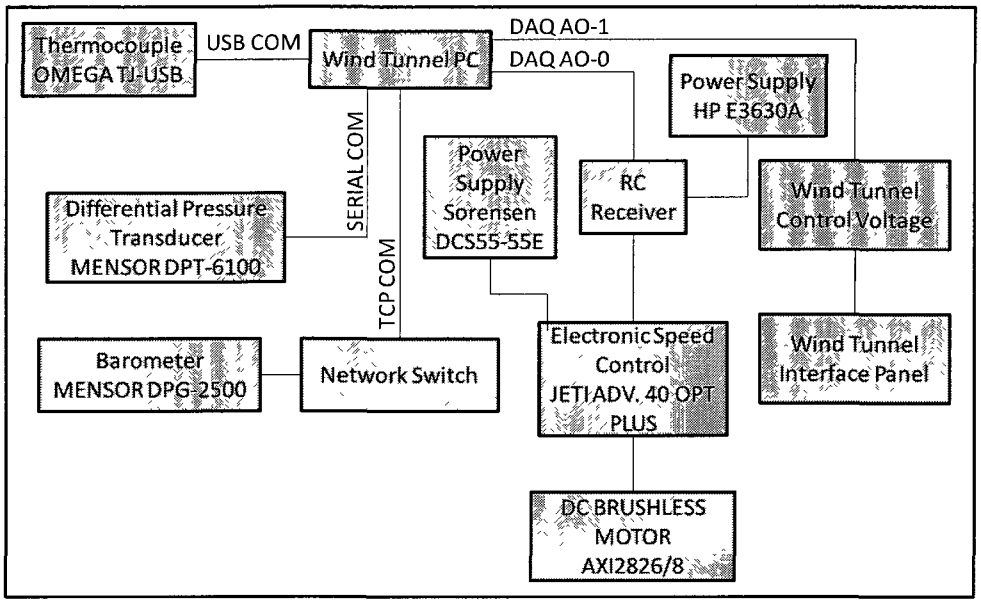

Figure 80: Schematic diagram of systems controlled by the wind tunnel computer

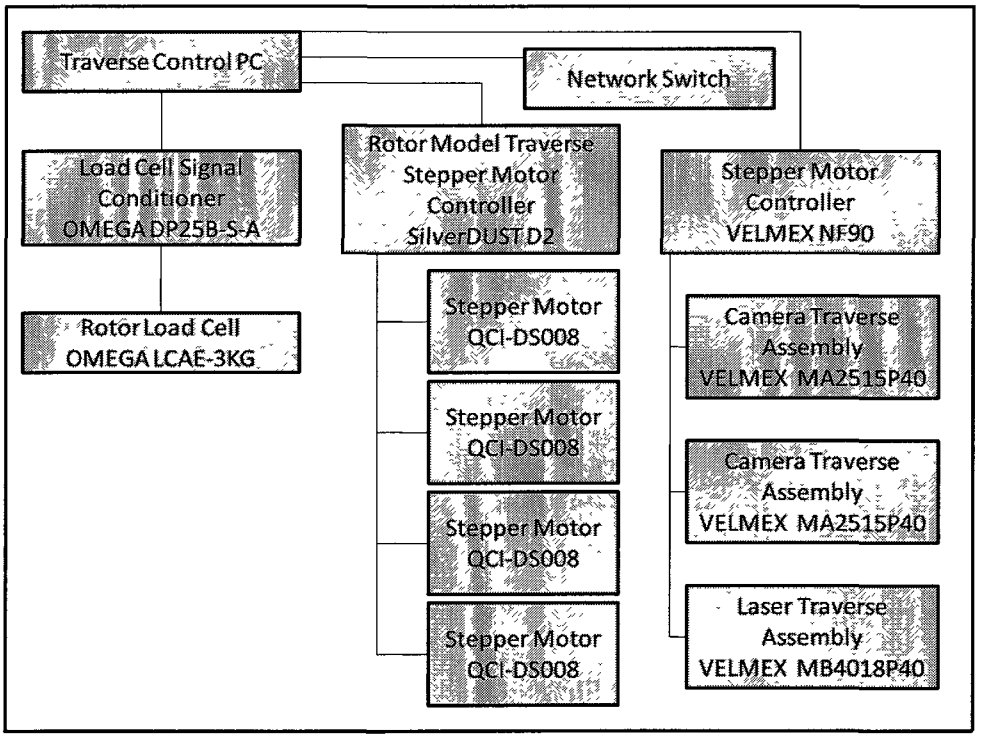

Figure 81: Schematic diagram of systems controlled by the traverse computer

4.5.1 Estimation of Wind Tunnel Velocity

Wind tunnel velocity in ODULSWT is determined by measuring the tunnel dynamic pressure (q). Raw uncorrected dynamic pressure is measured by the differential static pressure across the 7 x 8 ft and 3 x 4 ft. test sections (see Figure 79 for locations of static tap rings). The raw tunnel dynamic pressure is then corrected based on a previous pitot-static calibration. Tunnel velocity is found by measuring the dynamic pressure, atmospheric pressure, and tunnel fluid temperature through the following relationship.

$$V = \sqrt{\frac{2q}{\frac{P_{atm}}{R_{air}T}}} \tag{43}$$

Both tunnel fluid temperature and atmospheric pressure are measured in real-time. This allows for compensation of tunnel temperature and atmospheric pressure changes that occur during run-time.

4.6 Measurement Uncertainties

All experimental measurements contain uncertainties that must be considered in the planning of experiments and reporting of results. Generally, uncertainty can be divided into two error components called bias and precision[42]. Expressed mathematically the combined uncertainty (e_T^2) for any measured variable is the sum of the bias (e_b^2) and precision (e_p^2) uncertainties as shown in equation (44).

$$e_T^2 = e_b^2 + e_p^2 \tag{44}$$

Bias uncertainties (e_b^2) are hardware specific and are related to instrument resolution and accuracy. These values are often quoted in the technical specifications for

any given instrument. For instance, the bias error of a pressure transducer is typically listed in terms of accuracy such as 0.01% of full-scale (FS). Unlike bias errors, precision errors are random errors related to the variance (or standard deviation) associated with a given set of observations. For example, a thermocouple is used to find the average temperature of a fluid. The average temperature is calculated from 10 individual observations using the same thermocouple. The standard deviation associated with the 10 observations that make up the average is a measure of the random error associated with the measurement. Thus, following the methodology presented in Coleman and Steele[42], the precision (e_p^2) error variance can then be expressed in terms of the sample standard deviation of the mean as shown in equation (45).

$$e_p^2 = \frac{S^2}{N} \tag{45}$$

In equation (45) the variable S is the calculated sample standard deviation and N is the number of individual observations.

With the bias and precision errors known, the total uncertainty e_T^2 can be calculated according to equation (44) and reported in terms of a confidence interval[42]. Like the confidence intervals discussed in the section on Design of Experiments, a t-value is a coverage factor applied in this case to formulate a ± range that the actual value is expected to fall within. In the mathematical sense this is expressed as follows.

$$E_T = t_{\alpha/2,N} e_T \tag{46}$$

It should be noted that this technique considers a result that is a function of only one variable. In this study, wind tunnel velocity and rotor thrust coefficient are computed from several measured variables. In this case, a Taylor series approach must be used to

calculate the overall bias error[42]. The Taylor series approach incorporates the bias uncertainties from each sensor or instrument to determine the overall bias uncertainty. When a result is a function of M variables (W_i) associated with a data reduction equation $G = f(W_i)$ where $i = 1 \cdots M$, the bias error can be found as follows.

$$e_{bc}^2 = \sum_{i=1}^{M} \left(\frac{\partial G}{\partial W_i}\right)^2 e_{b_{W_i}}^2 \tag{47}$$

Thus the combined standard uncertainty is found as before.

$$e_T^2 = e_{bc}^2 + e_p^2 \tag{48}$$

Similarly, the confidence interval based on the t distribution is given as follows.

$$E_T = t_{\frac{\alpha}{2},n-1} e_T \tag{49}$$

4.6.1 Wind Tunnel Velocity Uncertainty Analysis

Using the Taylor Series approach outlined in the previous section, the uncertainty associated with the measurement of wind tunnel velocity can be assessed. Wind tunnel velocity is a function of three variables (static pressure differential, atmospheric pressure, and tunnel fluid temperature) as shown in equation (50). The required derivatives for the Taylor Series analysis are given in equations (51)-(53).

$$V = \sqrt{\frac{2\Delta P}{\frac{P_{atm}}{RT}}} \tag{50}$$

$$\frac{\partial V}{\partial \Delta P} = \frac{\sqrt{2}}{2} \frac{RT}{P_{atm}\sqrt{\frac{\Delta P RT}{P_{atm}}}} \tag{51}$$

$$\frac{\partial V}{\partial P_{atm}} = -\frac{\sqrt{2}}{2}\frac{\Delta PRT}{P_{atm}^2\sqrt{\frac{\Delta PRT}{P_{atm}}}} \quad (52)$$

$$\frac{\partial V}{\partial T} = \frac{\sqrt{2}}{2}\frac{\Delta PR}{P_{atm}\sqrt{\frac{\Delta PRT}{P_{atm}}}} \quad (53)$$

The individual bias uncertainty components for each measurement variable are summarized in Table 1.

Component	Bias
Differential Pressure	±0.01% of Full Scale
Temperature	±1 deg. C.
Barometric Pressure	±0.01% of Reading

Table 1: Individual bias errors for measurement components

Using the Taylor series approach, the overall uncertainty in the estimation of wind tunnel velocity for a nominal tunnel speed of 5 m/s, atmospheric pressure of 101324 Pa, and tunnel fluid temperature of 296K was calculated and is given in Table 2. Wind tunnel velocity measurements ($N = 600$) were recorded over a period of five minutes at a sample rate of two samples per second. Prior to recording, the tunnel was allowed to stabilize for 10 minutes during which the automatic speed control system was activated. Based on the sampled wind tunnel data for a nominal tunnel speed of 5 m/s the precision (defined as $P = S/\sqrt{N}$) in wind tunnel velocity estimation was found to be ±0.000411 m/s.

Component	Calculated Value
5 m/s	
Bias Limit (e_b)	±0.0432 m/s
Precision Limit (e_p)	±0.0008m/s
95% C.I.	±0.0433 m/s

Table 2: Uncertainty analysis of high speed test section velocity estimation

For this study, the nominal wind tunnel speed is 5 m/s. The uncertainty analysis reveals that the overall uncertainty in the estimation of wind tunnel velocity is ±0.0433m/s for this tunnel condition.

4.6.2 Rotor Thrust Coefficient Uncertainty Analysis

Using the Taylor series approach and the functional relationship presented in (37) the bias error of the calculated thrust coefficient is given by (54). Expanded derivative relations are shown in Equations (55)-(58).

$$(B_{C_T})^2 = \left(\frac{\partial C_T}{\partial F_{Thrust}}\right)^2 (B_{F_{Thrust}})^2 + \left(\frac{\partial C_T}{\partial P_{atm}}\right)^2 (B_{P_{atm}})^2 + \left(\frac{\partial C_T}{\partial T}\right)^2 (B_T)^2 + \left(\frac{\partial C_T}{\partial \Omega}\right)^2 (B_\Omega)^2 \quad \textbf{(54)}$$

$$\frac{\partial C_T}{\partial F_{Thrust}} = \frac{R_{air}T}{P_{atm}(\Omega r_{rotor})^2 \mathrm{A}} \quad \textbf{(55)}$$

$$\frac{\partial C_T}{\partial P_{atm}} = \frac{-F_{Thrust}RT}{{P_{atm}}^2(\Omega r_{rotor})^2 \mathrm{A}} \quad \textbf{(56)}$$

$$\frac{\partial C_T}{\partial T} = \frac{F_{Thrust}R_{air}}{P_{atm}(\Omega r_{rotor})^2 \mathrm{A}} \quad \textbf{(57)}$$

$$\frac{\partial C_T}{\partial \Omega} = \frac{-2F_{Thrust}R_{air}T}{P_{atm}\Omega^3 r_{rotor}^2 \mathrm{A}} \quad \textbf{(58)}$$

Using the Taylor series analysis technique the overall uncertainty for a nominal rotor loading (F_{Thrust}) of 1.0371 lbf. has been presented in Table 3. Based on the sampled rotor thrust (N=8) for a nominal tunnel speed of 5 m/s the standard deviation associated with rotor thrust coefficient was found to be ±0.000111.

Measurement Component	Reading	Bias
Thrust (F_{Thrust})	4.5289 N	±0.0009 N
Atmospheric Pressure (P_{atm})	101325 Pa	±10 Pa
Tunnel Fluid Temp (T)	296 °K	±1 °K
Rotor Rotation Rate (Ω)	524 radians/sec	0.5 radians/sec
	Thrust Coefficient (C_T)	**0.017253**
	Bias Limit	**±0.000067**
	Precision Limit	**±0.000093**
	95% C.I.	**±0.000115**

Table 3: Thrust coefficient uncertainty for 0.254 m rotor diameter

4.6.3 Particle Image Velocimetry Uncertainty Analysis

Particle image velocimetry is subject to the usual bias and precision errors found in other measurement techniques. Bias errors remain constant throughout a measurement and are typically estimated through calibration procedures[43]. Precision errors are a result of the random error associated with measurement data[43]. The estimation of the overall measurement error for particle image velocimetry requires the consideration of numerous inputs. In both two-dimensional and stereo PIV these errors are related to the statistical correlations of the interrogation area and optical setup[43].

Monte Carlo based error estimation techniques have been developed to assess the accuracy of particle image velocimetry systems. These techniques can be applied to both two-dimensional and stereo particle image velocimetry configurations. To apply the

Monte Carlo technique, particle displacements are simulated using artificially generated images. Particles are distributed randomly throughout the image using a uniformly distributed random number generator. Individual particles are described by a Gaussian intensity profile as found in Raffel et al.[40] and shown below as equation (59).

$$I(x,y) = I_0 exp\left(\frac{-(x_{img} - x_p)^2 - (y_{img} - y_p)^2}{(1/8)d_\tau^2}\right) \quad \textbf{(59)}$$

In equation (59) x_p and y_p are the particle locations (centroid), d_τ is the particle image diameter, and I_0 is the particle intensity. The particle intensity I_0 is a function of the particle's position within the light sheet. In this study, the light sheet was described as a Gaussian intensity distribution as recommended by Raffel et al.[40] Assuming the Gaussian intensity profile, I_0 can be expressed as shown in equation (60).

$$I_0(z_p) = qexp\left(-\frac{{z_p}^2}{(1/8)\Delta Z_L^2}\right) \quad \textbf{(60)}$$

Here z_p is the particle's position within the light sheet, ΔZ_L is the thickness of the light sheet, and q is the efficiency through which a particle scatters light.

To generate artificial images for a two dimensional PIV system, a matrix of zero intensity pixels is first created. Individual particles are then superimposed on the original zero matrix. The particle's x, y, and z location is determined using a uniform random number generator. The particle's light scattering efficiency q and diameter d_τ are specified and held constant throughout the image generation process. Similarly, the laser sheet thickness (ΔZ_L) is specified and kept constant. The generation of individual particles continues until the desired particle density is obtained. The second image is generated in parallel with this first image by adding two dimensional displacements to the

original particle locations. Thus particle displacement is known and can be compared to the calculated displacements obtained from the PIV software.

The generation of artificial images for a three dimensional PIV system is similar to the two dimensional procedure; however, an extra step is required to map the particles in the light sheet to the camera plane. Like before, a matrix of zero intensity pixels is first created. Individual particles are then superimposed on the original zero matrix. The particles x, y, and z location is determined using a uniform random number generator. At this point, the x, y, and z particle locations are reported with respect to the light sheet plane. Calibration equations are then used to map the light sheet plane to the camera plane, thereby generating the "camera view" of the light sheet. The particle's light scattering efficiency q and diameter d_τ are specified and held constant throughout the image generation process. Similarly, the laser sheet thickness (ΔZ_L) is specified and held constant. The generation of individual particles and mapping to the camera plane continues until the desired particle density is obtained. The second image is generated in parallel with this first image by adding three dimensional displacements to the original particle location. Thus, like the two-dimensional case, particle displacement is known and can be compared to the calculated displacements obtained from the PIV software. The simulation constants for the Monte Carlo uncertainty analysis of the stereo PIV system are given in Table 4. The computational algorithm for the generation of stereo PIV images has been included in Appendix D. The overall system bias is calculated using the recommended AIAA calibration procedure[44]. To determine the system bias, the mean difference between the velocity standard (specified in the Monte Carlo simulation)

and the measured velocity component (computed in the PIV software) was calculated as shown in equations (61) through (63).

$$\overline{\Delta U} = \frac{1}{N}\left[\sum_{i=1}^{N} \Delta U_i\right] \quad \textbf{(61)}$$

$$\overline{\Delta V} = \frac{1}{N}\left[\sum_{i=1}^{N} \Delta V_i\right] \quad \textbf{(62)}$$

$$\overline{\Delta W} = \frac{1}{N}\left[\sum_{i=1}^{N} \Delta W_i\right] \quad \textbf{(63)}$$

Here, ΔU_i,ΔV_i, and ΔW_i are the individual component-wise (U,V,W) velocity differences between the known standard (Monte Carlo simulation) and the measured velocity (PIV software). For a simulation the uncertainty of the calibration standard is assumed to be zero. Thus the component-wise bias ($\beta_U, \beta_V, \beta_W$) is equal to the average velocity differences directly as shown in equations (64) through (66).

$$\beta_{\Delta U} = \overline{\Delta U} \quad \textbf{(64)}$$

$$\beta_{\Delta V} = \overline{\Delta V} \quad \textbf{(65)}$$

$$\beta_{\Delta W} = \overline{\Delta W} \quad \textbf{(66)}$$

Similarly, the standard deviation of the component-wise velocity difference is calculated to determine the precision of the stereo PIV system as shown in equations (67) through (69).

$$S_{\Delta U} = \sqrt{\frac{1}{N-1}\left[\sum_{i=1}^{N} (\Delta U_i - \overline{\Delta U})^2\right]} \quad \textbf{(67)}$$

$$S_{\Delta V} = \sqrt{\frac{1}{N-1}\left[\sum_{i=1}^{N}(\Delta V_i - \overline{\Delta V})^2\right]} \quad (68)$$

$$S_{\Delta W} = \sqrt{\frac{1}{N-1}\left[\sum_{i=1}^{N}(\Delta W_i - \overline{\Delta W})^2\right]} \quad (69)$$

Hence the precision for each of the mean velocity difference components was determined as shown in equations (70)-(72).

$$P_{\overline{\Delta U}} = \frac{2S_{\Delta U}}{\sqrt{N}} \quad (70)$$

$$P_{\overline{\Delta V}} = \frac{2S_{\Delta V}}{\sqrt{N}} \quad (71)$$

$$P_{\overline{\Delta W}} = \frac{2S_{\Delta W}}{\sqrt{N}} \quad (72)$$

Finally, the total uncertainty (95%) was found in the familiar way by combining the bias and precision components as shown in equations (73) through (75).

$$U_{\overline{\Delta U}} = \sqrt{\beta_{\Delta U}{}^2 + P_{\overline{\Delta U}}{}^2} \quad (73)$$

$$U_{\overline{\Delta V}} = \sqrt{\beta_{\Delta V}{}^2 + P_{\overline{\Delta V}}{}^2} \quad (74)$$

$$U_{\overline{\Delta W}} = \sqrt{\beta_{\Delta W}{}^2 + P_{\overline{\Delta W}}{}^2} \quad (75)$$

The previously calculated uncertainty becomes a bias limit when used in the estimation of the uncertainty associated with stereo PIV measurements[44].

In this study, the Monte Carlo simulation considers a range of U-velocity components from -20 m/s to 20 m/s, V-velocity components from -5 m/s to 5 m/s, and W-velocity components from -20 m/s to 20 m/s. The specified component-wise velocity

ranges were chosen based on typical velocity ranges seen during experimentation. Results from this study are shown in Table 5. The analysis concluded that the average U, V, and W component-wise bias limits for the stereo PIV system used in this study was ±0.13 m/s, ±0.37 m/s, and ±0.26 m/s, respectively. Sample images generated using the described Monte Carlo technique are shown in Figure 82. In Figure 82 images labeled as "Image A" correspond to the first image pair recorded, and "Image B" refers to the second image pair recorded after a delay of Δt.

Parameter	Value
q	100
d_τ	0.2 pixels
ΔZ_L	3mm

Table 4: Stereo PIV uncertainty analysis simulation constants

	Bias Statistics		
Velocity Bias Component	**Max (m/s)**	**Min (m/s)**	**Average (m/s)**
U-Component (β_U)	±0.38	±0.01	±0.13
V-Component (β_V)	±1.00	±0.02	±0.37
W-Component (β_W)	±0.60	±0.09	±0.26

Table 5: Results of the Monte Carlo uncertainty analysis for stereo particle image velocimetry system

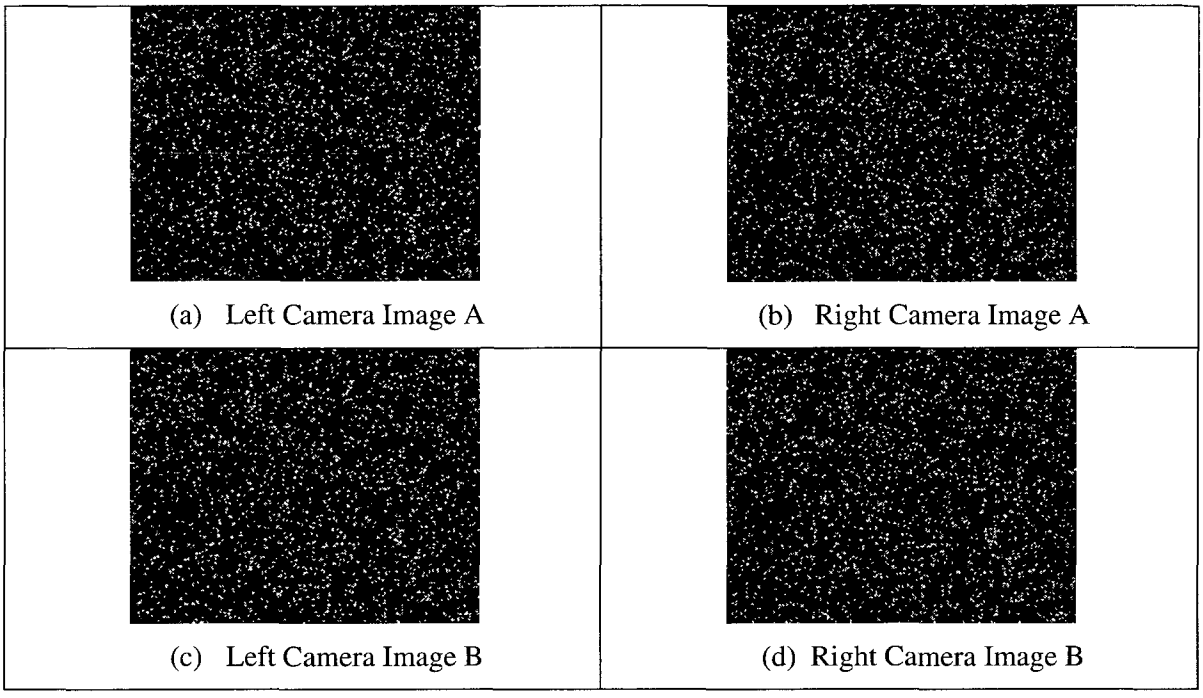

Figure 82: Computer generated images (320 X 256 pixels) for Monte Carlo evaluation of stereo PIV uncertainty.

5. SUMMARY OF EXPERIMENTS PERFORMED

5.1 Rotor Thrust Surveys

An experimental wind tunnel study was conducted to examine the variation of rotor thrust over the landing deck of the simplified frigate model. Rotor thrust was measured at 637 unique rotor locations with two replicates at each design point. The measurement volume extended from X/D=0.5125 to X/D=2.0125, Y/D=-0.5 to Y/D=0.5, and Z/D=0.35 to Z/D=0.85. The experiment was performed over a two day period divided in terms of the right and left half of the deck. Rotor rotation rate was set to 5000 RPM and wind tunnel speed was set to 5 m/s yielding a rotor advance ratio (AR) of 0.075. The computer controlled model traversing system mentioned previously was used to efficiently and accurately position the rotor model over the landing deck. Wind tunnel speed was computer controlled and incorporated compensation for fluid temperature rise and barometric pressure changes. Surface plots are reported corresponding to the 13 longitudinal planes shown in Figure 83.

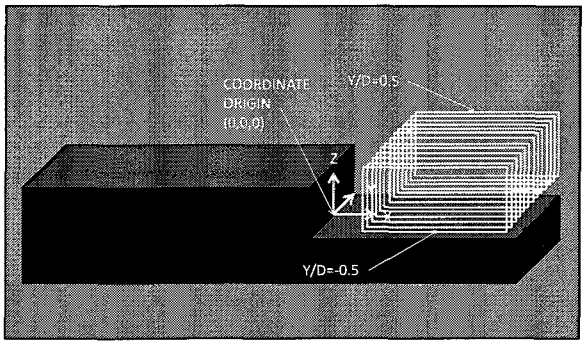

Figure 83: Illustration of measurement planes reported as surface plots of thrust coefficient

5.2 Stereo Particle Image Velocimetry Surveys

Stereo particle image velocimetry surveys were conducted to collect information about the velocity field in the immediate vicinity of the rotor for various ship/rotor configurations. Like the rotor thrust survey, rotor rotation rate was set to 5000 RPM and wind tunnel speed was set to 5 m/s yielding a rotor advance ratio (AR) of 0.075. A summary of rotor locations investigated in this study is given in Table 6. Stereo PIV was only used for the forward (X/D=0.5125) rotor location due to optical access limitations. Thrust coefficient was also collected at the same rotor locations as the PIV surveys.

X/D	Y/D	Z/D	X/D	Y/D	Z/D	X/D	Y/D	Z/D
0.5125	-0.5	0.45	0.5125	-0.5	1.2	0.5125	-0.5	2.4
0.5125	-0.4	0.45	0.5125	-0.4	1.2	0.5125	-0.4	2.4
0.5125	-0.3	0.45	0.5125	-0.3	1.2	0.5125	-0.3	2.4
0.5125	-0.2	0.45	0.5125	-0.2	1.2	0.5125	-0.2	2.4
0.5125	-0.1	0.45	0.5125	-0.1	1.2	0.5125	-0.1	2.4
0.5125	0	0.45	0.5125	0	1.2	0.5125	0	2.4
0.5125	0.1	0.45	0.5125	0.1	1.2	0.5125	0.1	2.4
0.5125	0.2	0.45	0.5125	0.2	1.2	0.5125	0.2	2.4
0.5125	0.3	0.45	0.5125	0.3	1.2	0.5125	0.3	2.4
0.5125	0.4	0.45	0.5125	0.4	1.2	0.5125	0.4	2.4
0.5125	0.5	0.45	0.5125	0.5	1.2	0.5125	0.5	2.4

Table 6: Summary of rotor hub positions for stereo PIV survey

5.3 Two Dimensional Particle Image Velocimetry Surveys

Similar to the stereo particle image velocimetry surveys mentioned in the previous section, two dimensional particle image velocimetry surveys were conducted for an additional longitudinal rotor location. Two-dimensional PIV (not stereo) was used to collect information about the velocity field in the immediate vicinity of the rotor for

various ship/rotor configurations. Like the rotor thrust survey, the rotor rotation rate was set to 5000 RPM and wind tunnel speed was set to 5 m/s yielding a rotor advance ratio (AR) of 0.075. A summary of rotor locations investigated in this study is given in Table 7. Thrust coefficient was also collected at the same rotor locations as the PIV surveys.

X/D	Y/D	Z/D	X/D	Y/D	Z/D	X/D	Y/D	Z/D
1.3	-0.5	0.45	1.3	-0.5	1.2	1.3	-0.5	2.4
1.3	-0.4	0.45	1.3	-0.4	1.2	1.3	-0.4	2.4
1.3	-0.3	0.45	1.3	-0.3	1.2	1.3	-0.3	2.4
1.3	-0.2	0.45	1.3	-0.2	1.2	1.3	-0.2	2.4
1.3	-0.1	0.45	1.3	-0.1	1.2	1.3	-0.1	2.4
1.3	0	0.45	1.3	0	1.2	1.3	0	2.4
1.3	0.1	0.45	1.3	0.1	1.2	1.3	0.1	2.4
1.3	0.2	0.45	1.3	0.2	1.2	1.3	0.2	2.4
1.3	0.3	0.45	1.3	0.3	1.2	1.3	0.3	2.4
1.3	0.4	0.45	1.3	0.4	1.2	1.3	0.4	2.4
1.3	0.5	0.45	1.3	0.5	1.2	1.3	0.5	2.4

Table 7: Summary of rotor hub positions for two-dimensional PIV survey

6. RESULTS

6.1 Near-Deck Thrust Coefficient Variations

Using the collected rotor thrust measurements, a global response surface was developed to show the effect of rotor position on rotor thrust. The measurement volume extends from X/D=0.5125 to X/D=2.0125, Y/D=-0.5 to Y/D=0.5, and Z/D=0.35 to Z/D=0.85. This measurement region is located behind the hangar door (landing area) of the simplified frigate model. All thrust coefficient results for the near-deck survey are tabulated in Appendix E.

6.1.1 ANOVA

A sixth order polynomial global model was considered in this case to predict rotor thrust coefficient as a function of three factors (X/D, Y/D, and Z/D). An analysis of variance (ANOVA) was used to identify significant model terms for inclusion (or exclusion) in the final response model. Backwards elimination was used to reduce the model such that it included only significant model terms. Additional terms required to maintain hierarchy were also included in the final model. The results of the ANOVA are given in Table 8. In this case $\alpha = 0.05$ thus $P < 0.01$ indicates significance. The ANOVA results show that the reduced sixth order polynomial model is significant.

Source	Sum of Squares	df	Mean Square	F Value	p-value Prob>F
Model	4.946E-005	72	6.870E-007	97.76	< 0.0001
A-X/D	*2.179E-008*	*1*	*2.179E-008*	*3.10*	*0.0785*
B-Y/D	*7.000E-007*	*1*	*7.000E-007*	*99.61*	*< 0.0001*
C-Z/D	*1.221E-007*	*1*	*1.221E-007*	*17.37*	*< 0.0001*
AB	*3.044E-007*	*1*	*3.044E-007*	*43.32*	*< 0.0001*
AC	*1.904E-007*	*1*	*1.904E-007*	*27.09*	*< 0.0001*
BC	*1.800E-009*	*1*	*1.800E-009*	*0.26*	*0.6128*

A^2	2.337E-007	1	2.337E-007	33.26	< 0.0001
B^2	3.527E-007	1	3.527E-007	50.19	< 0.0001
C^2	1.229E-007	1	1.229E-007	17.48	< 0.0001
ABC	1.044E-009	1	1.044E-009	0.15	0.7000
A^2B	1.691E-007	1	1.691E-007	24.07	< 0.0001
A^2C	6.623E-007	1	6.623E-007	94.25	< 0.0001
AB^2	8.317E-007	1	8.317E-007	118.34	< 0.0001
AC^2	2.981E-007	1	2.981E-007	42.42	< 0.0001
B^2C	4.767E-007	1	4.767E-007	67.83	< 0.0001
BC^2	6.537E-009	1	6.537E-009	0.93	0.3350
A^3	3.862E-008	1	3.862E-008	5.50	0.0192
B^3	4.190E-007	1	4.190E-007	59.63	< 0.0001
C^3	8.693E-009	1	8.693E-009	1.24	0.2663
A^2B^2	1.458E-006	1	1.458E-006	207.42	< 0.0001
A^2BC	2.277E-008	1	2.277E-008	3.24	0.0721
A^2C^2	2.570E-007	1	2.570E-007	36.58	< 0.0001
AB^2C	1.432E-008	1	1.432E-008	2.04	0.1537
ABC^2	2.188E-007	1	2.188E-007	31.14	< 0.0001
B^2C^2	1.921E-007	1	1.921E-007	27.33	< 0.0001
A^3B	2.383E-010	1	2.383E-010	0.034	0.8539
A^3C	6.408E-008	1	6.408E-008	9.12	0.0026
AB^3	4.648E-007	1	4.648E-007	66.14	< 0.0001
AC^3	1.609E-008	1	1.609E-008	2.29	0.1305
B^3C	8.132E-008	1	8.132E-008	11.57	0.0007
BC^3	3.383E-009	1	3.383E-009	0.48	0.4879
A^4	5.283E-008	1	5.283E-008	7.52	0.0062
B^4	4.286E-007	1	4.286E-007	60.99	< 0.0001
C^4	1.004E-007	1	1.004E-007	14.29	0.0002
A^2B^2C	1.745E-007	1	1.745E-007	24.83	< 0.0001
A^2BC^2	6.893E-007	1	6.893E-007	98.09	< 0.0001
AB^2C^2	4.002E-007	1	4.002E-007	56.95	< 0.0001
A^3B^2	3.792E-008	1	3.792E-008	5.40	0.0203
A^3BC	9.209E-008	1	9.209E-008	13.10	0.0003
A^3C^2	2.686E-008	1	2.686E-008	3.82	0.0508
A^2B^3	3.087E-008	1	3.087E-008	4.39	0.0363
A^2C^3	8.641E-007	1	8.641E-007	122.96	< 0.0001
AB^3C	5.637E-007	1	5.637E-007	80.21	< 0.0001
ABC^3	5.451E-007	1	5.451E-007	77.57	< 0.0001
B^3C^2	3.311E-007	1	3.311E-007	47.12	< 0.0001
B^2C^3	7.209E-008	1	7.209E-008	10.26	0.0014
A^4B	7.823E-008	1	7.823E-008	11.13	0.0009
A^4C	8.320E-007	1	8.320E-007	118.39	< 0.0001
AB^4	3.075E-007	1	3.075E-007	43.76	< 0.0001
AC^4	5.137E-008	1	5.137E-008	7.31	0.0069
B^4C	4.689E-007	1	4.689E-007	66.73	< 0.0001
BC^4	2.094E-008	1	2.094E-008	2.98	0.0846
A^5	4.086E-009	1	4.086E-009	0.58	0.4459
B^5	5.147E-007	1	5.147E-007	73.24	< 0.0001
$A^2B^2C^2$	5.109E-007	1	5.109E-007	72.70	< 0.0001
A^3B^3	3.466E-007	1	3.466E-007	49.33	< 0.0001
A^3B^2C	9.258E-008	1	9.258E-008	13.17	0.0003

A^3C^3	*7.690E-008*	*1*	*7.690E-008*	*10.94*	*0.0010*
A^2B^3C	*1.079E-007*	*1*	*1.079E-007*	*15.36*	*< 0.0001*
A^2BC^3	*1.338E-007*	*1*	*1.338E-007*	*19.05*	*< 0.0001*
AB^3C^2	*4.594E-007*	*1*	*4.594E-007*	*65.37*	*< 0.0001*
A^4B^2	*6.512E-007*	*1*	*6.512E-007*	*92.67*	*< 0.0001*
A^4BC	*1.372E-007*	*1*	*1.372E-007*	*19.53*	*< 0.0001*
A^4C^2	*1.332E-007*	*1*	*1.332E-007*	*18.96*	*< 0.0001*
A^2B^4	*3.199E-007*	*1*	*3.199E-007*	*45.52*	*< 0.0001*
A^2C^4	*7.942E-008*	*1*	*7.942E-008*	*11.30*	*0.0008*
ABC^4	*3.251E-008*	*1*	*3.251E-008*	*4.63*	*0.0317*
B^4C^2	*3.378E-008*	*1*	*3.378E-008*	*4.81*	*0.0285*
A^5B	*5.508E-008*	*1*	*5.508E-008*	*7.84*	*0.0052*
B^5C	*7.385E-008*	*1*	*7.385E-008*	*10.51*	*0.0012*
A^6	*3.398E-008*	*1*	*3.398E-008*	*4.84*	*0.0281*
B^6	*3.510E-007*	*1*	*3.510E-007*	*49.94*	*< 0.0001*
Residual	9.023E-006	1284	7.027E-009		
Lack of Fit	*7.002E-006*	*562*	*1.246E-008*	*4.45*	*< 0.0001*
Pure Error	*2.021E-006*	*722*	*2.799E-009*		
Cor Total	5.849E-005	1356			

Table 8: Analysis of variance (ANOVA) for sixth order response surface

6.1.2 Fit Statistics

In addition to the outcome of the ANOVA regarding model and factor significance, an additional set of statistics can be generated to examine model fit and prediction capabilities. Specifically, R^2 statistics report the model's ability to explain the variability associated with the observed response (R^2 and $R^2_{adj.}$) and the variability associated with predicting future responses ($R^2_{pred.}$). The R^2 statistics and other diagnostics are presented for the developed regression model in Table 9. In general, it is desired for the R^2 statistics to be close to one and in close agreement. In this study the R^2 statistics are in close agreement and indicate that the model describes and can predict 82% of the variability associated with the response.

Fit Statistic	Value
Std. Dev.	8.383E-005
Mean	0.017
C.V. %	0.50
PRESS	1.018E-005
R-Squared	0.8457
Adj R-Squared	0.8371
Pred R-Squared	0.8260
Adeq Precision	87.834

Table 9: Fit statistics for sixth order response surface

6.1.3 Residual Diagnostics

Residual diagnostics ensure that the assumptions associated with the ANOVA (normality, independence, and constant variance) are valid for a given response surface. In all cases, internally studentized residuals are used (versus raw residuals) to ensure constant variance in the residuals regardless of the location of any given design point. Figure 84 shows a normal probability plot of the residuals for the developed sixth order response surface. In this plot all residuals should fall along the line. Points away from the line indicate a potential violation. For the sixth order model developed in this study, the plot indicates that all residuals are normally distributed and the normality assumption holds. In addition, Figure 85 shows a plot of internally studentized residuals versus run order. This plot is used to determine if responses are independent of time. Residuals should appear to oscillate randomly across zero for the independence assumption to be valid. Any obvious trends in the residuals indicate a violation. Figure 85 shows a random oscillation of the residuals across zero and indicates no trends are present. Thus, the independence assumption holds. Finally, Figure 86 shows a plot of the residuals versus predicted values for the developed sixth order response surface. This plot is used

to determine if the constant variance assumption is satisfied. If trends are found such as barreling or coning, the constant variance assumption is not satisfied and a transform may be required. Figure 86 shows no trends and exhibits a random scatter of the residuals, hence the constant variance assumption is satisfied.

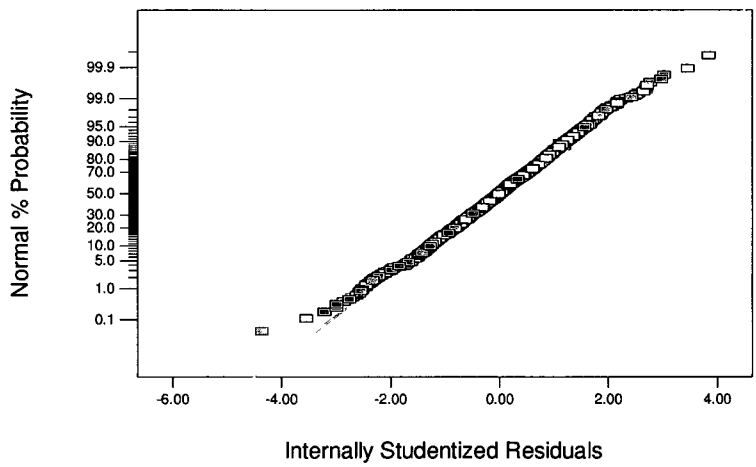

Figure 84: Normal probability plot of residuals for the sixth order response model

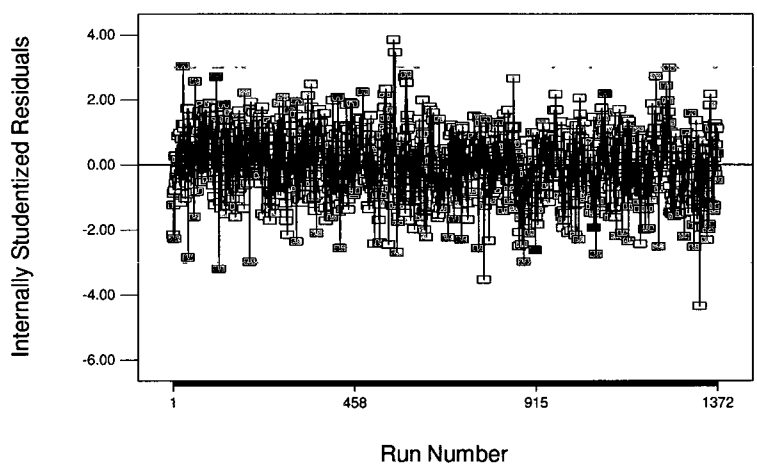

Figure 85: Plot of residuals vs. run order for the sixth order response model

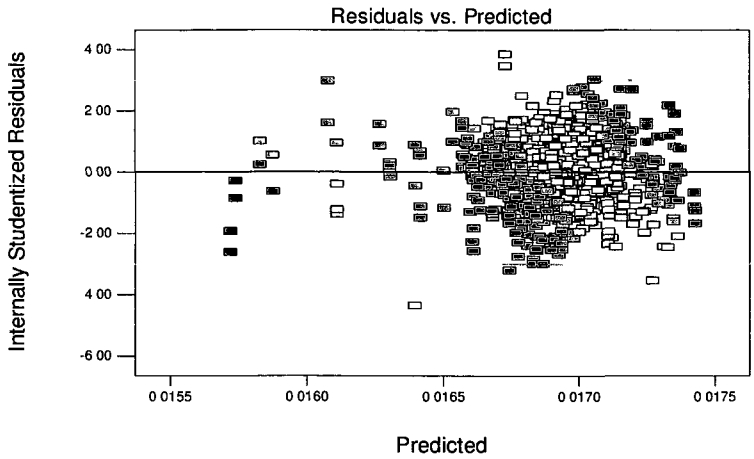

Figure 86: Plot of residuals vs. predicted values for the sixth order response model

6.1.4 Response Surface

Using the results from the ANOVA, a response surface was developed. The model was reduced to include only significant model terms ($P < 0.05$) and terms required to maintain heirarchy. Table 10 lists the model term coefficients for the sixth order response surface.

Coefficient Estimate	Model Term	Coefficient Estimate	Model Term
-6.36816E-003	*Intercept*	-0.12487	$*X/D*Y/D^2*Z/D^2$
+4.80128E-003	$*X/D$	-0.045776	$*X/D^3Y/D^2$
+0.080330	$*Y/D$	+0.035417	$*X/D^3*Y/D*Z/D$
+0.17202	$*Z/D$	-0.016462	$*X/D^3*Z/D^2$
-0.13038	$*X/D*Y/D$	-0.039149	$*X/D^2*Y/D^3$
-0.30652	$*X/D*Z/D$	+0.35723	$*X/D^2*Z/D^3$
-0.33508	$*Y/D*Z/D$	-0.12214	$*X/D*Y/D^3*Z/D$
+0.087892	$*X/D^2$	+0.36400	$*X/D*Y/D*Z/D^3$
+0.064820	$*Y/D^2$	-0.11667	$*Y/D^3*Z/D^2$
-0.34634	$*Z/D^2$	-0.026255	$*Y/D^2*Z/D^3$
+0.36856	$*X/D*Y/D*Z/D$	+0.018767	$*X/D^4*Y/D$
+0.10765	$*X/D^2*Y/D$	-0.020801	$*X/D^4*Z/D$
+0.056284	$*X/D^2*Z/D$	-0.034772	$*X/D*Y/D^4$
-0.11026	$*X/D*Y/D^2$	+0.19823	$*X/D*Z/D^4$
+0.76459	$*X/D*Z/D^2$	+0.060376	$*Y/D^4*Z/D$
-0.18497	$*Y/D^2*Z/D$	+0.14030	$*Y/D*Z/D^4$
+0.58457	$*Y/D*Z/D^2$	-0.017183	$*X/D^5$
-0.11078	$*X/D^3$	+0.031880	$*Y/D^5$
-0.083580	$*Y/D^3$	+0.042878	$*X/D^2*Y/D^2*Z/D^2$
+0.27425	$*Z/D^3$	+8.30813E-003	$*X/D^3*Y/D^3$
+0.10339	$*X/D^2*Y/D^2$	+6.68512E-003	$*X/D^3*Y/D^2*Z/D$
-0.13711	$*X/D^2*Y/D*Z/D$	-0.027035	$*X/D^3*Z/D^3$
-0.34298	$*X/D^2*Z/D^2$	+0.011151	$*X/D^2*Y/D^3*Z/D$
+0.18968	$*X/D*Y/D^2*Z/D$	-0.047434	$*X/D^2*Y/D*Z/D^3$
-0.52639	$*X/D*Y/D*Z/D^2$	+0.069087	$*X/D*Y/D^3*Z/D^2$
+0.15815	$*Y/D^2*Z/D^2$	+8.13064E-003	$*X/D^4*Y/D^2$
-0.060541	$*X/D^3*Y/D$	-6.63088E-003	$*X/D^4*Y/D*Z/D$
+0.074665	$*X/D^3*Z/D$	+0.013320	$*X/D^4*Z/D^2$
+0.085742	$*X/D*Y/D^3$	+0.011786	$*X/D^2*Y/D^4$
-0.69062	$*X/D*Z/D^3$	-0.091093	$*X/D^2*Z/D^4$
+0.18232	$*Y/D^3*Z/D$	-0.084358	$*X/D*Y/D*Z/D^4$
-0.46755	$*Y/D*Z/D^3$	-0.034717	$*Y/D^4*Z/D^2$
+0.058964	$*X/D^4$	-2.21328E-003	$*X/D^5*Y/D$
-0.017596	$*Y/D^4$	-0.030719	$*Y/D^5*Z/D$
-0.071232	$*Z/D^4$	+2.29207E-003	$*X/D^6$
-0.080388	$*X/D^2*Y/D^2*Z/D$	+0.044225	$*Y/D^6$
+0.099764	$*X/D^2*Y/D*Z/D^2$		

Table 10: Summary of model coefficients in terms of actual factors

6.1.5 Thrust Coefficient Surface Plots

To visually inspect model adequacy, surface plots of thrust coefficient with design points indicated have been included in Appendix F for eleven longitudinal Y/D planes. A

representative subset of the thrust coefficient surface plots has been included in this section as Figures 87 and 88. In the plots, a red design point indicates that the observed response falls above the response surface and a pink design point indicates that the observed response falls below the response surface. A rotor Y/D=-0.5 corresponds to the port side of the frigate model, while a Y/D=0.5 corresponds to the starboard side of the frigate model. As seen in Figure 87, the developed response surface fits the observed data points to an acceptable degree. This is in agreement with the reported R^2 statistics ($R^2 = 0.84$, $R^2_{adj.} = 0.83$, and $R^2_{pred.} = 0.83$). The plots also help to indentify regions where the response surface fails to capture all of the experimentally observed trends. For instance, along the Z/D=0.35 edge of Figure 88, a disagreement is observed between the response surface and the observed thrust coefficient. These instances occurred infrequently and do not appear to significantly alter the response surface. Interpolation techniques such as Kriging are able to better fit the observed responses; however, these techniques lack the ability to quantify uncertainty. In the context of this research, the variability associated with the experimental processes required a statistically robust data analysis technique capable of quantifying uncertainty and identifying the potential effect of nuisance factors. However, for implementation in flight simulations, a faster interpolation technique (linear or Kriging) based on the observed data may be better suited.

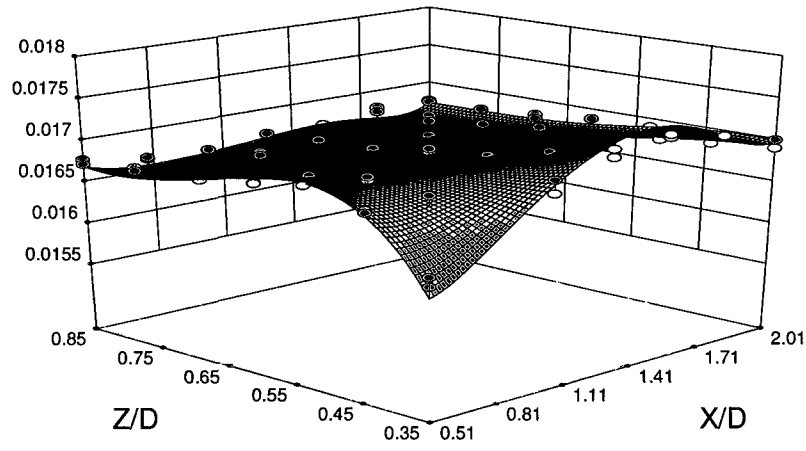

Figure 87: Surface plot of thrust coefficient for Y/D=-0.4165

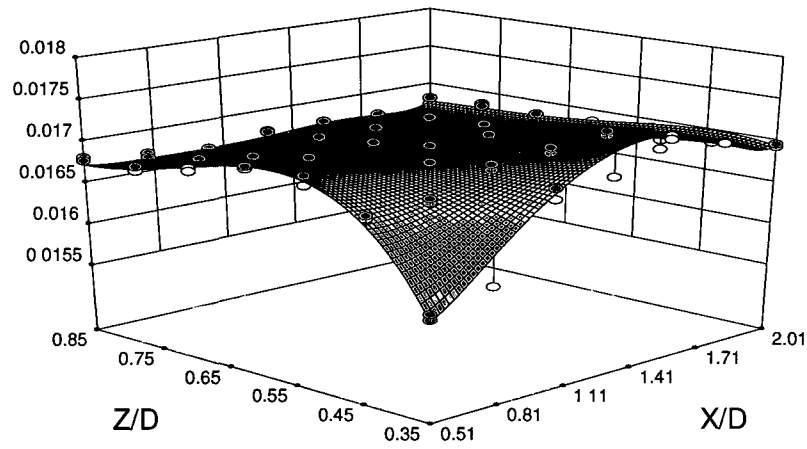

Figure 88: Surface plot of thrust coefficient for Y/D=-0.3333

6.1.6 Thrust Coefficient Contours

In addition to the thrust coefficient surface plots, contours plots are shown the fitted sixth order regression model. Thrust coefficient contours for eleven longitudinal planes (Y/D=-0.5, -0.4, -0.3, -0.2, -0.1, 0.0, 0.1, 0.2, 0.3, 0.4, and 0.5) have been included in Appendix G. A representative subset of the thrust coefficient contour plots are shown in this section as Figures 90-92. A rotor Y/D=-0.5 corresponds to the left side of the frigate model, while a Y/D=0.5 corresponds to the right side of the frigate model. Results highlight the asymmetry in the variation of rotor thrust coefficient over the landing deck of the frigate model.

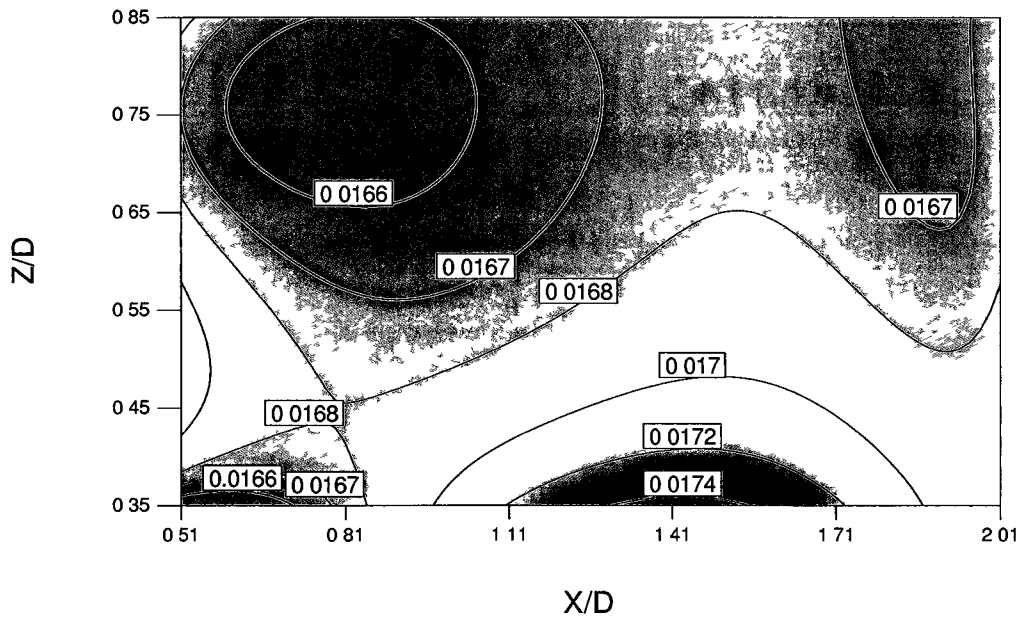

Figure 89: Thrust coefficient contours for rotor location of Y/D=-0.5

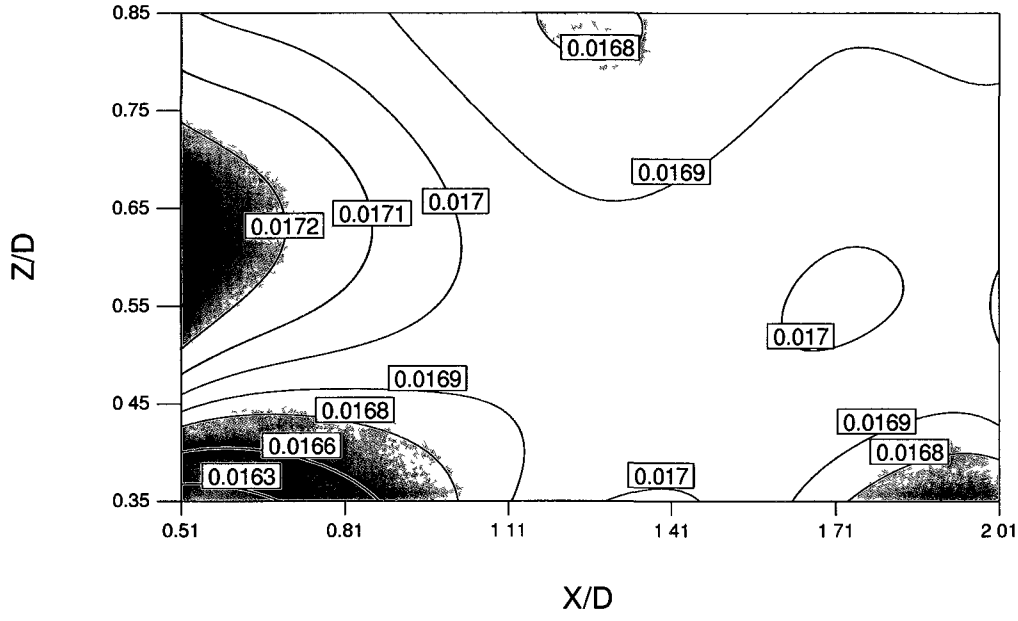

Figure 90: Thrust coefficient contours for rotor location of Y/D=0.0

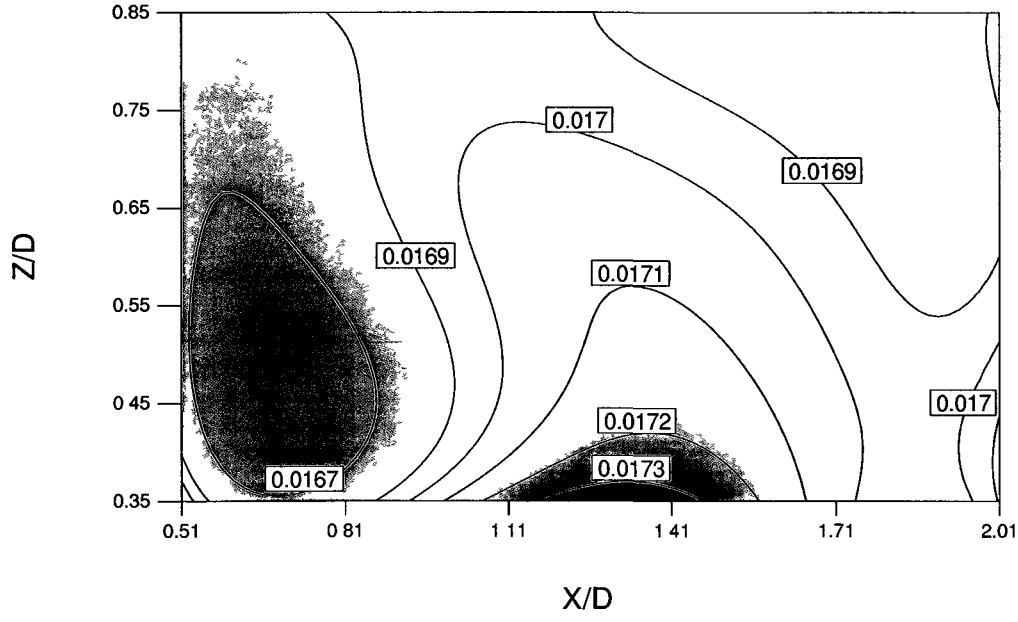

Figure 91: Thrust coefficient contours for rotor location of Y/D=0.5

6.1.7 Validation by Point Prediction

In addition to measuring rotor thrust at the design points, rotor thrust was also measured at a series of validation points. The validation points were measured at off design point locations to assess the prediction capabilities of the model. Table 11 shows the results of the point prediction validation study and reports rotor location, measured and predicted thrust coefficient, and the 95% prediction interval. In general, the measured response should fall within the reported 95% prediction interval. For this study the majority of the validation points fall within the 95% prediction interval. Points seven and ten fall outside of the prediction intervals by no more than $3x10^{-5}$. Thus based on the findings of the validation study and statistical analysis, it can be concluded that the response surface adequately models the observed data.

PT. #	X/D	Y/D	Z/D	Measured Thrust Coeff.	Predicted Thrust Coeff.	95% PI low	95% PI high
1	0.6125	0	0.4	0.01655	0.01657	0.01640	0.01674
2	1.0125	0.2	0.6	0.01709	0.01704	0.01687	0.01720
3	1.5125	0.5	0.5	0.01703	0.01711	0.01694	0.01728
4	2.0125	0.4	0.7	0.01691	0.01685	0.01668	0.01701
5	1.2125	0	0.4	0.01690	0.01693	0.01676	0.01710
6	0.7125	-0.4	0.5	0.01704	0.01690	0.01673	0.01707
7	1.2125	-0.1	0.4	0.01708	0.01691	0.01674	0.01707
8	2.0125	0	0.7	0.01697	0.01695	0.01678	0.01712
9	1.7125	-0.2	0.6	0.01708	0.01692	0.01676	0.01709
10	1.0125	-0.3	0.5	0.01716	0.01697	0.01680	0.01713

Table 11: Evaluation of model point prediction capabilities

6.2 Selected Results from the Particle Image Velocimetry Survey

The results presented in this section are a representative subset of all particle image velocimetry surveys conducted for various rotor and ship configurations. In all cases wind tunnel speed was 5 m/s and the AR=0.075. The collected survey data was used to generate the fictitious superimposed flowfield (isolated ship airwake, isolated freestream, and combined rotor and freestream) and in the velocity based coupling analysis between the superimposed flowfield and the observed flowfield (combined rotor and ship airwake). The coordinate system used in the reporting of rotor and laser plane location is shown in Figure 92. Note that in the case of stereo PIV measurements, the left most corner of the ship's hangar obstructs the left cameras view of the laser light sheet. This occurs for Y/D locations greater than 0 and a longitudinal rotor location of X/D=0.5125. This optical obstruction prohibits the resolution of the velocity vector field in these regions. The hangar door has been superimposed on the relevant plots to denote this optical interference. No interference occurred in the two-dimensional (single camera) PIV surveys.

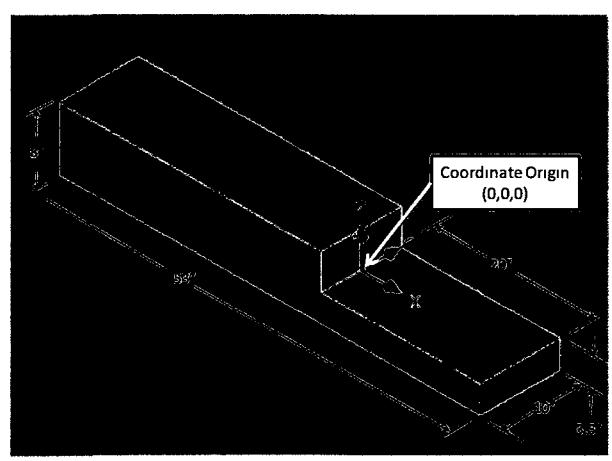

Figure 92: Detail of frigate model with indicated coordinate system

6.2.1 Ship Airwake Survey

A stereo particle image velocity survey was conducted of the ship airwake to gain a general understanding of the flowfield and to generate datasets for use in the velocity based coupling analysis. Figure 93 shows a representative longitudinal measurement plane for the ship airwake survey. Regions of significant recirculation are seen in the region immediately behind the hangar door. The complete longitudinal survey has been included in Appendix H for eleven Y/D planes spanning the deck of the frigate model. Note that the contour variable represents the out-of-plane (V) component of velocity and the arrows represent the in-plane velocity components (U, W).

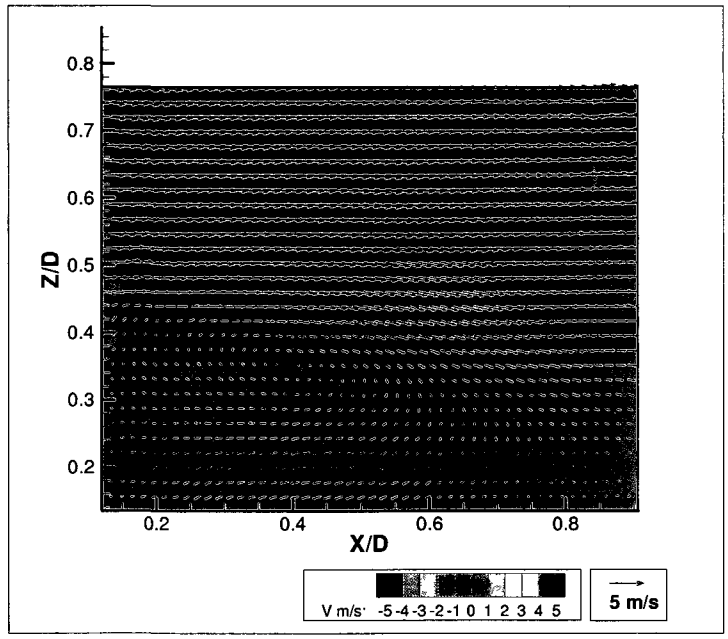

Figure 93: Observed velocity field for isolated ship airwake configuration and longitudinal measurement plane Y/D=-0.1

6.2.2 Experimentally Observed Ship Airwake/Rotor Downwash Interaction

The results presented in this section are a representative subset of the flowfields observed for the combined rotor and ship configuration. Presentation of these results allows for a qualitative identification of coupling and supports the finding of the quantitative analysis technique developed as part of this study. Figures 94-96 show longitudinal measurement planes for the combined rotor and ship configuration. Results presented in this section and in Appendix I are for a single longitudinal and lateral rotor position of X/D=0.5125, Y/D=0.0, and three vertical positions Z/D=0.45, 1.2, 2.4. Note that the contour variable represents the out-of-plane (V) component of velocity and the arrows represent the in-plane velocity components (U, W).

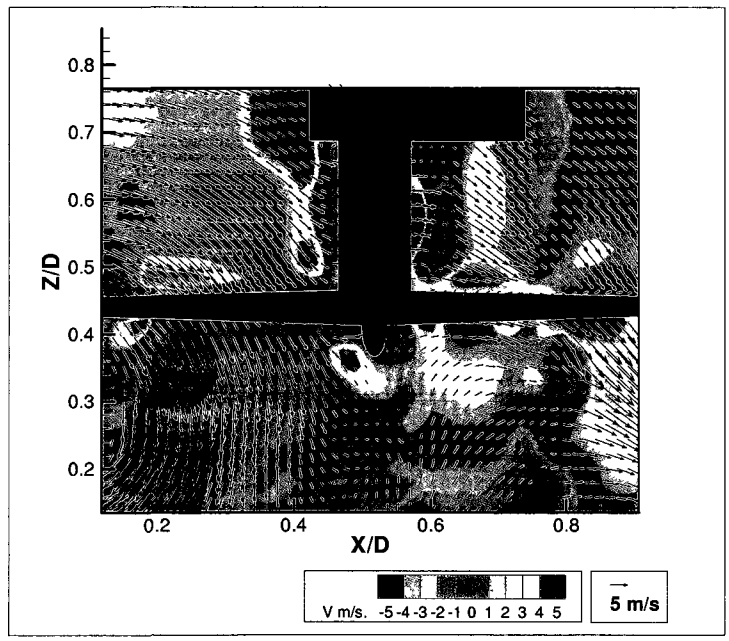

Figure 94: Observed velocity field for rotor Z/D=0.45 and longitudinal measurement plane Y/D=-0.1

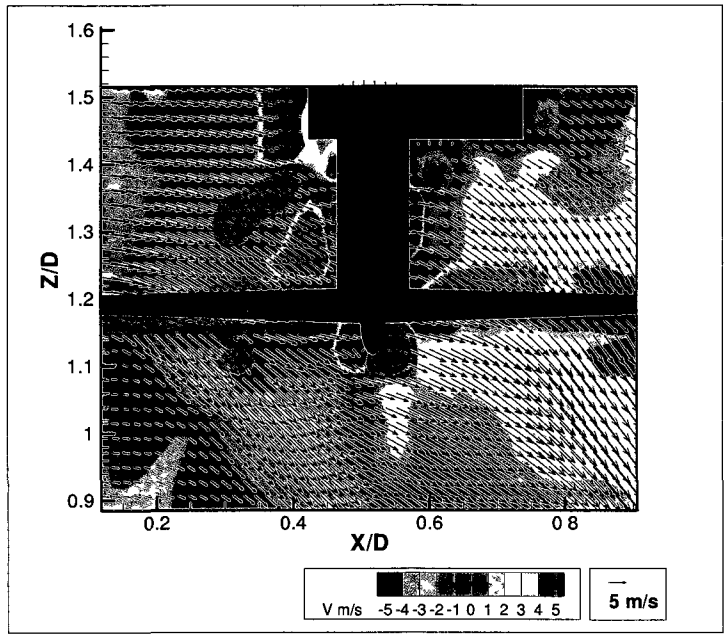

Figure 95: Observed velocity field for rotor Z/D=1.2 and longitudinal measurement plane Y/D=-0.1

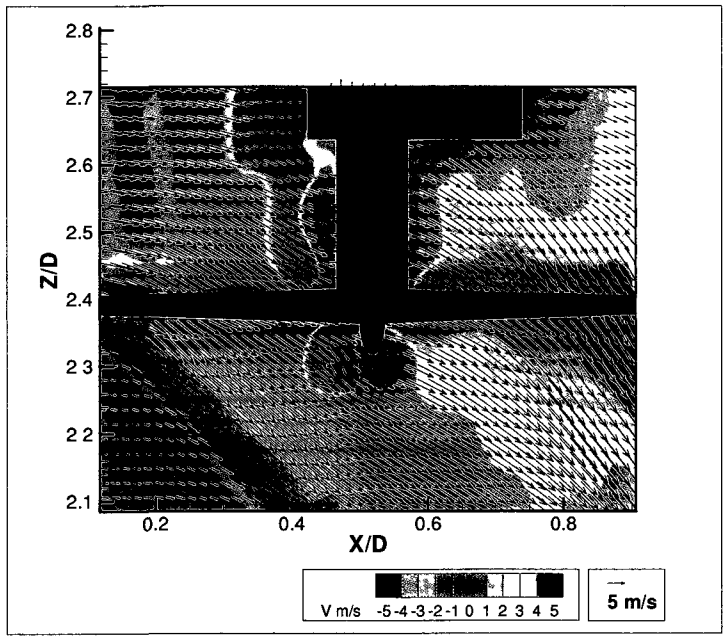

Figure 96: Observed velocity field for rotor Z/D=2.4 and longitudinal measurement plane Y/D=-0.1

6.2.3 Isolated Rotor and Freestream

The result presented in this section is a representative subset of the flowfields observed for the isolated rotor and freestream configuration. The frigate model and ground board were removed for this set of measurements. Presentation of these results allows for a qualitative identification of coupling and supports the finding of the quantitative analysis technique developed as part of this study. Figure 97 shows longitudinal measurement planes for the isolated rotor and freestream configuration. Results presented here and in Appendix J are for a single rotor position of X/D=0.5125, Y/D=0, and Z/D=3.0. Rotor height is measured from the wind tunnel floor to the rotor hub.

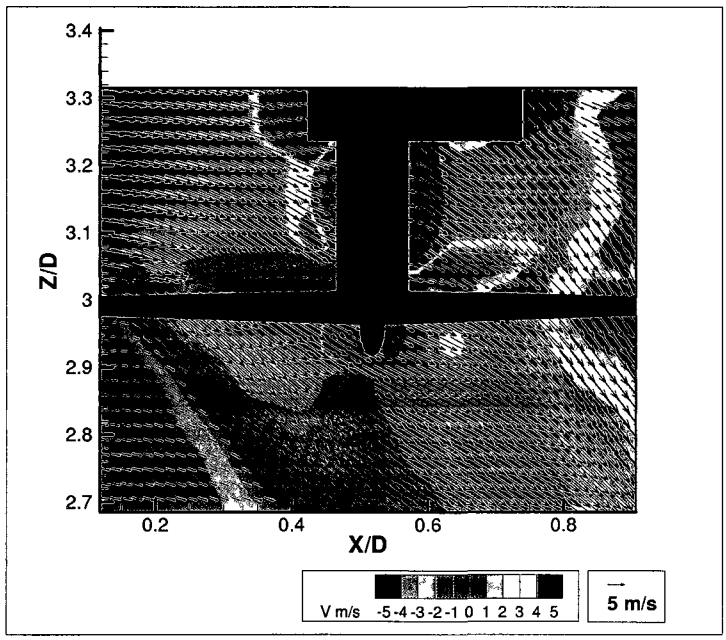

Figure 97: Observed velocity field for isolated rotor and freestream rotor configuration for longitudinal measurement plane Y/D=-0.1

6.2.4 Superimposed Flowfield

The results presented in this section are a representative subset of the superimposed flowfields generated for the velocity based coupling analysis. Comparing the fictitious superimposed flowfields shown in this section and Appendix G with the observed flowfields presented in section 6.2.2 and Appendix E allows for a qualitative identification of coupling. This visual comparison supports the finding of the quantitative analysis technique developed as part of this study. Figures 98-100 and the figures in Appendix K show longitudinal measurement planes for the superimposed flowfield for a single longitudinal and lateral rotor position of X/D=0.5125, Y/D=0, and three vertical positions Z/D=0.45, 1.2, 2.4.

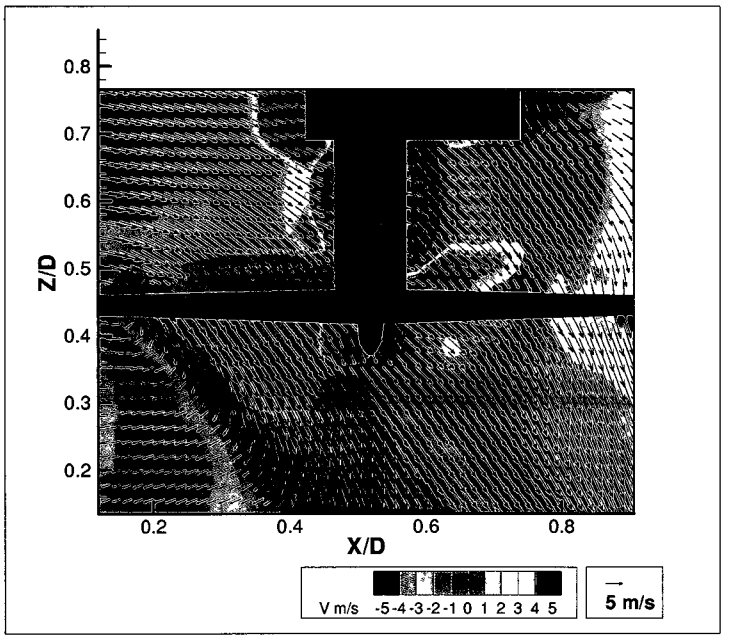

Figure 98: Generated superimposed flowfield for rotor Z/D=0.45 and longitudinal measurement plane Y/D=-0.1

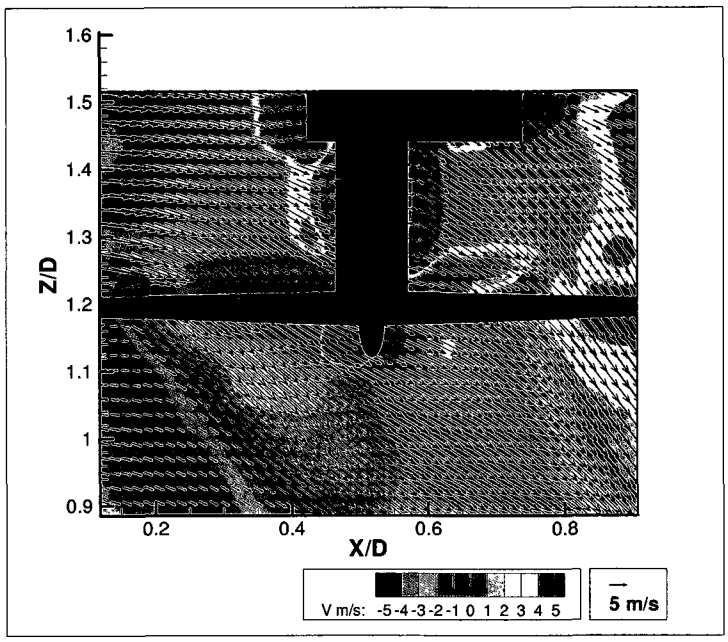

Figure 99: Generated superimposed flowfield for rotor Z/D=1.2 and longitudinal measurement plane Y/D=-0.1

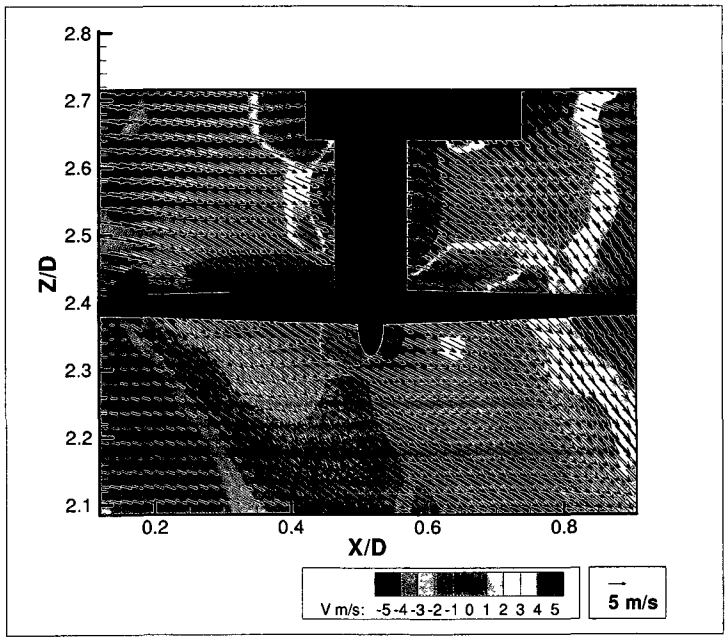

Figure 100: Generated superimposed flowfield for rotor Z/D=2.4 and longitudinal measurement plane Y/D=-0.1

6.3 Regional Component-Wise Velocity Based Coupling Analysis

A representative subset of the computed regional velocity discrepancies between a fictitious superimposed velocity field and the observed velocity field for various rotor over deck heights (Z/D) and various rotor configurations is shown in the upcoming sections. The complete results are presented in Appendices L-P. Results are presented on a velocity component basis normalized by wind tunnel freestream velocity (U=5 m/s) to more clearly understand what velocity components contribute most to ship airwake/rotor downwash coupling. All average velocity component disagreements are developed from 10 velocity measurement planes covering the rotor disk. Two X/D measurement locations were chosen to evaluate the coupling identification technique. The forward most measurement location (X/D=0.5125) was selected based on the results of the rotor thrust survey. While not practical in normal flight conditions (i.e. the rotor is very close to the hangar door) this location contains the maximum variation of rotor thrust when compared with freestream rotor thrust values. The second measurement location (X/D=1.300) was selected to better represent a realistic helicopter landing configuration. Sections 6.3.1, 6.3.2, and 6.3.3 report U, V, and W velocity component discrepancies, respectively, for a rotor location of X/D=0.5125. Sections 6.3.4 and 6.3.5 report U and W velocity component disagreements, respectively, for a rotor location of X/D=1.3000.

6.3.1 U-Velocity Results for X/D=0.5125 Rotor Locations

A representative plot of the computed average U-velocity component discrepancy between the superimposed velocity field and experimentally observed velocity field is presented in Figure 101 for the forward-most measurement location (X/D=0.5125). The

full set of U-velocity component discrepancy plots are given in Appendix L for eleven lateral rotor positions (Y/D=-0.5, -0.4, -0.3, -0.2, -0.1, 0.0, 0.1, 0.2, 0.3, 0.4, and 0.5) with three rotor over-deck locations (Z/D=0.45, 1.2, and 2.4) at each Y/D rotor position. All average velocity component discrepancies are reported with 95% confidence intervals ($\alpha = 0.05$and $N = 200$). Results have been normalized by tunnel freestream velocity ($U_{freestream} = 5\ m/s$). The plots reveal that below a rotor vertical height over deck of Z/D=1.2 U-component aerodynamic coupling becomes significant.

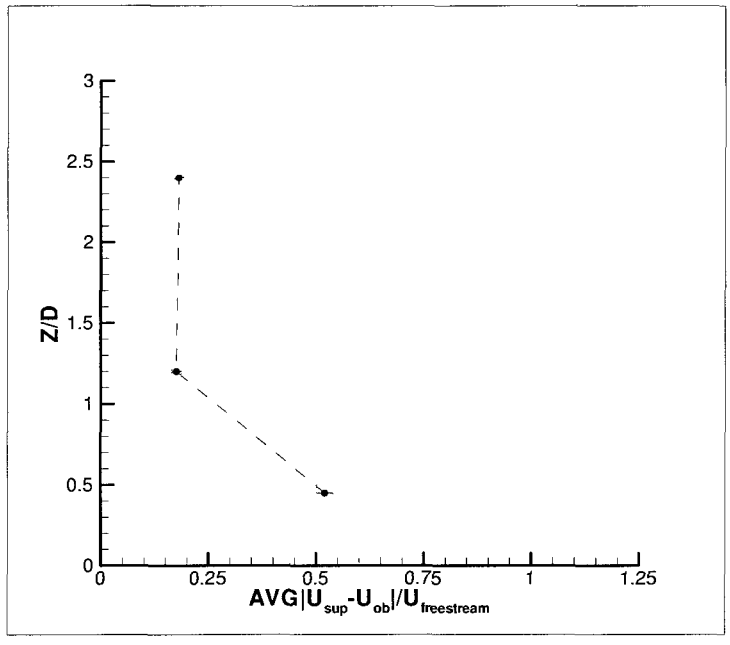

Figure 101: U-Velocity disagreement versus rotor height above deck for rotor location X/D=0.5125 and Y/D=-0.1

6.3.2 V-Velocity Results for X/D=0.5125 Rotor Locations

A representative subset of the computed average V-velocity component discrepancy between the superimposed velocity field and experimentally observed velocity field are presented in Figures 102-103 for the forward-most measurement location (X/D=0.5125). The full set of V-velocity component discrepancy plots are given in Appendix M for eleven lateral rotor positions (Y/D=-0.5, -0.4, -0.3, -0.2, -0.1, 0.0, 0.1, 0.2, 0.3, 0.4, and 0.5) with three rotor over-deck locations (Z/D=0.45, 1.2, and 2.4) at each Y/D rotor position. All average velocity component discrepancies are reported with 95% confidence intervals ($\alpha = 0.05$ and $N = 200$). Results have been normalized by tunnel freestream velocity ($U_{freestream} = 5\ m/s$). For a rotor of deck location greater than Z/D=1.2 no significant coupling is detected. However, unlike the findings of the U-velocity component discrepancies in section 6.3.1 V-component coupling was found for some rotor locations (Figure 102) and not others (Figure 103).

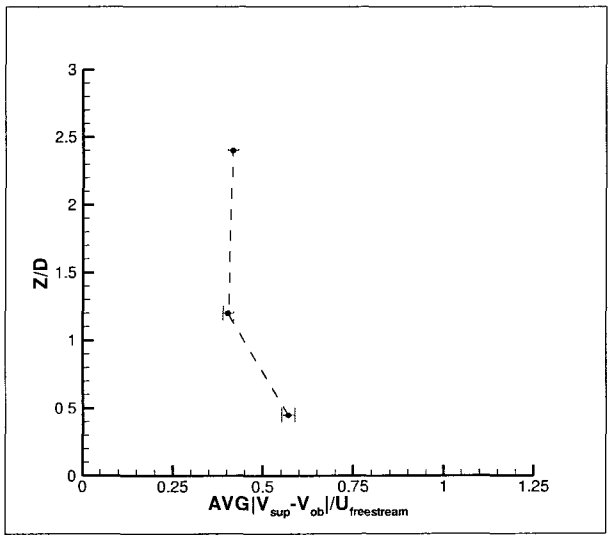

Figure 102: V-Velocity disagreement versus rotor height above deck for rotor location X/D=0.5125 and Y/D=-0.4

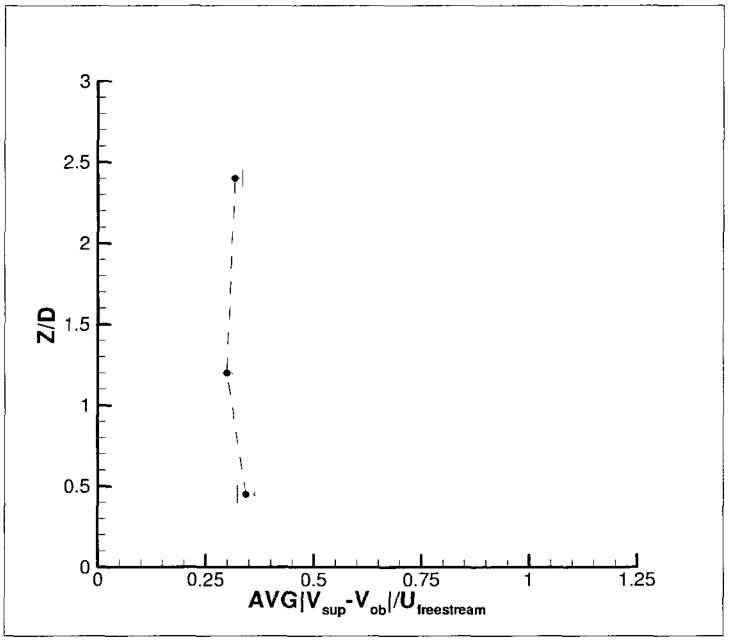

Figure 103: V-Velocity disagreement versus rotor height above deck for rotor location X/D=0.5125 and Y/D=0.5

6.3.3 W-Velocity Results for X/D=0.5125 Rotor Locations

A representative plot of the computed average W-velocity component discrepancy between the superimposed velocity field and experimentally observed velocity field is shown in Figure 104 for the forward-most measurement location (X/D=0.5125). The full set of W-velocity component discrepancy plots are given in Appendix N for eleven lateral rotor positions (Y/D=-0.5, -0.4, -0.3, -0.2, -0.1, 0.0, 0.1, 0.2, 0.3, 0.4, and 0.5) with three rotor over-deck locations (Z/D=0.45, 1.2, and 2.4) at each Y/D rotor position. All average velocity component discrepancies are reported with 95% confidence intervals ($\alpha = 0.05$ and $N = 200$) and have been normalized by tunnel freestream velocity ($U_{freestream} = 5\, m/s$). The results conclude that, similar to the findings of the U-

component coupling analysis, W-component aerodynamic coupling becomes significant below a rotor vertical height over deck of Z/D=1.2.

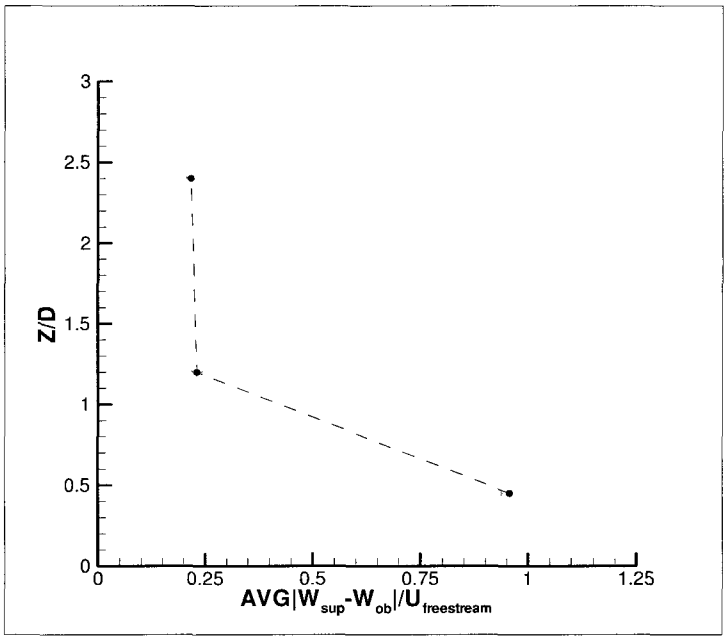

Figure 104: W-Velocity disagreement versus rotor height above deck for rotor location X/D=0.5125 and Y/D=-0.1

6.3.4 U-Velocity Results for X/D=1.3 Rotor Locations

A representative plot of the computed average U-velocity component discrepancy between the superimposed velocity field and experimentally observed velocity field is shown in Figure 105 for the aft measurement location (X/D=1.3). The full set of U-velocity component discrepancy plots are given in Appendix O for eleven lateral rotor positions (Y/D=-0.5, -0.4, -0.3, -0.2, -0.1, 0.0, 0.1, 0.2, 0.3, 0.4, and 0.5) with three rotor over-deck locations (Z/D=0.45, 1.2, and 2.4) at each Y/D rotor position. All average velocity component discrepancies are reported with 95% confidence intervals and have been normalized by tunnel freestream velocity ($U_{freestream} = 5\ m/s$). The results

conclude that, similar to the findings of the U-component coupling analysis in section 6.3.1, U-component aerodynamic coupling becomes significant below a rotor vertical height over deck of Z/D=1.2.

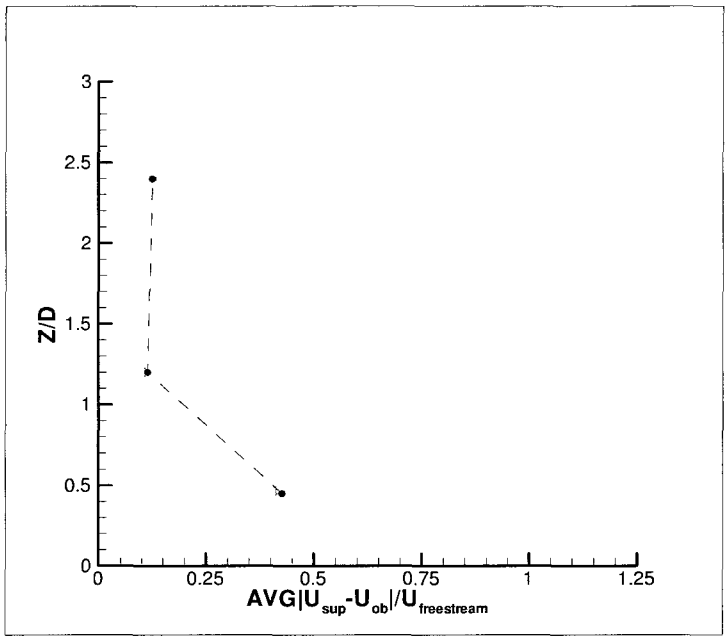

Figure 105: U-Velocity disagreement versus rotor height above deck for rotor location X/D=1.3 and Y/D=-0.1

6.3.5 W-Velocity Results for X/D=1.3 Rotor Locations

A representative plot of the computed average W-velocity component discrepancy between the superimposed velocity field and experimentally observed velocity field is shown in Figure 106 for the aft measurement location (X/D=1.3). The full set of W-velocity component discrepancy plots are given in Appendix P for eleven lateral rotor positions (Y/D=-0.5, -0.4, -0.3, -0.2, -0.1, 0.0, 0.1, 0.2, 0.3, 0.4, and 0.5) with three rotor over-deck locations (Z/D=0.45, 1.2, and 2.4) at each Y/D rotor position. All average velocity component discrepancies are reported with 95% confidence intervals and have

been normalized by tunnel freestream velocity ($U_{freestream} = 5\ m/s$). The results conclude that, similar to the findings of the U-component coupling analysis in section 6.3.1, W-component aerodynamic coupling becomes significant below a rotor vertical height over deck of Z/D=1.2.

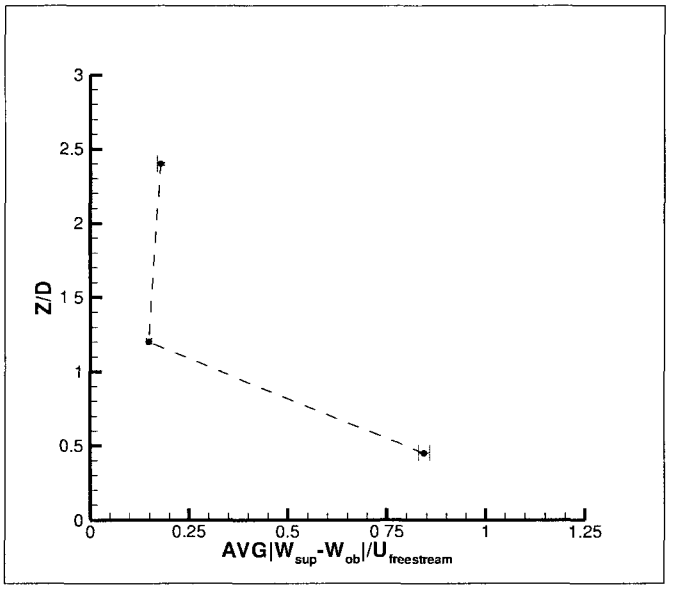

Figure 106: W-Velocity disagreement versus rotor height above deck for rotor location X/D=1.3 and Y/D=-0.1

6.4 Rotor Thrust Coefficient Versus Height for Various Rotor Y/D Locations

Sections 6.4.1 and 6.4.2 report measured rotor thrust coefficients for three rotor above-deck locations (Z/D) for each of the X/D measurement locations (forward and aft). These measurement locations correspond to the rotor locations used during the PIV survey and allow for a comparison with the findings of the velocity based coupling analysis. In all cases rotor advance ratio was 0.075.

6.4.1 Results for forward measurement locations X/D=0.5125

Figures 107-109 report a representative subset of the rotor thrust survey for a longitudinal rotor location of X/D=0.5125. The complete set of rotor thrust measurements for a longitudinal rotor location of X/D=0.5125, lateral rotor locations Y/D=-0.5, -0.4, -0.3, -0.2, -0.1, 0, 0.1, 0.2, 0.3, 0.4, and 0.5 and vertical rotor locations Z/D=0.45, 1.2, and 2.4 are given in Appendix Q. Results (Figure 108 and Figure 109) indicate that rotor thrust coefficient does not necessarily correlate with the findings of the aerodynamic coupling analysis.

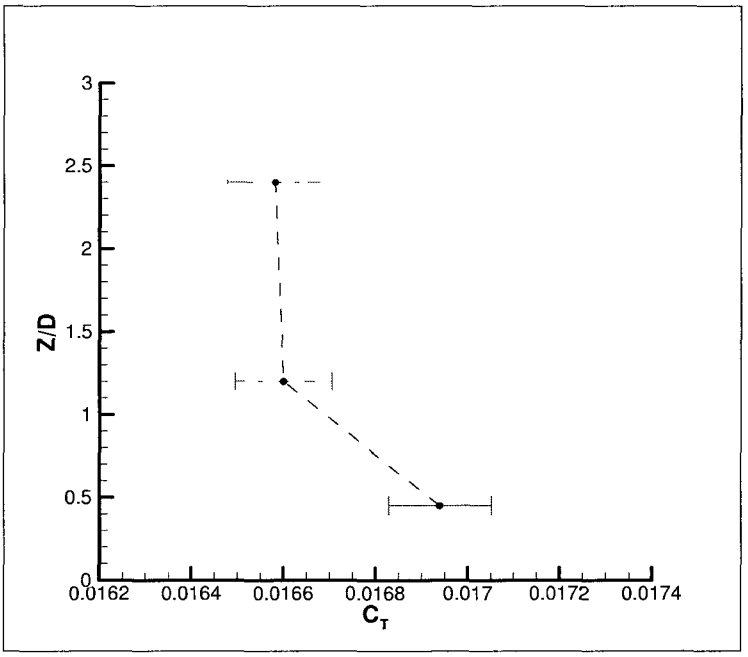

Figure 107: Rotor thrust coefficient for Y/D=-0.5

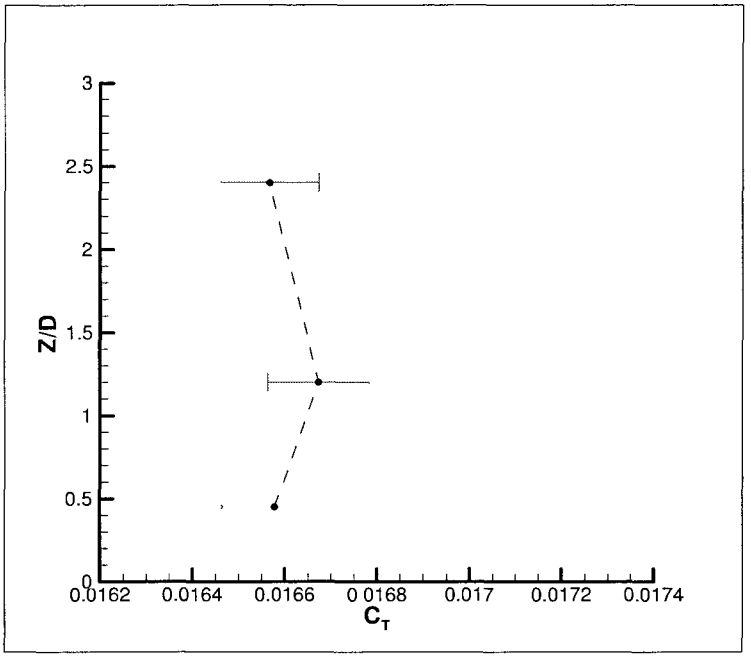

Figure 108: Rotor thrust coefficient for Y/D=-0.1

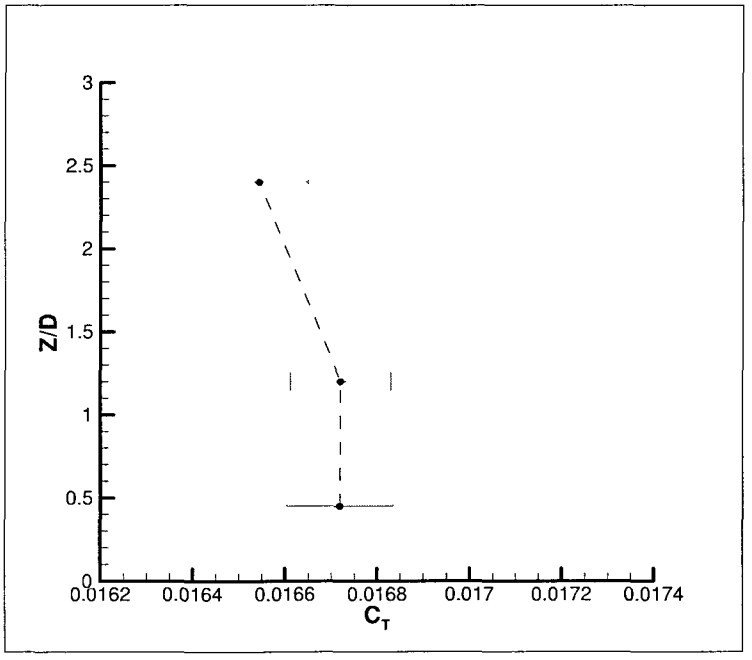

Figure 109: Rotor thrust coefficient for Y/D=0.0

6.4.2 Results for aft measurement locations X/D=1.3

Figures 110-112 report a representative subset of the rotor thrust survey for a longitudinal rotor location of X/D=1.3. The complete set of rotor thrust measurements for a longitudinal rotor location of X/D=1.3, lateral rotor locations Y/D=-0.5, -0.4, -0.3, -0.2, -0.1, 0, 0.1, 0.2, 0.3, 0.4, and 0.5 and vertical rotor locations Z/D=0.45, 1.2, and 2.4 are given in Appendix R. Similar to the findings in the previous section (6.4.1), results indicate that rotor thrust coefficient does not necessarily correlate with the findings of the aerodynamic coupling analysis.

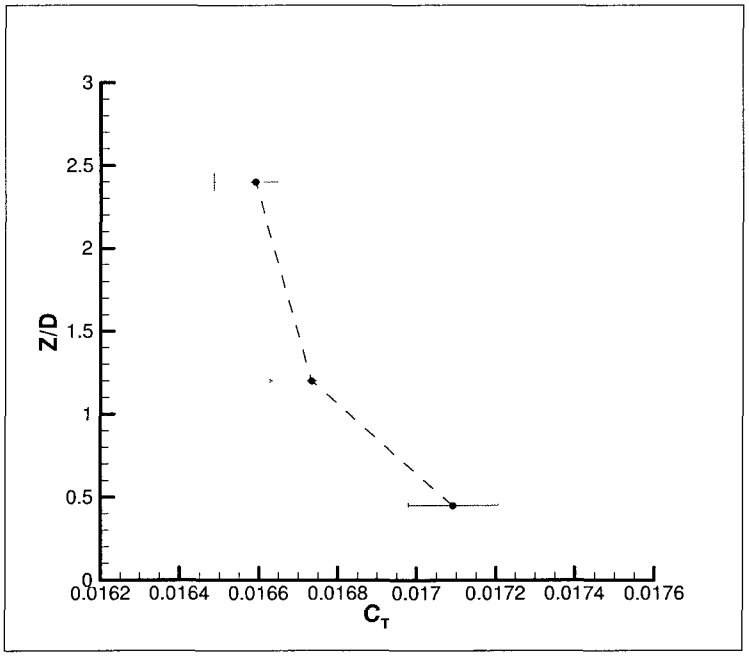

Figure 110: Rotor thrust coefficient for Y/D=-0.5

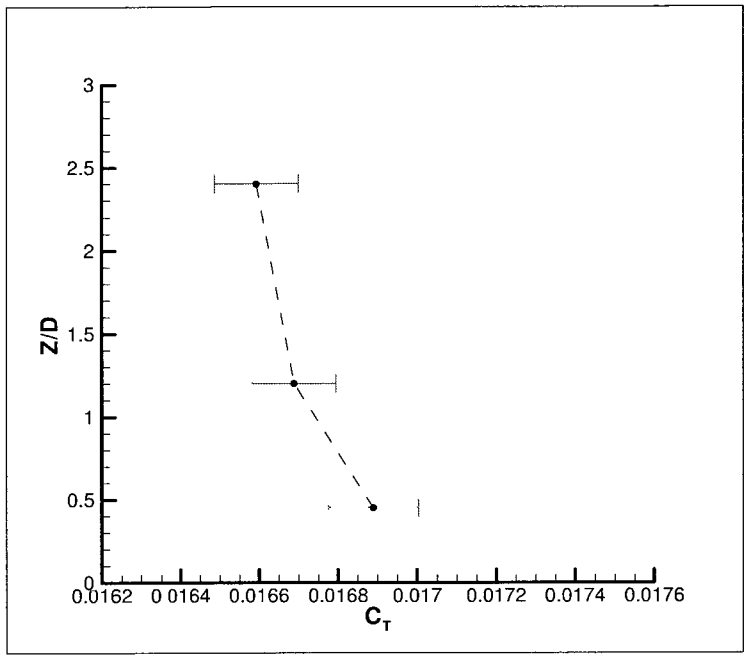

Figure 111: Rotor thrust coefficient for Y/D=-0.1

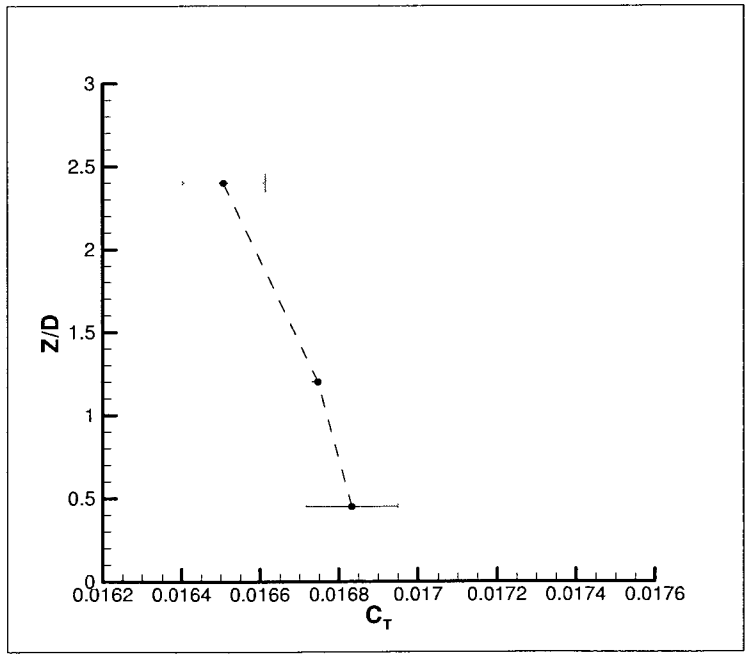

Figure 112: Rotor thrust coefficient for Y/D=0.0

7. DISCUSSION

7.1 Rotor Thrust Coefficient

In section 6.1 rotor thrust coefficient was mapped over the landing deck of a simplified frigate model. A sixth order response surface was selected and found to be significant (P<0.0001) based on the results from an ANOVA. The sixth order model was reduced to include only significant model terms and terms required for hierarchy. The fitted response surface covers a volume above the landing deck extending longitudinally from X/D=0.5125 to 2.0125, laterally from Y/D=-0.5 to 0.5, and vertically from Z/D=0.35 to 0.85. Rotor thrust coefficient (C_T) was found to be nominally 0.017 and is representative of full scale rotorcraft with relatively high disc loadings.

7.1.2 Important trends and findings

Thrust coefficient contours reveal important characteristics with regards to the variation of rotor thrust coefficient over the deck of the simplified frigate geometry. An important observation is the lack of symmetry associated with the rotor thrust variations. As shown by Zan[31], an increase in rotor thrust coefficient is observed as the rotor is moved aft. In addition, for a near hangar rotor position (X/D=0.5125), lateral thrust variations are highly asymmetric about the deck centerline (see Figure 113). As the rotor is moved towards the stern of the ship near the touchdown location (X/D=1.3), the lateral variation in rotor thrust becomes more symmetric (see Figure 114).

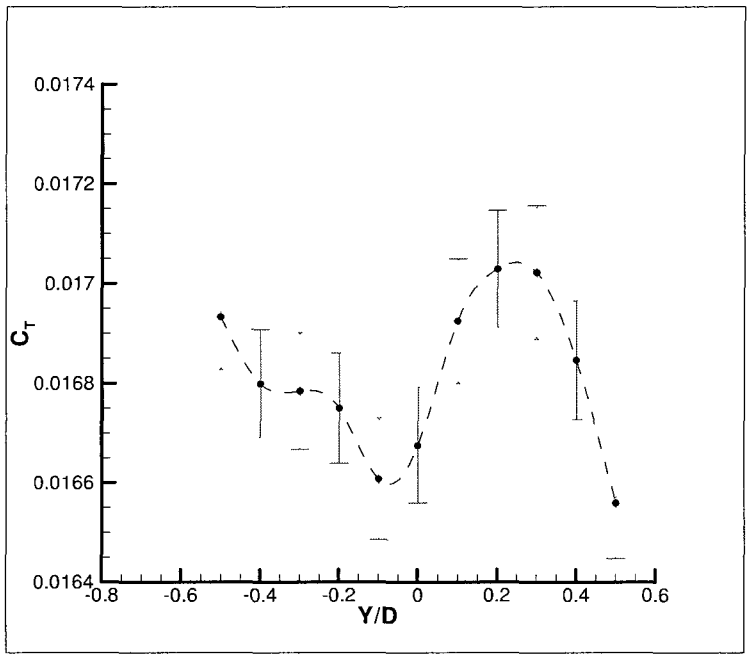

Figure 113: Lateral variation of rotor thrust coefficient for X/D=0.5125 and Z/D=0.45

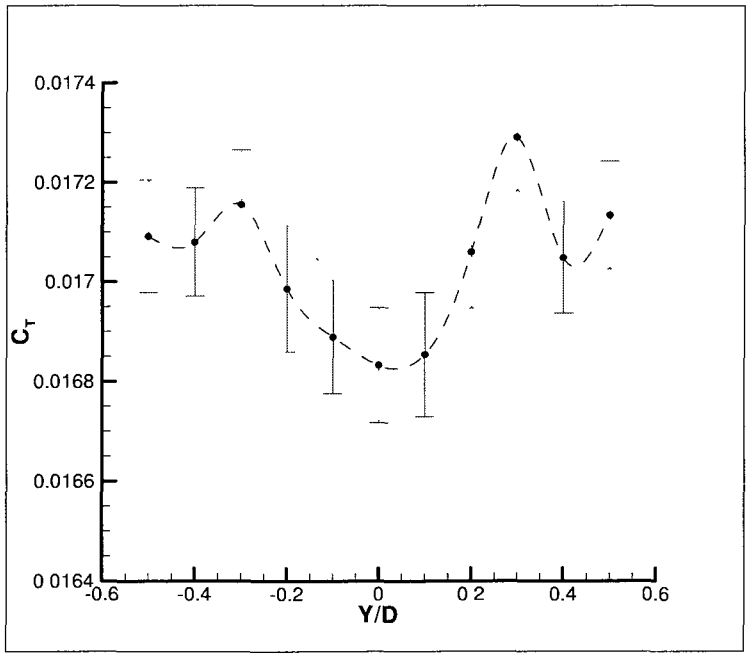

Figure 114: Lateral variation of rotor thrust coefficient for X/D=1.3 and Z/D=0.45

Also, this finding illustrates the complexity of the flowfield associated with rotorcraft landing on the decks of non-aviation ships. It is believed the apparent asymmetry is caused by several fundamental phenomena associated with rotorcraft aerodynamics. It is well known that advancing blades see a higher relative freestream when compared to the retreating blades thus the advancing blades generate more lift. In addition, as the rotor nears a solid surface (infinite ground plane) a ground effect is seen that yields an increase in lift. Finally, in the vicinity of the hangar door, regions of strong recirculation may reduce the thrust due to reingestion of the downwash. A recirculatory region from this study is shown in Figure 115 and compares to the results of Lee and Silva et al.[13] (Figure 116).

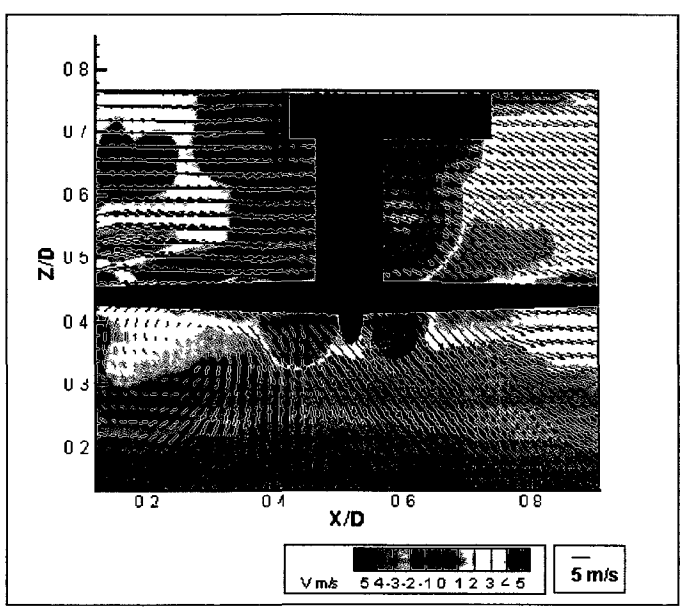

Figure 115: Observed velocity field for rotor Z/D=0.45 and longitudinal measurement plane Y/D=-0.4

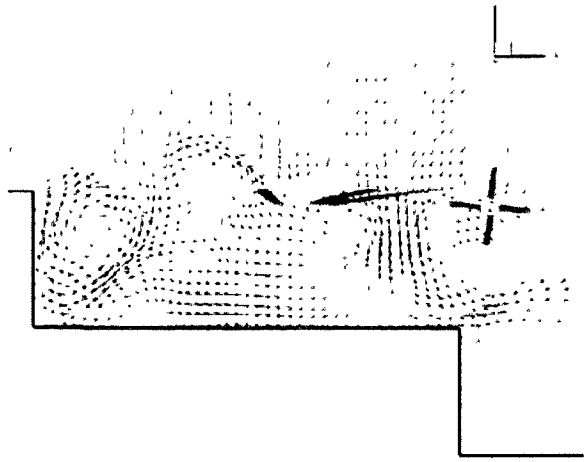

Figure 116: Recirculation in flowfield[13]

These three phenomena combine to yield a very complex interaction between ship airwake and rotor downwash when the rotor is in close proximity to the ship. From the standpoint of CFD and modeling of the helicopter landing configuration this evidence supports the need for a fully coupled simulation[45].

7.2 Particle Image Velocimetry Surveys

The particle image velocimetry surveys of the various rotor and ship configurations identify complex flowfields with recirculation and swirl. The isolated ship airwake (no rotor) was found to contain regions of recirculation in the area immediately behind the hangar door. This recirculation was intensified with the addition of the rotor at a vertical rotor position of Z/D=0.45. For increasing rotor vertical positions, namely Z/D=1.2 and Z/D=2.4, the ship airwake more closely resembled a steady freestream. In this configuration, the primary flow feature was found to be rotor downwash. Also, as expected, an out of plane swirl was observed with fluid rotating in the same direction as

the rotor. Results are also presented showing the generated superimposed flowfield. Visual comparison of the superimposed and observed flowfields indicate that for a rotor over deck height of Z/D=0.45 the superimposed case did not match the experimentally observed case. However, for increased rotor over deck heights (Z/D=1.2 and 2.4) visual inspection reveals good agreement between superimposed cases and experimentally observed cases. These findings are precursors to the outcome of the velocity based coupling analysis.

7.3 Finding of the Ship Airwake/Rotor Downwash Coupling Analysis

The coupling analysis technique developed in this study compared a flowfield constructed by superposition of measured fundamental flowfields to the combined case. The technique quantifies the component wise velocity disagreement between the superimposed and observed cases. A rectangular analysis region located under the rotor was selected for computation of the component wise velocity disagreement. The location of the analysis region was chosen for easy optical access. While it was desirable to choose an analysis region to be above the rotor (inflow), interference occurred between the laser light sheet and the electric motor assembly, leaving voids in the calculated vector's fields. These voids can be easily seen in the reported PIV surveys appearing as "ghost" motors and hubs. In CFD simulations, the inflow condition is used in correcting for airwake effects when using the rotor disk superposition and blade element rotor model[8]. In addition, 95% confidence intervals shown with error bars have been reported with all results and can be used to visually determine significant differences. Confidence intervals that do not overlap indicate a significant difference between measurements.

For the areas surveyed, the general finding of the velocity based coupling technique was that significant coupling occurs below a rotor over deck height of Z/D=1.2. For rotor over deck heights of Z/D=1.2 and Z/D=2.4 disagreements between the superimposed flowfield and the observed flowfield were smaller than for the Z/D=0.45 configurations. Also, for rotor locations of Z/D=1.2 and Z/D=2.4 the computed velocity disagreement was nearly constant and relatively small. These findings suggest that the region where CFD modeling must include coupling is in very close proximity to the ship (Z/D < 1.2). Figures 117 and 118 show the normalized velocity discrepancy magnitude for the forward most rotor location and the aft most rotor location X=1.3, respectively. This confirms the finding that for rotor locations less than Z/D=1.2, coupling becomes significant. It should be noted that in Figures 117 and 118 the contours are based on a sparse dataset (indicated by black circular symbols). Increased spatial resolution in the vertical direction will be required to more clearly define a coupling envelope.

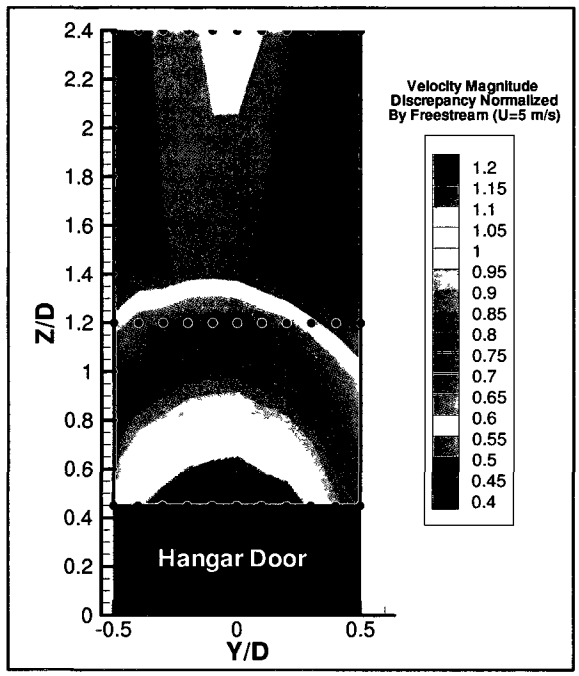

Figure 117: Normalized velocity discrepancy magnitude for X/D=0.5125

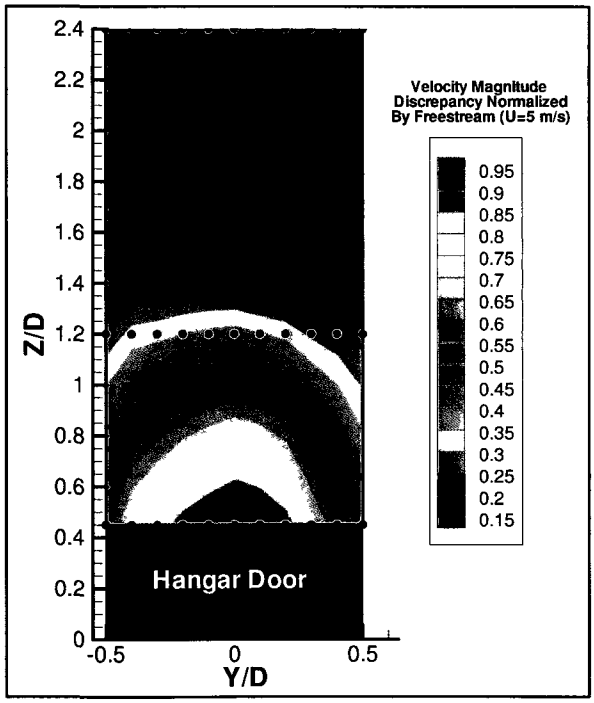

Figure 118: Normalized velocity discrepancy magnitude for X/D=1.3

Rotor thrust was measured at the same rotor positions used for the particle image velocimetry surveys. An attempt was made to correlate areas identified as coupled regions and their thrust measurements. To perform this correlation, the statistical significance between all possible rotor Z/D locations (e.g. Z/D=2.4 vs. 1.2, Z/D=2.4 vs. 0.45, and Z/D=1.2 vs. 0.45) was tabulated for each rotor Y/D location and measurement technique (thrust coefficient and velocity discrepancy). If a comparison found that values were significantly different this was given a value of one. Similarly, if the comparison found that values were not significantly different (overlapping error bars) this was given a value of zero. Finally, the results for each measurement technique were compared. If both analyses were significant or not significant at a given region, the two were thought to correlate. For each rotor Z/D location the total number of correlations was divided by the total number of possible correlations to yield a correlation percentage (1=100%). Results from the correlation study were mixed. The results of the correlation for the longitudinal rotor locations X/D=0.5125 and X/D=1.3 are shown in Table 12 and Table 13, respectively. A correlation of one indicates 100% correlation.

Correlation Component	**Z/D=2.4 vs. 1.2**	**Z/D=2.4 vs. 0.45**	**Z/D=1.2 vs. 0.45**	**Average Correlation**
U-Velocity	1.0	0.64	0.36	0.67
V-Velocity	0.73	0.46	0.36	0.52
W-Velocity	0.91	0.64	0.36	0.64

Table 12: Correlation of rotor thrust coefficient and component-wise velocity discrepancy for a longitudinal rotor location of X/D=0.5125

Correlation Component	Z/D=2.4 vs. 1.2	Z/D=2.4 vs. 0.45	Z/D=1.2 vs. 0.45	Average Correlation
U-Velocity	0.73	0.91	0.73	0.79
W-Velocity	0.73	0.91	0.73	0.79

Table 13: Correlation of rotor thrust coefficient and component-wise velocity discrepancy for a longitudinal rotor location of X/D=1.3

The results of the correlation analysis suggest that in general, thrust coefficient is not necessarily directly correlated with the observed/superimposed component-wise velocity discrepancies. The aft survey results are comparatively more convincing than the forward survey results, suggesting that the highly recirculative flow regions are more challenging. This suggests a difference between ground or structure proximity effects in which rotor thrust changes and true aerodynamic coupling in which the rotor downwash and ship airwake interact. It may be possible to compare the observed rotor thrust coefficient with the computed (based on superposition) rotor thrust coefficient.

8. CONCLUSION

8.1 Summary of Findings

In this study, a wind tunnel measurement technique was successfully developed to indentify ship airwake/rotor downwash coupling. The developed coupling analysis technique has far reaching effects on many aspects of maritime rotorcraft operations by providing a way to quantify the degree of aerodynamic coupling between ship airwake and rotor downwash. Given that current flight simulation technology relies on superposition techniques to simulate the effect of ship airwake on helicopter handling, the developed technique can be used to guide CFD and flight simulation development by clearly defining where a fully coupled simulation must be used and where traditional superposition techniques are sufficient. The ability to define regions of significant coupling will reduce computational requirements for CFD and flight simulations by reducing the domain where computationally expensive fully coupled computations must be made. Reductions in computational requirements will permit the improvement in flight simulation fidelity with currently available resources. Improvements in flight simulation fidelity will ultimately lead to better training for pilots and the potential reduction in the number of accidents, saving lives and resources. In addition, this technique is not limited to the simplistic ship and rotor geometries used in this study but can be applied for a variety of ship/helicopter configurations. This allows for the study of a prospective ship design and its effect on rotorcraft prior to construction. Also, a valuable byproduct of the developed analysis technique is collection of validation data for CFD and other computer simulations.

For the simplified ship geometry and chosen rotor locations used in this study, it can be concluded that below a rotor over deck height of Z/D=1.2 (Figure 119) a fully coupled CFD solution is required. This limit is suggested as a guide for grid generation and simulation purposes. This finding is limited to a single wind over deck angle of zero degrees and to the simple frigate geometry. The addition of ship super structures adds an additional degree of complexity to the flowfield and was not considered in this fundamental study.

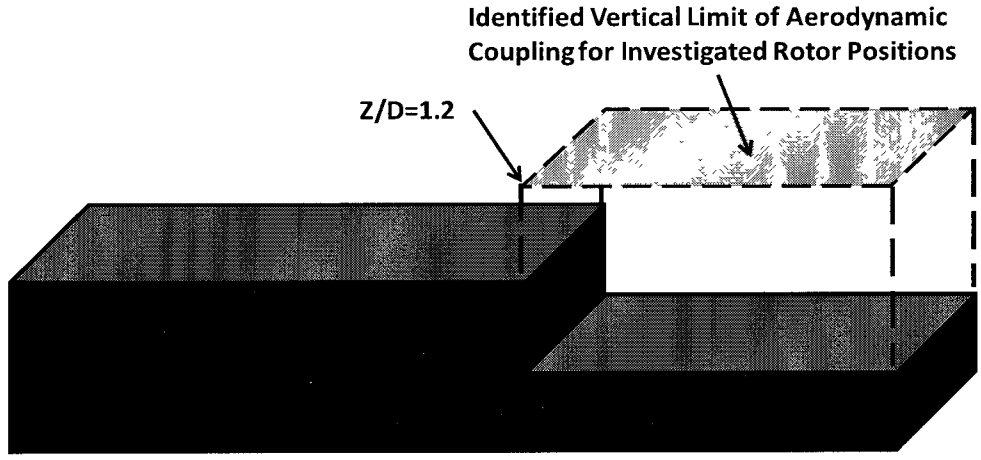

Figure 119: Vertical limit of significant aerodynamic coupling

8.2 Recommendations for Future Work

Future work should first focus on the investigation of additional ship/rotor configurations with a finer grid of rotor locations (particularly in the vertical direction) using the current ship/rotor model. Next, the effect of wind-over-deck angle on aerodynamic coupling and the effect of rotor advance ratio should be investigated. Subsequent studies could strive to increase ship model fidelity. Ship superstructures,

helicopter fuselages, and varying hangar door aspect ratios may have a significant effect on ship airwake/rotor downwash coupling. Also, it is important to note that the results of this study were based on time-averaged data. However, for simulation development purposes, examination of the time dependent unsteady velocity field and rotor thrust could also prove useful. Finally, improving wind tunnel optical access for the particle image velocimetry system would improve the accuracy of out-of-plane velocity component estimations and allow for larger analysis regions (e.g. above the rotor) to be examined.

REFERENCES

[1]Hess, R.A., "A Simplified Technique For Modeling Piloted Rotorcraft Operations Near Ships", AIAA paper 2005-6030, *AIAA Atmospheric Flight Mechanics Conference and Exhibit*, San Francisco, CA, August, 2005.

[2]http://hsl-37.ahf.nmci.navy.mil/02SH60B.htm.

[3]Silva, M.J., Yamauchi, G.K., Wadcock, A.J., and Long, K.R., "Wind Tunnel Investigation of the Aerodynamic Interactions Between Helicopters and Tiltrotors in a Shipboard Environment", American Helicopter Society 60th Annual Forum, Baltimore, MD, June 7-10, 2004.

[4]Czerwiec, R. M., and Polsky, S. A., "LHA Airwake Wind Tunnel and CFD Comparison With and Without Bow Flap", AIAA Paper 2004-4832, 22nd Applied Aerodynamics Conference and Exhibit, Providence, RI, August 16-19, 2004.

[5]Rhodes, M.M., and Healey, J.V., "Flight Deck Aerodynamics of a Nonaviation Ship", *Journal of Aircraft*, Vol. 29, No. 4, 1992, pp. 619-262.

[6]Wakefield, N. H., Newman, S. J., and Wilson, P. A., "Helicopter Flight Around a Ship's Superstructure", *Journal of Aerospace Engineering*, Vol. 216, Part G, 2002, pp. 13-28.

[7]http://www.navy.mil/view_single.asp?id=52334.

[8]http://www.navy.mil/view_single.asp?id=15091.

[9]Polsky, S., and Naylor, S., "CVN Airwake Modeling and Integration: Initial Steps in the Creation and Implementation of a Virtual Burble for F-18 Carrier Landing Simulations," AIAA Paper 2005-6298, *AIAA Modeling and Simulation Technologies Conference and Exhibit*, San Francisco, CA, August 15-18, 2005.

[10]http://www.navy.mil/view_single.asp?id=20321.

[11]http://www.navy.mil/management/photodb/photos/091004-N-9740S-011.jpg.

[12]Polsky, S. A., and Wilkinson, C. H., "A Computational Study of Outwash For a Helicopter Operating Near a Vertical Face with Comparison to Experimental Data," AIAA Paper 2009-5684, *AIAA Modeling and Simulation Technologies Conference*, Chicago, IL, August 10-13, 2009.

[13]Lee, Y., and Silva, M., "CFD Modeling of Rotor Flowfield Aboard Ship," AIAA 2010-867, *48th AIAA Aerospace Sciences Meeting Including the New Horizons Forum and Aerospace Exposition*, Orlando, FL, January 4-7, 2010.

[14]http://www.history.navy.mil/photos/images/u170000/u172866.jpg.

[15]http://www.aviationnews.eu/2009/10/23/black-hawk-helicopter-crashed-into-a-navy-ship/.

[16]Syms, G. F., "Simulation of Simplified-Frigate Airwakes Using a Lattice-Boltzmann method," *Journal of Wind Engineering and Industrial Aerodynamics*, Vol. 96, 2007, pp. 1197-1206.

[17]McKillip, J. R., Boschitsch, A., Quackenbush, T., Keller, J., and Wachspress, D. (2002). "Dyanmic Interface Simulation Using a Coupled Vortex-Based Ship Airwake and Rotor Wake Model," *American Helicopter Society 58th Annual Forum*, Montreal, Canada, June 11-13, 2002.

[18]Zan, S. J., Syms, G. F., and Cheney, B. T. (1998). "Analysis of Patrol Frigate Airwakes," *Presented at the NATO RTO Symposium on Fluid Dynamics Problems of Vehicles Operating Near or in the Air-Sea Interface*, Amsterdam, The Netherlands, October 5-8, 1998.

[19]Zhang, H., Prasad, J. V., and Mavris, D. N., "Ship Airwake Effects on Helicopter Rotor Aerodynamic Loads," AIAA Paper 94-3509-CP, 1994.

[20]Wilkinson, C. H., Zan, S. J., Gilbert, N. E., and Funk, J. D., "Modeling and Simulation of Ship Air Wakes For Helicopter Operations-A Collaborative Venture," *NATO RTO Symposium on Fluid Dynamics Problems of Vehicles Operating Near or in the Air-Sea Interface*, Amsterdam, The Netherlands, October 5-8, 1998.

[21]Modi, A., and Long, L. N., "Unsteady Separated Flow Simulations Using a Cluster of Workstations," AIAA Paper 2000-0272, *38th Aerospace Sciences Meeting and Exhibit*, Reno, NV, January 10-13, 2000.

[22]Reddy, K. R., Toffoletto, R., and Jones, K. R., "Numerical Simulation of Ship Airwake," *Journal of Computers and Fluids*, Vol. 29, 2000, pp. 451-465.

[23]Liu, J., and Long, L. N. (1998). "Higher Order Accurate Ship Airwake Predictions for the Helicopter/Ship Interface Problem," *American Helicopter Society 54th Annual Forum*, Washington, DC, May 20-22, 1998.

[24]Zhang, F., Xu, H., and Ball, N. G., "Numerical Simulation of Unsteady Flow Over SFS 2 Ship Model," AIAA Paper 2009-81, *47th AIAA Aerospace Sciences Meeting Including the New Horizons Forum and Aerospace Exposition*, Orlando, FL, January 5-8, 2009.

[25]Swales, C., and Breeze, G. (1997). "LDV Measurements Above the Flight Deck of a Model Frigate," AIAA Paper 97-0712, *35th AIAA Aerospace Sciences Meeting & Exhibit*, Reno, NV, January 6-9, 1997.

[26]Guillot, M. J., and Walker, M. A., "Unsteady Analysis of the Air Wake over the LPD-17," AIAA Paper 2000-4125, *18th Applied Aerodynamics Conference*, Denver, CO, August 14-17, 2000.

[27]Sharma, A., and Long, L. N., "Airwake Simulations on an LPD 17 ship," AIAA Paper 2001-2589, *15th AIAA Computational Fluid Dynamics Conference*, Anaheim, CA, June 11-14, 2001.

[28]Shipman, J., Arunajatesan, S., Menchini, C., and Sinha, N., "Ship Airwake Sensitivities to Modeling Parameters," AIAA Paper 2005-1105, *43rd AIAA Aerospace Sciences Meeting and Exhibit*, Reno, NV, January 10-13, 2005.

[29]Woodson, S. H., and Ghee, T. A., "A Computational and Experimental Determination of the Air Flow Around the Landing Deck of a US Navy Destroyer (DDG)," AIAA Paper 2005-4958, *23rd AIAA Applied Aerodynamics Conference*, June 6-9, 2005.

[30]Polsky, S. A., and Bruner, C. W., "Time-Accurate Computational Simulations of an LHA Ship Airwake," AIAA Paper 2000-4126.

[31]Zan, S. J., "Experimental Determination of Rotor Thrust in a Ship Airwake," *Journal of the American Helicopter Society*, Vol. 47, No. 2, 2002, pp. 100-108.

[32]Wadcock, A. J., Yamauchi, G. K., Heineck, J. T., Silva, M. J., and Long, K. R., "PIV Measurements of the Wake of a Tandem-Rotor Helicopter in Proximity to a Ship," *The American Helicopter Society's 4th Decennial Specialist's Conference on Aeromechanics*, San Francisco, CA, January 21-23, 2004.

[33]Shipman, J. D., Arunajatesan, S., Cavallo, P. A., Sinha, N., and Polsky, S. A., "Dynamic CFD Simulation of Aircraft Recovery to an Aircraft Carrier," AIAA Paper 2008-6227, *26th AIAA Applied Aerodynamics Conference*, Honolulu, HI, August 18-21, 2008.

[34]Smith, A. L., and Kunz, D. L., "Dynamic Coupling of the KC-135 Tanker and Boom for Modeling and Simulation," AIAA Paper 2006-6480, *AIAA Modeling and Simulation Technologies Conference and Exhibit*, Keystone, CO, August 21-24, 2006.

[35]Dietiker, J.-F., and Hoffman, K. A., "Predicting Wall Pressure Fluctuation over a Backward-Facing Step Using Detached Eddy Simulation," *Journal of Aircraft* , Vol. 46, No. 6, 2009, pp. 2115-2120.

[36]Montgomery, D. C., *Design and Analysis of Experiments,* 7th ed., John Wiley & Sons, New York, 2005.

[37]Nacakli, Y., "Analysis of Helicopter Downwash/Frigate Airwake Interaction Using Statistically Designed Experiments," PhD Thesis, Aerospace Engineering Department, Old Dominion University, Norfolk, VA, May 2010.

[38]Myers, R. H., Montgomery, D. C., and Anderson-Cook, C. M., *Response Surface Methodology: Process and Product Optimization Using Designed Experiments*, John Wiley & Sons., New Jersey, 2009.

[39]Prasad, A. K., "Stereoscopic Particle Image Velocimetry," *Experiments in Fluids*, Vol. 29, 2000, pp. 103-116.

[40]Raffel, M., Willert, C., and Kompenhans, J., *Particle Image Velocimetry: A Practical Guide*, Springer, New York, 1998.

[41]http://www.apcprop.com/v/Engineering/engineering_design.html#airfoil.

[42]Coleman, H. W., and Steele, W. G., *Experimentation, Validation, and Uncertainty Analysis for Engineers*, John Wiley & Sons, New Jersey, 2009.

[43]Adeyinka, O. B., and Naterer, G. F., "Experimental Uncertainty of Measured Entropy Production with Pulsed Laser PIV and Planar Laser Induced Fluorescence," *International Journal of Heat and Mass Transfer*, Vol. 48, 2005, 1450-1461.

[44]"AIAA Assessment of Experimental Uncertainty With Application to Wind Tunnel Testing," AIAA-S-071A-1999, Reston, VA, 1999.

[45]Nacakli, Y., Landman, D., and Doane, S., "Investigation of Backward Facing Step Flowfield for Dynamic Interface Application," *Journal of the American Helicopter Society*, in press.

APPENDIX A: TECPLOT Plotting and Data Extraction Macro

```
#!MC 1000
$!VarSet |MFBD| = 'C:\TEC100\Bin'

$!VarSet |rep|=2
$!VarSet |airwake_flag|=0
$!VarSet |station_num|=5
#! 1) Station One
#! 2) Station Two
#! 3) Station Three
#! 4) Freestream
#! 5) Combined Rotor and Freestream

$!IF |station_num|==1
$!VarSet |rotorx|=5.125
$!VarSet |rotory|=-5.000
$!VarSet |rotorz|=4.500
$!IF |airwake_flag|==0
$!VarSet |rotor_loop_num|=11
$!VarSet |laser_loop_num|=11
$!ELSEIF |airwake_flag|==1
$!VarSet |rotor_loop_num|=1
$!VarSet |laser_loop_num|=11
$!ENDIF

$!ELSEIF |station_num|==2
$!VarSet |rotorx|=5.125
$!VarSet |rotory|=-5.000
$!VarSet |rotorz|=12.000
$!IF |airwake_flag|==0
$!VarSet |rotor_loop_num|=11
$!VarSet |laser_loop_num|=11
$!ELSEIF |airwake_flag|==1
$!VarSet |rotor_loop_num|=1
$!VarSet |laser_loop_num|=11
$!ENDIF

$!ELSEIF |station_num|==3
$!VarSet |rotorx|=5.125
$!VarSet |rotory|=-5.000
$!VarSet |rotorz|=24.000
$!IF |airwake_flag|==0
$!VarSet |rotor_loop_num|=11
$!VarSet |laser_loop_num|=11
$!ELSEIF |airwake_flag|==1
```

```
$!VarSet |rotor_loop_num|=1
$!VarSet |laser_loop_num|=11
$!ENDIF

$!ELSEIF |station_num|==4
$!VarSet |rotorx|=5.125
$!VarSet |rotory|=0
$!VarSet |rotorz|=30.000
$!VarSet |rotor_loop_num|=1
$!VarSet |laser_loop_num|=1


$!ELSEIF |station_num|==5
$!VarSet |rotorx|=5.125
$!VarSet |rotory|=0.000
$!VarSet |rotorz|=30.000
$!VarSet |rotor_loop_num|=1
$!VarSet |laser_loop_num|=21

$!ENDIF

#!ROTOR Y POSITION LOOP
$!LOOP |rotor_loop_num|
$!IF |station_num|==5
$!VarSet |laserplane|=-10
$!ELSE
$!VarSet |laserplane|=-5
$!ENDIF

#!LASER PLANE LOOP
$!LOOP |laser_loop_num|


$!IF |station_num|==1
$!IF |airwake_flag|==0
$!VarSet |read_file|='"C:\Forward Stations\StationOne\Rep|rep|\[|rotorx%.3f| |rotory%.3f|
|rotorz%.3f|]-(|laserplane|).dat"'
$!VarSet |export_plot|='C:\Forward Stations\Velocity
Plots\StationOne\Rep|rep|\[|rotorx%.3f| |rotory%.3f| |rotorz%.3f|]-(|laserplane|).wmf'
$!VarSet |write_data|="C:\Forward Stations\Extracted Velocity
Data\StationOne\Rep|rep|\[|rotorx%.3f| |rotory%.3f| |rotorz%.3f|]-(|laserplane|).dat"
$!VarSet |rotor_overlay|=1
$!ELSEIF |airwake_flag|==1
$!VarSet |read_file|='"C:\Forward Stations\StationOne\Airwake\Rep|rep|\[0.000 0.000
0.000]-(|laserplane|).dat"'
```

```
$!VarSet |export_plot|='C:\Forward Stations\Velocity Plots\StationOne\Airwake\Rep|rep|\[0.000 0.000 0.000]-(|laserplane|).wmf'
$!VarSet |write_data|="C:\Forward Stations\Extracted Velocity Data\StationOne\Airwake\Rep|rep|\[0.000 0.000 0.000]-(|laserplane|).dat"
$!VarSet |rotor_overlay|=0
$!ENDIF

$!ELSEIF |station_num|==2
$!IF |airwake_flag|==0
$!VarSet |read_file|='"C:\Forward Stations\StationTwo\Rep|rep|\[|rotorx%.3f| |rotory%.3f| |rotorz%.3f|]-(|laserplane|).dat"'
$!VarSet |export_plot|='C:\Forward Stations\Velocity Plots\StationTwo\Rep|rep|\[|rotorx%.3f| |rotory%.3f| |rotorz%.3f|]-(|laserplane|).wmf'
$!VarSet |write_data|="C:\Forward Stations\Extracted Velocity Data\StationTwo\Rep|rep|\[|rotorx%.3f| |rotory%.3f| |rotorz%.3f|]-(|laserplane|).dat"
$!VarSet |rotor_overlay|=1
$!ELSEIF |airwake_flag|==1
$!VarSet |read_file|='"C:\Forward Stations\StationTwo\Airwake\Rep|rep|\[0.000 0.000 0.000]-(|laserplane|).dat"'
$!VarSet |export_plot|='C:\Forward Stations\Velocity Plots\StationTwo\Airwake\Rep|rep|\[0.000 0.000 0.000]-(|laserplane|).wmf'
$!VarSet |write_data|="C:\Forward Stations\Extracted Velocity Data\StationTwo\Airwake\Rep|rep|\[0.000 0.000 0.000]-(|laserplane|).dat"
$!VarSet |rotor_overlay|=0
$!ENDIF

$!ELSEIF |station_num|==3
$!IF |airwake_flag|==0
$!VarSet |read_file|='"C:\Forward Stations\StationThree\Rep|rep|\[|rotorx%.3f| |rotory%.3f| |rotorz%.3f|]-(|laserplane|).dat"'
$!VarSet |export_plot|='C:\Forward Stations\Velocity Plots\StationThree\Rep|rep|\[|rotorx%.3f| |rotory%.3f| |rotorz%.3f|]-(|laserplane|).wmf'
$!VarSet |write_data|="C:\Forward Stations\Extracted Velocity Data\StationThree\Rep|rep|\[|rotorx%.3f| |rotory%.3f| |rotorz%.3f|]-(|laserplane|).dat"
$!VarSet |rotor_overlay|=1
$!ELSEIF |airwake_flag|==1
$!VarSet |read_file|='"C:\Forward Stations\StationThree\Airwake\Rep|rep|\[0.000 0.000 0.000]-(|laserplane|).dat"'
$!VarSet |export_plot|='C:\Forward Stations\Velocity Plots\StationThree\Airwake\Rep|rep|\[0.000 0.000 0.000]-(|laserplane|).wmf'
$!VarSet |write_data|="C:\Forward Stations\Extracted Velocity Data\StationThree\Airwake\Rep|rep|\[0.000 0.000 0.000]-(|laserplane|).dat"
$!VarSet |rotor_overlay|=0
$!ENDIF

$!ELSEIF |station_num|==4
```

```
$!VarSet |laserplane|=0
$!VarSet |read_file|='"C:\Forward Stations\Freestream\Rep|rep|\[0.000 0.000 0.000]-(|laserplane|).dat"'
$!VarSet |export_plot|='C:\Forward Stations\Velocity Plots\Freestream\Rep|rep|\[0.000 0.000 0.000]-(|laserplane|).wmf'
$!VarSet |write_data|="C:\Forward Stations\Extracted Velocity Data\Freestream\Rep|rep|\[0.000 0.000 0.000]-(|laserplane|).dat"
$!VarSet |rotor_overlay|=0

$!ELSEIF |station_num|==5
$!VarSet |read_file|='"C:\Forward Stations\CombinedRotorFreestream\Rep|rep|\[|rotorx%.3f| |rotory%.3f| |rotorz%.3f|]-(|laserplane|).dat"'
$!VarSet |export_plot|='C:\Forward Stations\Velocity Plots\CombinedRotorFreestream\Rep|rep|\[|rotorx%.3f| |rotory%.3f| |rotorz%.3f|]-(|laserplane|).wmf'
$!VarSet |write_data|="C:\Forward Stations\Extracted Velocity Data\CombinedRotorFreestream\Rep|rep|\[|rotorx%.3f| |rotory%.3f| |rotorz%.3f|]-(|laserplane|).dat"
$!VarSet |rotor_overlay|=1
$!ENDIF

#!SKIP CONTROL
$!IF |station_num|==1

$!IF |airwake_flag|==0
$!IF |laserplane| != |rotory|
$!VarSet |go|=1
$!ELSE
$!VarSet |go|=0
$!ENDIF
$!ELSEIF |airwake_flag|==1
$!VarSet |go|=1
$!ENDIF

$!ELSEIF |station_num|==2

$!IF |airwake_flag|==0
$!IF |laserplane| != |rotory|
$!VarSet |go|=1
$!ELSE
$!VarSet |go|=0
$!ENDIF
$!ELSEIF |airwake_flag|==1
$!VarSet |go|=1
$!ENDIF
```

```
$!ELSEIF |station_num|==3

$!IF |airwake_flag|==0
$!IF |laserplane| != |rotory|
$!VarSet |go|=1
$!ELSE
$!VarSet |go|=0
$!ENDIF
$!ELSEIF |airwake_flag|==1
$!VarSet |go|=1
$!ENDIF


$!ELSEIF |station_num|==4

$!IF |laserplane| == |rotory|
$!VarSet |go|=1
$!ELSE
$!VarSet |go|=0
$!ENDIF

$!ELSEIF |station_num|==5

$!IF |laserplane| != |rotory|
$!VarSet |go|=1
$!ELSE
$!VarSet |go|=0
$!ENDIF

$!ENDIF

$!IF |go| == 1
$!FRAMELAYOUT SHOWHEADER = NO
$!REDRAWALL
$!READDATASET  '|read_file|'
  READDATAOPTION = NEW
  RESETSTYLE = YES
  INCLUDETEXT = NO
  INCLUDEGEOM = NO
  INCLUDECUSTOMLABELS = NO
  VARLOADMODE = BYNAME
  INITIALPLOTTYPE = CARTESIAN2D
  VARNAMELIST = '"X mm" "Y mm" "Z mm" "U m/s" "V m/s" "W m/s"'
$!FIELDLAYERS SHOWMESH = NO
```

```
$!GLOBALTWODVECTOR UVAR = 4
$!GLOBALTWODVECTOR VVAR = 5
$!RESETVECTORLENGTH
$!FIELDLAYERS SHOWVECTOR = YES
$!REDRAWALL
$!CREATERECTANGULARZONE
  IMAX = 50
  JMAX = 30
  KMAX = 1
  X1 = -100
  Y1 = -80
  Z1 = 0
  X2 = 100
  Y2 = 80
  Z2 = 0
  XVAR = 1
  YVAR = 2
$!PICK SETMOUSEMODE
  MOUSEMODE = SELECT
$!REDRAWALL
$!RENAMEDATASETZONE
  ZONE = 2
  NAME = 'Interpolated Zone'
$!KRIG
  SOURCEZONES =  [1]
  DESTINATIONZONE = 2
  VARLIST =  [3-6]
  KRIGRANGE = 0.4
  KRIGZEROVALUE = 0
  KRIGDRIFT = NONE
  INTERPPTSELECTION = OCTANTNPOINTS
  INTERPNPOINTS = 16
$!REDRAWALL
$!FIELD [2]  VECTOR{COLOR = BLACK}
$!ACTIVEFIELDZONES -= [1]
$!FIELD [2]  BOUNDARY{COLOR = BLACK}
$!REDRAWALL
$!GLOBALCONTOUR 1  VAR = 6
$!CONTOURLEVELS RESETTONICE
  CONTOURGROUP = 1
  APPROXNUMVALUES = 15
$!FIELDLAYERS SHOWCONTOUR = YES
$!REDRAWALL
$!CONTOURLEVELS NEW
  CONTOURGROUP = 1
  RAWDATA
```

```
11
-10
-8
-6
-4
-2
0
2
4
6
8
10
$!REDRAWALL
$!VIEW FIT
$!REDRAWALL
$!ALTERDATA
  EQUATION = '{X/D}=({X mm}*0.0393700787+|rotorx|)/10'
$!ALTERDATA
  EQUATION = '{Z/D}=({Y mm}*0.0393700787+|rotorz|)/10'
$!TWODAXIS XDETAIL{VARNUM = 7}
$!TWODAXIS YDETAIL{VARNUM = 8}
$!VIEW FIT
$!REDRAWALL
$!GLOBALTWODVECTOR RELATIVELENGTH = 0.005
$!REDRAWALL



$!VarSet |rotorzd|=|rotorz|
$!VarSet |rotorzd|/=10
#!**************ROTOR OVERLAY******************
$!IF |rotor_overlay|==1
$!ATTACHGEOM
  GEOMTYPE = ELLIPSE
  ANCHORPOS
    {
    X = 5.125
    Y = |rotorzd|
    }
  COLOR = CUSTOM1
  ISFILLED = YES
  FILLCOLOR = CUSTOM1
  RAWDATA
1 0.0250000003725
$!REDRAWALL
$!ATTACHGEOM
```

```
  GEOMTYPE = ELLIPSE
  ANCHORPOS
    {
    X = 0.5125
    Y = |rotorzd|
    }
  COLOR = CUSTOM1
  ISFILLED = YES
  FILLCOLOR = CUSTOM1
  CLIPPING = CLIPTOFRAME
  RAWDATA
0.40000000596 0.0250000003725
$!REDRAWALL
$!ATTACHGEOM
  GEOMTYPE = RECTANGLE
  ANCHORPOS
    {
    X = 0.4625
    Y = |rotorzd|
    }
  COLOR = CUSTOM1
  ISFILLED = YES
  FILLCOLOR = CUSTOM1
  CLIPPING = CLIPTOFRAME
  RAWDATA
0.10000000149 0.317000001669
$!REDRAWALL
$!REDRAWALL
$!ATTACHGEOM
  GEOMTYPE = ELLIPSE
  ANCHORPOS
    {
    X = 0.5125
    Y = |rotorzd|
    }
  COLOR = CUSTOM1
  ISFILLED = YES
  FILLCOLOR = CUSTOM1
  CLIPPING = CLIPTOFRAME
  RAWDATA
0.0250000003725 0.0750000029802

$!ENDIF

$!GLOBALCONTOUR 1  LEGEND{SHOW = YES}
$!REDRAWALL
```

```
$!PICK SETMOUSEMODE
  MOUSEMODE = SELECT
$!PICK ADD
  X = 2.18344252531
  Y = 1.50768645358
$!PICK SHIFT
  X = -0.012805241215
  Y = -0.706849315068
$!REDRAWALL
$!PICK ADD
  X = 9.52084574151
  Y = 1.92656012177
$!PICK ADD
  X = 9.30315664086
  Y = 1.86111111111
$!GLOBALCONTOUR 1  LEGEND{ISVERTICAL = NO}
$!REDRAWALL
$!PICK SHIFT
  X = -1.7030970816
  Y = 5.53698630137
$!REDRAWALL
$!GLOBALTWODVECTOR REFVECTOR{SHOW = YES}
$!GLOBALTWODVECTOR REFVECTOR{XYPOS{X = 87}}
$!GLOBALTWODVECTOR REFVECTOR{XYPOS{Y = 9}}
$!GLOBALTWODVECTOR REFVECTOR{MAGNITUDE = 5}
$!GLOBALTWODVECTOR REFVECTOR{MAGNITUDELABEL{SHOW = NO}}
$!GLOBALTWODVECTOR REFVECTOR{MAGNITUDELABEL{SHOW = YES}}
$!GLOBALTWODVECTOR
REFVECTOR{MAGNITUDELABEL{NUMFORMAT{FORMATTING                =
INTEGER}}}
$!GLOBALTWODVECTOR
REFVECTOR{MAGNITUDELABEL{NUMFORMAT{POSITIVESUFFIX = 'm/s'}}}
$!GLOBALTWODVECTOR
REFVECTOR{MAGNITUDELABEL{NUMFORMAT{NEGATIVESUFFIX = 'm/s'}}}
$!GLOBALTWODVECTOR
REFVECTOR{MAGNITUDELABEL{NUMFORMAT{ZEROSUFFIX = 'm/s'}}}
$!REDRAWALL
$!ATTACHGEOM
  GEOMTYPE = RECTANGLE
  POSITIONCOORDSYS = FRAME
  ANCHORPOS
    {
    X = 85
    Y = 3
    }
  FILLCOLOR = CUSTOM1
```

```
  CLIPPING = CLIPTOFRAME
  RAWDATA
10.000000149 7.99999982119
$!REDRAWALL
#!*************EXPORT VECTOR AND CONTOUR PLOT*************
$!EXPORTSETUP IMAGEWIDTH = 1275
$!EXPORTSETUP EXPORTFNAME = '|export_plot|'
$!EXPORT

$!VarSet |Y1EX|=|rotorzd|
$!VarSet |Y1EX|-=0.25
$!VarSet |Y2EX|=|rotorzd|
$!VarSet |Y2EX|-=0.1

$!CREATERECTANGULARZONE
  IMAX = 20
  JMAX = 10
  KMAX = 1
  X1 = 0.2125
  Y1 = |Y1EX|
  Z1 = 0
  X2 = 0.8125
  Y2 = |Y2EX|
  Z2 = 0
$!PICK SETMOUSEMODE
  MOUSEMODE = SELECT
$!REDRAWALL
$!RENAMEDATASETZONE
  ZONE = 3
  NAME = 'Extracted Zone'
$!KRIG
  SOURCEZONES =  [1]
  DESTINATIONZONE = 3
  VARLIST =  [1-6]
  KRIGRANGE = 0.4
  KRIGZEROVALUE = 0
  KRIGDRIFT = NONE
  INTERPPTSELECTION = OCTANTNPOINTS
  INTERPNPOINTS = 16
$!ALTERDATA  [3]
  EQUATION = '{X/D}=({X mm}*0.0393700787+|rotorx|)/10'
$!ALTERDATA  [3]
  EQUATION = '{Z/D}=({Y mm}*0.0393700787+|rotorz|)/10'
$!WRITEDATASET  "|write_data|"
  INCLUDETEXT = NO
  INCLUDEGEOM = NO
```

```
  INCLUDECUSTOMLABELS = NO
  ASSOCIATELAYOUTWITHDATAFILE = NO
  ZONELIST =  [3]
  BINARY = NO
  USEPOINTFORMAT = YES
  PRECISION = 9

$!ENDIF
$!VarSet |laserplane|+=1
#!END LASER PLANE LOOP
$!ENDLOOP

$!VarSet |rotory|+=1
#!END ROTOR Y POSITION LOOP
$!ENDLOOP

$!RemoveVar |MFBD|
$!RemoveVar |rep|
$!RemoveVar |rotorx|
$!RemoveVar |rotory|
$!RemoveVar |rotorz|
$!RemoveVar |laserplane|
$!RemoveVar |rotor_overlay|
$!RemoveVar |rotorzd|
$!RemoveVar |Y1EX|
$!RemoveVar |Y2EX|
$!RemoveVar |rotor_loop_num|
$!RemoveVar |laser_loop_num|
$!RemoveVar |station_num|
$!RemoveVar |go|
$!RemoveVar |airwake_flag|
```

APPENDIX B: Three Component Coupling Analysis Code

```
%Three Component Velocity Discrepancy Based Coupling Analysis
clear;
clc;

%Corrected PIV Bias Estimates from Monte Carlo Simulation
PIV_U_BIAS=0.1;%(m/s)
PIV_W_BIAS=0.1;%(m/s)
PIV_V_BIAS=0.4;%(m/s)

ROTORX=5.125;
ROTORY=5;

for s=1:1:3

if s==1
ROTORZ=4.5;
station='StationOne';
elseif s==2
ROTORZ=12.000;
station='StationTwo';
elseif s==3
ROTORZ=24.000;
station='StationThree';
end

k=1;
cur_row=1;
for LASERY=-5:1:5

if LASERY~=ROTORY

file1=sprintf('C:\\Forward Stations\\Extracted Velocity
Data\\%s\\Rep1\\[%.3f %.3f %.3f]-(%i).dat','Freestream',0,0,0,0);
file2=sprintf('C:\\Forward Stations\\Extracted Velocity
Data\\%s\\Rep2\\[%.3f %.3f %.3f]-(%i).dat','Freestream',0,0,0,0);

file3=sprintf('C:\\Forward Stations\\Extracted Velocity
Data\\%s\\Rep1\\[%.3f %.3f %.3f]
(%i).dat','CombinedRotorFreestream',5.125,0,30,LASERY-ROTORY);
file4=sprintf('C:\\Forward Stations\\Extracted Velocity
Data\\%s\\Rep2\\[%.3f %.3f %.3f]-
(%i).dat','CombinedRotorFreestream',5.125,0,30,LASERY-ROTORY);

file5=sprintf('C:\\Forward Stations\\Extracted Velocity
Data\\%s\\Rep1\\[%.3f %.3f %.3f]-
(%i).dat',station,ROTORX,ROTORY,ROTORZ,LASERY);
file6=sprintf('C:\\Forward Stations\\Extracted Velocity
Data\\%s\ Rep2\\[%.3f %.3f %.3f]-
(%i).dat',station,ROTORX,ROTORY,ROTORZ,LASERY);
```

```
file7=sprintf('C:\\Forward Stations\\Extracted Velocity
Data\\%s\\%s\\Rep1\\[%.3f %.3f %.3f]-
(%i).dat',station,'Airwake',0,0,0,LASERY);
file8=sprintf('C:\\Forward Stations \Extracted Velocity
Data\\%s\\%s\ Rep2\\[%.3f %.3f %.3f]
(%i).dat',station,'Airwake',0,0,0,LASERY);

M1(:,:,k)=dlmread(file1,' ',13,1);
M2(:,:,k)=dlmread(file2,' ',13,1);
M3(:,:,k)=dlmread(file3,' ',13,1);
M4(:,:,k)=dlmread(file4,' ',13,1);
M5(:,:,k)=dlmread(file5,' ',13,1);
M6(:,:,k)=dlmread(file6,' ',13,1);
M7(:,:,k)=dlmread(file7,' ',13,1);
M8(:,:,k)=dlmread(file8,' ',13,1);
k=k+1;
end
end

[rows cols sets]=size(M1);
for i=1:1:sets
for j=1:1:rows
FREESTREAM1(cur_row,:)=M1(j,:,i);
FREESTREAM2(cur_row,:)=M2(j,:,i);

COMBINED1(cur_row,:)=M3(j,:,i);
COMBINED2(cur_row,:)=M4(j,:,i);

OBSERVED1(cur_row,:)=M5(j,:,i);
OBSERVED2(cur_row,:)=M6(j,:,i);

AIRWAKE1(cur_row,:)=M7(j,:,i);
AIRWAKE2(cur_row,:)=M8(j,:,i);
cur_row=cur_row+1;
end
end

%CHECK FOR DATA ALIGNMENT MISMATCH
freestream_check=sum(size(FREESTREAM1)==size(FREESTREAM2));
combined_check=sum(size(COMBINED1)==size(COMBINED2));
observed_check=sum(size(OBSERVED1)==size(OBSERVED2));
airwake_check=sum(size(AIRWAKE1)==size(AIRWAKE2));
if
(freestream_check==2)&&(combined_check==2)&&(observed_check==2)&&(airwa
ke_check==2);
 ERRORCODE1=0;
else
ERRORCODE1=1;
end

%CHECK FOR DATA ALIGNMENT MISMATCH
[n m]=size(FREESTREAM1);

freestream_diff=max(abs(FREESTREAM1(:,1)-FREESTREAM2(:,1)));
combined_diff=max(abs(COMBINED1(:,1)-COMBINED2(:,1)));
```

```
observed_diff=max(abs(OBSERVED1(:,1)-OBSERVED2(:,1)));
airwake_diff=max(abs(AIRWAKE1(:,1)-AIRWAKE2(:,1)));

if
(freestream_diff>2)||(combined_diff>2)||(observed_diff>2)||(airwake_dif
f>2)
        ERRORCODE2=1;
else
        ERRORCODE2=0;
end

maxdiff(1)=max(abs(FREESTREAM1(:,1)-COMBINED1(:,1)));
maxdiff(2)=max(abs(FREESTREAM1(:,1)-OBSERVED1(:,1)));
maxdiff(3)=max(abs(FREESTREAM1(:,1)-AIRWAKE1(:,1)));
maxdiff(4)=max(abs(COMBINED1(:,1)-OBSERVED1(:,1)));
maxdiff(5)=max(abs(COMBINED1(:,1)-AIRWAKE1(:,1)));
maxdiff(6)=max(abs(OBSERVED1(:,1)-AIRWAKE1(:,1)));

if max(maxdiff)>2
        ERRORCODE3=1;
else
        ERRORCODE3=0;
end

if (ERRORCODE1==1)
fprintf('ERROR: DATA SIZE MISMATCH DETECTED\r');
elseif (ERRORCODE2==1)
fprintf('ERROR: DATA MISMATCH BETWEEN REPLICATES DETECTED\r');
elseif (ERRORCODE3==1)
fprintf('ERROR: DATA MISMATCH BETWEEN COMPONENTS\r');
else
fprintf('DATA ALIGNMENT VALIDATION SUCCESSFUL\r');
end



%CALCULATE AVERAGE VELOCITIES AND SUM OF SQUARES VARIANCE FROM
REPLICATES
%AVERAGE
    AVG_U_FREESTREAM=(FREESTREAM1(:,4)+FREESTREAM2(:,4))./2;
    AVG_W_FREESTREAM=(FREESTREAM1(:,5)+FREESTREAM2(:,5))./2;
    AVG_V_FREESTREAM=(FREESTREAM1(:,6)+FREESTREAM2(:,6))./2;

    AVG_U_COMBINED=(COMBINED1(:,4)+COMBINED2(:,4))./2;
    AVG_W_COMBINED=(COMBINED1(:,5)+COMBINED2(:,5))./2;
    AVG_V_COMBINED=(COMBINED1(:,6)+COMBINED2(:,6))./2;

    AVG_U_OBSERVED=(OBSERVED1(:,4)+OBSERVED2(:,4))./2;
    AVG_W_OBSERVED=(OBSERVED1(:,5)+OBSERVED2(:,5))./2;
    AVG_V_OBSERVED=(OBSERVED1(:,6)+OBSERVED2(:,6))./2;

    AVG_U_AIRWAKE=(AIRWAKE1(:,4)+AIRWAKE2(:,4))./2;
    AVG_W_AIRWAKE=(AIRWAKE1(:,5)+AIRWAKE2(:,5))./2;
    AVG_V_AIRWAKE=(AIRWAKE1(:,6)+AIRWAKE2(:,6))./2;
```

```
%SUM OF SQUARES VARIANCE
    VAR_U_FREESTREAM=sum((FREESTREAM1(:,4)-FREESTREAM2(:,4)).^2)/(n-
1)+PIV_U_BIAS^2;
    VAR_W_FREESTREAM=sum((FREESTREAM1(:,5)-FREESTREAM2(:,5)).^2)/(n-
1)+PIV_W_BIAS^2;
    VAR_V_FREESTREAM=sum((FREESTREAM1(:,6)-FREESTREAM2(:,6)).^2)/(n-
1)+PIV_V_BIAS^2;

    VAR_U_COMBINED=sum((COMBINED1(:,4)-COMBINED2(:,4)).^2)/(n-
1)+PIV_U_BIAS^2;
    VAR_W_COMBINED=sum((COMBINED1(:,5)-COMBINED2(:,5)).^2)/(n-
1)+PIV_W_BIAS^2;
    VAR_V_COMBINED=sum((COMBINED1(:,6)-COMBINED2(:,6)).^2)/(n-
1)+PIV_V_BIAS^2;

    VAR_U_OBSERVED=sum((OBSERVED1(:,4)-OBSERVED2(:,4)).^2)/(n-
1)+PIV_U_BIAS^2;
    VAR_W_OBSERVED=sum((OBSERVED1(:,5)-OBSERVED2(:,5)).^2)/(n-
1)+PIV_W_BIAS^2;
    VAR_V_OBSERVED=sum((OBSERVED1(:,6)-OBSERVED2(:,6)).^2)/(n-
1)+PIV_V_BIAS^2;

    VAR_U_AIRWAKE=sum((AIRWAKE1(:,4)-AIRWAKE2(:,4)).^2)/(n-
1)+PIV_U_BIAS^2;
    VAR_W_AIRWAKE=sum((AIRWAKE1(:,5)-AIRWAKE2(:,5)).^2)/(n-
1)+PIV_W_BIAS^2;
    VAR_V_AIRWAKE=sum((AIRWAKE1(:,6)-AIRWAKE2(:,6)).^2)/(n-
1)+PIV_V_BIAS^2;

%GENERATE SUPERIMPOSED SOLUTION
    AVG_U_SUPERIMPOSED=AVG_U_AIRWAKE-AVG_U_FREESTREAM+AVG_U_COMBINED;
    AVG_W_SUPERIMPOSED=AVG_W_AIRWAKE-AVG_W_FREESTREAM+AVG_W_COMBINED;
    AVG_V_SUPERIMPOSED=AVG_V_AIRWAKE-AVG_V_FREESTREAM+AVG_V_COMBINED;

    VAR_U_SUPERIMPOSED=VAR_U_AIRWAKE+VAR_U_FREESTREAM+VAR_U_COMBINED;
    VAR_W_SUPERIMPOSED=VAR_W_AIRWAKE+VAR_W_FREESTREAM+VAR_W_COMBINED;
    VAR_V_SUPERIMPOSED=VAR_V_AIRWAKE+VAR_V_FREESTREAM+VAR_V_COMBINED;

%COMPUTE VELOCITY DISCREPANCY BETWEEN OBSERVED AND SUPERIMPOSED
VELOCITY FIELD

    AVG_U_DIFF=mean(abs(AVG_U_SUPERIMPOSED-AVG_U_OBSERVED));
    AVG_W_DIFF=mean(abs(AVG_W_SUPERIMPOSED-AVG_W_OBSERVED));
    AVG_V_DIFF=mean(abs(AVG_V_SUPERIMPOSED-AVG_V_OBSERVED));

    VAR_U_DIFF=var(abs(AVG_U_SUPERIMPOSED-
AVG_U_OBSERVED))+VAR_U_SUPERIMPOSED+VAR_U_OBSERVED;
    VAR_W_DIFF=var(abs(AVG_U_SUPERIMPOSED-
AVG_U_OBSERVED))+VAR_W_SUPERIMPOSED+VAR_W_OBSERVED;
    VAR_V_DIFF=var(abs(AVG_U_SUPERIMPOSED-
AVG_U_OBSERVED))+VAR_V_SUPERIMPOSED+VAR_V_OBSERVED;

    CI_U_DIFF=tinv(1-0.05/2,n-1)*sqrt(VAR_U_DIFF)/sqrt(n);
    CI_W_DIFF=tinv(1-0.05/2,n-1)*sqrt(VAR_W_DIFF)/sqrt(n);
    CI_V_DIFF=tinv(1-0.05/2,n-1)*sqrt(VAR_V_DIFF)/sqrt(n);
```

```
    RESULT(s,1)=ROTORZ;
    RESULT(s,2)=AVG_U_DIFF;
    RESULT(s,3)=AVG_W_DIFF;
    RESULT(s,4)=AVG_V_DIFF;
    RESULT(s,5)=VAR_U_DIFF;
    RESULT(s,6)=VAR_W_DIFF;
    RESULT(s,7)=VAR_V_DIFF;
    RESULT(s,8)=CI_U_DIFF;
    RESULT(s,9)=CI_W_DIFF;
    RESULT(s,10)=CI_V_DIFF;

end

%PRINT RESULTS TO FILE
output_file=sprintf('C:\\Forward Stations\\Processed Data\\[%.3f
%.3f].dat',ROTORX,ROTORY);
output_id=fopen(output_file,'wt');
fprintf(output_id,'TITLE="[%.3f %.3f]"\n',ROTORX,ROTORY);
fprintf(output_id,'VARIABLES="Z/D" "AVG U DIFF" "AVG W DIFF" "AVG V
DIFF" "VAR U DIFF" "VAR W DIFF" "VAR V DIFF" "CI U DIFF" "CI W DIFF"
"CI V DIFF"\n');
fprintf(output_id,'ZONE I=%i F=POINT\n',3);
for d=1:3
fprintf(output_id,'%.4f,%.4f,%.4f,%.4f,%.4f,%.4f,%.4f,%.4f,%.4f,%.4f\n'
,RESULT(d,1)/10,RESULT(d,2),RESULT(d,3),RESULT(d,4),RESULT(d,5),RESULT(
d,6),RESULT(d,7),RESULT(d,8),RESULT(d,9),RESULT(d,10));
end
fclose(output_id);
```

APPENDIX C: Summary of Developed Wind Tunnel Software

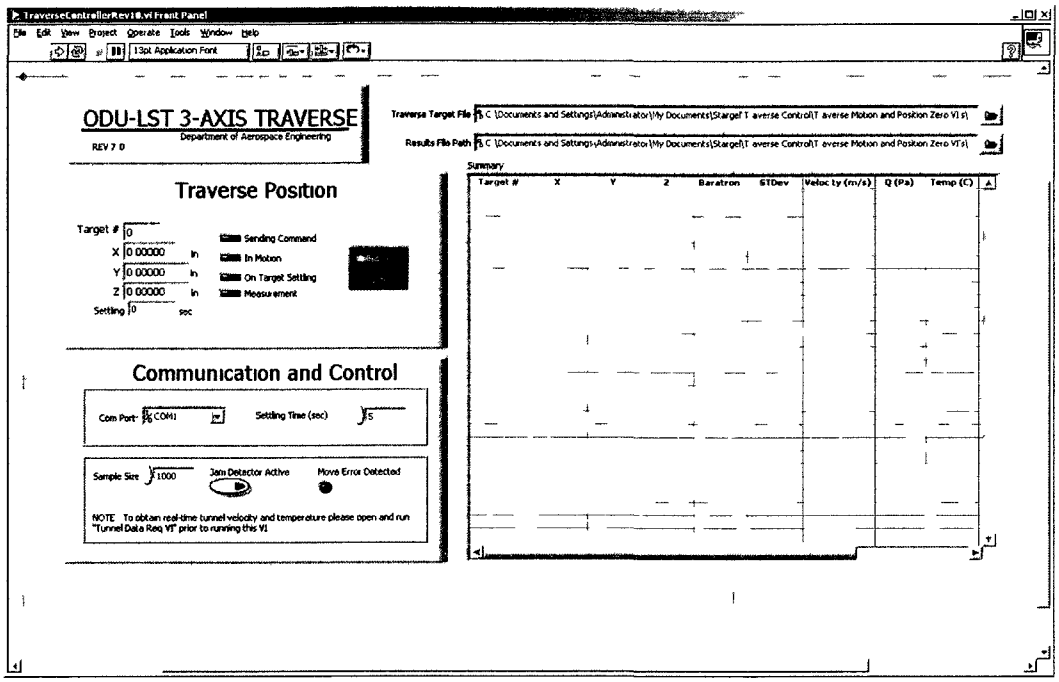

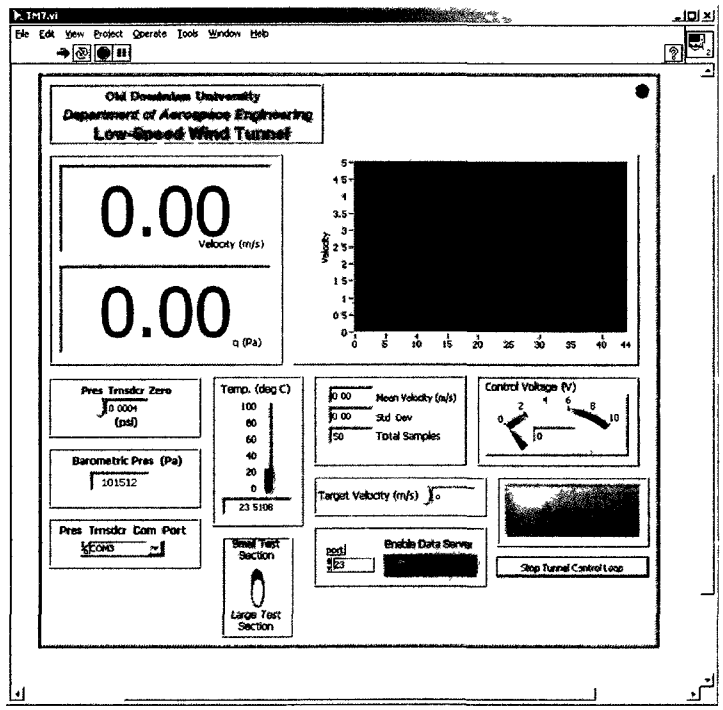

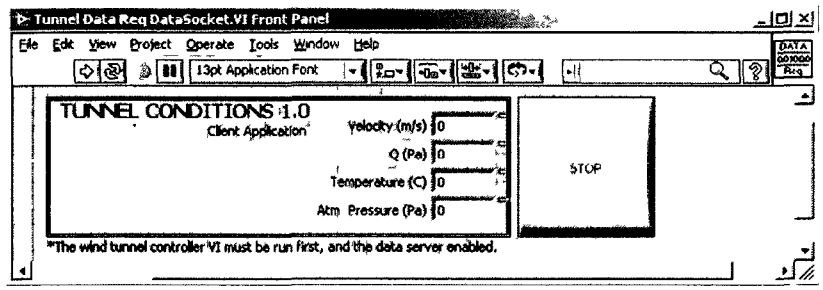
Tunnel Data Req DataSocket.VI Front Panel
File Edit View Project Operate Tools Window Help
13pt Application Font
TUNNEL CONDITIONS 1.0
Client Application
Velocity (m/s)
Q (Pa)
Temperature (C)
Atm Pressure (Pa)
STOP
*The wind tunnel controller VI must be run first, and the data server enabled.

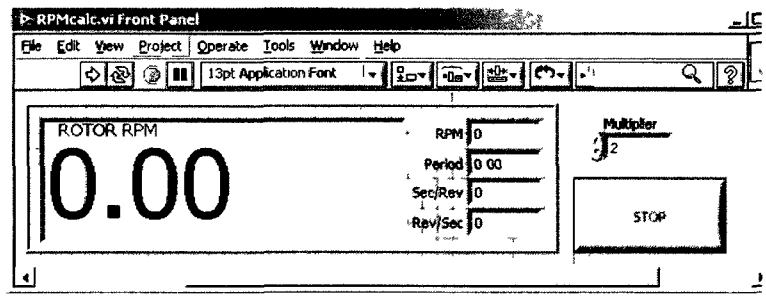
RPMcalc.vi Front Panel
File Edit View Project Operate Tools Window Help
13pt Application Font
ROTOR RPM
0.00
RPM
Period
Sec/Rev
Rev/Sec
Multiplier
STOP

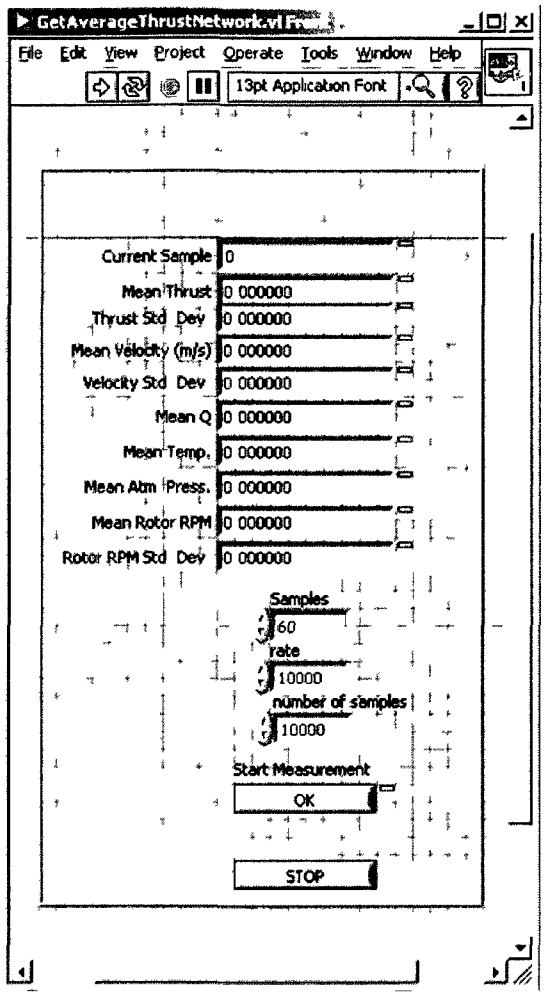
GetAverageThrustNetwork.vi Fr
File Edit View Project Operate Tools Window Help
13pt Application Font
Current Sample
0
Mean Thrust
0.000000
Thrust Std Dev
0.000000
Mean Velocity (m/s)
0.000000
Velocity Std Dev
0.000000
Mean Q
0.000000
Mean Temp.
0.000000
Mean Atm Press.
0.000000
Mean Rotor RPM
0.000000
Rotor RPM Std Dev
0.000000
Samples
60
rate
10000
number of samples
10000
Start Measurement
OK
STOP

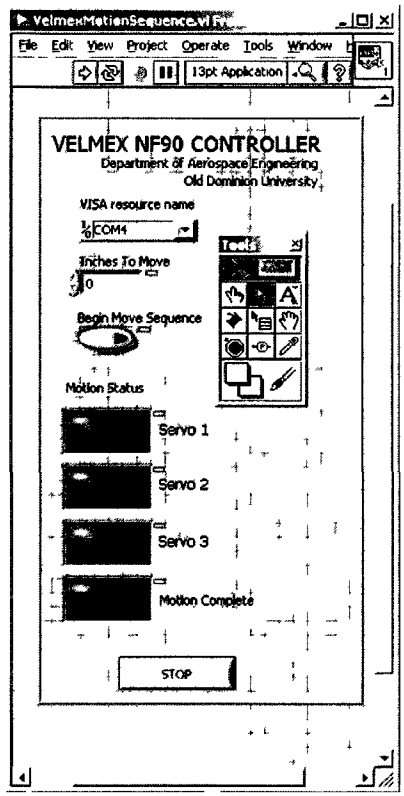
VelmexMotionSequence.vi Fr
File Edit View Project Operate Tools Window
13pt Application
VELMEX NF90 CONTROLLER
Department of Aerospace Engineering
Old Dominion University
VISA resource name
COM1
Inches To Move
0
Begin Move Sequence
Motion Status
Servo 1
Servo 2
Servo 3
Motion Complete
STOP

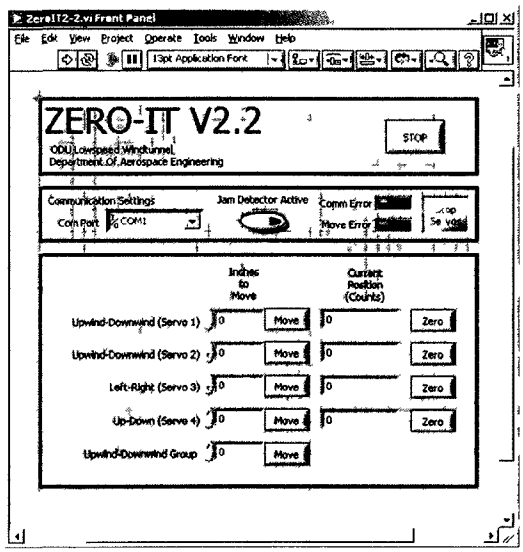
ZeroIT2-2.vi Front Panel
File Edit View Project Operate Tools Window Help
13pt Application Font
ZERO-IT V2.2
ODU Lowspeed Windtunnel
Department Of Aerospace Engineering
STOP
Communication Settings
Com Port
COM1
Jam Detector Active
Comm Error
Move Error
Inches to Move
Current Position (Counts)
Upwind-Downwind (Servo 1)
Upwind-Downwind (Servo 2)
Left-Right (Servo 3)
Up-Down (Servo 4)
Upwind-Downwind Group
Move
Zero

APPENDIX D: Monte Carlo Stereo PIV Image Generation Algorithm

```
clear;
clc;

%Calibration Equations
Left_Camera_x_mm=@(xpix,ypix,zmm)-
119.955+0.181739.*xpix+0.00114229.*ypix-0.117082.*zmm+5.02817e-
006.*xpix.^2-1.9942e-007.*xpix.*ypix-1.29221e-007.*ypix.^2-
0.000140106.*xpix.*zmm+2.87984e-006.*ypix.*zmm;
Left_Camera_y_mm=@(xpix,ypix,zmm)-92.2816-
0.00345827.*xpix+0.181219.*ypix+0.0776158.*zmm+1.73291e-
009.*xpix.^2+4.89664e-006.*xpix.*ypix+2.65745e-008.*ypix.^2-5.31084e-
006.*xpix.*zmm-0.000118238.*ypix.*zmm;
Right_Camera_x_mm=@(xpix,ypix,zmm)-
124.168+0.191966.*xpix+0.00303101.*ypix+0.289226.*zmm-4.83314e-
006.*xpix.^2+7.78692e-008.*xpix.*ypix+1.00813e-007.*ypix.^2-
0.000142603.*xpix.*zmm-3.04742e-006.*ypix.*zmm;
Right_Camera_y_mm=@(xpix,ypix,zmm)-90.9543-
0.000829306.*xpix+0.183936.*ypix+0.0857377.*zmm+3.32252e-008.*xpix.^2-
4.65712e-006.*xpix.*ypix+2.06932e-007.*ypix.^2-1.27237e-005.*xpix.*zmm-
0.000124759.*ypix.*zmm;

%Simulation Constants
dt=0.2;
q=100;
delta_zo=3;
xpixels=1280/4;
ypixels=1024/4;
particle_number=2000;
xdisp=0.1;%mm
ydisp=0.0;%mm
zdisp=0.0;%mm


forimage_num=0:1:39
[x,y] = meshgrid(1:1:xpixels, 1:1:ypixels);
xmin=min(min(x));
xmax=max(max(x));
ymin=min(min(y));
ymax=max(max(y));
[xlength,ylength]=size(x);

xmm_max1=max(max(Left_Camera_x_mm(x,y,0)));
xmm_min1=min(min(Left_Camera_x_mm(x,y,0)));
ymm_max1=max(max(Left_Camera_y_mm(x,y,0)));
ymm_min1=min(min(Left_Camera_y_mm(x,y,0)));
xo1=(xmm_max1+xmm_min1)/2;
yo1=(ymm_max1+ymm_min1)/2;

xmm_max2=max(max(Right_Camera_x_mm(x,y,0)));
xmm_min2=min(min(Right_Camera_x_mm(x,y,0)));
ymm_max2=max(max(Right_Camera_y_mm(x,y,0)));
ymm_min2=min(min(Right_Camera_y_mm(x,y,0)));
```

```
xo2=(xmm_max2+xmm_min2)/2;
yo2=(ymm_max2+ymm_min2)/2;

Io1=@(z)q.*exp(-(z.^2)/((delta_zo.^2)./8));
I1=@(x,y,z)Io1(z).*exp((-(x-xo1).^2-(y-yo1).^2)./((dt.^2)./8));
Io2=@(z)q.*exp(-(z.^2)/((delta_zo.^2)./8));
I2=@(x,y,z)Io2(z).*exp((-(x-xo2).^2-(y-yo2).^2)./((dt.^2)./8));


final_pic1(1:xlength,1:ylength)=0;
final_pic2(1:xlength,1:ylength)=0;
final_pic3(1:xlength,1:ylength)=0;
final_pic4(1:xlength,1:ylength)=0;

%GENERATE PARTICLES
inner_count=1;
for k=1:1:particle_number;
%fprintf('Generating spot %i\n',k);
pert_x=rand*xmax-xmax/2;
pert_y=rand*ymax-ymax/2;
pert_z=rand*delta_zo-delta_zo/2;
pic1=I1(Left_Camera_x_mm(x+pert_x,y+pert_y,pert_z),Left_Camera_y_mm(x+p
ert_x,y+pert_y,pert_z),pert_z);
pic2=I1(Left_Camera_x_mm(x+pert_x,y+pert_y,pert_z+zdisp)-
xdisp,Left_Camera_y_mm(x+pert_x,y+pert_y,pert_z+zdisp)-
ydisp,pert_z+zdisp);
pic3=I2(Right_Camera_x_mm(x+pert_x,y+pert_y,pert_z),Right_Camera_y_mm(x
+pert_x,y+pert_y,pert_z),pert_z);
pic4=I2(Right_Camera_x_mm(x+pert_x,y+pert_y,pert_z+zdisp)-
xdisp,Right_Camera_y_mm(x+pert_x,y+pert_y,pert_z+zdisp)-
ydisp,pert_z+zdisp);
final_pic1=final_pic1+pic1;
final_pic2=final_pic2+pic2;
final_pic3=final_pic3+pic3;
final_pic4=final_pic4+pic4;

end

%Limit Particle Intensity
for i=1:xlength
for j=1:ylength
if final_pic1(i,j)>q
            final_pic1(i,j)=q;
end
if final_pic2(i,j)>q
            final_pic2(i,j)=q;
end
if final_pic3(i,j)>q
            final_pic3(i,j)=q;
end
if final_pic4(i,j)>q
            final_pic4(i,j)=q;
end
end
end
```

```
%Output Image File
filename1=sprintf('C:\\Documents and Settings\\Home Box\\My
Documents\\PIV Uncertainty
Analysis\\Images\\analysis%05iLe.tif',image_num);
filename2=sprintf('C:\\Documents and Settings\\Home Box\\My
Documents\\PIV Uncertainty
Analysis\\Images\\analysis%05iLo.tif',image_num);
filename3=sprintf('C:\\Documents and Settings\\Home Box\\My
Documents\\PIV Uncertainty
Analysis\\Images\\analysis%05iRe.tif',image_num);
filename4=sprintf('C:\\Documents and Settings\\Home Box\\My
Documents\\PIV Uncertainty
Analysis\\Images\\analysis%05iRo.tif',image_num);

imwrite(final_pic1,filename1,'tif');
imwrite(final_pic2,filename2,'tif');
imwrite(final_pic3,filename3,'tif');
imwrite(final_pic4,filename4,'tif');
end
```

APPENDIX E: Near Deck Thrust Coefficient Survey Experimental Design and Response Data

Run Order	X/D	Y/D	Z/D	C_T
1	1.76	0.17	0.60	0.0169431
2	0.76	0.42	0.60	0.0166012
3	1.01	0.08	0.77	0.0168682
4	0.76	0.42	0.43	0.0164209
5	1.26	0.25	0.85	0.0168772
6	1.01	0.08	0.68	0.0169405
7	2.01	0.33	0.77	0.0169047
8	1.51	0.00	0.35	0.0169349
9	1.76	0.42	0.68	0.0169215
10	1.26	0.25	0.85	0.0169162
11	1.26	0.50	0.52	0.0170806
12	1.26	0.50	0.77	0.0169446
13	1.76	0.17	0.60	0.017135
14	1.51	0.08	0.60	0.0171048
15	1.51	0.33	0.68	0.016993
16	0.51	0.25	0.60	0.0170897
17	1.01	0.25	0.35	0.0170837
18	1.01	0.42	0.35	0.0170621
19	1.01	0.17	0.35	0.0171208
20	1.26	0.08	0.43	0.0169116
21	1.51	0.50	0.52	0.0170746
22	1.01	0.50	0.68	0.0169706
23	1.01	0.00	0.68	0.017049
24	0.51	0.33	0.35	0.0170198
25	1.26	0.17	0.85	0.017015
26	1.51	0.08	0.35	0.0173073
27	1.01	0.08	0.60	0.0170693
28	1.76	0.08	0.52	0.0171583
29	1.76	0.33	0.68	0.0170349
30	0.76	0.50	0.85	0.016988
31	1.51	0.42	0.43	0.0170533
32	2.01	0.50	0.35	0.017142
33	1.01	0.00	0.85	0.0169109
34	0.76	0.17	0.77	0.0170238
35	1.01	0.33	0.60	0.0169585
36	0.51	0.00	0.77	0.0172891
37	1.51	0.33	0.60	0.0170477
38	1.01	0.00	0.52	0.0168867
39	0.76	0.33	0.35	0.0166028
40	1.76	0.50	0.85	0.0169247
41	0.51	0.17	0.52	0.0172131
42	0.76	0.25	0.77	0.0169303
43	1.51	0.50	0.35	0.0172768

44	1.01	0.42	0.68	0.0170086
45	1.51	0.42	0.60	0.0170781
46	0.51	0.17	0.77	0.0170342
47	2.01	0.50	0.52	0.017008
48	1.76	0.17	0.77	0.017065
49	1.76	0.17	0.68	0.0171055
50	1.51	0.17	0.77	0.0169505
51	1.76	0.08	0.52	0.017065
52	1.51	0.33	0.52	0.0171981
53	2.01	0.17	0.68	0.0169833
54	0.76	0.33	0.52	0.0166525
55	0.51	0.50	0.85	0.0167981
56	1.01	0.42	0.60	0.0169102
57	0.51	0.25	0.43	0.017242
58	2.01	0.25	0.85	0.0168951
59	0.51	0.33	0.52	0.017028
60	1.26	0.17	0.68	0.0170323
61	0.51	0.00	0.43	0.0168536
62	2.01	0.17	0.35	0.0167323
63	0.51	0.42	0.52	0.0166973
64	1.76	0.08	0.43	0.0169586
65	0.76	0.08	0.52	0.0171279
66	1.01	0.42	0.68	0.0169495
67	1.76	0.00	0.60	0.0171267
68	0.51	0.17	0.77	0.0170653
69	1.51	0.25	0.35	0.0173841
70	1.01	0.00	0.77	0.0170142
71	1.76	0.50	0.77	0.0168988
72	1.26	0.17	0.68	0.0169594
73	1.01	0.33	0.68	0.0169572
74	1.76	0.25	0.60	0.0170803
75	1.26	0.33	0.52	0.0172373
76	1.26	0.33	0.77	0.0169811
77	0.76	0.50	0.68	0.0168258
78	1.01	0.08	0.43	0.0169046
79	1.51	0.25	0.35	0.0173742
80	1.01	0.50	0.52	0.0169964
81	2.01	0.17	0.43	0.0170993
82	1.51	0.00	0.68	0.0170609
83	1.76	0.33	0.77	0.0169541
84	1.76	0.00	0.60	0.017119
85	0.51	0.33	0.35	0.0169794
86	0.76	0.00	0.77	0.0171891
87	1.01	0.08	0.43	0.016945
88	1.26	0.42	0.52	0.017106
89	0.76	0.42	0.52	0.0166371
90	0.76	0.42	0.35	0.016731
91	0.51	0.42	0.43	0.0169117
92	2.01	0.17	0.52	0.0171251

93	1.01	0.42	0.52	0.0169849
94	1.76	0.50	0.60	0.0170626
95	0.76	0.00	0.77	0.0172051
96	1.51	0.50	0.85	0.0169399
97	2.01	0.42	0.43	0.0171254
98	1.26	0.50	0.85	0.0169419
99	2.01	0.17	0.68	0.0170032
100	1.01	0.25	0.52	0.0170487
101	1.51	0.25	0.43	0.0173099
102	0.51	0.42	0.77	0.0167292
103	1.76	0.00	0.52	0.0169458
104	1.01	0.00	0.60	0.0169879
105	2.01	0.33	0.43	0.0169517
106	1.51	0.00	0.60	0.017043
107	1.51	0.50	0.35	0.017166
108	1.01	0.17	0.68	0.0171129
109	2.01	0.42	0.68	0.0169333
110	0.76	0.00	0.60	0.01738
111	0.51	0.42	0.60	0.0167619
112	1.51	0.00	0.43	0.0169601
113	1.76	0.50	0.35	0.0170534
114	1.76	0.00	0.68	0.0171162
115	2.01	0.00	0.68	0.0170147
116	1.01	0.17	0.52	0.0170343
117	0.76	0.33	0.43	0.016481
118	1.51	0.50	0.68	0.0169704
119	0.76	0.42	0.52	0.0166402
120	2.01	0.00	0.77	0.0169791
121	0.76	0.33	0.52	0.0166902
122	1.51	0.00	0.43	0.0169732
123	1.01	0.33	0.35	0.017045
124	1.51	0.42	0.52	0.0170793
125	1.26	0.42	0.85	0.016948
126	0.76	0.42	0.68	0.0168222
127	1.51	0.08	0.85	0.016979
128	1.51	0.00	0.77	0.0169926
129	1.51	0.17	0.35	0.0173174
130	0.76	0.50	0.77	0.0169019
131	0.76	0.00	0.35	0.016471
132	1.76	0.25	0.85	0.0168976
133	2.01	0.08	0.43	0.0170533
134	1.26	0.00	0.60	0.0168025
135	0.76	0.08	0.60	0.017255
136	0.76	0.25	0.52	0.0168239
137	1.51	0.33	0.35	0.0172564
138	1.76	0.33	0.77	0.0169001
139	1.76	0.00	0.77	0.0170069
140	1.01	0.50	0.60	0.0169606
141	0.51	0.50	0.60	0.0167825

142	1.26	0.50	0.60	0.0170121
143	1.51	0.42	0.60	0.0169978
144	1.26	0.33	0.60	0.0171759
145	0.51	0.08	0.35	0.0164684
146	1.26	0.17	0.43	0.0170004
147	0.76	0.50	0.60	0.0167581
148	1.51	0.25	0.52	0.0172234
149	1.51	0.08	0.77	0.0169318
150	1.26	0.42	0.77	0.0169478
151	1.26	0.08	0.35	0.0170655
152	0.51	0.50	0.35	0.0170256
153	1.26	0.42	0.77	0.0169602
154	2.01	0.17	0.85	0.016916
155	1.51	0.42	0.77	0.0168883
156	1.26	0.08	0.77	0.0169476
157	1.51	0.33	0.43	0.0172689
158	1.26	0.08	0.52	0.0168618
159	0.51	0.50	0.52	0.0166374
160	1.01	0.17	0.52	0.0170666
161	1.76	0.42	0.60	0.0169699
162	2.01	0.08	0.52	0.0171216
163	1.01	0.17	0.43	0.0170491
164	2.01	0.25	0.43	0.0169787
165	1.51	0.25	0.52	0.0172914
166	0.76	0.42	0.43	0.0165941
167	1.01	0.33	0.77	0.0170266
168	1.26	0.08	0.85	0.0169893
169	1.26	0.00	0.43	0.0168752
170	1.76	0.33	0.35	0.0170575
171	1.26	0.08	0.68	0.0169778
172	1.01	0.33	0.77	0.0170199
173	1.76	0.42	0.68	0.0169846
174	1.76	0.42	0.52	0.0169841
175	2.01	0.42	0.85	0.0168772
176	0.51	0.42	0.60	0.0167803
177	2.01	0.25	0.77	0.0169118
178	2.01	0.50	0.68	0.0168756
179	0.76	0.00	0.35	0.016459
180	1.76	0.00	0.43	0.0168201
181	0.51	0.17	0.43	0.0172118
182	2.01	0.17	0.77	0.0169147
183	1.76	0.17	0.52	0.0170745
184	2.01	0.42	0.77	0.0168809
185	1.01	0.08	0.60	0.0169863
186	2.01	0.00	0.85	0.0168669
187	1.01	0.00	0.35	0.0168862
188	1.76	0.42	0.35	0.0169752
189	1.26	0.25	0.77	0.0169494
190	1.76	0.25	0.35	0.0169821

191	1.26	0.50	0.60	0.0170372
192	0.51	0.33	0.60	0.0169304
193	1.26	0.00	0.35	0.0170288
194	0.76	0.33	0.35	0.0165917
195	1.01	0.50	0.68	0.0169796
196	1.51	0.08	0.43	0.0171952
197	2.01	0.42	0.60	0.0170314
198	0.51	0.08	0.77	0.0172153
199	1.26	0.08	0.35	0.01709
200	1.51	0.00	0.77	0.0169573
201	2.01	0.08	0.77	0.0169599
202	1.76	0.50	0.35	0.0169878
203	1.01	0.42	0.43	0.0169783
204	0.51	0.00	0.77	0.0172789
205	0.76	0.42	0.85	0.0168941
206	2.01	0.50	0.35	0.0170928
207	1.26	0.00	0.85	0.0168738
208	1.01	0.50	0.52	0.0169617
209	0.51	0.42	0.43	0.0168807
210	0.51	0.50	0.77	0.0168356
211	0.76	0.33	0.85	0.0168919
212	0.76	0.00	0.85	0.0170788
213	2.01	0.25	0.68	0.0170032
214	2.01	0.33	0.60	0.0169783
215	1.26	0.42	0.52	0.017066
216	0.76	0.25	0.60	0.0169687
217	0.51	0.33	0.77	0.0169226
218	1.51	0.08	0.43	0.0170675
219	0.51	0.00	0.43	0.0168173
220	0.76	0.25	0.35	0.0168629
221	1.01	0.33	0.52	0.016991
222	1.01	0.50	0.85	0.0169146
223	1.01	0.00	0.52	0.0169606
224	1.26	0.33	0.43	0.0172922
225	0.76	0.17	0.68	0.0172337
226	1.26	0.33	0.35	0.0172253
227	1.01	0.08	0.35	0.0170537
228	1.51	0.33	0.85	0.0170048
229	1.76	0.50	0.77	0.0168824
230	1.51	0.50	0.85	0.0169026
231	2.01	0.33	0.35	0.0168606
232	1.01	0.42	0.43	0.0169645
233	1.26	0.08	0.52	0.016864
234	1.01	0.08	0.77	0.0170452
235	1.01	0.17	0.68	0.0170081
236	1.26	0.00	0.68	0.0169225
237	1.51	0.08	0.77	0.0169725
238	1.51	0.00	0.52	0.0170249
239	1.26	0.25	0.77	0.0170118

240	0.76	0.08	0.77	0.0171228
241	0.51	0.17	0.68	0.0170909
242	2.01	0.17	0.52	0.0170385
243	0.51	0.42	0.77	0.0168113
244	1.01	0.00	0.85	0.0168363
245	0.51	0.08	0.68	0.0171324
246	1.51	0.33	0.77	0.0168941
247	0.76	0.00	0.52	0.0170618
248	0.51	0.33	0.68	0.0168274
249	0.76	0.33	0.43	0.016384
250	1.76	0.25	0.77	0.0169137
251	0.51	0.50	0.68	0.0167363
252	0.76	0.08	0.43	0.0168686
253	1.51	0.17	0.85	0.016887
254	1.51	0.33	0.52	0.0171546
255	2.01	0.00	0.43	0.0170124
256	0.76	0.08	0.77	0.0171279
257	1.51	0.17	0.77	0.0169349
258	1.26	0.50	0.52	0.0170564
259	1.26	0.00	0.60	0.0168044
260	1.01	0.25	0.52	0.0170719
261	1.01	0.42	0.85	0.0168424
262	1.51	0.17	0.60	0.0171057
263	1.76	0.00	0.85	0.0168988
264	0.51	0.42	0.35	0.0171233
265	1.26	0.42	0.60	0.0169904
266	0.51	0.25	0.77	0.0168989
267	1.51	0.50	0.43	0.0171143
268	1.26	0.08	0.77	0.0169694
269	0.51	0.17	0.43	0.0171861
270	0.76	0.25	0.77	0.0169287
271	1.51	0.17	0.85	0.0169079
272	1.51	0.50	0.43	0.0170764
273	1.51	0.33	0.35	0.0172861
274	0.76	0.50	0.35	0.0168711
275	0.76	0.17	0.68	0.0171606
276	2.01	0.33	0.35	0.0168554
277	1.26	0.42	0.68	0.0170153
278	1.01	0.17	0.35	0.0172108
279	1.51	0.25	0.85	0.016975
280	1.26	0.17	0.43	0.0170415
281	2.01	0.25	0.68	0.0169871
282	2.01	0.00	0.35	0.0165897
283	0.51	0.33	0.85	0.016925
284	1.76	0.42	0.52	0.0169476
285	0.51	0.17	0.85	0.0169247
286	1.51	0.00	0.85	0.0168447
287	0.51	0.25	0.68	0.0169187
288	1.51	0.50	0.60	0.0169228

289	1.26	0.08	0.60	0.0168015
290	1.51	0.08	0.60	0.0170633
291	2.01	0.42	0.35	0.0169335
292	1.51	0.42	0.85	0.0168846
293	1.76	0.33	0.43	0.0170169
294	1.26	0.25	0.43	0.0172905
295	0.51	0.33	0.60	0.0169237
296	1.26	0.50	0.43	0.0172014
297	0.51	0.17	0.60	0.017205
298	0.76	0.42	0.85	0.0169331
299	1.51	0.25	0.85	0.0169874
300	1.01	0.25	0.85	0.0170235
301	1.26	0.17	0.35	0.0172103
302	1.76	0.25	0.77	0.0170012
303	1.26	0.17	0.77	0.0169696
304	1.26	0.33	0.68	0.0170719
305	0.76	0.33	0.77	0.0168317
306	1.26	0.00	0.77	0.0168328
307	1.76	0.25	0.43	0.0170678
308	2.01	0.00	0.68	0.0169678
309	1.01	0.33	0.43	0.0169336
310	2.01	0.50	0.77	0.0168821
311	0.76	0.08	0.60	0.0172687
312	0.76	0.17	0.43	0.0166761
313	1.26	0.25	0.52	0.0172588
314	0.51	0.08	0.77	0.0171745
315	1.76	0.33	0.85	0.0168443
316	1.01	0.50	0.77	0.0168785
317	2.01	0.50	0.43	0.0170265
318	2.01	0.08	0.68	0.0169508
319	1.01	0.08	0.35	0.016941
320	0.76	0.08	0.52	0.0170696
321	0.76	0.25	0.60	0.0169012
322	2.01	0.42	0.35	0.0169725
323	1.26	0.25	0.68	0.0170128
324	1.26	0.50	0.43	0.0171721
325	0.51	0.17	0.52	0.0171791
326	2.01	0.08	0.85	0.0169483
327	0.51	0.17	0.60	0.0171711
328	1.76	0.50	0.68	0.0169584
329	1.76	0.25	0.43	0.0170938
330	1.51	0.33	0.68	0.0170177
331	1.26	0.25	0.43	0.0172163
332	1.51	0.17	0.43	0.0172291
333	1.51	0.33	0.60	0.0170211
334	1.76	0.33	0.52	0.0170134
335	1.76	0.08	0.77	0.0170169
336	1.01	0.50	0.43	0.017017
337	1.01	0.42	0.35	0.0171179

338	1.76	0.00	0.85	0.0169898
339	1.01	0.08	0.52	0.0169838
340	1.01	0.08	0.52	0.017
341	1.01	0.25	0.43	0.0171846
342	1.51	0.25	0.60	0.0171402
343	1.26	0.00	0.35	0.0170519
344	1.76	0.25	0.60	0.0170956
345	0.51	0.50	0.52	0.0166949
346	1.76	0.33	0.60	0.0170261
347	1.26	0.42	0.35	0.0172417
348	1.26	0.50	0.35	0.0173734
349	1.01	0.00	0.35	0.0169954
350	1.76	0.50	0.68	0.0170042
351	2.01	0.08	0.60	0.0170805
352	1.76	0.25	0.52	0.0171966
353	0.51	0.25	0.85	0.0169301
354	0.76	0.08	0.85	0.017075
355	1.76	0.00	0.35	0.0166828
356	0.76	0.25	0.85	0.0168745
357	1.26	0.00	0.85	0.0168761
358	1.26	0.42	0.43	0.0169978
359	1.76	0.08	0.68	0.0170784
360	1.01	0.25	0.35	0.0171098
361	2.01	0.17	0.60	0.0169841
362	0.76	0.25	0.43	0.0166724
363	1.76	0.25	0.35	0.0170689
364	1.76	0.17	0.43	0.0171734
365	1.51	0.42	0.52	0.0171298
366	1.76	0.00	0.52	0.0170351
367	2.01	0.25	0.35	0.0168199
368	1.26	0.50	0.35	0.0174617
369	1.01	0.50	0.35	0.0174181
370	1.01	0.00	0.60	0.0171485
371	2.01	0.17	0.60	0.0171613
372	0.51	0.50	0.68	0.0168796
373	1.26	0.17	0.60	0.0171012
374	2.01	0.17	0.43	0.0171236
375	0.76	0.33	0.77	0.0169417
376	0.51	0.33	0.43	0.0172305
377	2.01	0.50	0.77	0.016917
378	0.76	0.42	0.68	0.0167515
379	1.76	0.08	0.35	0.0168329
380	0.51	0.25	0.85	0.0169016
381	2.01	0.25	0.52	0.0170266
382	1.76	0.00	0.68	0.0171018
383	1.76	0.25	0.68	0.0170317
384	1.26	0.50	0.68	0.0169281
385	1.51	0.25	0.77	0.0169374
386	0.51	0.25	0.68	0.0169186

387	0.51	0.08	0.60	0.0172643
388	1.26	0.33	0.60	0.0170836
389	0.51	0.33	0.85	0.0168489
390	1.51	0.50	0.77	0.0168683
391	2.01	0.00	0.60	0.016964
392	2.01	0.33	0.85	0.0168362
393	1.76	0.17	0.35	0.0169735
394	1.26	0.42	0.60	0.0169487
395	0.51	0.33	0.52	0.0169843
396	1.51	0.42	0.35	0.0171368
397	2.01	0.00	0.77	0.016959
398	0.51	0.08	0.60	0.0173024
399	0.51	0.50	0.43	0.0166895
400	1.01	0.25	0.77	0.016946
401	1.51	0.08	0.52	0.0171433
402	0.76	0.25	0.85	0.0168994
403	0.51	0.00	0.85	0.0171741
404	1.01	0.42	0.77	0.0169509
405	1.76	0.25	0.85	0.0169326
406	0.76	0.00	0.43	0.0168139
407	1.01	0.00	0.43	0.0167948
408	1.76	0.50	0.43	0.017009
409	0.76	0.00	0.43	0.0167399
410	1.51	0.08	0.68	0.0170021
411	1.51	0.17	0.43	0.0172175
412	0.76	0.25	0.52	0.0168447
413	1.76	0.33	0.68	0.0169536
414	2.01	0.33	0.52	0.0170365
415	1.76	0.17	0.85	0.0169346
416	0.76	0.00	0.60	0.0173274
417	2.01	0.42	0.68	0.0169036
418	2.01	0.50	0.60	0.0168578
419	0.76	0.33	0.68	0.0167438
420	0.51	0.50	0.85	0.0168012
421	0.76	0.25	0.43	0.0166339
422	2.01	0.08	0.68	0.0169383
423	1.51	0.50	0.60	0.0169467
424	0.76	0.00	0.68	0.0172193
425	1.51	0.17	0.35	0.0172643
426	1.01	0.00	0.77	0.0169047
427	2.01	0.08	0.52	0.0170831
428	1.01	0.17	0.85	0.0168695
429	1.01	0.00	0.43	0.0167544
430	0.51	0.33	0.68	0.0168867
431	1.01	0.42	0.77	0.0168726
432	1.01	0.25	0.85	0.0168983
433	2.01	0.42	0.52	0.016985
434	1.76	0.42	0.60	0.0169016
435	1.26	0.33	0.68	0.0170039

436	0.51	0.00	0.68	0.0173893
437	2.01	0.42	0.52	0.0169259
438	0.51	0.00	0.85	0.0171631
439	1.26	0.00	0.68	0.016807
440	1.01	0.50	0.43	0.0170011
441	0.76	0.00	0.85	0.0170163
442	1.76	0.08	0.43	0.0168829
443	0.51	0.25	0.77	0.0168875
444	1.01	0.33	0.52	0.0169704
445	2.01	0.25	0.60	0.0169933
446	2.01	0.08	0.35	0.016617
447	1.26	0.42	0.43	0.0170951
448	0.51	0.00	0.60	0.0175113
449	1.76	0.42	0.43	0.0169876
450	0.51	0.17	0.85	0.0169588
451	1.26	0.00	0.77	0.0168864
452	1.01	0.50	0.35	0.0172728
453	1.26	0.00	0.43	0.0168783
454	1.76	0.42	0.43	0.0169949
455	1.76	0.08	0.77	0.0170515
456	1.26	0.25	0.35	0.0172377
457	1.51	0.25	0.68	0.0170332
458	2.01	0.08	0.85	0.0169252
459	2.01	0.00	0.35	0.0165465
460	1.01	0.33	0.85	0.0169481
461	0.51	0.17	0.35	0.0167697
462	1.76	0.42	0.85	0.0168777
463	1.26	0.25	0.60	0.0171458
464	1.51	0.50	0.77	0.0168949
465	1.51	0.00	0.52	0.0170082
466	1.76	0.08	0.60	0.0171034
467	1.76	0.17	0.52	0.0170792
468	1.51	0.00	0.35	0.0169921
469	1.01	0.33	0.60	0.0169517
470	0.76	0.50	0.43	0.016686
471	1.01	0.25	0.60	0.0170189
472	0.76	0.17	0.60	0.0172025
473	2.01	0.50	0.68	0.0169288
474	1.76	0.42	0.35	0.0170511
475	1.26	0.08	0.85	0.0169685
476	0.51	0.08	0.85	0.0170965
477	1.76	0.50	0.52	0.0169972
478	1.26	0.17	0.85	0.016951
479	1.26	0.33	0.52	0.0172682
480	2.01	0.08	0.35	0.0166646
481	2.01	0.17	0.77	0.0169409
482	0.51	0.17	0.35	0.0166606
483	0.76	0.08	0.43	0.0168707
484	1.76	0.42	0.85	0.0167951

485	0.51	0.42	0.85	0.0167792
486	2.01	0.33	0.68	0.0168765
487	2.01	0.00	0.52	0.0170781
488	1.26	0.25	0.60	0.0170978
489	0.76	0.25	0.35	0.0168133
490	2.01	0.00	0.52	0.0171154
491	1.51	0.33	0.77	0.0169453
492	1.76	0.33	0.60	0.0169539
493	1.76	0.25	0.52	0.0171
494	1.01	0.42	0.60	0.0168989
495	1.26	0.08	0.60	0.0168672
496	0.76	0.00	0.52	0.0171169
497	1.01	0.25	0.68	0.0169439
498	1.26	0.50	0.85	0.0168972
499	1.76	0.00	0.77	0.0170512
500	0.51	0.00	0.52	0.0172465
501	0.76	0.25	0.68	0.0169314
502	1.01	0.17	0.60	0.0170532
503	2.01	0.17	0.85	0.0168786
504	0.76	0.42	0.77	0.0167347
505	1.76	0.08	0.85	0.0168865
506	1.01	0.25	0.60	0.0170083
507	0.76	0.08	0.35	0.0165879
508	1.26	0.25	0.35	0.0171144
509	1.51	0.33	0.43	0.0172015
510	1.01	0.50	0.60	0.0169273
511	1.51	0.17	0.68	0.0170114
512	1.76	0.42	0.77	0.01684
513	0.76	0.33	0.85	0.016832
514	2.01	0.42	0.77	0.0168234
515	1.51	0.33	0.85	0.0168563
516	1.51	0.00	0.60	0.0170255
517	0.51	0.50	0.35	0.0170349
518	1.76	0.17	0.85	0.0169166
519	0.51	0.17	0.68	0.0170591
520	1.26	0.50	0.77	0.0168582
521	0.51	0.50	0.43	0.0166284
522	0.76	0.33	0.68	0.0167931
523	1.26	0.33	0.85	0.0169382
524	1.76	0.00	0.35	0.0166933
525	1.01	0.33	0.68	0.0170199
526	1.76	0.08	0.35	0.0168791
527	0.51	0.25	0.60	0.0172003
528	1.51	0.42	0.43	0.0171062
529	0.51	0.42	0.52	0.0167637
530	0.51	0.25	0.43	0.0173029
531	1.76	0.25	0.68	0.01711
532	1.26	0.33	0.85	0.0169531
533	2.01	0.08	0.43	0.0171052

534	1.51	0.08	0.35	0.017237
535	0.51	0.42	0.68	0.0168078
536	2.01	0.00	0.43	0.0171023
537	1.51	0.50	0.52	0.0170812
538	0.76	0.50	0.52	0.0167301
539	1.76	0.08	0.85	0.0169512
540	2.01	0.17	0.35	0.016749
541	0.51	0.08	0.52	0.0173334
542	1.26	0.08	0.68	0.0169569
543	1.26	0.42	0.35	0.0171295
544	1.26	0.17	0.52	0.0170481
545	0.51	0.25	0.52	0.0171298
546	1.76	0.50	0.52	0.0169823
547	0.76	0.50	0.43	0.0167034
548	1.76	0.08	0.68	0.0171176
549	0.51	0.25	0.35	0.0168258
550	1.76	0.00	0.43	0.0168988
551	2.01	0.25	0.52	0.0171328
552	1.01	0.25	0.77	0.0169525
553	1.01	0.17	0.77	0.0170289
554	1.51	0.25	0.68	0.0170372
555	0.76	0.17	0.43	0.0167664
556	0.76	0.17	0.35	0.0170422
557	0.51	0.50	0.60	0.0167963
558	1.51	0.08	0.85	0.0169277
559	0.76	0.08	0.35	0.0166196
560	0.76	0.17	0.35	0.0170109
561	1.76	0.33	0.43	0.0170154
562	0.51	0.00	0.60	0.0174229
563	1.76	0.50	0.85	0.0168039
564	2.01	0.50	0.85	0.0167348
565	2.01	0.50	0.52	0.016932
566	0.76	0.17	0.85	0.016868
567	0.76	0.33	0.60	0.0166976
568	0.76	0.50	0.60	0.0166828
569	1.51	0.17	0.52	0.0171621
570	2.01	0.25	0.43	0.0169162
571	2.01	0.33	0.60	0.0170107
572	1.51	0.42	0.85	0.0168482
573	1.26	0.17	0.77	0.0169543
574	0.76	0.42	0.35	0.016679
575	2.01	0.00	0.85	0.0168847
576	0.51	0.42	0.85	0.016816
577	1.51	0.42	0.68	0.0169919
578	1.76	0.50	0.43	0.0169873
579	2.01	0.25	0.35	0.0167136
580	1.26	0.42	0.85	0.0168667
581	0.76	0.17	0.52	0.0169738
582	2.01	0.33	0.77	0.0168974

583	1.01	0.42	0.52	0.0169375
584	0.51	0.25	0.35	0.0167777
585	1.01	0.33	0.35	0.0170336
586	1.51	0.25	0.43	0.0174187
587	1.26	0.00	0.52	0.0168795
588	0.51	0.42	0.35	0.0172328
589	1.51	0.00	0.68	0.017129
590	1.26	0.17	0.60	0.0171242
591	2.01	0.42	0.85	0.0169105
592	2.01	0.00	0.60	0.0171214
593	0.76	0.50	0.77	0.0169348
594	0.76	0.33	0.60	0.0168252
595	2.01	0.50	0.43	0.017081
596	1.51	0.17	0.52	0.0171726
597	1.01	0.17	0.77	0.0169759
598	1.01	0.50	0.85	0.0168266
599	0.51	0.08	0.52	0.0172322
600	1.01	0.25	0.68	0.0169243
601	2.01	0.08	0.60	0.0169756
602	1.51	0.08	0.52	0.0170937
603	0.76	0.17	0.77	0.0169507
604	2.01	0.33	0.68	0.0168966
605	0.76	0.08	0.85	0.0169643
606	2.01	0.33	0.85	0.0168239
607	1.01	0.08	0.68	0.0169976
608	1.51	0.42	0.35	0.0170803
609	0.51	0.33	0.77	0.0168289
610	0.76	0.50	0.35	0.0168062
611	1.01	0.50	0.77	0.0168808
612	2.01	0.25	0.77	0.0169058
613	1.51	0.25	0.60	0.0171203
614	0.51	0.00	0.52	0.0172737
615	1.51	0.42	0.68	0.016902
616	0.51	0.08	0.35	0.0163608
617	1.76	0.17	0.35	0.0169651
618	1.01	0.17	0.43	0.0170106
619	1.76	0.33	0.52	0.0169983
620	0.51	0.42	0.68	0.0167444
621	1.01	0.25	0.43	0.0171249
622	1.76	0.33	0.35	0.0170097
623	0.51	0.08	0.68	0.0172442
624	1.26	0.33	0.35	0.0172169
625	1.26	0.17	0.35	0.0172434
626	1.01	0.42	0.85	0.016956
627	1.26	0.17	0.52	0.0170684
628	1.51	0.00	0.85	0.0169453
629	0.51	0.08	0.43	0.0171172
630	0.51	0.00	0.35	0.0161871
631	1.76	0.17	0.77	0.01698

632	0.76	0.17	0.85	0.0168714
633	1.26	0.00	0.52	0.0167719
634	1.26	0.42	0.68	0.0169499
635	1.01	0.08	0.85	0.016865
636	1.51	0.25	0.77	0.0168858
637	2.01	0.50	0.60	0.0168481
638	2.01	0.50	0.85	0.0167679
639	1.26	0.25	0.68	0.0169591
640	1.51	0.50	0.68	0.0168631
641	0.76	0.25	0.68	0.0168877
642	1.01	0.08	0.85	0.0168995
643	1.51	0.08	0.68	0.0169587
644	0.76	0.50	0.52	0.0166466
645	1.76	0.08	0.60	0.0170518
646	0.76	0.08	0.68	0.0172537
647	0.51	0.33	0.43	0.0170927
648	1.01	0.00	0.68	0.0169407
649	1.01	0.33	0.43	0.0169784
650	0.76	0.08	0.68	0.017271
651	1.26	0.08	0.43	0.0169064
652	2.01	0.33	0.43	0.0169972
653	0.76	0.17	0.52	0.0169789
654	2.01	0.08	0.77	0.0169728
655	0.76	0.00	0.68	0.017257
656	0.51	0.08	0.43	0.0170854
657	1.01	0.17	0.60	0.017004
658	0.76	0.50	0.85	0.01685
659	0.51	0.25	0.52	0.0171053
660	1.01	0.33	0.85	0.0168858
661	1.26	0.33	0.77	0.0169085
662	1.76	0.42	0.77	0.016818
663	2.01	0.42	0.43	0.0169834
664	0.76	0.17	0.60	0.0171136
665	0.51	0.00	0.35	0.0160781
666	0.76	0.50	0.68	0.0167049
667	1.26	0.50	0.68	0.0169032
668	1.76	0.50	0.60	0.0168894
669	1.76	0.33	0.85	0.0168365
670	2.01	0.25	0.60	0.0169163
671	1.26	0.25	0.52	0.0172139
672	2.01	0.33	0.52	0.0169513
673	1.76	0.17	0.68	0.0170433
674	1.01	0.17	0.85	0.0168335
675	1.51	0.42	0.77	0.0168302
676	2.01	0.42	0.60	0.0168929
677	0.51	0.00	0.68	0.0173211
678	1.51	0.17	0.68	0.0169515
679	2.01	0.25	0.85	0.016776
680	0.76	0.42	0.77	0.0167502

681	0.51	0.08	0.85	0.0169998
682	0.51	0.50	0.77	0.0166722
683	1.76	0.17	0.43	0.0170145
684	1.51	0.17	0.60	0.0170041
685	1.26	0.33	0.43	0.0171935
686	0.76	0.42	0.60	0.0166535
687	1.51	-0.33	0.52	0.0169879
688	1.51	-0.25	0.85	0.0166979
689	2.01	-0.17	0.60	0.0168807
690	0.51	-0.42	0.52	0.0170183
691	2.01	0.00	0.85	0.0167595
692	2.01	-0.25	0.85	0.0167769
693	1.01	-0.42	0.52	0.0167035
694	0.76	-0.25	0.60	0.0170685
695	1.26	-0.33	0.43	0.0171224
696	0.51	-0.25	0.52	0.0171123
697	0.51	-0.17	0.77	0.0169692
698	1.01	0.00	0.35	0.0167623
699	1.01	-0.50	0.52	0.0168383
700	2.01	-0.25	0.52	0.0169912
701	1.51	-0.50	0.43	0.0172157
702	0.51	-0.50	0.60	0.017031
703	0.51	-0.25	0.60	0.0171493
704	1.01	-0.33	0.68	0.0168039
705	2.01	0.00	0.43	0.0169074
706	0.76	-0.17	0.77	0.016989
707	0.51	-0.33	0.43	0.0168046
708	1.51	-0.42	0.35	0.0172923
709	1.51	-0.50	0.68	0.0167508
710	0.51	-0.08	0.35	0.0159197
711	1.51	-0.50	0.35	0.0173363
712	1.76	-0.25	0.35	0.01703
713	1.51	-0.25	0.60	0.0169996
714	1.51	0.00	0.43	0.0169341
715	0.51	-0.42	0.60	0.0170758
716	1.51	-0.17	0.68	0.0168127
717	1.51	-0.42	0.68	0.0167162
718	1.26	-0.25	0.68	0.016905
719	1.01	-0.33	0.52	0.0170095
720	2.01	-0.50	0.60	0.0168689
721	1.51	-0.42	0.52	0.0169325
722	1.51	0.00	0.35	0.0168808
723	0.76	0.00	0.52	0.0170528
724	0.76	-0.25	0.35	0.0162918
725	0.76	-0.17	0.43	0.0168123
726	0.51	-0.08	0.85	0.0169671
727	0.76	-0.50	0.52	0.0165922
728	0.51	-0.17	0.68	0.0171428
729	1.76	-0.17	0.60	0.0170235

730	2.01	-0.50	0.77	0.0168533
731	0.76	-0.33	0.68	0.0169414
732	2.01	-0.50	0.35	0.0169837
733	0.76	-0.33	0.85	0.0167413
734	2.01	-0.08	0.68	0.0168933
735	0.51	-0.42	0.60	0.0170594
736	2.01	-0.42	0.85	0.0167781
737	2.01	-0.25	0.77	0.0168158
738	1.76	-0.42	0.68	0.0167493
739	2.01	0.00	0.68	0.0168667
740	0.76	-0.25	0.35	0.016331
741	1.01	-0.33	0.85	0.01667
742	1.76	0.00	0.52	0.0168581
743	1.01	0.00	0.60	0.0169085
744	2.01	-0.17	0.52	0.016995
745	1.01	0.00	0.77	0.0169089
746	1.51	0.00	0.77	0.016847
747	2.01	-0.42	0.60	0.0168974
748	0.76	-0.17	0.60	0.0171701
749	2.01	-0.08	0.85	0.0168146
750	1.76	-0.33	0.52	0.0169325
751	1.51	-0.33	0.85	0.0167484
752	1.51	-0.42	0.60	0.0168175
753	1.51	-0.08	0.68	0.016892
754	0.76	-0.17	0.68	0.0170949
755	1.01	-0.08	0.35	0.0167912
756	2.01	-0.17	0.85	0.0168124
757	1.51	-0.17	0.85	0.0167442
758	1.01	-0.50	0.60	0.0167425
759	0.51	-0.42	0.77	0.0168203
760	1.76	0.00	0.77	0.0169106
761	0.51	-0.08	0.68	0.0172896
762	1.76	-0.17	0.77	0.0168636
763	0.76	-0.50	0.68	0.0165883
764	1.01	-0.50	0.43	0.0169426
765	1.01	-0.50	0.77	0.0166239
766	1.76	-0.17	0.52	0.016949
767	1.76	-0.33	0.35	0.0171069
768	1.76	-0.33	0.77	0.0168146
769	2.01	0.00	0.35	0.0164029
770	1.01	0.00	0.68	0.0168877
771	1.01	-0.17	0.68	0.0169908
772	1.76	-0.42	0.77	0.0168184
773	1.51	-0.33	0.43	0.0172012
774	1.26	0.00	0.77	0.0167955
775	1.76	-0.50	0.35	0.0172502
776	1.76	-0.42	0.60	0.0169146
777	1.51	0.00	0.85	0.0168486
778	1.51	-0.50	0.43	0.0171874

779	1.01	-0.17	0.52	0.0169525
780	1.51	-0.17	0.77	0.0168176
781	1.26	-0.08	0.85	0.0167369
782	0.76	-0.42	0.85	0.0166616
783	1.26	-0.33	0.35	0.016984
784	0.76	0.00	0.43	0.016717
785	0.51	-0.08	0.77	0.0171217
786	1.51	-0.42	0.35	0.0173259
787	1.76	-0.50	0.35	0.0172577
788	2.01	-0.08	0.68	0.0169037
789	1.51	0.00	0.68	0.016945
790	1.51	-0.08	0.85	0.0167982
791	2.01	-0.25	0.60	0.0169096
792	0.76	-0.50	0.35	0.0150694
793	1.26	-0.42	0.85	0.0167036
794	1.26	-0.33	0.60	0.0169614
795	1.51	-0.08	0.52	0.0168916
796	0.51	-0.25	0.68	0.0169161
797	2.01	-0.42	0.35	0.0169139
798	1.01	-0.42	0.85	0.0166357
799	1.51	-0.50	0.68	0.0166976
800	1.76	-0.25	0.77	0.0168027
801	1.01	-0.25	0.43	0.0168529
802	0.76	-0.50	0.85	0.0166087
803	0.76	0.00	0.35	0.0163239
~~804~~	~~0.76~~	~~-0.42~~	~~0.35~~	~~0.0149748~~
805	0.51	-0.50	0.60	0.0169839
806	2.01	-0.42	0.85	0.0167623
807	1.76	-0.50	0.85	0.016702
808	1.01	0.00	0.77	0.016837
809	0.76	-0.08	0.52	0.0169954
810	1.26	-0.25	0.52	0.0170476
811	1.26	-0.25	0.85	0.0168037
812	1.26	0.00	0.85	0.016805
813	1.01	-0.08	0.43	0.016781
814	2.01	-0.50	0.77	0.0167705
815	1.01	-0.08	0.77	0.0168851
816	1.76	-0.17	0.35	0.0169148
817	2.01	-0.50	0.43	0.0168906
818	1.76	-0.50	0.60	0.0168592
819	1.51	-0.25	0.35	0.0172954
820	1.01	-0.08	0.77	0.0169263
821	0.76	-0.08	0.68	0.017173
822	1.01	-0.42	0.68	0.0167067
823	0.51	-0.17	0.85	0.0169412
824	0.51	-0.33	0.60	0.0171043
825	1.76	-0.33	0.68	0.0168347
826	0.76	-0.42	0.60	0.0168614
827	1.01	-0.08	0.52	0.0169001

828	1.51	-0.42	0.85	0.0166991
829	1.76	-0.08	0.68	0.0169228
830	0.51	-0.25	0.43	0.0166738
831	1.51	0.00	0.52	0.016884
832	1.51	-0.42	0.60	0.0167693
833	1.01	-0.50	0.68	0.0166281
834	2.01	-0.17	0.35	0.0168355
835	0.76	-0.33	0.68	0.0169545
836	0.76	-0.08	0.35	0.0163215
837	0.51	-0.33	0.68	0.0169577
838	0.51	-0.33	0.77	0.0168423
839	1.01	-0.25	0.52	0.0170413
840	1.76	-0.42	0.35	0.0171836
841	2.01	-0.42	0.60	0.0169014
842	1.01	-0.17	0.35	0.0167427
843	1.51	-0.25	0.77	0.0168109
844	1.26	-0.17	0.52	0.0170685
845	1.01	0.00	0.85	0.0167566
846	0.76	-0.33	0.85	0.0166885
847	1.51	-0.50	0.35	0.017372
848	0.76	-0.08	0.85	0.0169084
849	1.26	-0.17	0.60	0.0169689
850	1.26	-0.08	0.35	0.0169519
851	1.01	-0.42	0.43	0.0169091
852	1.26	0.00	0.35	0.016949
853	0.51	-0.25	0.43	0.0167219
854	1.51	-0.08	0.60	0.01698
855	1.01	-0.50	0.35	0.0171498
856	1.76	-0.42	0.68	0.0168253
857	1.51	-0.17	0.77	0.0167821
858	1.26	-0.33	0.52	0.0172021
859	2.01	-0.33	0.77	0.016864
860	2.01	-0.25	0.85	0.0168629
861	1.76	-0.08	0.43	0.0167941
862	0.76	-0.50	0.35	0.0150301
863	1.01	-0.17	0.43	0.0168528
864	1.51	-0.25	0.60	0.0169543
865	2.01	-0.08	0.60	0.0169328
866	1.51	-0.50	0.60	0.0168313
867	1.26	-0.08	0.52	0.0168337
868	1.01	-0.08	0.68	0.0169457
869	0.76	-0.17	0.85	0.0168322
870	1.51	-0.33	0.35	0.0173207
871	0.51	-0.33	0.35	0.0158484
872	0.51	0.00	0.43	0.0166387
873	0.51	-0.25	0.68	0.0169383
874	1.51	-0.42	0.43	0.0170958
875	1.26	-0.42	0.68	0.0167245
876	1.51	-0.33	0.68	0.0167625

877	0.51	-0.50	0.35	0.0164207
878	2.01	-0.17	0.77	0.0167378
879	1.01	-0.25	0.68	0.0167157
880	1.26	0.00	0.60	0.0166299
881	1.76	-0.50	0.85	0.0166282
882	1.51	-0.50	0.60	0.0167502
883	1.26	-0.50	0.77	0.0165934
884	1.01	0.00	0.43	0.0166209
885	1.26	-0.50	0.52	0.0168476
886	0.76	-0.50	0.85	0.0164981
887	1.01	-0.42	0.35	0.0169252
888	2.01	-0.50	0.85	0.016711
889	1.76	-0.17	0.68	0.0168588
890	1.51	0.00	0.68	0.0168657
891	1.26	-0.25	0.60	0.0169753
892	2.01	-0.33	0.85	0.0167457
893	0.51	0.00	0.43	0.0167427
894	1.01	-0.08	0.68	0.0169168
895	0.51	-0.17	0.35	0.0156686
896	1.26	-0.08	0.43	0.0167403
897	0.51	0.00	0.68	0.0172505
898	0.51	-0.08	0.52	0.0171861
899	1.76	-0.33	0.68	0.0167883
900	1.76	-0.50	0.68	0.0167291
901	1.01	-0.17	0.77	0.0167977
902	2.01	-0.17	0.60	0.0168703
903	1.01	0.00	0.68	0.016839
904	1.76	-0.08	0.85	0.0167487
905	0.76	-0.33	0.52	0.0169634
906	0.76	-0.50	0.77	0.0166151
907	1.51	-0.17	0.52	0.0170092
908	1.76	-0.33	0.60	0.0168369
909	1.76	-0.08	0.77	0.0168485
910	1.26	-0.33	0.68	0.0168333
911	1.26	-0.50	0.77	0.0166733
912	2.01	-0.25	0.68	0.0168181
913	0.51	-0.25	0.35	0.0155112
914	0.76	-0.08	0.52	0.0169905
915	2.01	-0.50	0.43	0.0168057
916	1.51	-0.08	0.35	0.0169033
917	2.01	-0.25	0.43	0.0170582
918	0.76	-0.42	0.68	0.0166338
919	2.01	-0.33	0.43	0.0168661
920	0.51	0.00	0.35	0.0159987
921	2.01	0.00	0.43	0.0168693
922	1.26	0.00	0.68	0.0168095
923	0.76	-0.08	0.77	0.0170367
924	2.01	-0.17	0.85	0.0168067
925	1.26	-0.50	0.85	0.0167184

926	1.01	-0.50	0.60	0.0167246
927	1.01	-0.08	0.85	0.0167062
928	0.76	-0.33	0.35	0.0159106
929	2.01	-0.33	0.35	0.0169408
930	0.76	-0.17	0.52	0.0170968
931	1.51	-0.08	0.52	0.0170049
932	0.51	-0.17	0.52	0.0172562
933	1.01	-0.25	0.85	0.0167753
934	1.76	-0.25	0.43	0.0170892
935	1.76	0.00	0.68	0.0170381
936	1.76	-0.42	0.43	0.0170412
937	0.76	-0.33	0.77	0.0168002
938	1.26	-0.50	0.35	0.0174332
939	1.26	-0.17	0.68	0.016924
940	1.26	-0.17	0.68	0.0168771
941	1.76	0.00	0.60	0.0170077
942	1.51	-0.33	0.35	0.0172804
943	1.01	-0.08	0.35	0.0167886
944	1.76	-0.25	0.60	0.0169415
945	1.76	-0.25	0.68	0.0168761
946	1.76	-0.25	0.85	0.0167896
947	1.26	-0.08	0.85	0.0167355
948	0.51	-0.25	0.77	0.0168488
949	1.26	-0.25	0.52	0.0170401
950	1.01	-0.50	0.35	0.0170795
951	1.26	-0.25	0.77	0.0168054
952	1.01	-0.42	0.35	0.0170794
953	2.01	-0.17	0.68	0.0168815
954	0.51	-0.08	0.68	0.0172372
955	1.01	-0.42	0.85	0.0166436
956	1.76	-0.17	0.43	0.0169298
957	0.76	-0.17	0.43	0.0167954
958	2.01	-0.08	0.35	0.0165532
959	0.76	0.00	0.68	0.0172168
960	2.01	0.00	0.60	0.0169661
961	1.76	-0.42	0.85	0.0168007
962	0.51	-0.33	0.52	0.017132
963	1.26	0.00	0.85	0.0168344
964	1.01	-0.25	0.35	0.01701
965	1.51	-0.50	0.52	0.0170318
966	1.26	-0.42	0.52	0.0169515
967	1.51	-0.17	0.35	0.017191
968	1.51	-0.17	0.68	0.0168913
969	1.01	-0.25	0.35	0.0168982
970	1.26	-0.17	0.85	0.0167746
971	2.01	-0.25	0.60	0.0169414
972	1.51	-0.33	0.85	0.0167535
973	1.76	-0.42	0.52	0.016903
974	1.01	0.00	0.85	0.0167705

975	0.51	-0.08	0.77	0.017098
976	1.76	0.00	0.77	0.0169044
977	0.76	-0.50	0.43	0.0168242
978	1.51	-0.33	0.52	0.016993
979	0.76	-0.42	0.43	0.0169046
980	0.76	-0.42	0.68	0.0166217
981	0.51	0.00	0.60	0.0173314
982	1.01	-0.08	0.85	0.0166718
983	0.51	-0.50	0.52	0.0169574
984	0.51	-0.17	0.77	0.0169291
985	0.76	-0.08	0.35	0.0163027
986	0.51	-0.42	0.68	0.0169098
987	0.51	-0.25	0.77	0.0168034
988	0.76	0.00	0.52	0.0169523
989	0.76	0.00	0.35	0.0162933
990	0.51	-0.08	0.35	0.0158244
991	1.76	-0.50	0.68	0.0166773
992	0.76	-0.25	0.43	0.0167207
993	1.26	-0.50	0.68	0.0166824
994	1.51	-0.42	0.85	0.0166558
995	1.01	-0.50	0.68	0.016609
996	1.26	-0.42	0.35	0.0171948
997	0.76	0.00	0.77	0.0170292
998	1.76	-0.08	0.85	0.0167651
999	0.76	-0.33	0.52	0.0169284
1000	1.01	-0.25	0.60	0.0170501
1001	1.26	-0.42	0.43	0.0171273
1002	1.26	-0.42	0.60	0.0168708
1003	0.51	-0.50	0.43	0.016963
1004	1.01	-0.42	0.60	0.0166472
1005	0.76	-0.50	0.43	0.0168037
1006	0.76	-0.08	0.43	0.0166885
1007	0.76	-0.08	0.60	0.0171756
1008	1.01	-0.33	0.43	0.0170623
1009	1.51	0.00	0.60	0.016995
1010	0.76	-0.08	0.43	0.0167974
1011	1.76	-0.33	0.43	0.0170212
1012	0.51	-0.50	0.43	0.0169898
1013	0.51	-0.50	0.77	0.0167404
1014	0.51	0.00	0.35	0.0160105
1015	1.26	0.00	0.68	0.0167052
1016	1.01	-0.33	0.60	0.0168351
1017	0.51	-0.33	0.85	0.0168177
1018	2.01	-0.17	0.43	0.0170243
1019	1.76	-0.25	0.85	0.0167834
1020	1.76	-0.42	0.60	0.0167637
1021	2.01	0.00	0.85	0.0167438
1022	1.76	0.00	0.60	0.0169044
1023	0.51	-0.50	0.85	0.0166895

1024	1.76	-0.17	0.52	0.017023
1025	1.01	-0.33	0.43	0.017125
1026	0.76	-0.17	0.35	0.0163375
1027	0.51	-0.33	0.43	0.0168377
1028	1.01	-0.17	0.60	0.0170471
1029	1.76	-0.33	0.77	0.0168043
1030	2.01	-0.33	0.43	0.0169537
1031	1.51	-0.25	0.52	0.0170272
1032	0.51	-0.42	0.43	0.0168843
1033	2.01	-0.42	0.77	0.0167764
1034	1.01	-0.33	0.35	0.0168697
1035	0.76	-0.33	0.43	0.0168357
1036	1.01	-0.17	0.43	0.016829
1037	0.76	-0.25	0.85	0.0167251
1038	1.26	-0.50	0.43	0.0171574
1039	1.51	-0.08	0.77	0.0167896
1040	1.51	-0.50	0.85	0.0166787
1041	0.76	0.00	0.43	0.0167225
1042	2.01	-0.08	0.77	0.0168106
1043	1.51	-0.42	0.77	0.0167221
1044	1.26	-0.33	0.68	0.0168623
1045	1.01	-0.33	0.77	0.0167314
1046	1.26	-0.50	0.60	0.0168208
1047	2.01	-0.50	0.68	0.0167547
1048	1.26	-0.33	0.35	0.0169509
1049	2.01	-0.50	0.68	0.0167343
1050	1.51	-0.08	0.35	0.016929
1051	1.76	-0.33	0.85	0.0167267
1052	1.01	-0.17	0.60	0.0170178
1053	1.76	-0.50	0.52	0.016824
1054	0.51	-0.17	0.43	0.0165602
1055	1.26	0.00	0.35	0.0169045
1056	1.01	-0.42	0.60	0.0167099
1057	2.01	-0.42	0.52	0.0168954
1058	2.01	-0.17	0.68	0.0168425
1059	0.76	-0.33	0.77	0.0167519
1060	2.01	-0.17	0.43	0.0170454
1061	0.51	-0.25	0.35	0.0155656
1062	1.76	-0.25	0.52	0.0169587
1063	1.51	-0.08	0.85	0.0167088
1064	1.51	-0.50	0.85	0.0166446
1065	0.51	-0.33	0.77	0.0167875
1066	0.76	-0.50	0.52	0.0165558
1067	1.51	-0.08	0.68	0.016814
1068	1.01	-0.50	0.85	0.0166132
1069	1.01	-0.25	0.85	0.0166642
1070	0.51	-0.33	0.85	0.0167789
1071	1.76	-0.50	0.52	0.0167997
1072	1.01	-0.33	0.77	0.0166579

1073	1.51	0.00	0.52	0.016919
1074	0.76	-0.17	0.68	0.0170763
1075	1.76	-0.25	0.43	0.0170447
1076	0.51	-0.08	0.43	0.0166272
1077	1.51	-0.08	0.43	0.0169365
1078	0.51	-0.42	0.85	0.0167805
1079	0.76	-0.42	0.60	0.0168555
1080	1.76	-0.25	0.35	0.0170845
1081	2.01	-0.08	0.43	0.0170404
1082	1.51	-0.33	0.43	0.0172508
1083	0.51	-0.25	0.52	0.017193
1084	1.26	-0.08	0.68	0.0168433
1085	1.51	-0.25	0.43	0.017188
1086	2.01	-0.08	0.85	0.0168459
1087	1.26	-0.50	0.68	0.0167897
1088	1.01	-0.17	0.52	0.0170475
1089	0.51	-0.08	0.60	0.0175112
1090	1.26	-0.08	0.60	0.0168519
1091	0.51	0.00	0.77	0.0171897
1092	1.26	0.00	0.60	0.016802
1093	2.01	-0.33	0.60	0.0168741
1094	1.76	0.00	0.68	0.0169655
1095	0.76	-0.33	0.43	0.0168805
1096	1.26	-0.50	0.60	0.0168535
1097	0.76	-0.33	0.60	0.0169652
1098	2.01	0.00	0.52	0.0170219
1099	0.76	-0.25	0.60	0.0170795
1100	2.01	-0.33	0.60	0.0168789
1101	1.51	0.00	0.85	0.0167875
1102	1.76	-0.08	0.35	0.0166438
1103	2.01	0.00	0.77	0.016878
1104	0.76	-0.42	0.43	0.0169447
1105	2.01	-0.33	0.68	0.0168504
1106	1.26	-0.42	0.85	0.0167121
1107	1.51	-0.25	0.68	0.0168222
1108	1.51	-0.25	0.35	0.0172006
1109	1.26	-0.50	0.52	0.0169244
1110	0.51	-0.42	0.43	0.0168586
1111	1.26	-0.17	0.77	0.0167309
1112	1.76	-0.33	0.60	0.016773
1113	1.26	-0.25	0.43	0.0169141
1114	0.51	-0.42	0.35	0.0162031
1115	1.76	-0.33	0.43	0.0169103
1116	1.01	-0.25	0.52	0.0169426
1117	1.76	-0.08	0.43	0.0167258
1118	1.26	-0.17	0.43	0.0170051
1119	1.76	-0.17	0.43	0.016967
1120	1.01	-0.17	0.85	0.0167125
1121	2.01	-0.42	0.43	0.0169467

1122	2.01	-0.33	0.35	0.0169706
1123	1.26	-0.50	0.85	0.0167106
1124	1.01	-0.42	0.77	0.0167346
1125	1.01	-0.50	0.52	0.0169042
1126	1.26	-0.42	0.60	0.0169028
1127	1.76	-0.17	0.35	0.0169172
1128	2.01	-0.25	0.35	0.0168858
1129	0.51	0.00	0.85	0.0170691
1130	1.76	-0.50	0.77	0.0167612
1131	1.26	-0.42	0.77	0.0167537
1132	0.51	-0.50	0.85	0.0167036
1133	0.51	-0.50	0.77	0.0167482
1134	1.51	-0.17	0.43	0.0170766
1135	1.01	-0.33	0.35	0.0169956
1136	1.51	-0.25	0.52	0.017081
1137	1.26	-0.08	0.77	0.0167458
1138	1.01	-0.25	0.77	0.0167245
1139	2.01	0.00	0.60	0.0169213
1140	2.01	-0.33	0.52	0.0169252
1141	0.76	-0.50	0.68	0.0166183
1142	2.01	-0.50	0.85	0.0167485
1143	0.76	-0.08	0.60	0.0172464
1144	2.01	-0.33	0.52	0.0169149
1145	0.51	-0.42	0.68	0.0169433
1146	0.76	-0.50	0.60	0.0165755
1147	2.01	-0.08	0.77	0.0168201
1148	1.76	0.00	0.43	0.0167373
1149	1.26	-0.25	0.60	0.0170245
1150	0.51	-0.08	0.60	0.0174298
1151	1.76	-0.50	0.77	0.0167547
1152	1.51	-0.50	0.77	0.0166955
1153	0.76	0.00	0.68	0.0171287
1154	1.76	-0.42	0.52	0.0168363
1155	1.01	-0.17	0.68	0.0170377
1156	2.01	-0.50	0.52	0.0168623
1157	0.51	0.00	0.60	0.0173382
1158	1.76	-0.17	0.85	0.0167423
1159	1.76	-0.33	0.85	0.0166863
1160	0.76	-0.25	0.52	0.0169589
1161	1.01	-0.25	0.60	0.0169837
1162	1.76	-0.17	0.85	0.0167611
1163	2.01	-0.25	0.77	0.0167942
1164	2.01	-0.08	0.52	0.0169692
1165	0.51	0.00	0.77	0.017156
1166	0.76	-0.42	0.77	0.0166175
1167	0.76	0.00	0.85	0.0168684
1168	0.76	0.00	0.60	0.017238
1169	2.01	-0.33	0.77	0.016832
1170	2.01	0.00	0.68	0.0168948

1171	0.51	0.00	0.85	0.0170361
1172	1.76	-0.50	0.43	0.0169785
1173	0.51	-0.42	0.77	0.0167859
1174	1.26	-0.08	0.43	0.0168307
1175	1.76	-0.08	0.52	0.0168592
1176	1.51	0.00	0.77	0.0168218
1177	0.51	-0.17	0.43	0.016569
1178	1.26	-0.25	0.35	0.0169376
1179	0.76	-0.42	0.35	0.0150262
1180	1.26	-0.25	0.43	0.0169508
1181	1.51	-0.17	0.85	0.016757
1182	1.26	-0.33	0.77	0.0168032
1183	1.01	-0.50	0.85	0.0166849
1184	1.76	-0.08	0.68	0.0169927
1185	1.26	-0.42	0.68	0.0167758
1186	2.01	-0.42	0.68	0.0168308
1187	1.51	-0.08	0.43	0.0168862
1188	1.76	-0.25	0.77	0.0168039
1189	1.26	-0.33	0.85	0.0167543
1190	1.51	0.00	0.43	0.016814
1191	2.01	-0.33	0.68	0.016833
1192	1.01	-0.33	0.85	0.0166646
1193	0.76	-0.08	0.85	0.0168635
1194	0.51	-0.17	0.35	0.0157144
1195	1.26	-0.25	0.35	0.016841
1196	1.26	0.00	0.77	0.016708
1197	2.01	-0.08	0.52	0.0169929
1198	1.51	-0.42	0.52	0.01691
1199	1.76	-0.08	0.35	0.0166142
1200	1.76	-0.50	0.43	0.0170115
1201	1.26	-0.08	0.52	0.016857
1202	1.01	-0.33	0.60	0.0168441
1203	2.01	-0.42	0.68	0.0167817
1204	0.76	-0.25	0.77	0.0168441
1205	0.51	-0.17	0.60	0.0173157
1206	1.01	0.00	0.52	0.0168701
1207	2.01	0.00	0.77	0.0168527
1208	1.51	-0.17	0.52	0.0171127
1209	1.01	-0.17	0.35	0.0168217
1210	1.01	-0.50	0.77	0.0166613
1211	2.01	-0.25	0.35	0.0168695
1212	1.76	-0.33	0.35	0.0171578
1213	0.76	-0.33	0.60	0.017073
1214	0.76	-0.25	0.43	0.016905
1215	2.01	-0.50	0.52	0.0169392
1216	0.76	-0.25	0.85	0.0167923
1217	1.26	-0.33	0.52	0.0172077
1218	1.51	-0.42	0.68	0.0168083
1219	1.51	-0.25	0.85	0.0167512

1220	1.26	-0.25	0.77	0.0168157
1221	0.76	-0.25	0.52	0.017021
1222	0.51	-0.25	0.85	0.016818
1223	1.51	0.00	0.60	0.01698
1224	1.26	0.00	0.43	0.0167279
1225	0.76	-0.17	0.77	0.0169689
1226	2.01	-0.25	0.52	0.016977
1227	0.51	-0.33	0.60	0.0170763
1228	1.51	-0.08	0.77	0.0167594
1229	1.76	-0.25	0.52	0.0169815
1230	1.26	-0.33	0.85	0.0167394
1231	1.26	0.00	0.52	0.0166597
1232	1.01	-0.08	0.52	0.0169092
1233	1.26	-0.08	0.35	0.0169591
1234	0.76	0.00	0.60	0.0173117
1235	0.76	-0.42	0.52	0.0169384
1236	0.76	0.00	0.85	0.0169405
1237	1.26	-0.17	0.43	0.0170697
1238	1.01	-0.17	0.77	0.0168743
1239	1.01	-0.25	0.68	0.0169437
1240	2.01	-0.42	0.35	0.0170113
1241	1.26	-0.08	0.68	0.0168956
1242	1.76	-0.17	0.60	0.0170456
1243	1.51	-0.17	0.35	0.0172517
1244	2.01	-0.42	0.52	0.0169214
1245	1.26	-0.25	0.85	0.016803
1246	1.01	-0.08	0.43	0.0168517
1247	0.76	-0.50	0.77	0.0166929
1248	1.01	-0.08	0.60	0.0170608
1249	0.76	-0.42	0.52	0.0169741
1250	1.26	-0.25	0.68	0.0169797
1251	0.51	-0.42	0.35	0.01631
1252	2.01	-0.17	0.35	0.0168135
1253	1.51	0.00	0.35	0.0169272
1254	1.01	-0.42	0.52	0.0167672
1255	0.51	-0.33	0.35	0.0159103
1256	1.76	-0.42	0.77	0.0167427
1257	0.76	-0.17	0.85	0.0167691
1258	0.51	-0.08	0.85	0.0168413
1259	0.76	-0.42	0.77	0.0165359
1260	0.76	-0.25	0.77	0.0167823
1261	1.51	-0.33	0.60	0.0167992
1262	0.51	-0.50	0.68	0.0167641
1263	1.01	-0.08	0.60	0.0169031
1264	1.01	-0.42	0.43	0.0168222
1265	1.51	-0.08	0.60	0.0168865
1266	0.51	-0.25	0.60	0.0171314
1267	0.76	-0.17	0.52	0.0171089
1268	1.76	-0.33	0.52	0.0169387

1269	1.51	-0.33	0.77	0.0167969
1270	2.01	-0.25	0.68	0.016892
1271	0.51	0.00	0.52	0.0172238
1272	1.26	-0.50	0.35	0.0173721
1273	1.01	-0.42	0.77	0.0166948
1274	0.51	-0.17	0.85	0.0168726
1275	0.51	-0.42	0.85	0.0167264
1276	0.51	-0.25	0.85	0.0168026
1277	1.01	-0.33	0.68	0.0167213
1278	1.51	-0.25	0.68	0.0167898
1279	1.51	-0.42	0.77	0.0166729
1280	0.51	-0.33	0.52	0.0170238
1281	2.01	-0.08	0.60	0.0168644
1282	2.01	-0.50	0.60	0.0167657
1283	1.01	-0.33	0.52	0.0170142
1284	1.76	-0.50	0.60	0.0167363
1285	1.26	-0.42	0.52	0.0168515
1286	1.26	-0.33	0.77	0.016739
1287	0.51	0.00	0.68	0.0172086
1288	1.01	0.00	0.43	0.0166847
1289	0.51	-0.08	0.52	0.0171979
1290	1.01	-0.17	0.85	0.0166967
1291	1.76	-0.17	0.77	0.0168339
1292	1.76	-0.08	0.60	0.0169505
1293	1.51	-0.50	0.52	0.0169335
1294	0.76	0.00	0.77	0.0170331
1295	1.76	-0.42	0.85	0.016746
1296	1.76	0.00	0.85	0.0167787
1297	1.01	-0.25	0.43	0.0169782
1298	1.76	0.00	0.43	0.0168092
1299	1.76	-0.08	0.52	0.0169286
1300	1.01	-0.25	0.77	0.0167715
1301	2.01	0.00	0.52	0.0170454
1302	1.76	-0.08	0.60	0.0170045
1303	2.01	-0.17	0.52	0.017029
1304	1.76	-0.42	0.35	0.0172026
1305	0.76	-0.17	0.35	0.0163955
1306	0.51	-0.50	0.35	0.0165058
1307	0.51	-0.17	0.68	0.0170883
1308	1.26	-0.17	0.85	0.01667
1309	1.01	-0.50	0.43	0.0168468
1310	2.01	-0.42	0.77	0.0167048
1311	0.76	-0.25	0.68	0.0169366
1312	1.26	-0.08	0.77	0.0166344
1313	1.26	-0.08	0.60	0.0166913
1314	2.01	-0.08	0.43	0.0169013
1315	1.76	0.00	0.35	0.0165069
1316	1.76	-0.25	0.68	0.016812
1317	1.51	-0.50	0.77	0.016729

1318	1.26	-0.17	0.52	0.0170424
1319	0.76	-0.08	0.68	0.0171832
1320	0.51	-0.08	0.43	0.0166066
1321	2.01	-0.33	0.85	0.0168279
1322	0.76	-0.08	0.77	0.01703
1323	1.76	-0.17	0.68	0.0169247
1324	2.01	-0.25	0.43	0.0170518
1325	1.51	-0.42	0.43	0.0170744
1326	0.51	-0.33	0.68	0.0169202
1327	0.76	-0.33	0.35	0.0160491
1328	1.26	-0.33	0.60	0.0169516
1329	0.76	-0.25	0.68	0.0169304
1330	2.01	-0.42	0.43	0.0168452
1331	1.51	-0.33	0.77	0.0167042
1332	1.76	0.00	0.52	0.0168889
1333	1.51	-0.17	0.60	0.0169159
1334	1.51	-0.25	0.43	0.0171276
1335	1.26	-0.42	0.77	0.0166959
1336	1.26	-0.42	0.43	0.0170223
1337	1.26	0.00	0.43	0.0167774
1338	1.01	0.00	0.60	0.0168974
1339	1.01	-0.42	0.68	0.0167134
1340	1.76	-0.08	0.77	0.0168891
1341	1.76	0.00	0.85	0.0168331
1342	1.26	-0.17	0.60	0.0169416
1343	2.01	-0.17	0.77	0.0168592
1344	1.76	-0.42	0.43	0.0170174
1345	1.26	0.00	0.52	0.0167449
1346	1.26	-0.17	0.77	0.0167919
1347	1.26	-0.42	0.35	0.0172887
1348	1.01	0.00	0.52	0.0168633
1349	1.76	0.00	0.35	0.0166066
1350	2.01	0.00	0.35	0.0164626
1351	1.26	-0.33	0.43	0.0171864
1352	2.01	-0.50	0.35	0.0170307
1353	1.26	-0.50	0.43	0.0171995
1354	1.51	-0.17	0.43	0.0171713
1355	0.76	-0.42	0.85	0.0166787
1356	0.51	-0.42	0.52	0.0170871
1357	1.51	-0.25	0.77	0.0167903
1358	0.51	-0.50	0.52	0.0170125
1359	1.01	0.00	0.35	0.0168062
1360	1.51	-0.17	0.60	0.0169877
1361	0.51	0.00	0.52	0.0171247
1362	1.51	-0.33	0.68	0.0167229
1363	0.76	-0.50	0.60	0.0165768
1364	1.76	-0.25	0.60	0.0169262
1365	0.76	-0.17	0.60	0.017121
1366	0.51	-0.50	0.68	0.0168655

1367	1.51	-0.33	0.60	0.0168958
1368	1.26	-0.17	0.35	0.0170684
1369	0.51	-0.17	0.52	0.0172444
1370	0.51	-0.17	0.60	0.01731
1371	1.26	-0.17	0.35	0.0171081
1372	2.01	-0.08	0.35	0.016588

APPENDIX F: Thrust Coefficient Surface Plots for Near Deck Survey

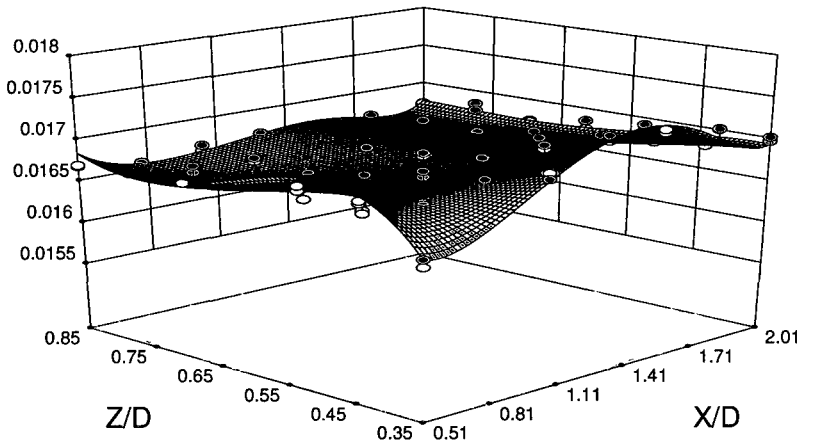

Figure 120: Surface plot of thrust coefficient for Y/D=-0.5

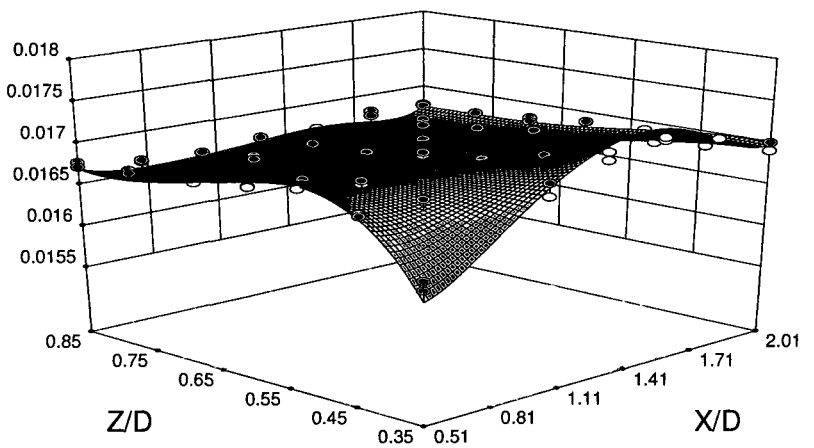

Figure 121: Surface plot of thrust coefficient for Y/D=-0.4165

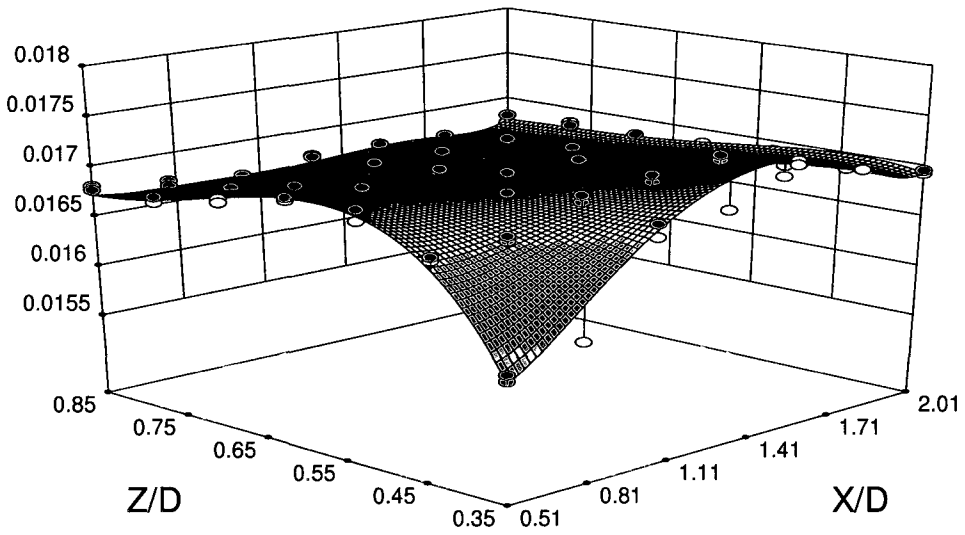

Figure 122: Surface plot of thrust coefficient for Y/D=-0.3333

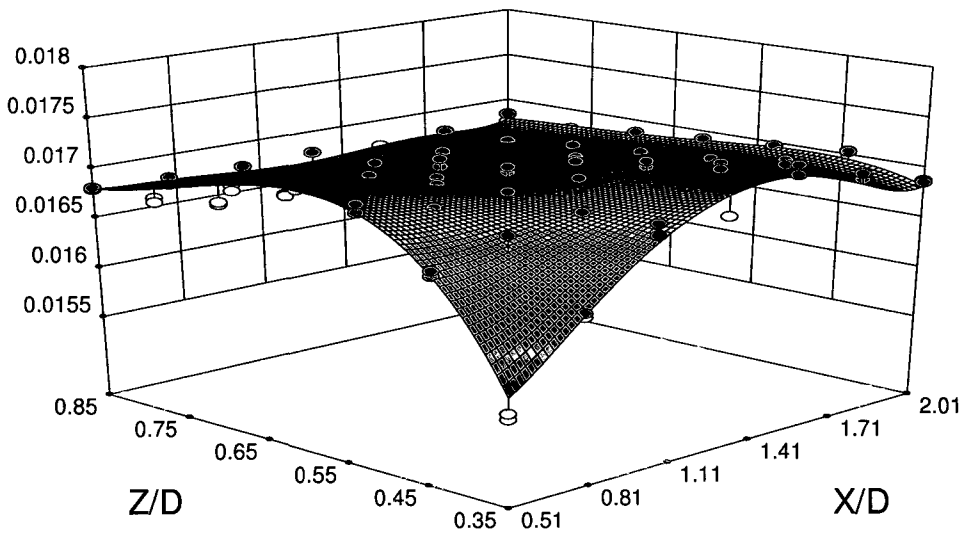

Figure 123: Surface plot of thrust coefficient for Y/D=-0.25

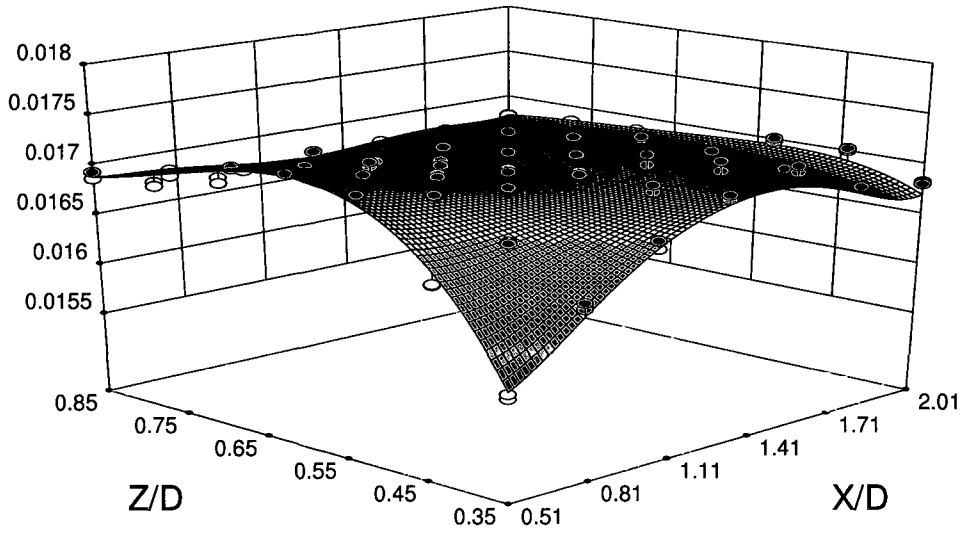

Figure 124: Surface plot of thrust coefficient for Y/D=-0.1667

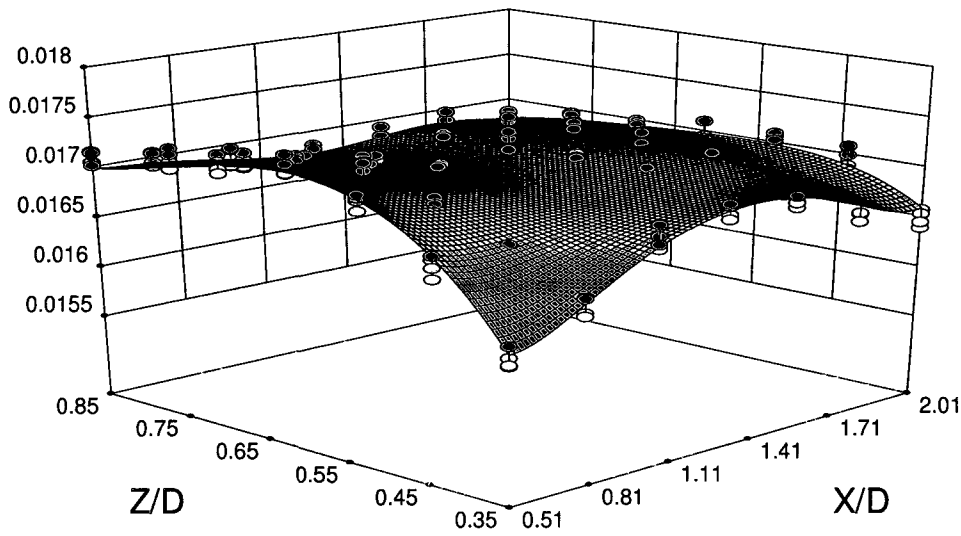

Figure 125: Surface plot of thrust coefficient for Y/D=0.0

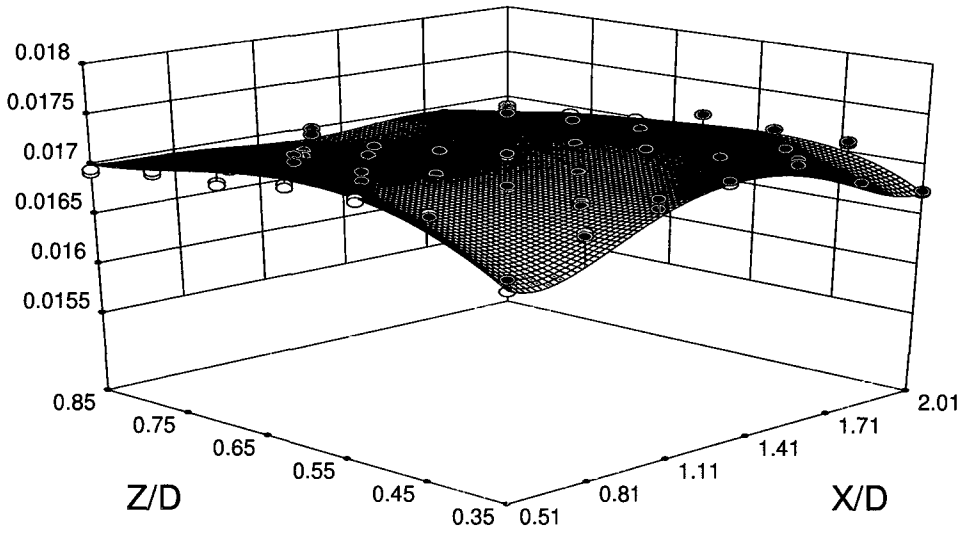

Figure 126: Surface plot of thrust coefficient for Y/D=0.1667

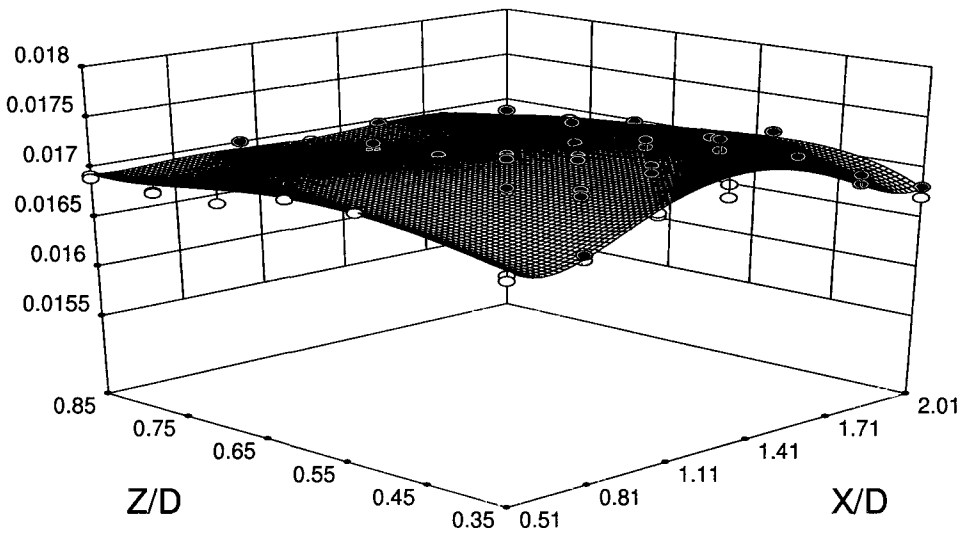

Figure 127: Surface plot of thrust coefficient for Y/D=0.25

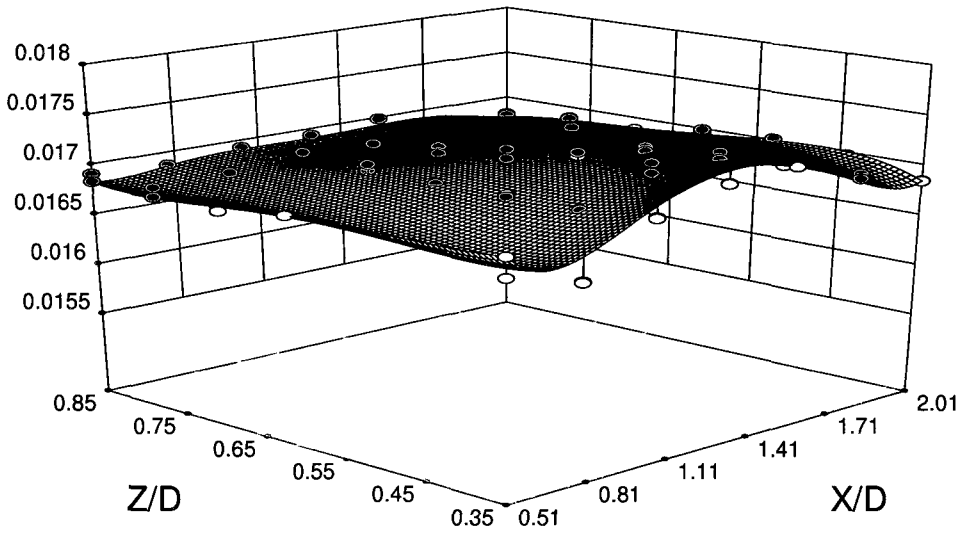

Figure 128: Surface plot of thrust coefficient for Y/D=0.3333

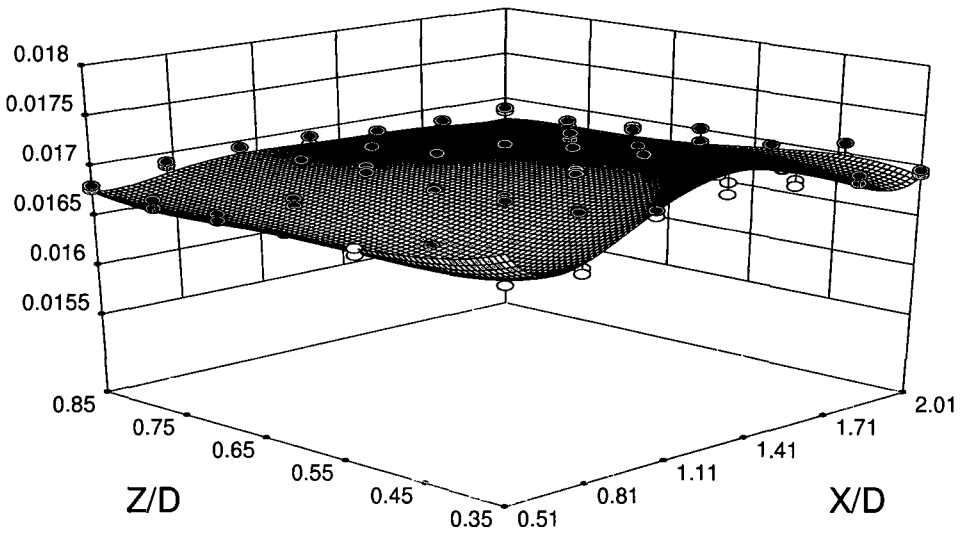

Figure 129: Surface plot of thrust coefficient for Y/D=0.4165

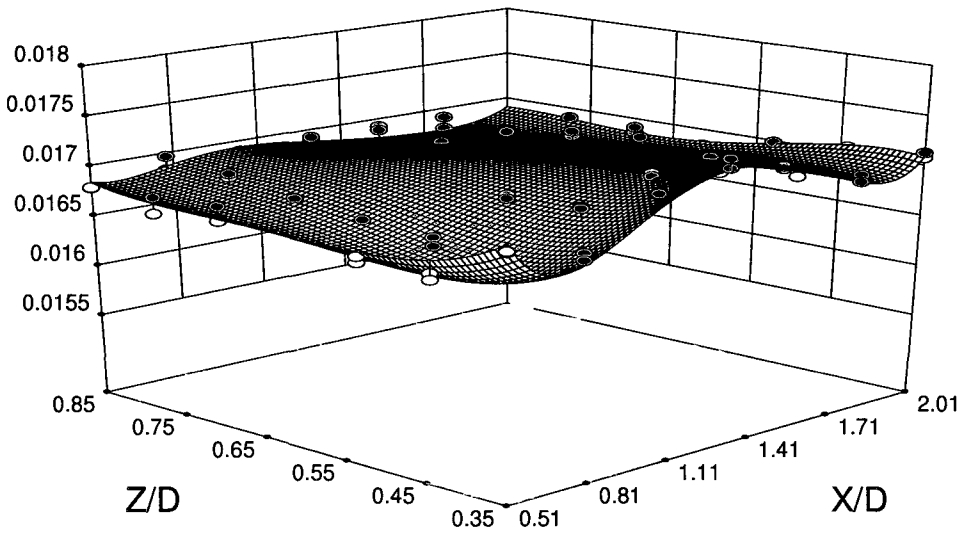

Figure 130: Surface plot of thrust coefficient for Y/D=0.5

APPENDIX G: Thrust Coefficient Contours for Near Deck Survey

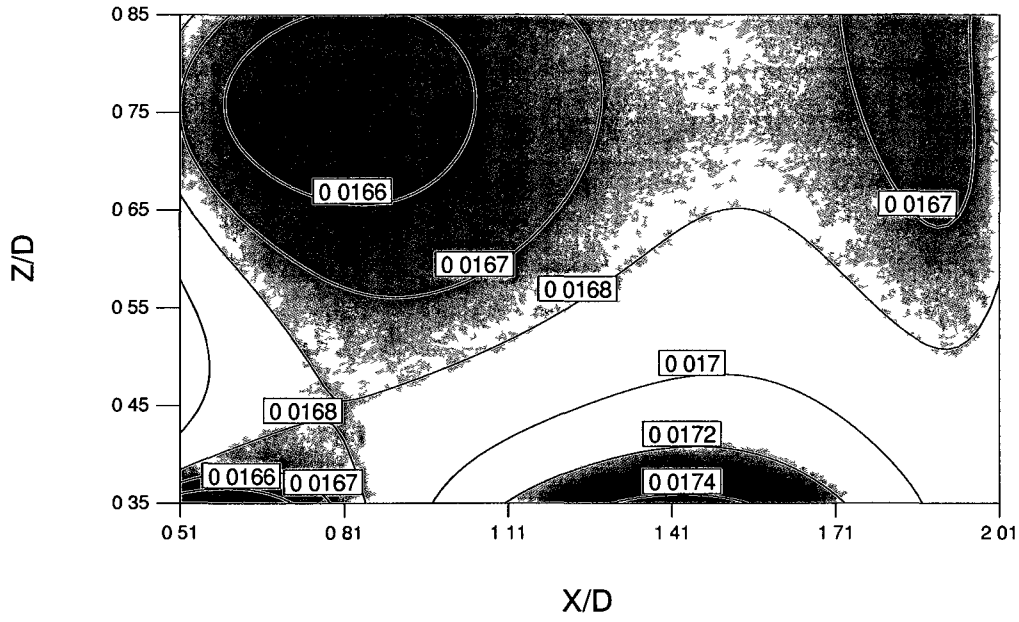

Figure 131: Thrust coefficient contours for rotor location of Y/D=-0.5

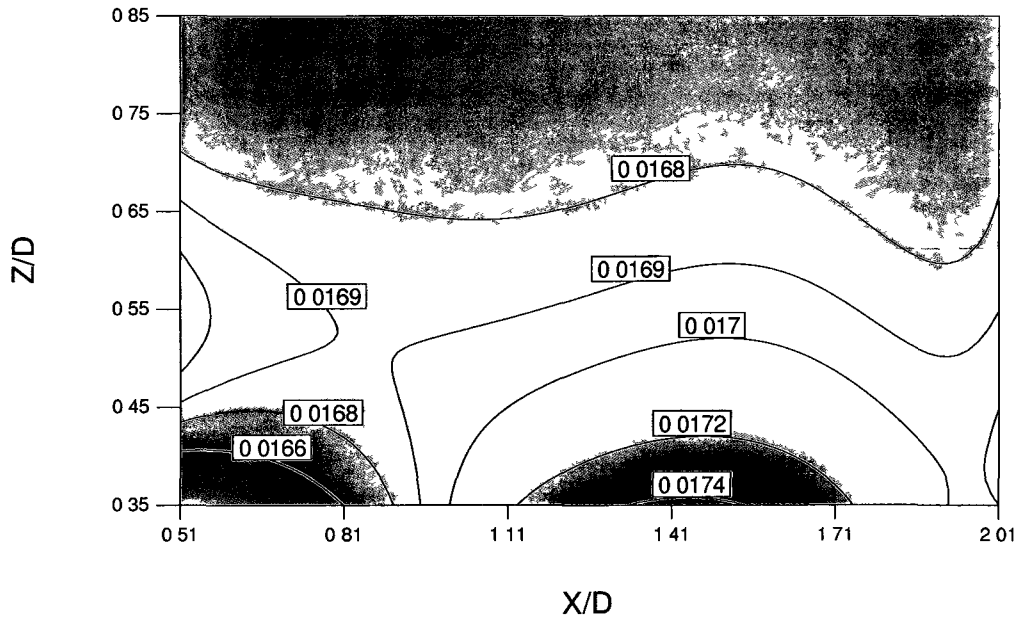

Figure 132 Thrust coefficient contours for rotor location of Y/D=-0.4

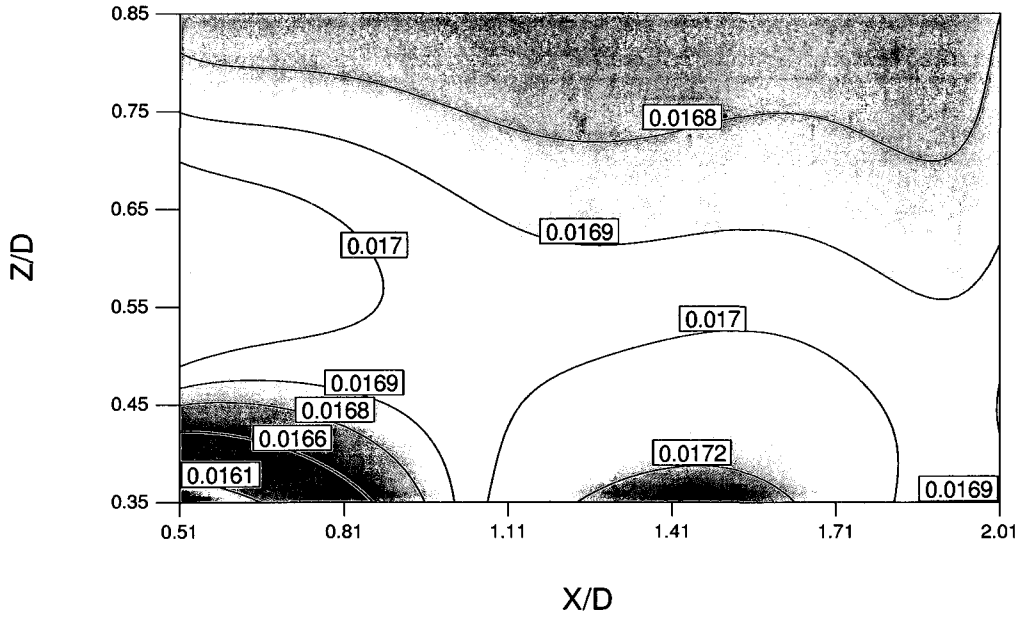

Figure 133: Thrust coefficient contours for rotor location of Y/D=-0.3

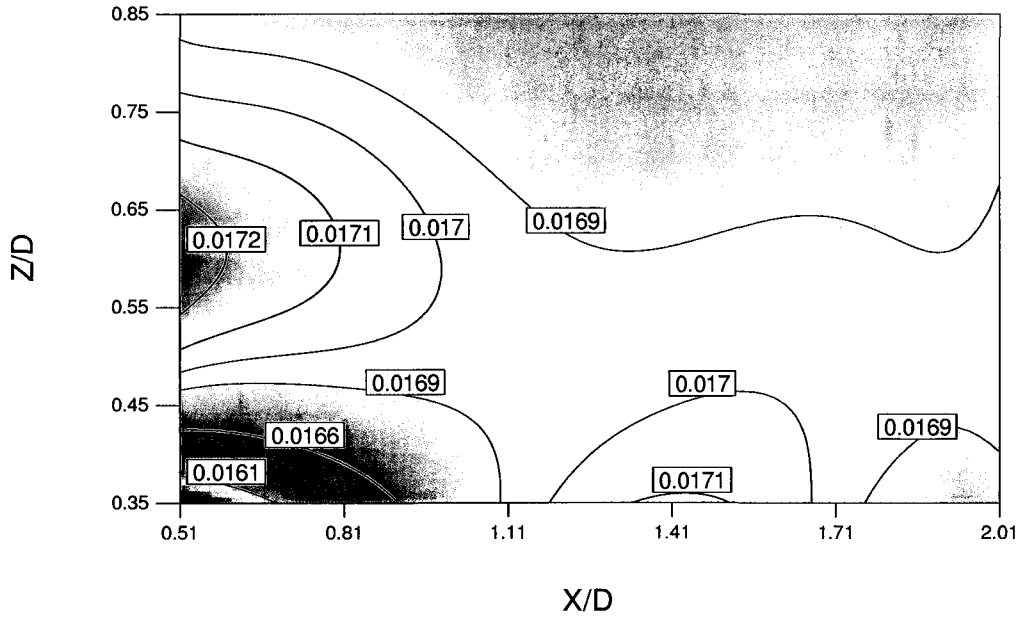

Figure 134: Thrust coefficient contours for rotor location of Y/D=-0.2

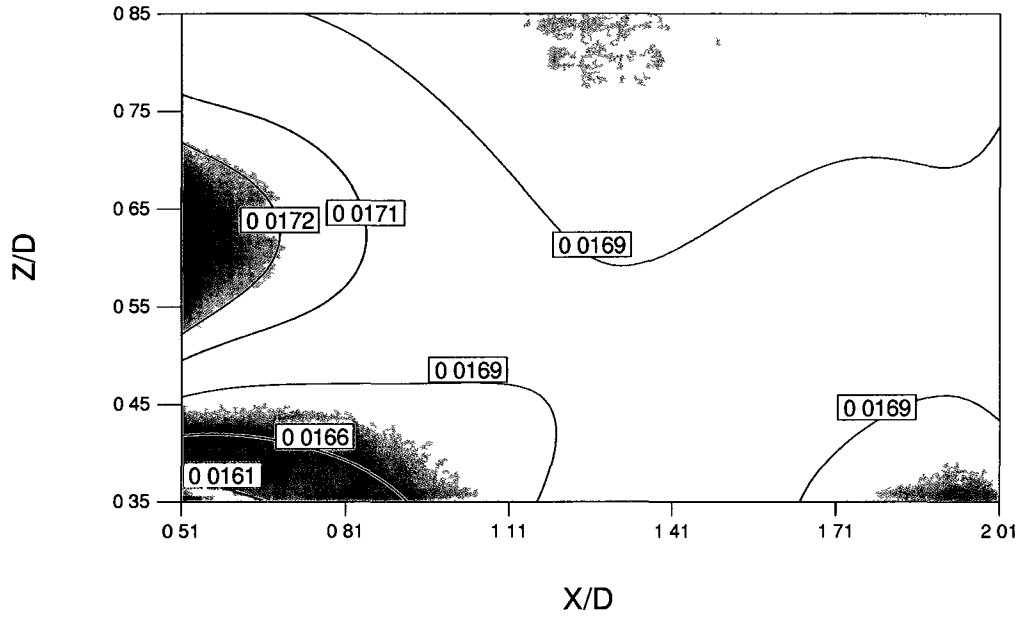

Figure 135: Thrust coefficient contours for rotor location of Y/D=-0.1

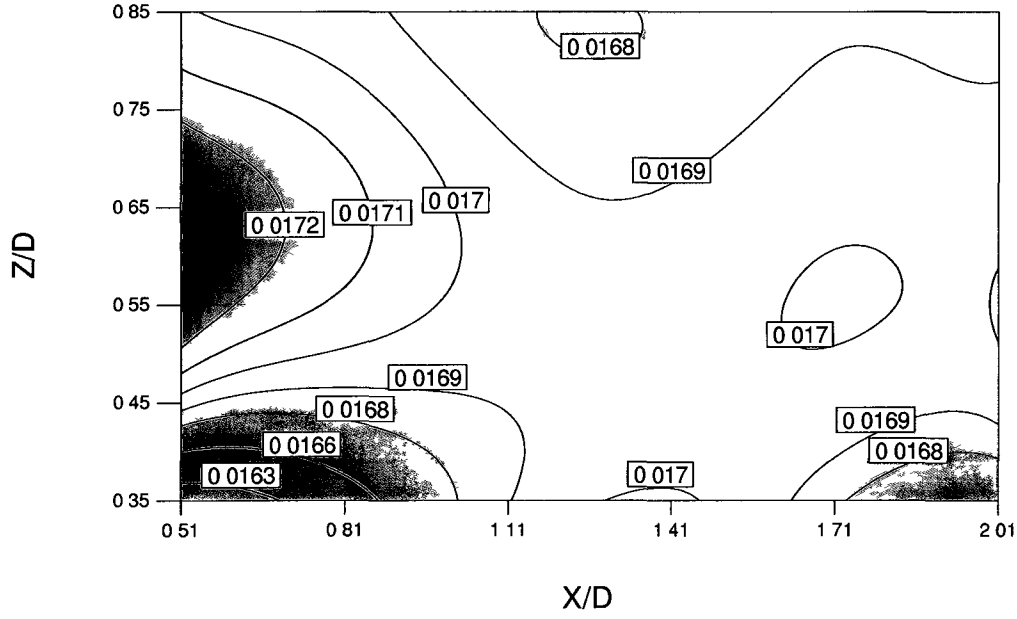

Figure 136: Thrust coefficient contours for rotor location of Y/D=0.0

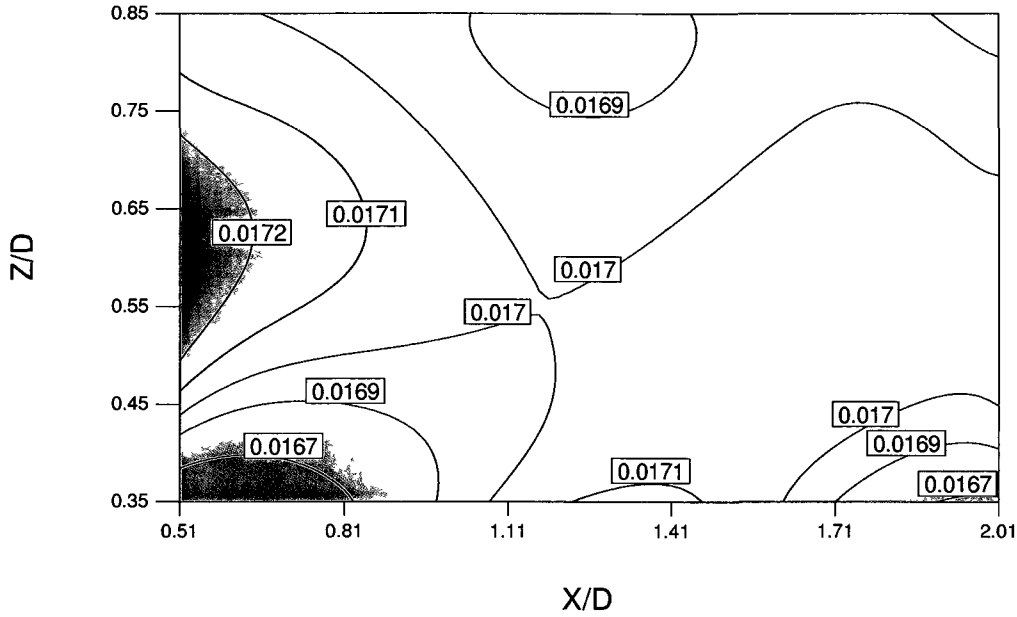

Figure 137: Thrust coefficient contours for rotor location of Y/D=0.1

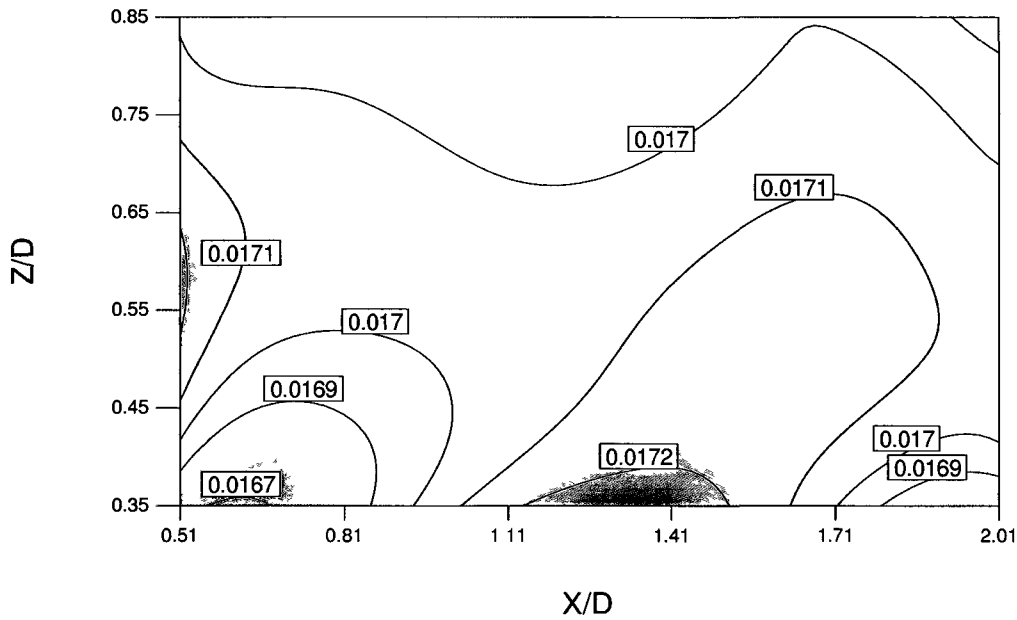

Figure 138: Thrust coefficient contours for rotor location of Y/D=0.2

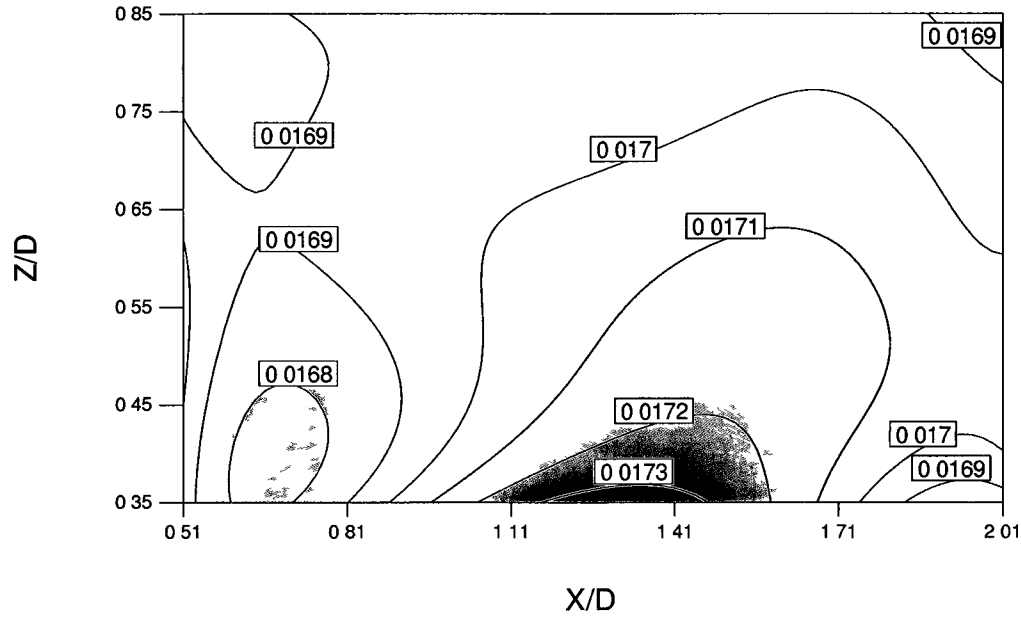

Figure 139: Thrust coefficient contours for rotor location of Y/D=0.3

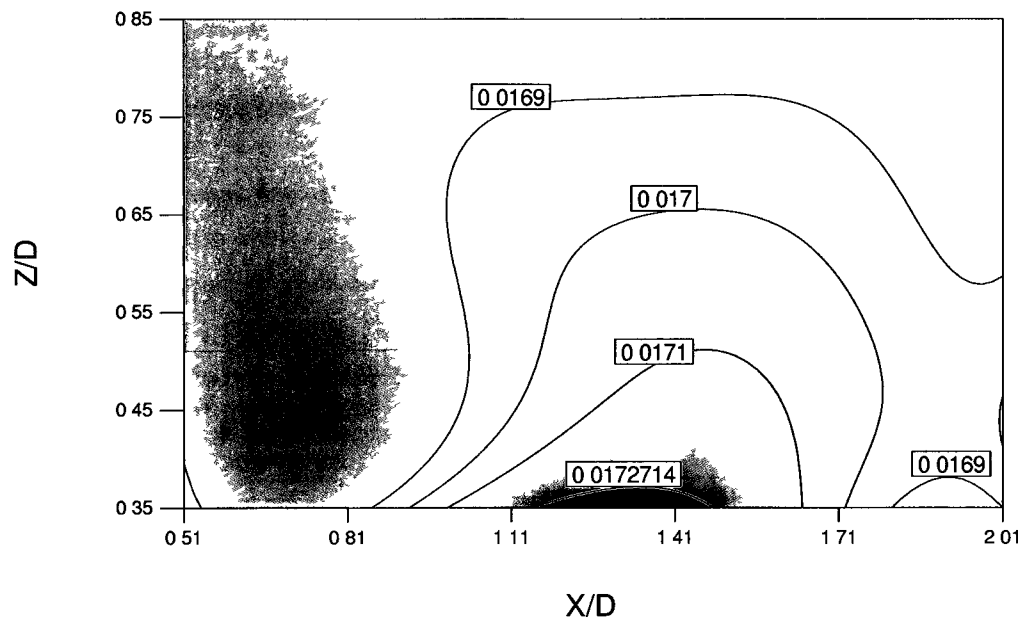

Figure 140: Thrust coefficient contours for rotor location of Y/D=0.4

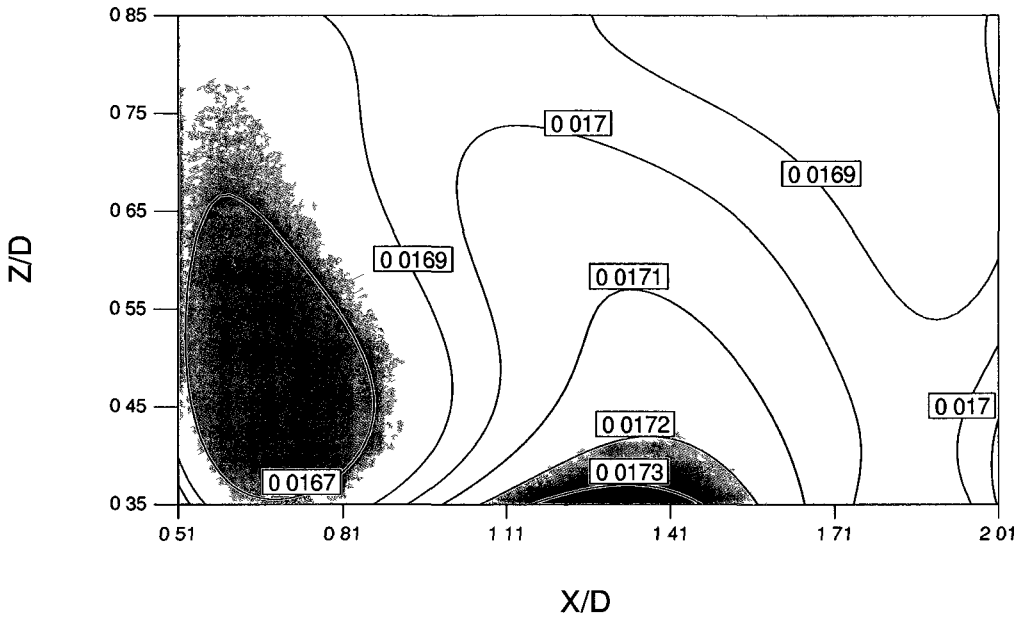

Figure 141: Thrust coefficient contours for rotor location of Y/D=0.5

APPENDIX H: Velocity Vector and Contour Plots for Isolated Ship Airwake

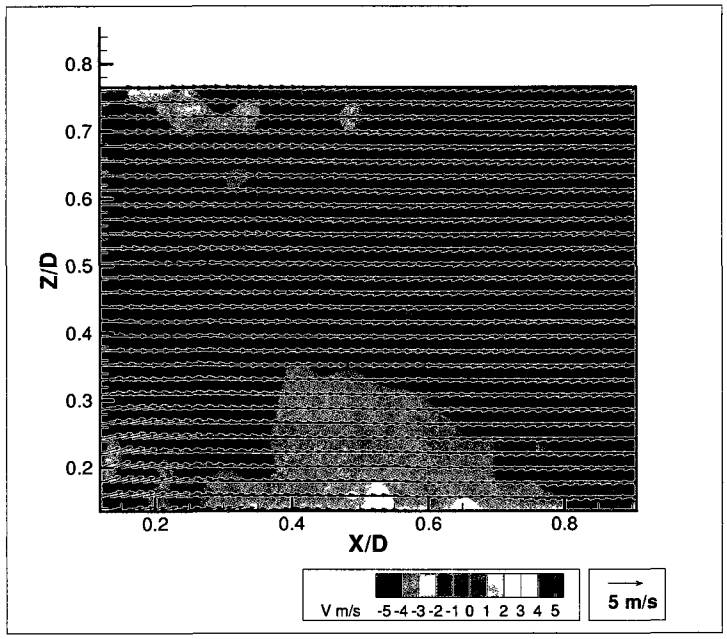

Figure 142: Observed velocity field for isolated ship airwake configuration and longitudinal measurement plane Y/D=-0.5

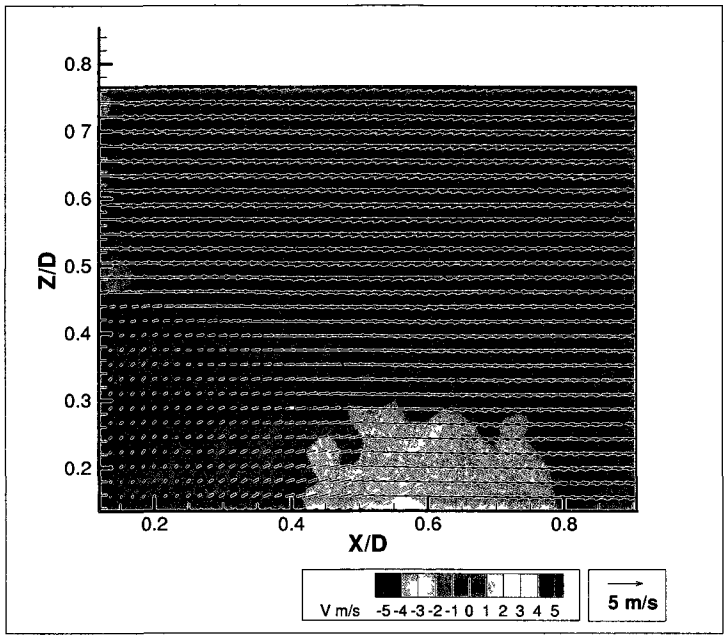

Figure 143: Observed velocity field for isolated ship airwake configuration and longitudinal measurement plane Y/D=-0.4

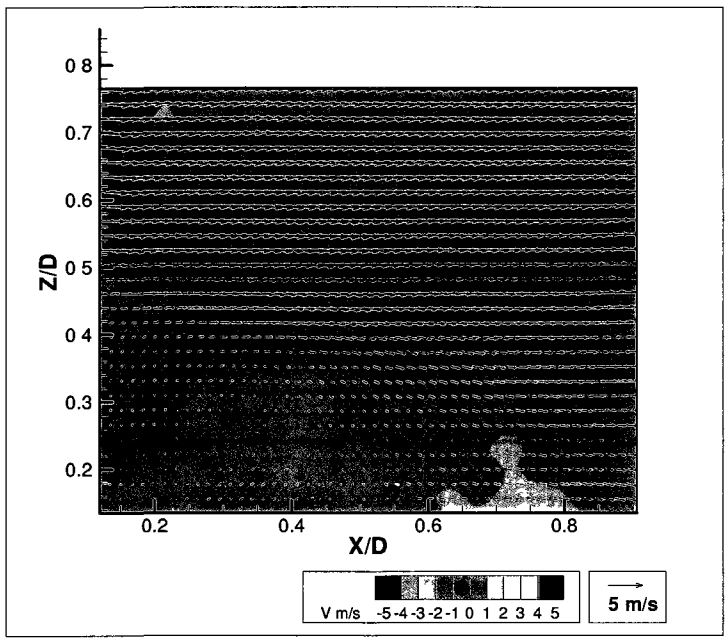

Figure 144: Observed velocity field for isolated ship airwake configuration and longitudinal measurement plane Y/D=-0.3

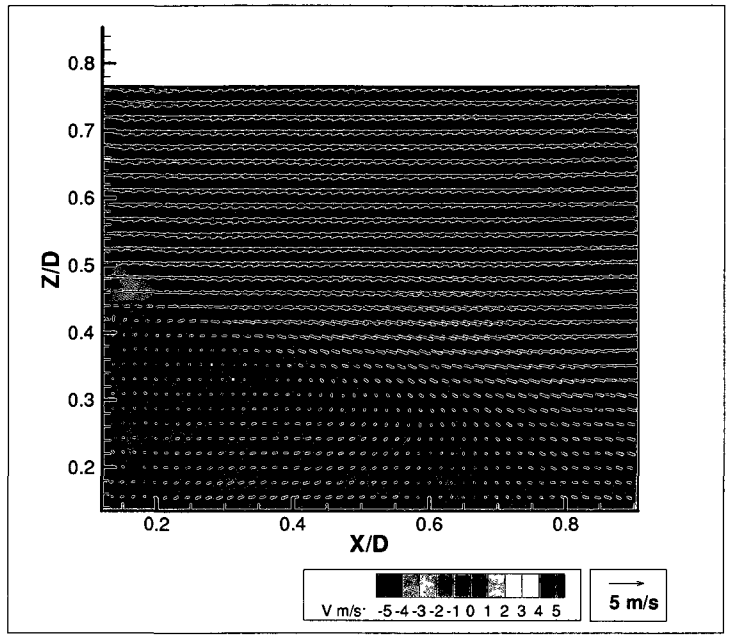

Figure 145: Observed velocity field for isolated ship airwake configuration and longitudinal measurement plane Y/D=-0.2

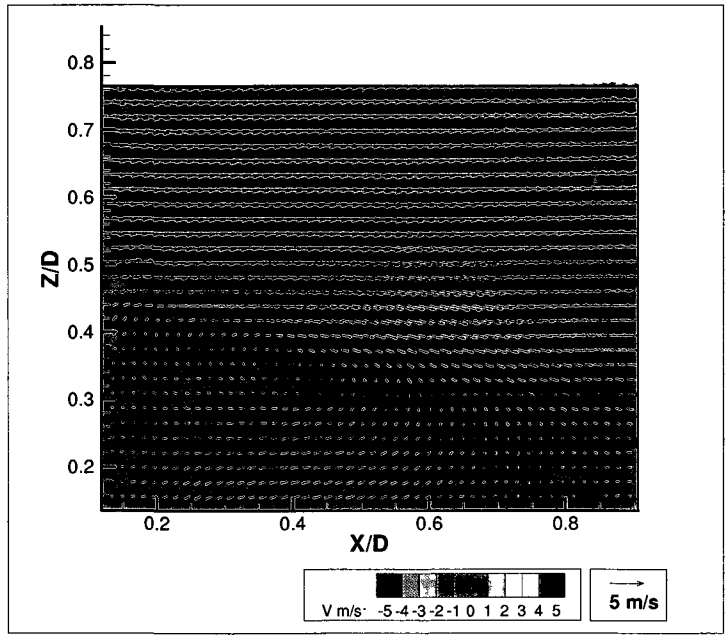

Figure 146: Observed velocity field for isolated ship airwake configuration and longitudinal measurement plane Y/D=-0.1

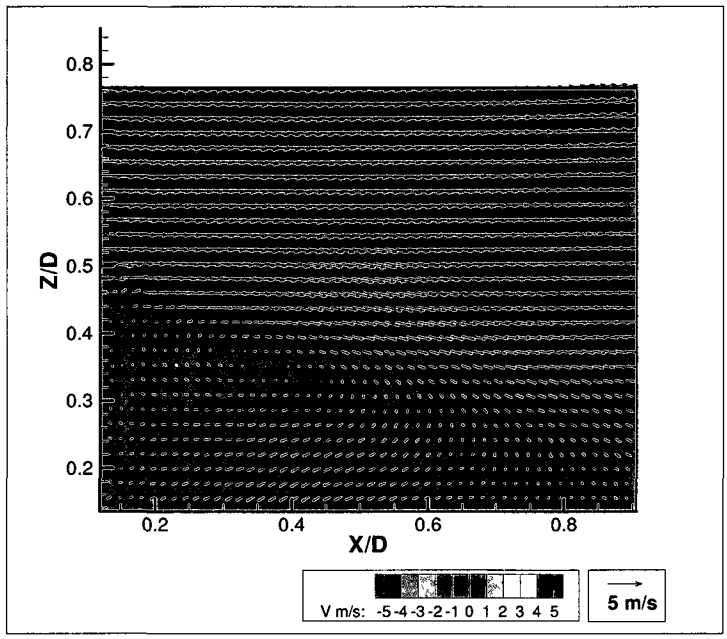

Figure 147: Observed velocity field for isolated ship airwake configuration and longitudinal measurement plane Y/D=0.0

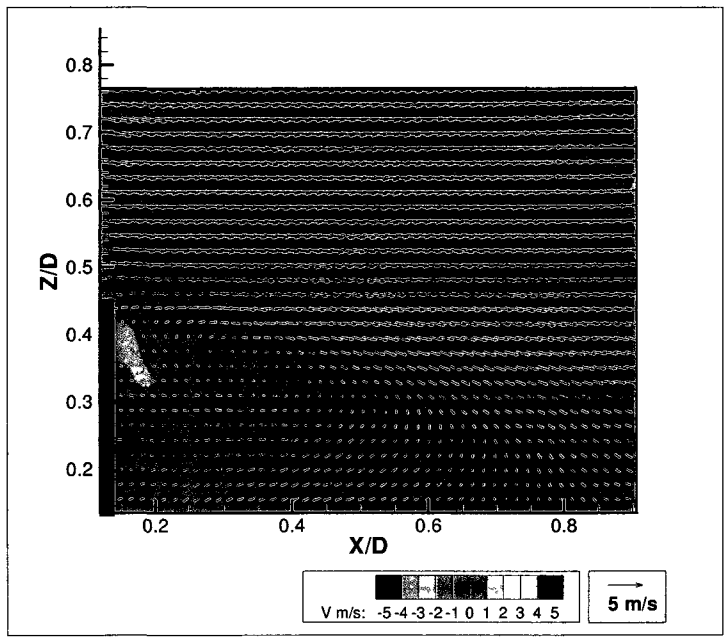

Figure 148: Observed velocity field for isolated ship airwake configuration and longitudinal measurement plane Y/D=0.1

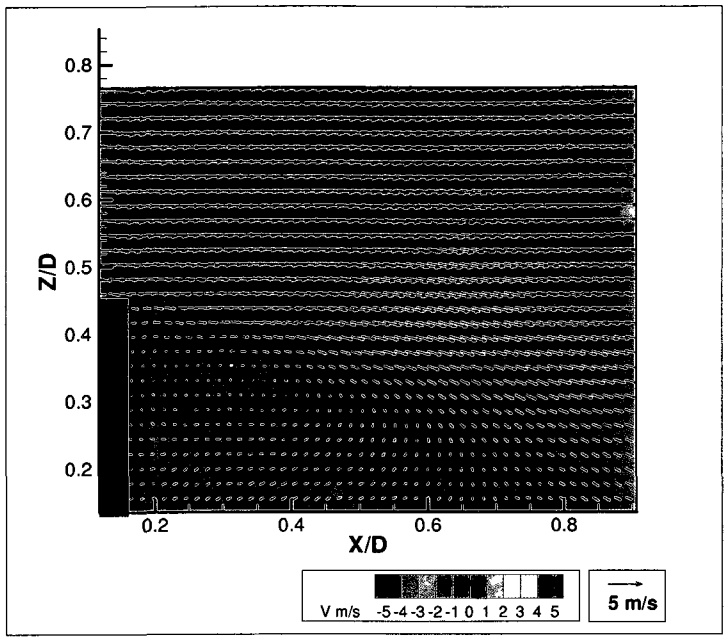

Figure 149: Observed velocity field for isolated ship airwake configuration and longitudinal measurement plane Y/D=0.2

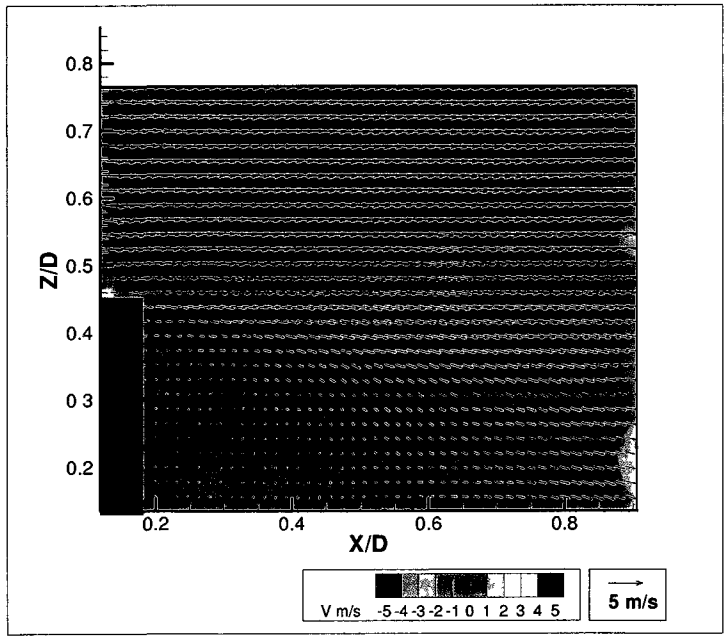

Figure 150: Observed velocity field for isolated ship airwake configuration and longitudinal measurement plane Y/D=0.3

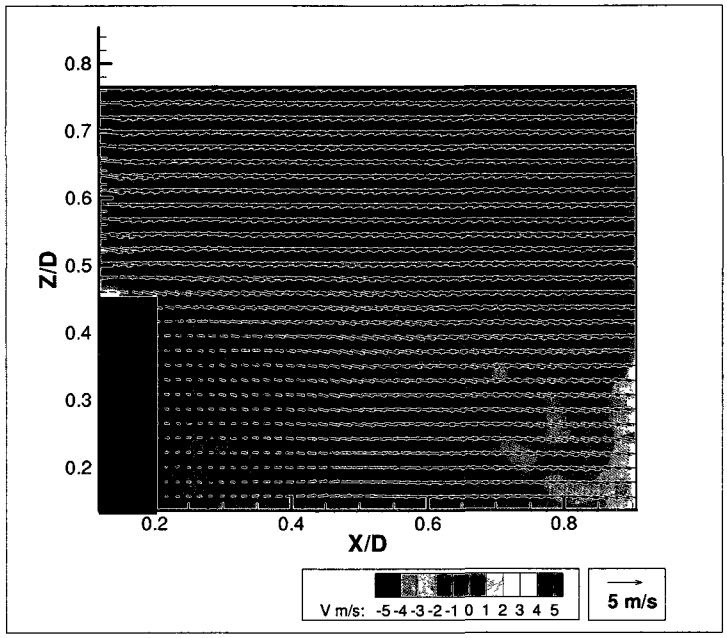

Figure 151: Observed velocity field for isolated ship airwake configuration and longitudinal measurement plane Y/D=0.4

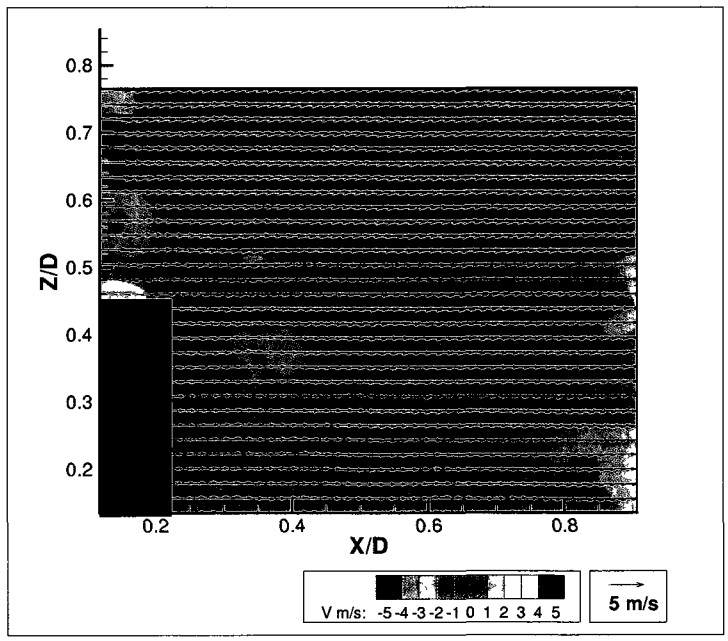

Figure 152: Observed velocity field for isolated ship airwake configuration and longitudinal measurement plane Y/D=0.5

APPENDIX I: Observed Velocity Fields for Combined Rotor and Airwake

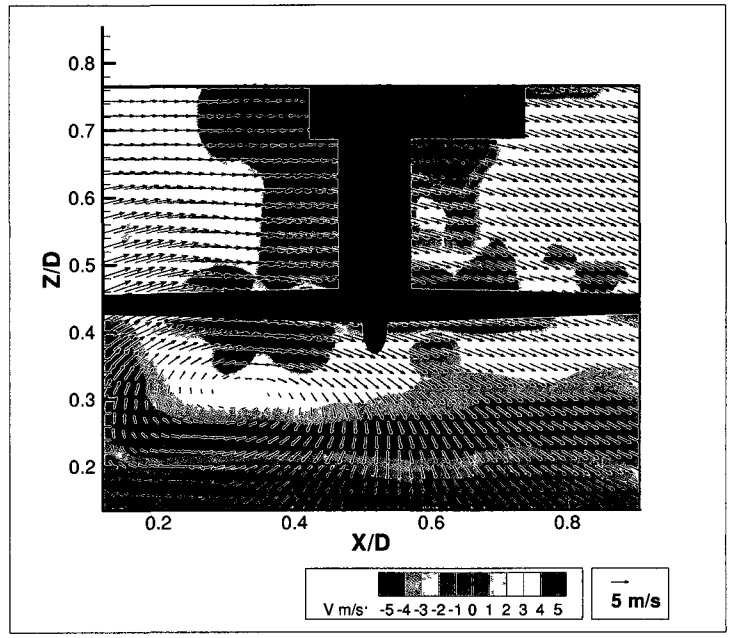

Figure 153: Observed velocity field for rotor Z/D=0.45 and longitudinal measurement plane Y/D=-0.5

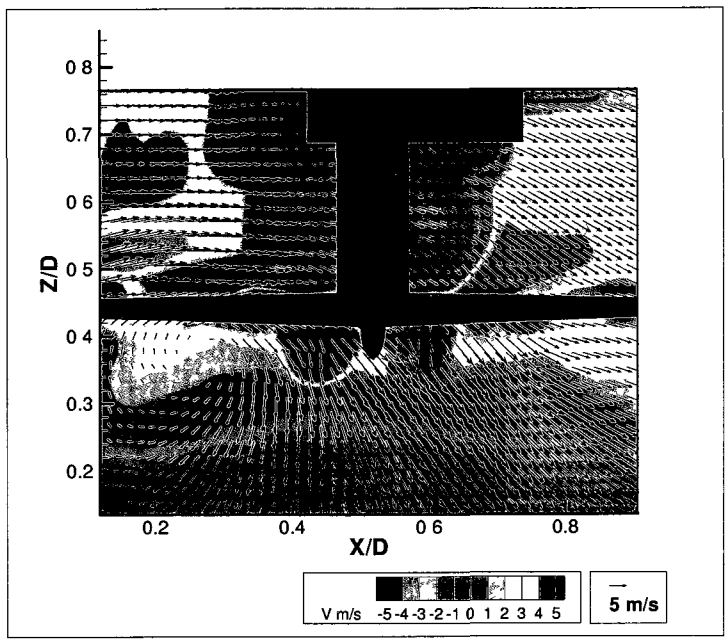

Figure 154: Observed velocity field for rotor Z/D=0.45 and longitudinal measurement plane Y/D=-0.4

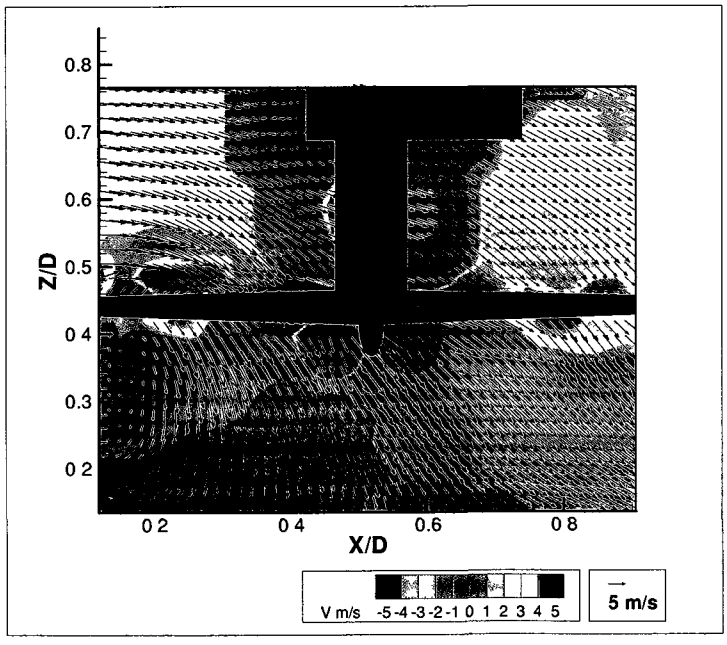

Figure 155: Observed velocity field for rotor Z/D=0.45 and longitudinal measurement plane Y/D=-0.3

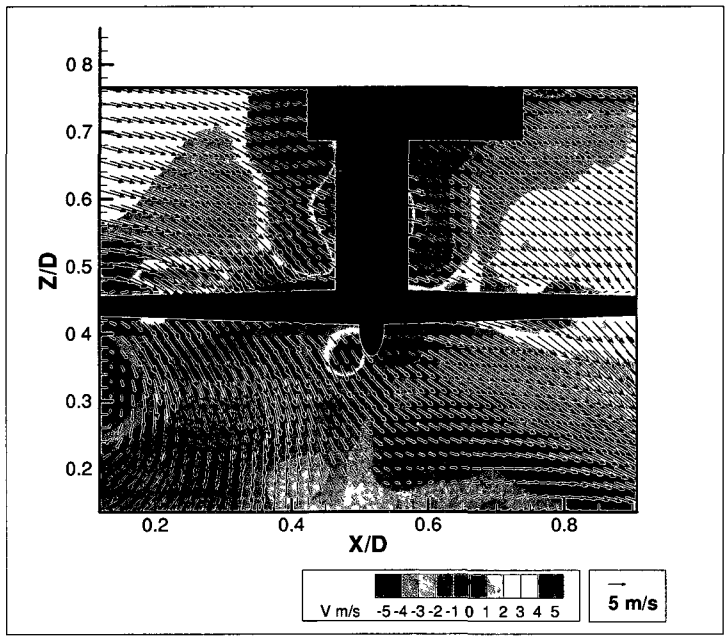

Figure 156: Observed velocity field for rotor Z/D=0.45 and longitudinal measurement plane Y/D=-0.2

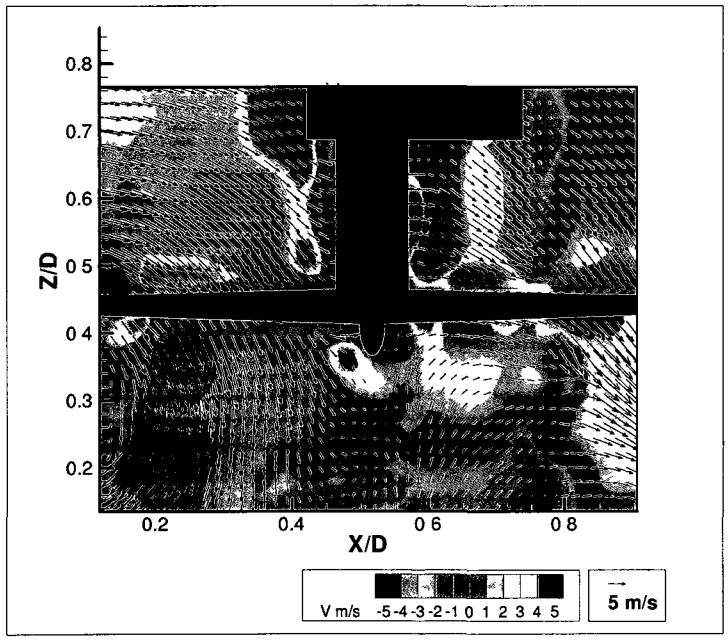

Figure 157: Observed velocity field for rotor Z/D=0.45 and longitudinal measurement plane Y/D=-0.1

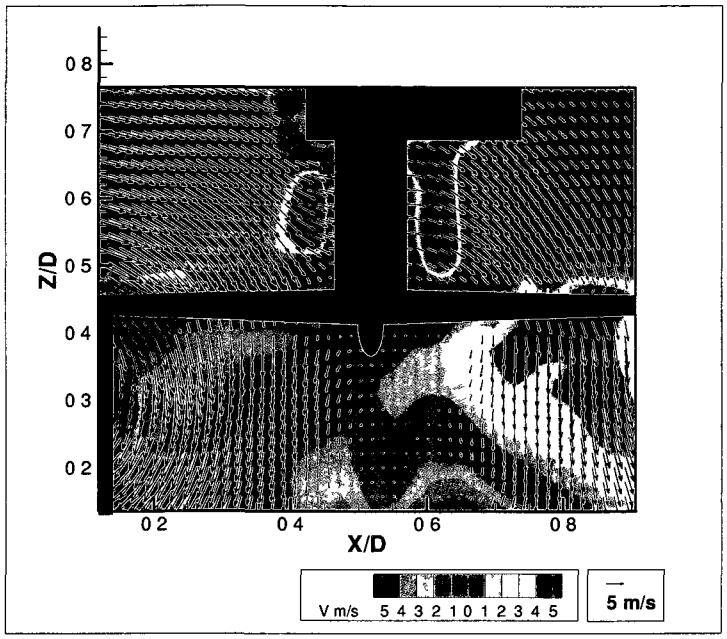

Figure 158: Observed velocity field for rotor Z/D=0.45 and longitudinal measurement plane Y/D=0.1

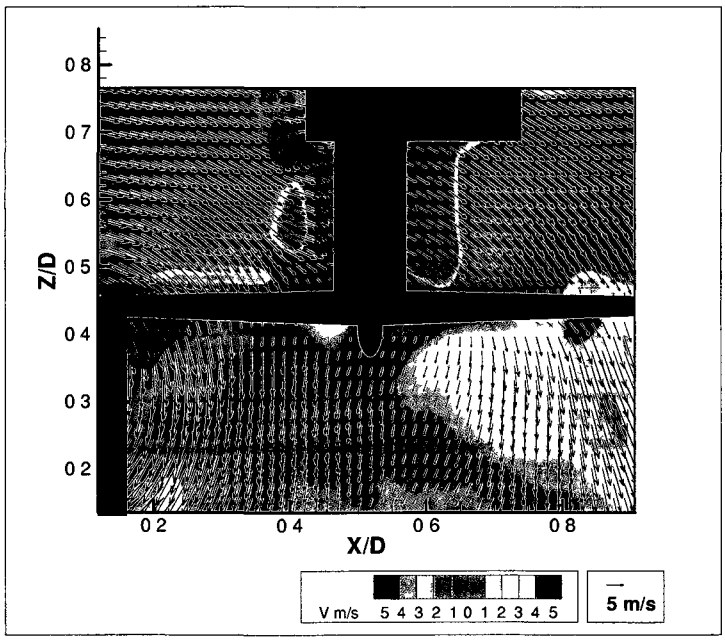

Figure 159: Observed velocity field for rotor Z/D=0.45 and longitudinal measurement plane Y/D=0.2

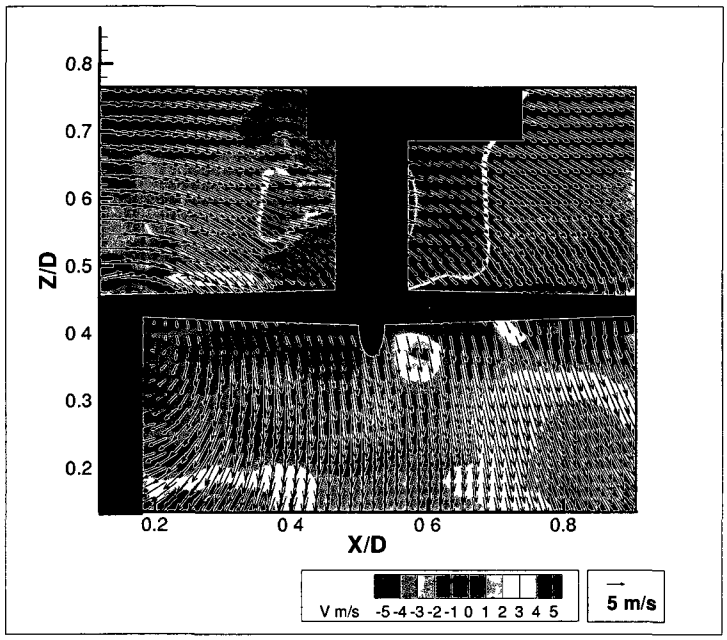

Figure 160: Observed velocity field for rotor Z/D=0.45 and longitudinal measurement plane Y/D=0.3

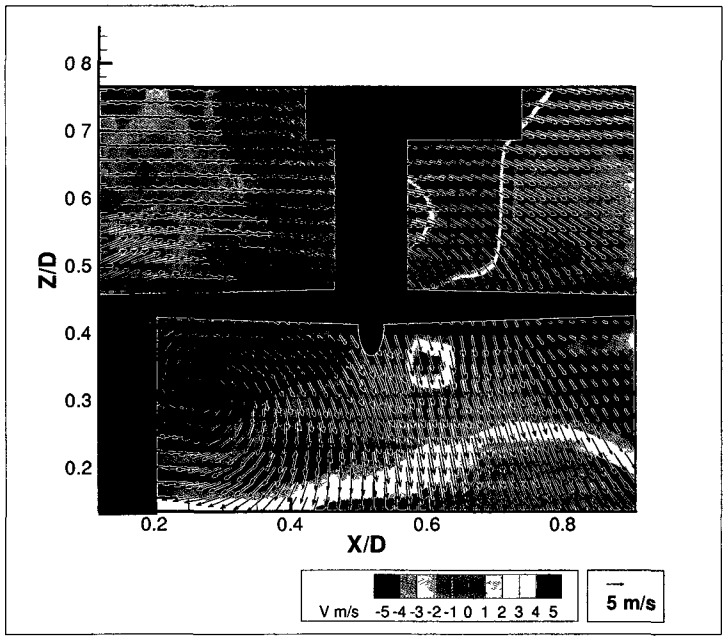

Figure 161: Observed velocity field for rotor Z/D=0.45 and longitudinal measurement plane Y/D=0.4

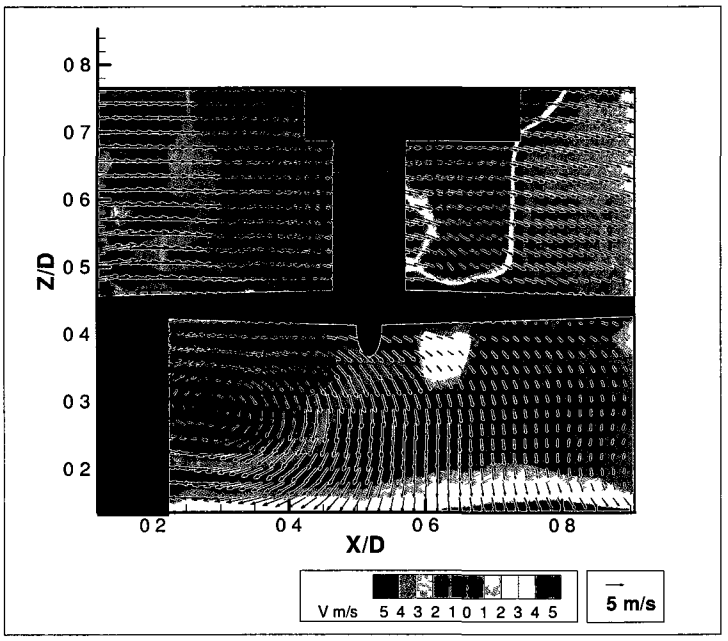

Figure 162: Observed velocity field for rotor Z/D=0.45 and longitudinal measurement plane Y/D=0.5

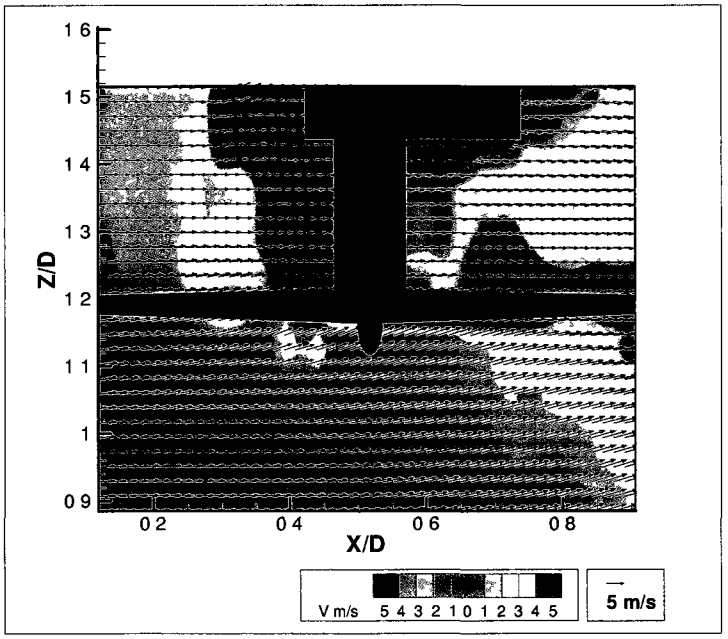

Figure 163: Observed velocity field for rotor Z/D=1.2 and longitudinal measurement plane Y/D=-0.5

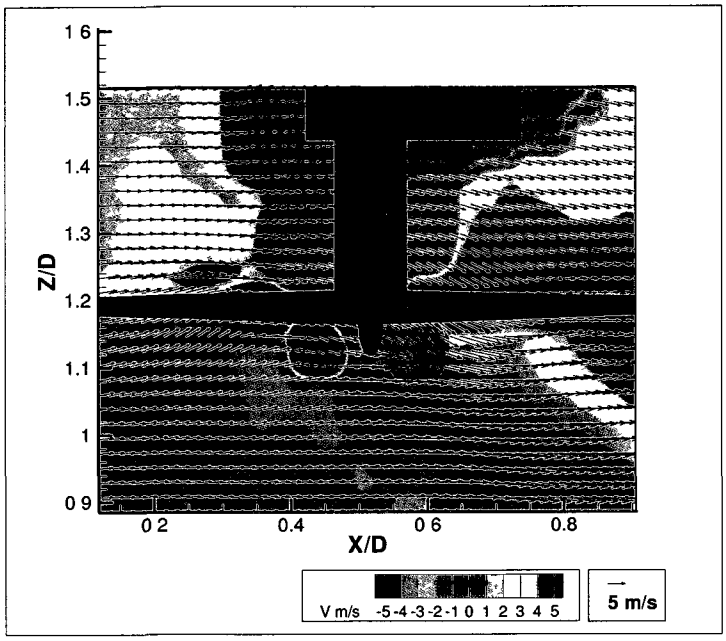

Figure 164: Observed velocity field for rotor Z/D=1.2 and longitudinal measurement plane Y/D=-0.4

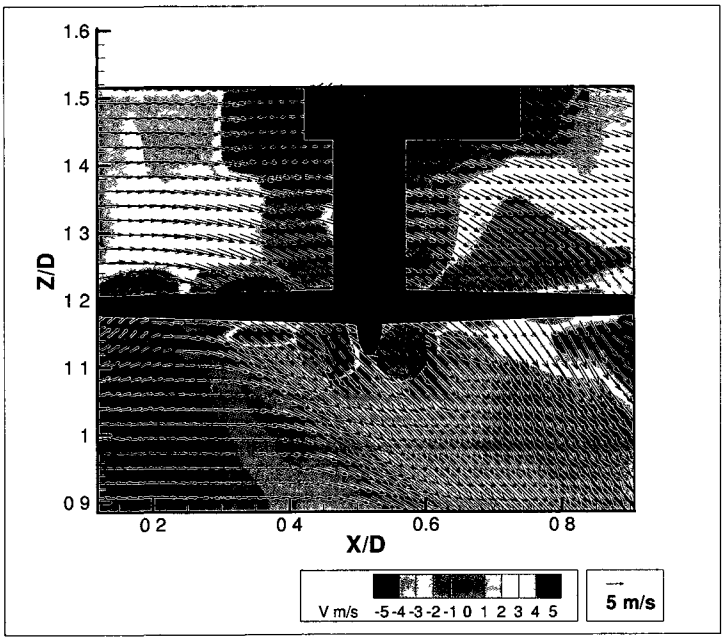

Figure 165: Observed velocity field for rotor Z/D=1.2 and longitudinal measurement plane Y/D=-0.3

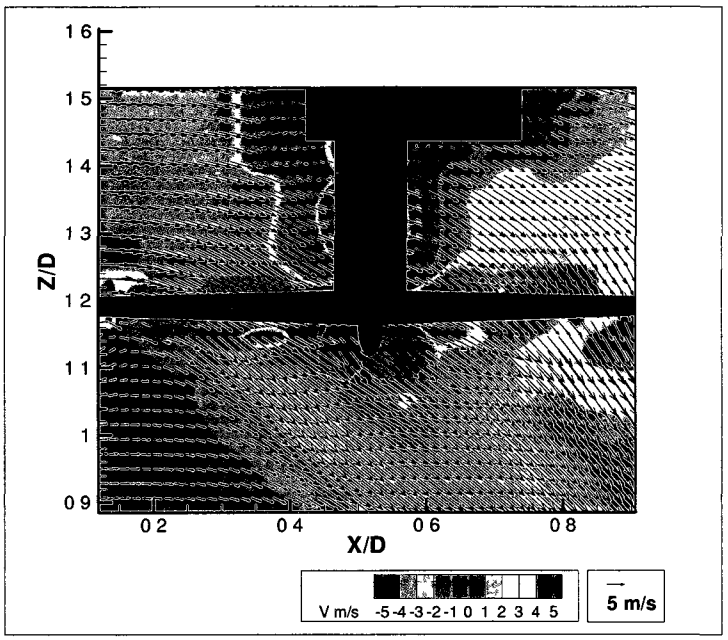

Figure 166: Observed velocity field for rotor Z/D=1.2 and longitudinal measurement plane Y/D=-0.2

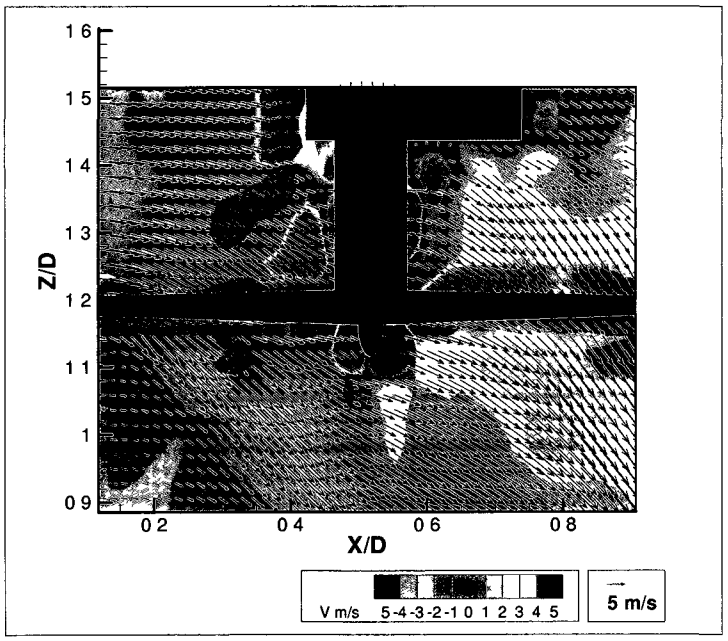

Figure 167: Observed velocity field for rotor Z/D=1.2 and longitudinal measurement plane Y/D=-0.1

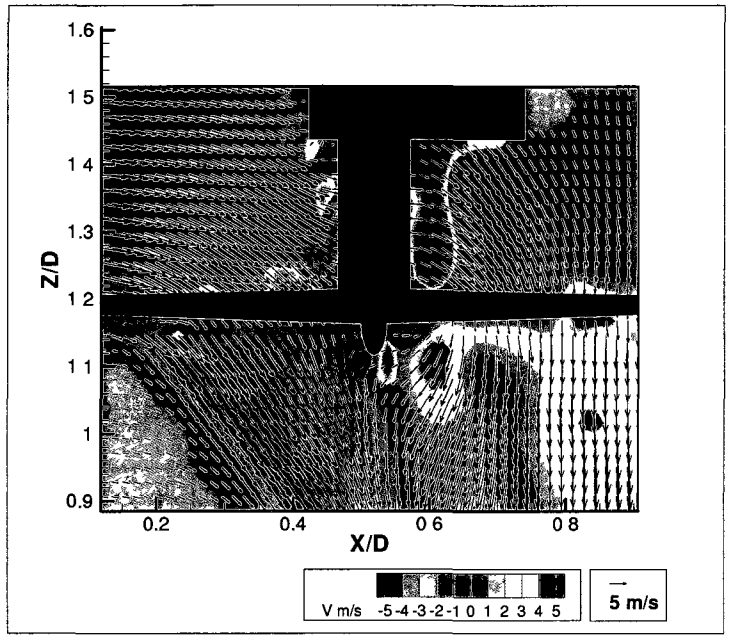

Figure 168: Observed velocity field for rotor Z/D=1.2 and longitudinal measurement plane Y/D=0.1

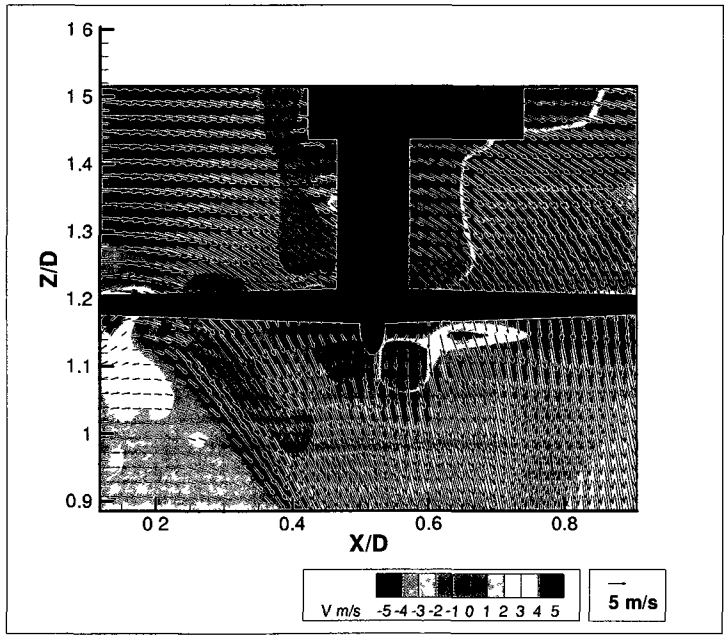

Figure 169: Observed velocity field for rotor Z/D=1.2 and longitudinal measurement plane Y/D=0.2

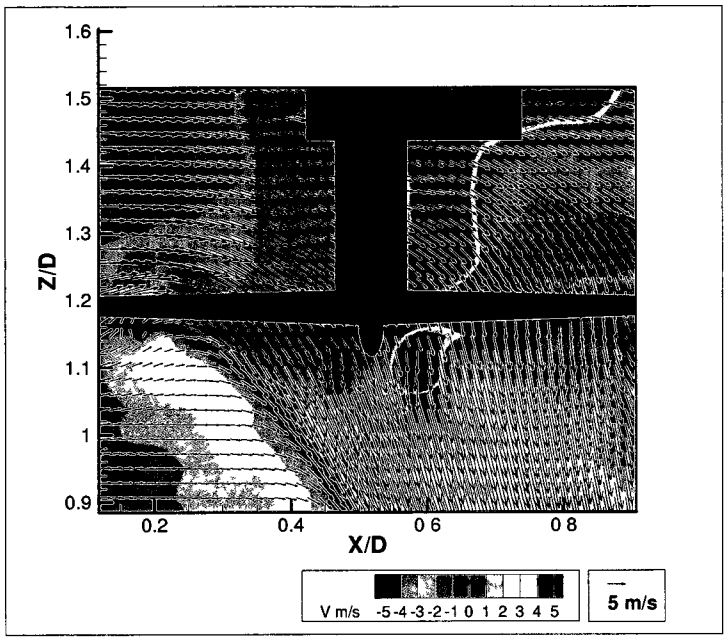

Figure 170: Observed velocity field for rotor Z/D=1.2 and longitudinal measurement plane Y/D=0.3

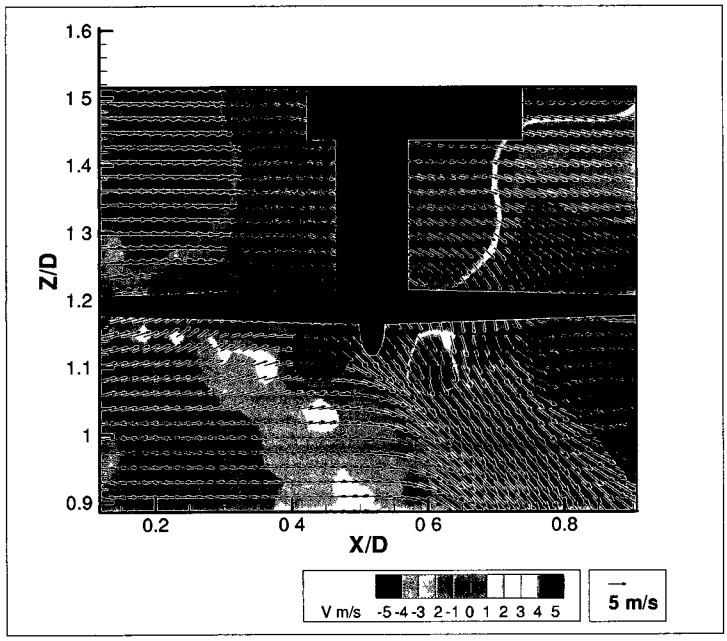

Figure 171: Observed velocity field for rotor Z/D=1.2 and longitudinal measurement plane Y/D=0.4

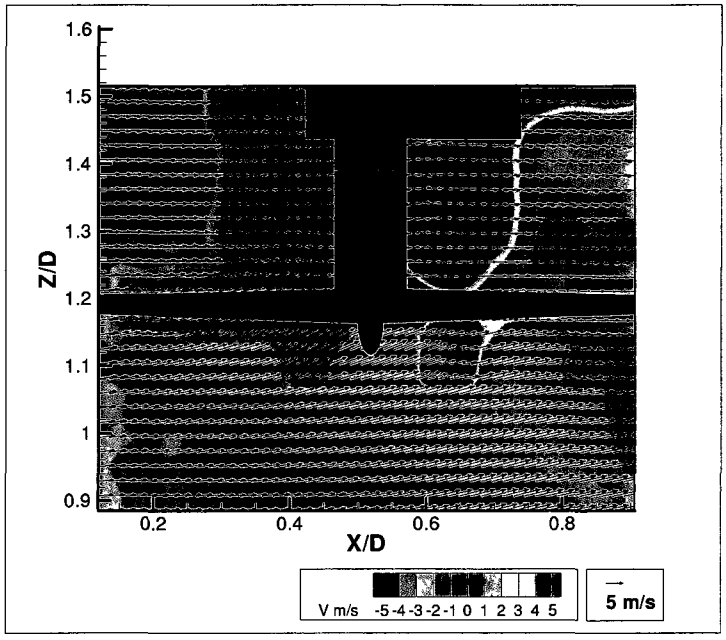

Figure 172: Observed velocity field for rotor Z/D=1.2 and longitudinal measurement plane Y/D=0.5

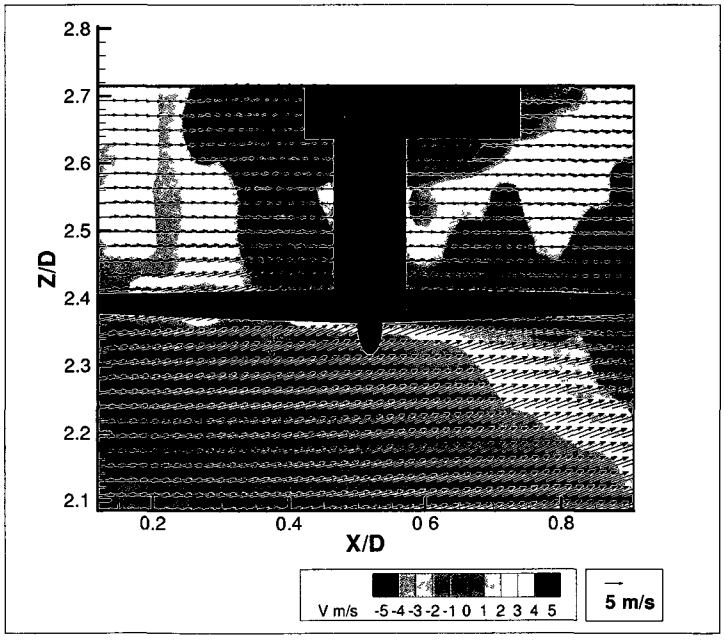

Figure 173: Observed velocity field for rotor Z/D=2.4 and longitudinal measurement plane Y/D=-0.5

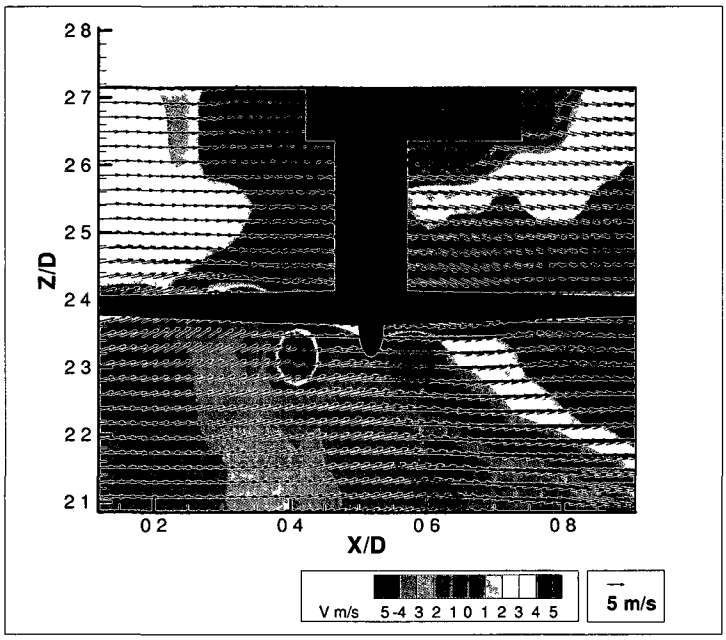

Figure 174: Observed velocity field for rotor Z/D=2.4 and longitudinal measurement plane Y/D=-0.4

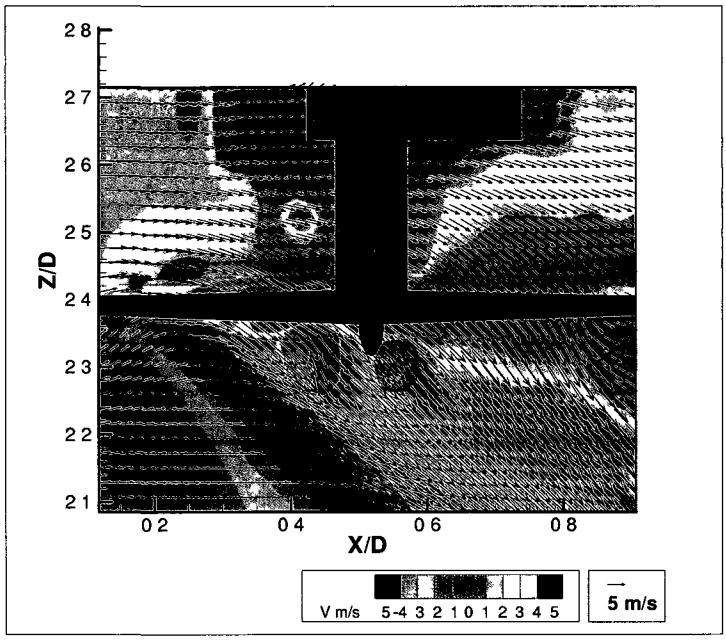

Figure 175: Observed velocity field for rotor Z/D=2.4 and longitudinal measurement plane Y/D=-0.3

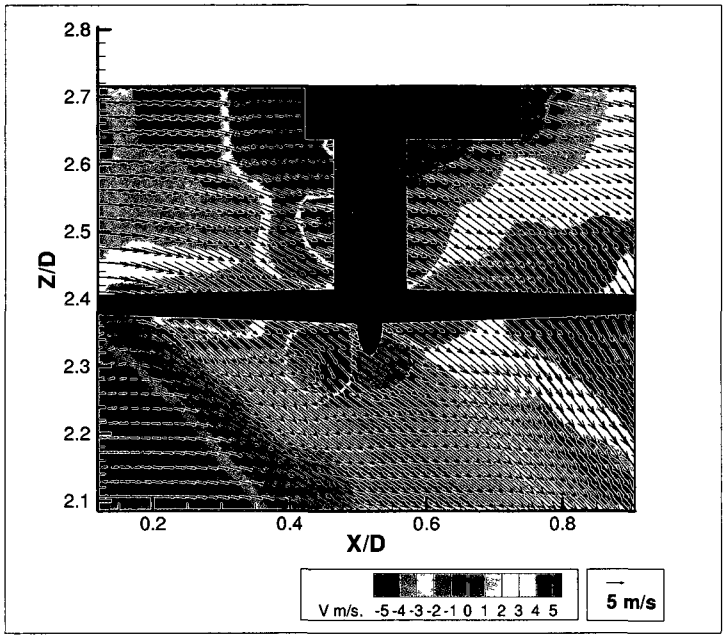

Figure 176: Observed velocity field for rotor Z/D=2.4 and longitudinal measurement plane Y/D=-0.2

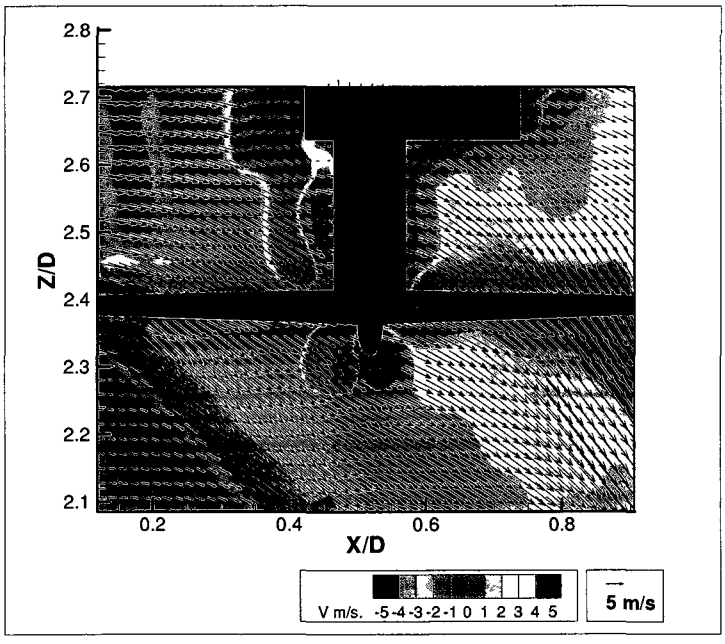

Figure 177: Observed velocity field for rotor Z/D=2.4 and longitudinal measurement plane Y/D=-0.1

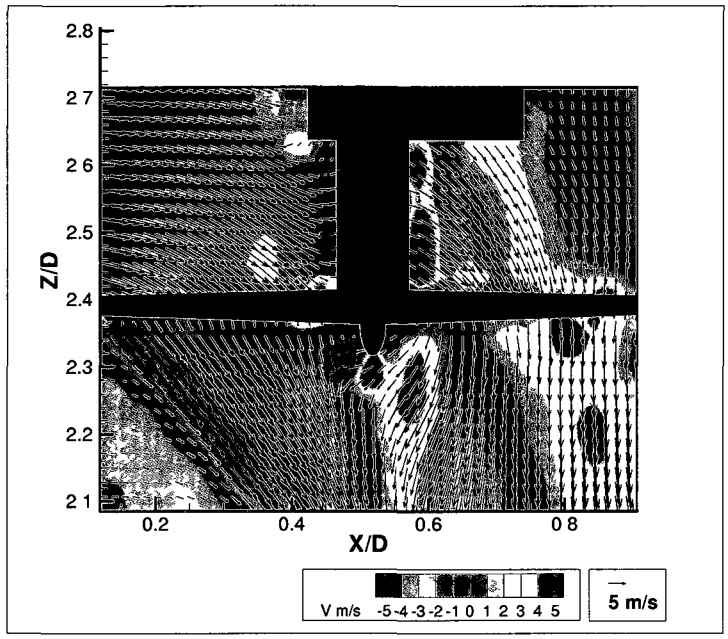

Figure 178: Observed velocity field for rotor Z/D=2.4 and longitudinal measurement plane Y/D=0.1

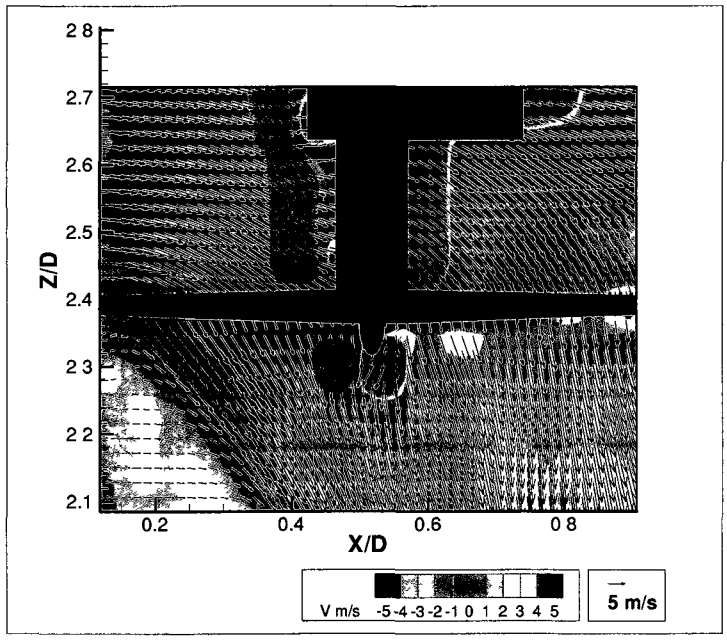

Figure 179: Observed velocity field for rotor Z/D=2.4 and longitudinal measurement plane Y/D=0.2

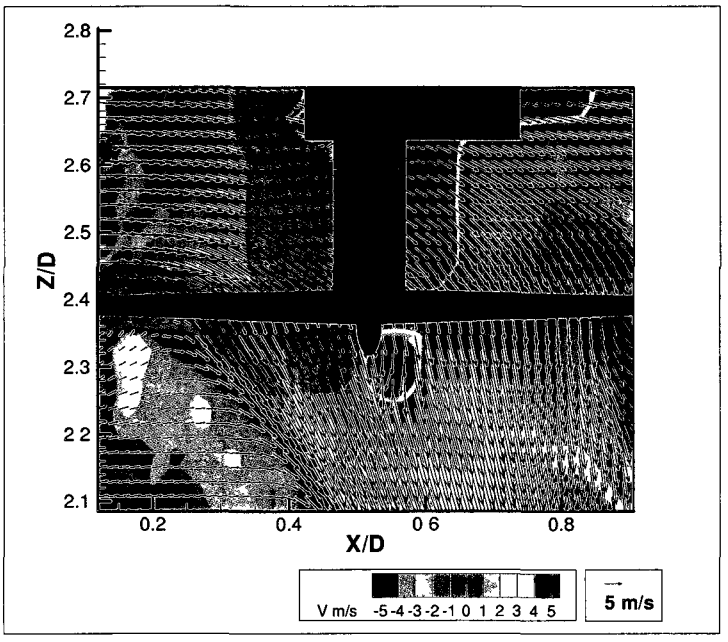

Figure 180: Observed velocity field for rotor Z/D=2.4 and longitudinal measurement plane Y/D=0.3

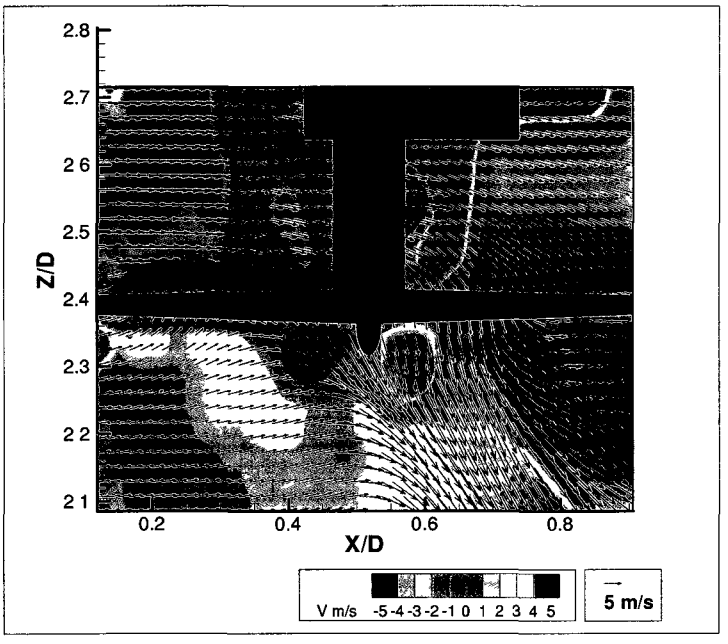

Figure 181: Observed velocity field for rotor Z/D=2.4 and longitudinal measurement plane Y/D=0.4

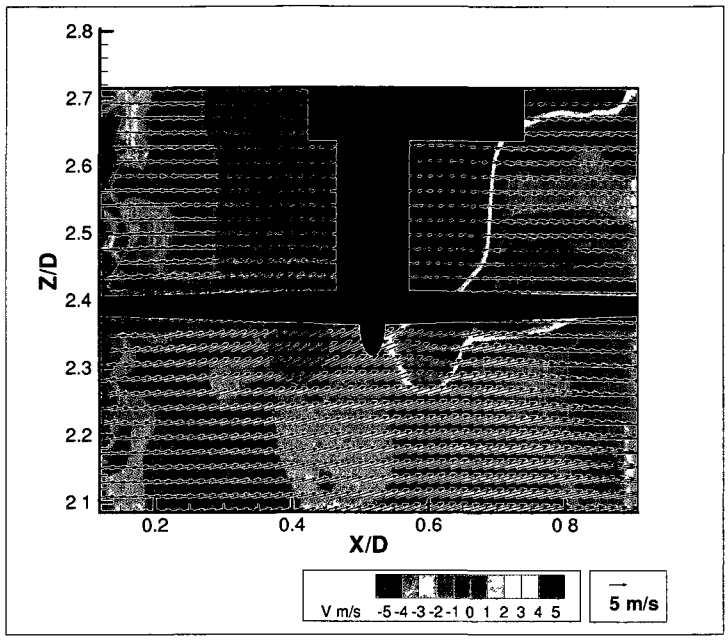

Figure 182: Observed velocity field for rotor Z/D=2.4 and longitudinal measurement plane Y/D=0.5

APPENDIX J: Observed Velocity Field for Isolated Rotor and Freestream

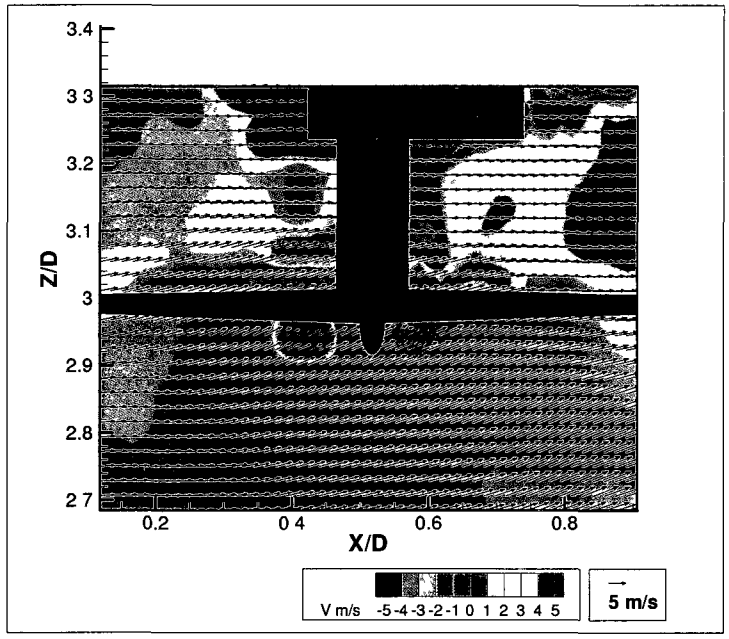

Figure 183: Observed velocity field for isolated rotor and freestream rotor configuration for longitudinal measurement plane Y/D=-0.5

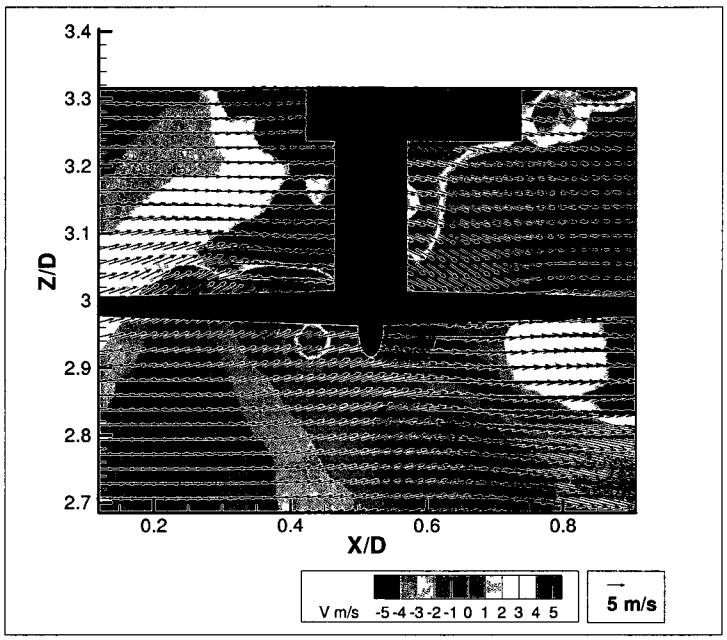

Figure 184: Observed velocity field for isolated rotor and freestream rotor configuration for longitudinal measurement plane Y/D=-0.4

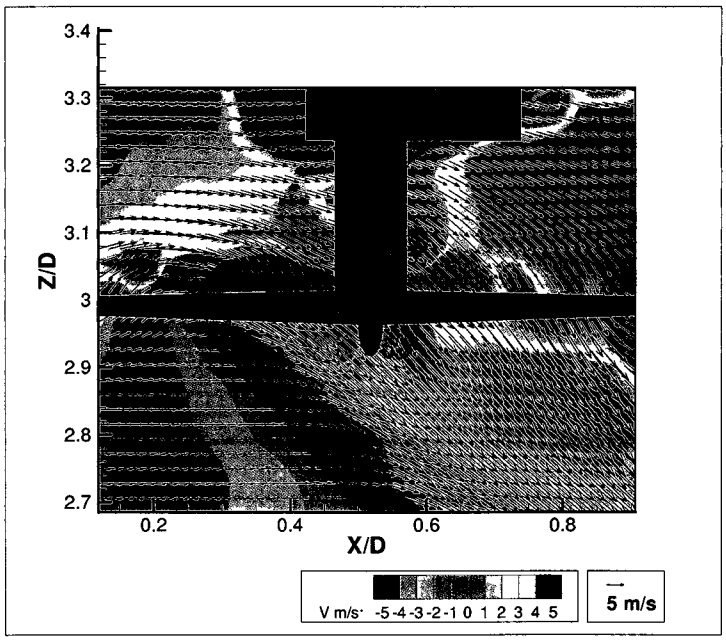

Figure 185: Observed velocity field for isolated rotor and freestream rotor configuration for longitudinal measurement plane Y/D=-0.3

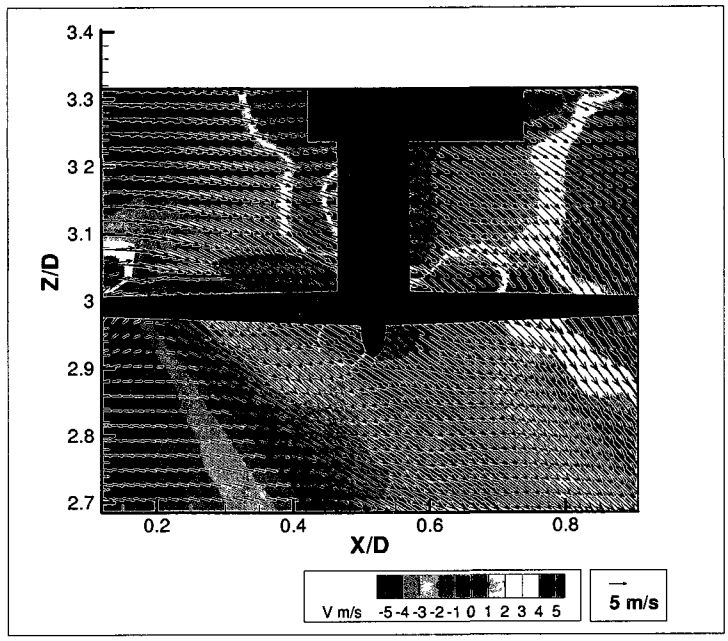

Figure 186: Observed velocity field for isolated rotor and freestream rotor configuration for longitudinal measurement plane Y/D=-0.2

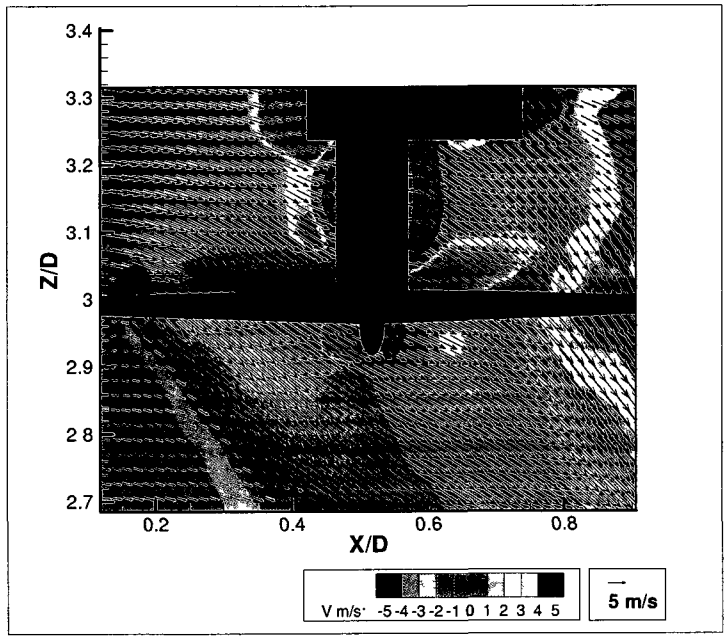

Figure 187: Observed velocity field for isolated rotor and freestream rotor configuration for longitudinal measurement plane Y/D=-0.1

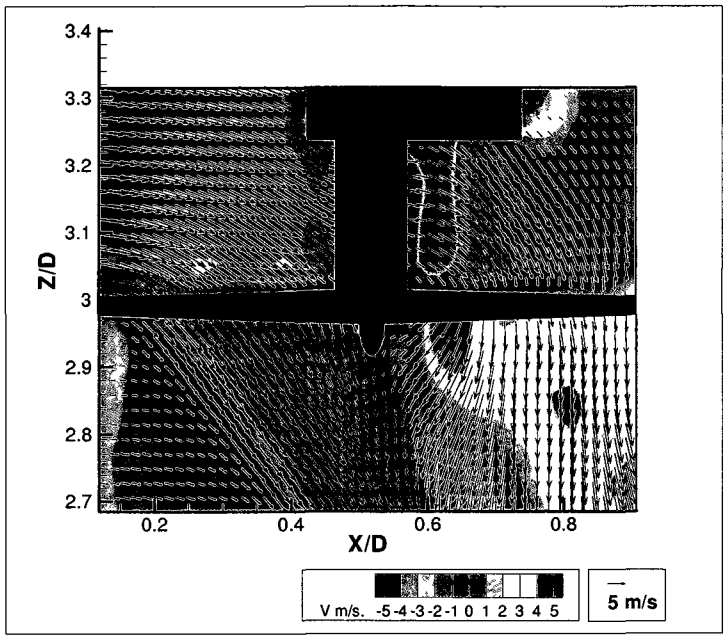

Figure 188: Observed velocity field for isolated rotor and freestream rotor configuration for longitudinal measurement plane Y/D=0.1

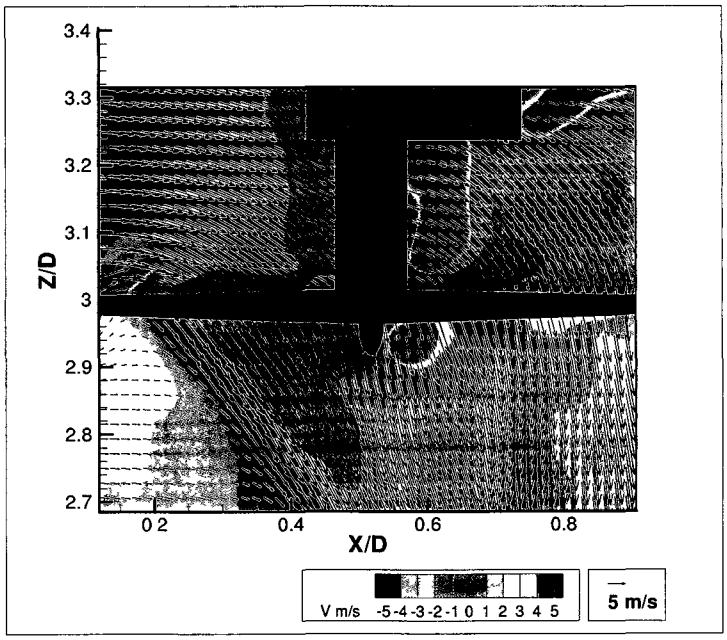

Figure 189: Observed velocity field for isolated rotor and freestream rotor configuration for longitudinal measurement plane Y/D=0.2

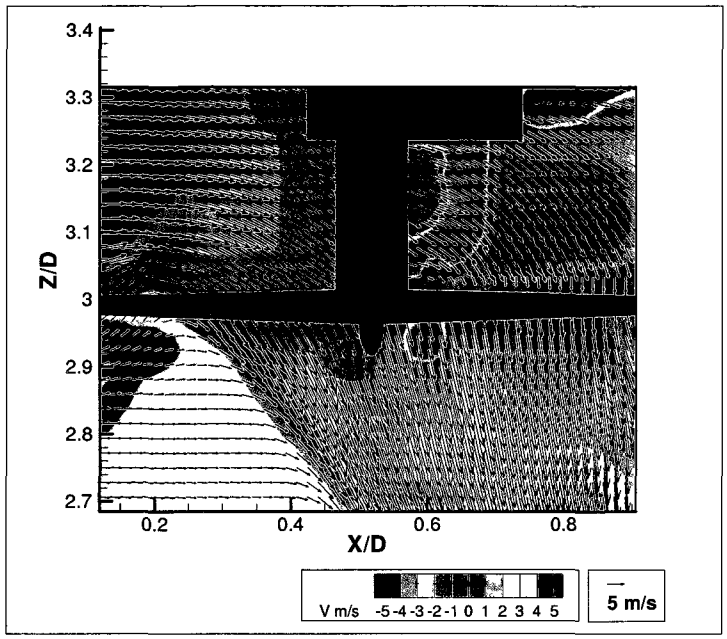

Figure 190: Observed velocity field for isolated rotor and freestream rotor configuration for longitudinal measurement plane Y/D=0.3

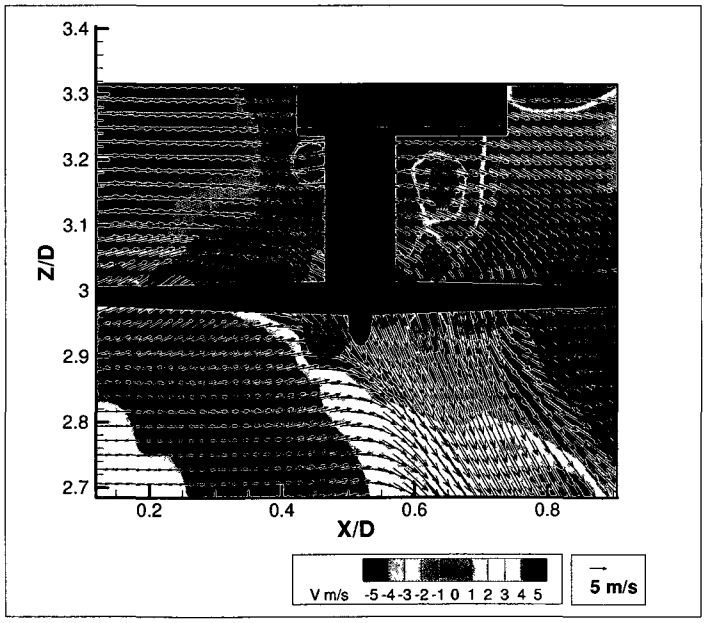

Figure 191: Observed velocity field for isolated rotor and freestream rotor configuration for longitudinal measurement plane Y/D=0.4

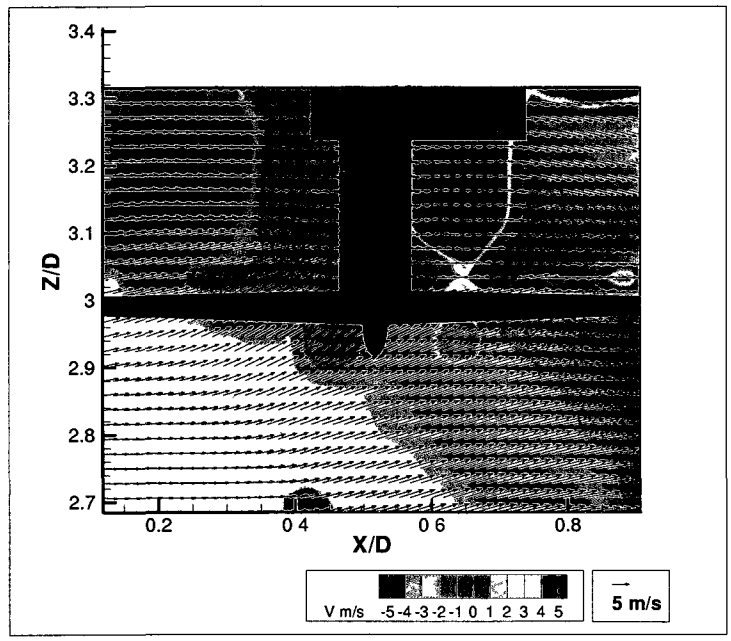

Figure 192: Observed velocity field for isolated rotor and freestream rotor configuration for longitudinal measurement plane Y/D=0.5

APPENDIX K: Generated Superimposed Velocity Fields

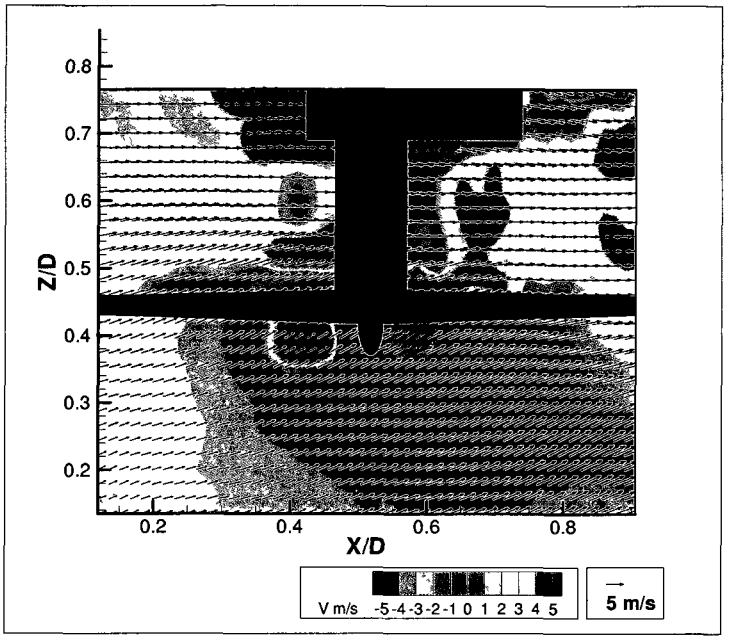

Figure 193: Generated superimposed flowfield for rotor Z/D=0.45 and longitudinal measurement plane Y/D=-0.5

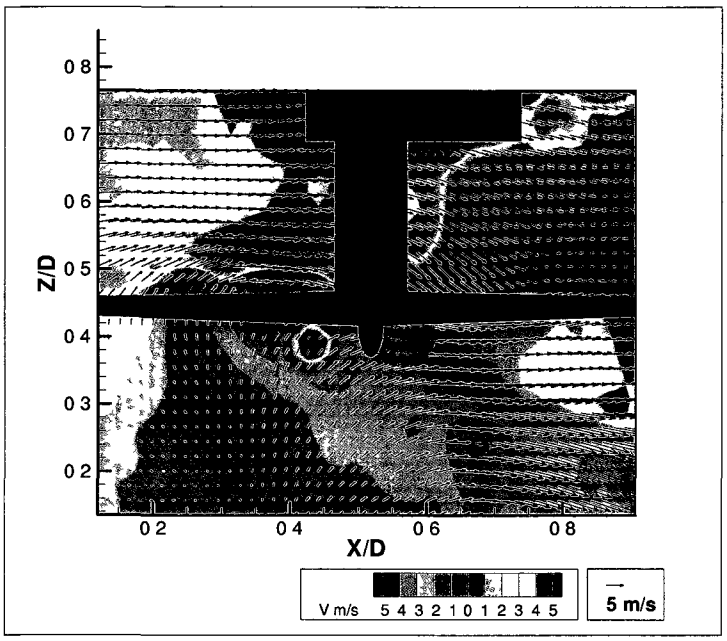

Figure 194: Generated superimposed flowfield for rotor Z/D=0.45 and longitudinal measurement plane Y/D=-0.4

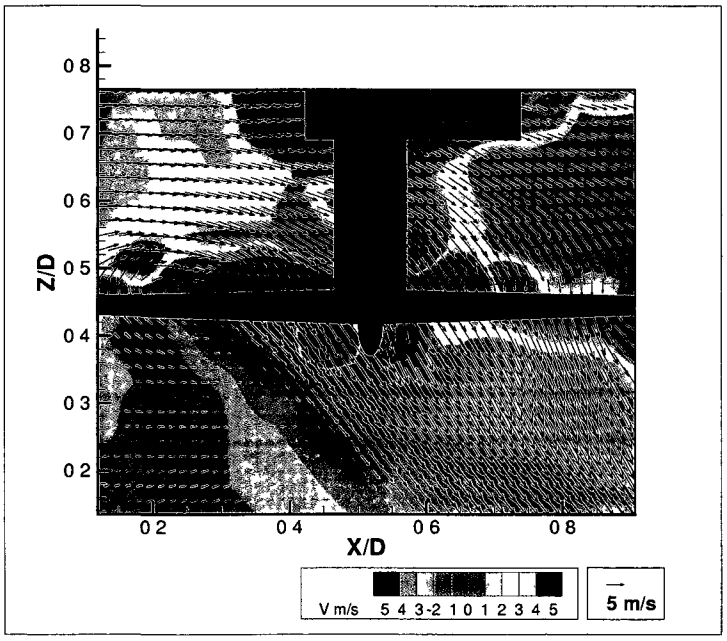

Figure 195: Generated superimposed flowfield for rotor Z/D=0.45 and longitudinal measurement plane Y/D=-0.3

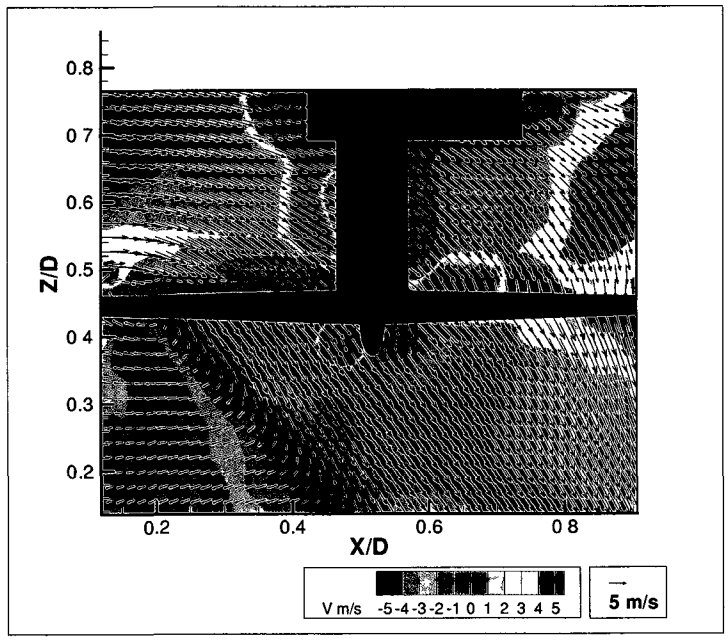

Figure 196: Generated superimposed flowfield for rotor Z/D=0.45 and longitudinal measurement plane Y/D=-0.2

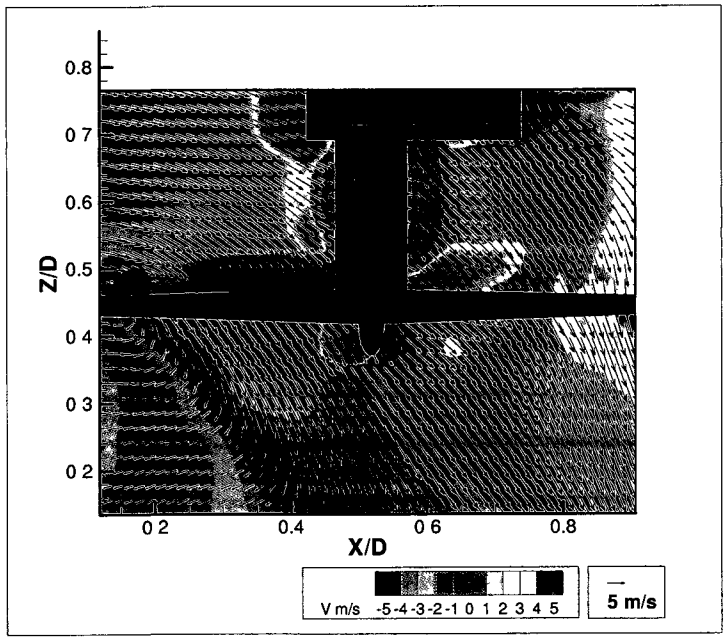

Figure 197: Generated superimposed flowfield for rotor Z/D=0.45 and longitudinal measurement plane Y/D=-0.1

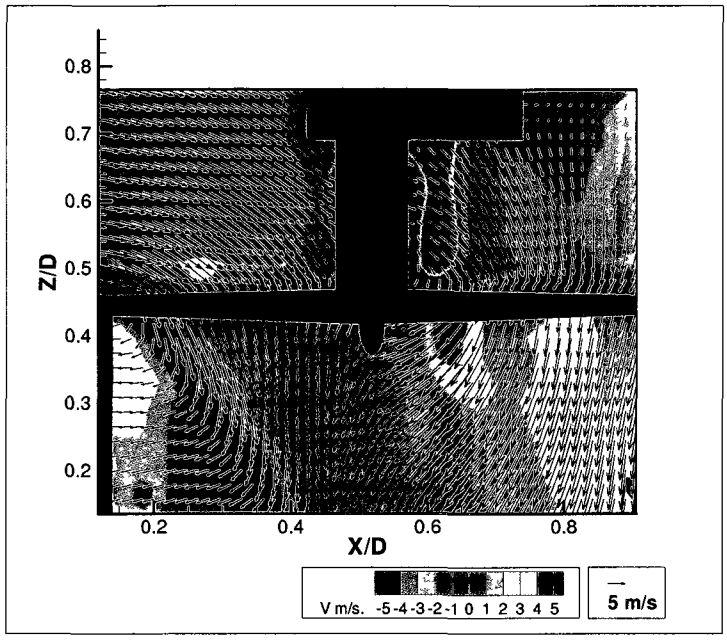

Figure 198: Generated superimposed flowfield for rotor Z/D=0.45 and longitudinal measurement plane Y/D=0.1

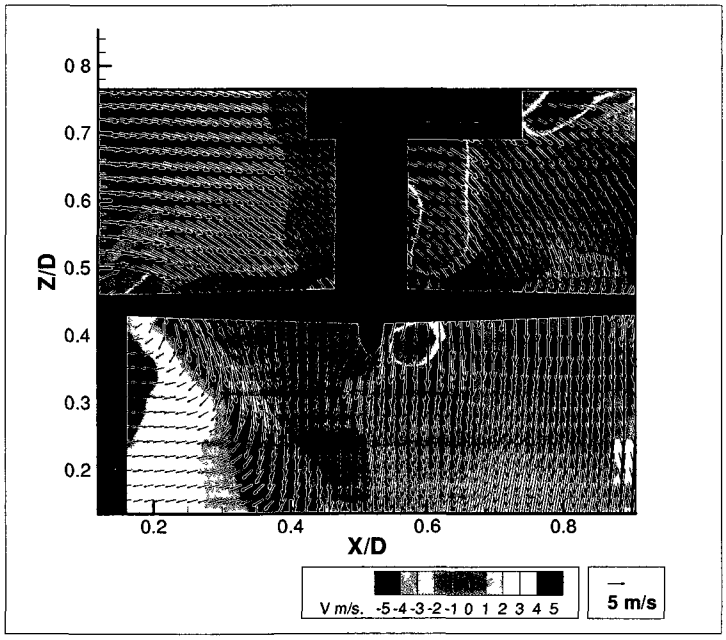

Figure 199: Generated superimposed flowfield for rotor Z/D=0.45 and longitudinal measurement plane Y/D=0.2

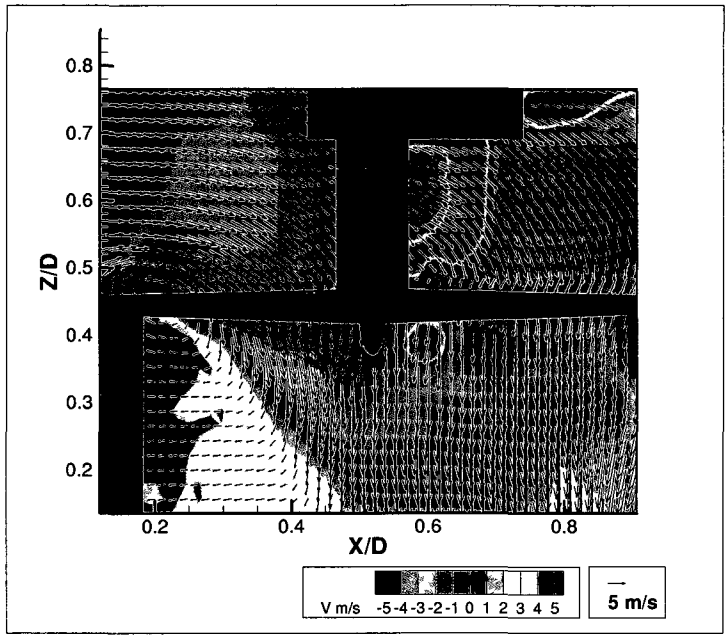

Figure 200: Generated superimposed flowfield for rotor Z/D=0.45 and longitudinal measurement plane Y/D=0.3

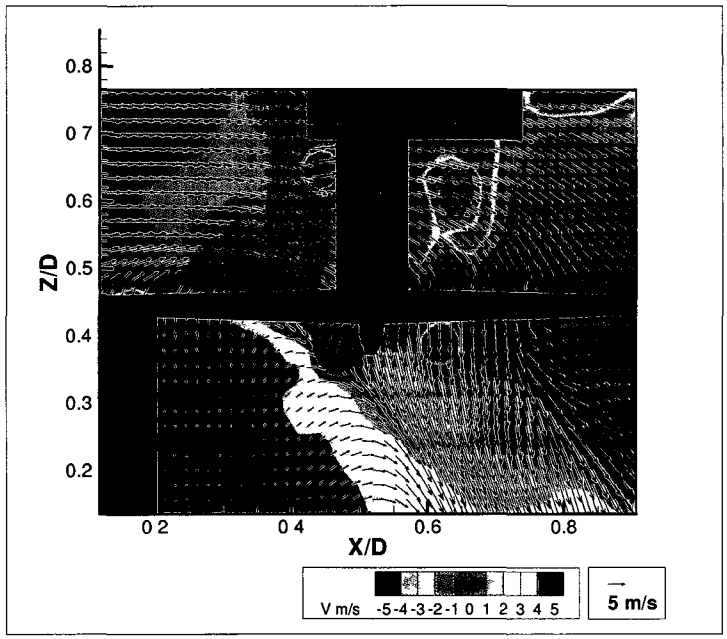

Figure 201: Generated superimposed flowfield for rotor Z/D=0.45 and longitudinal measurement plane Y/D=0.4

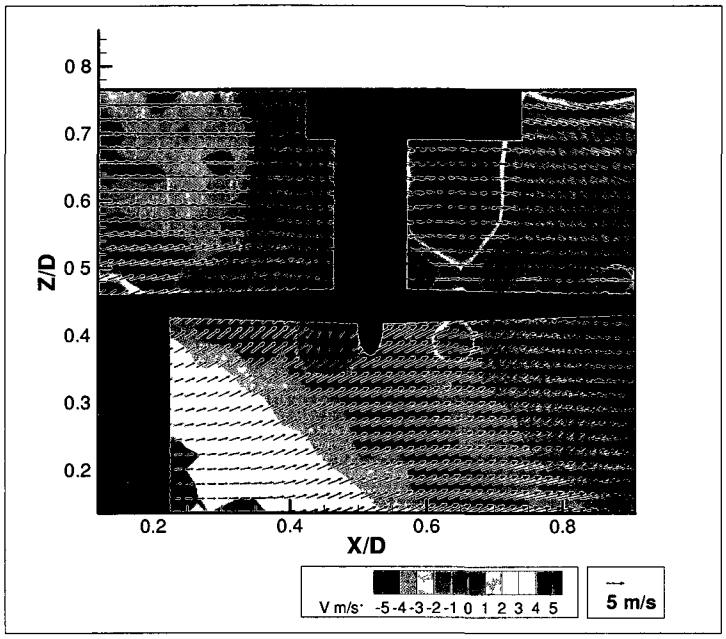

Figure 202: Generated superimposed flowfield for rotor Z/D=0.45 and longitudinal measurement plane Y/D=0.5

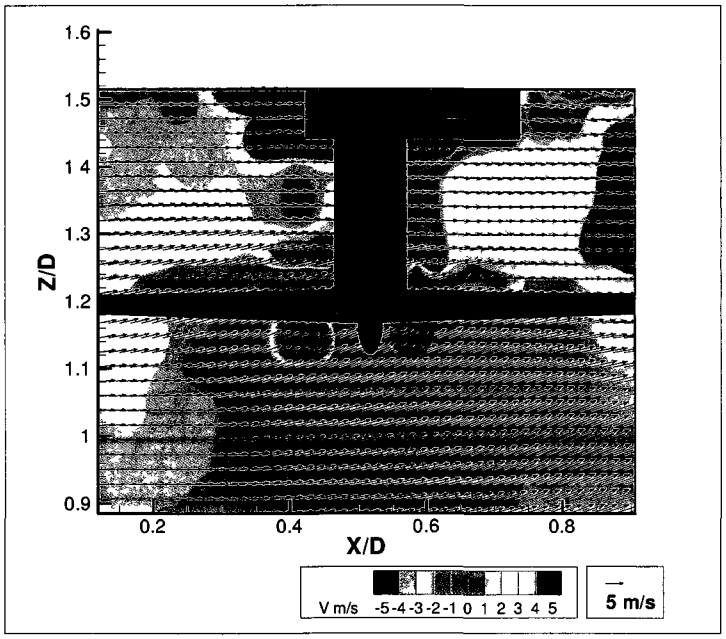

Figure 203: Generated superimposed flowfield for rotor Z/D=1.2 and longitudinal measurement plane Y/D=-0.5

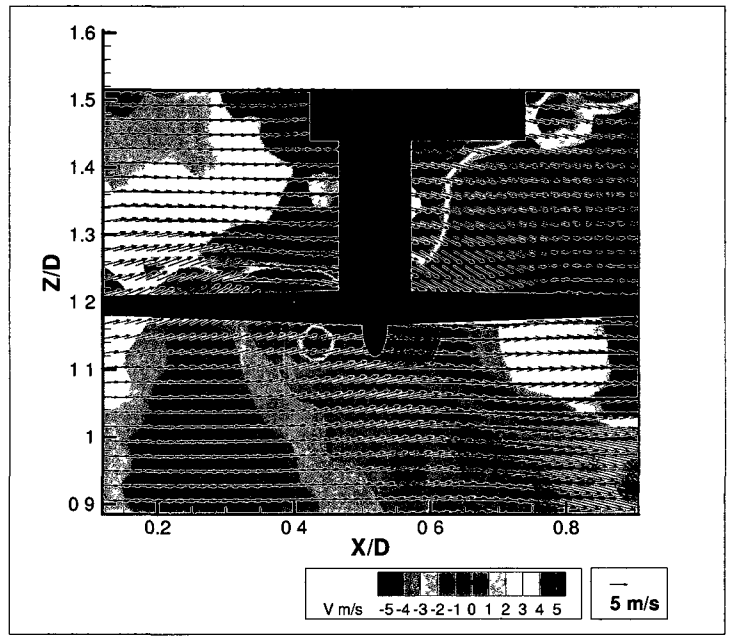

Figure 204: Generated superimposed flowfield for rotor Z/D=1.2 and longitudinal measurement plane Y/D=-0.4

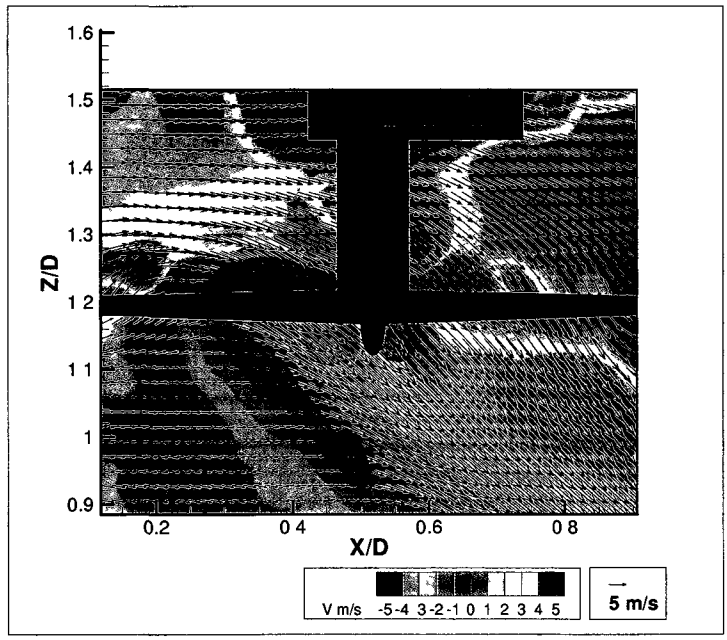

Figure 205: Generated superimposed flowfield for rotor Z/D=1.2 and longitudinal measurement plane Y/D=-0.3

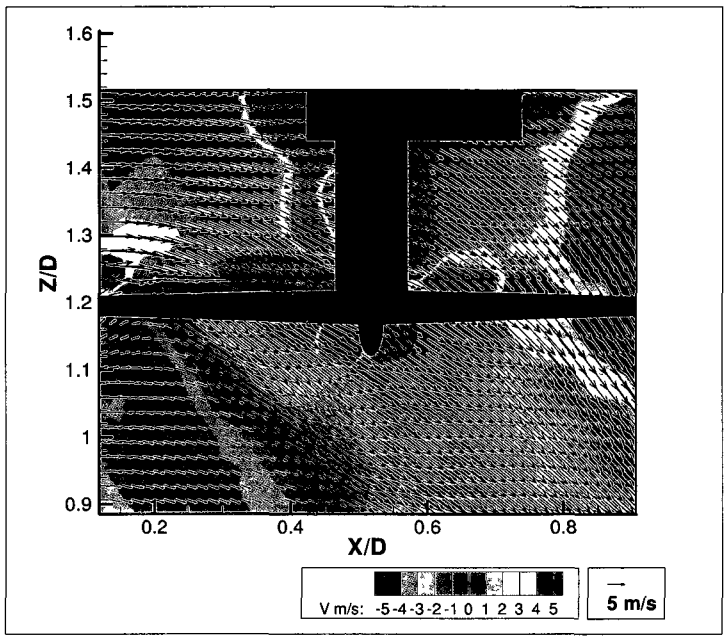

Figure 206: Generated superimposed flowfield for rotor Z/D=1.2 and longitudinal measurement plane Y/D=-0.2

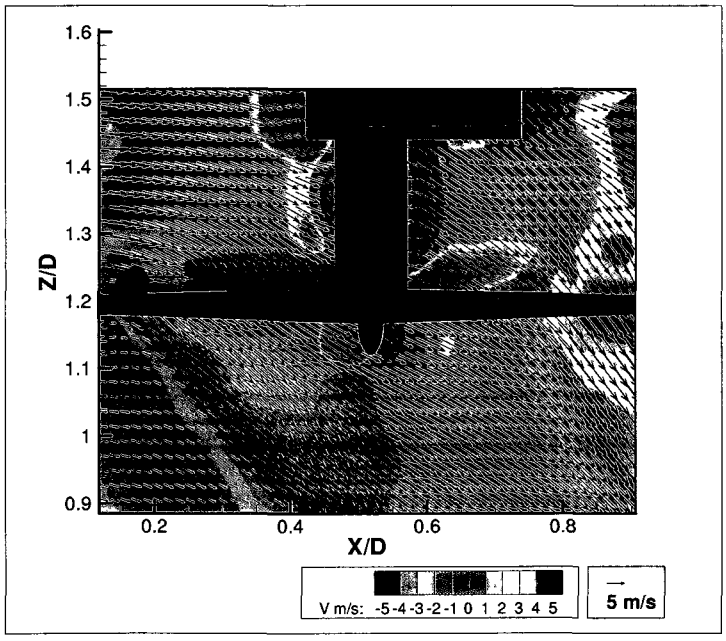

Figure 207: Generated superimposed flowfield for rotor Z/D=1.2 and longitudinal measurement plane Y/D=-0.1

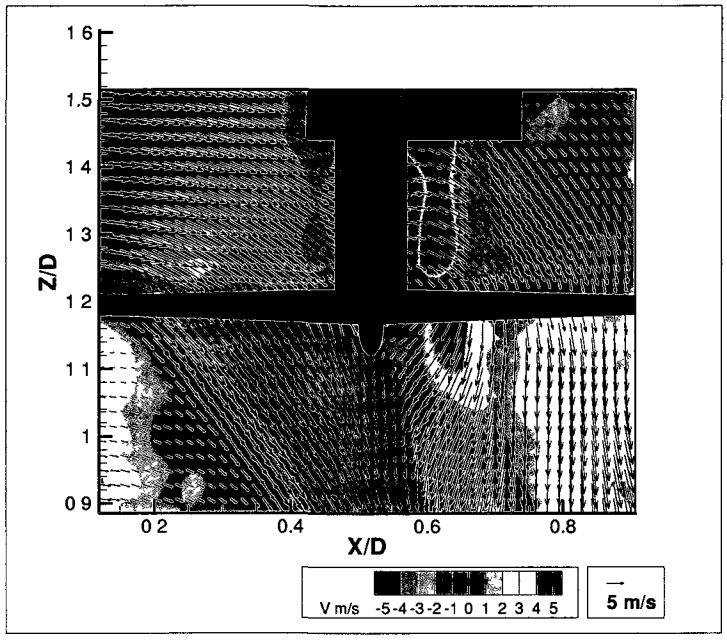

Figure 208: Generated superimposed flowfield for rotor Z/D=1.2 and longitudinal measurement plane Y/D=0.1

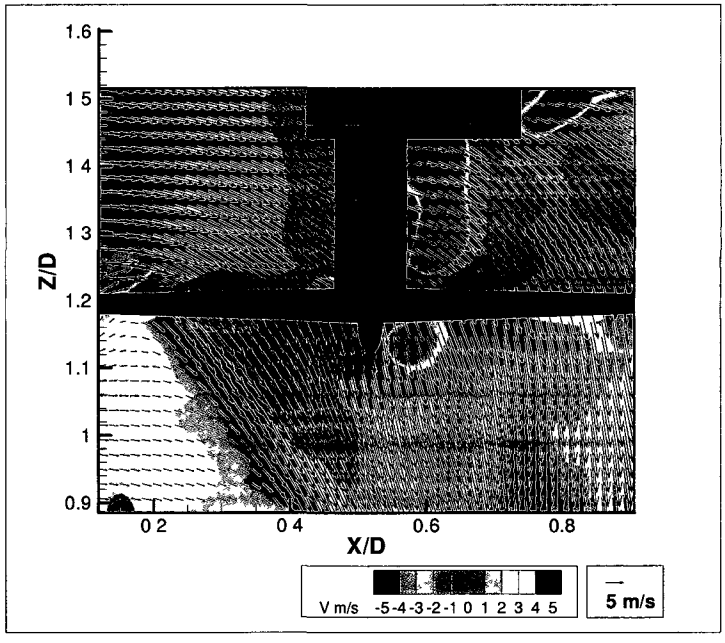

Figure 209: Generated superimposed flowfield for rotor Z/D=1.2 and longitudinal measurement plane Y/D=0.2

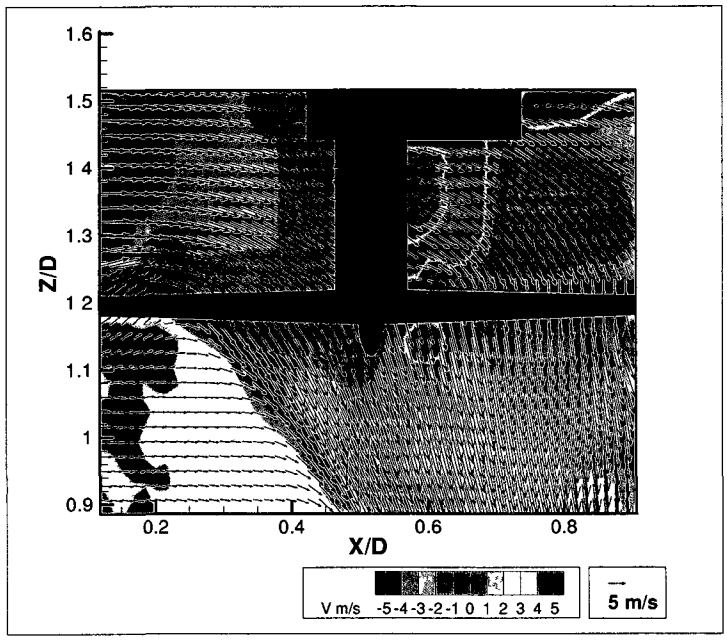

Figure 210: Generated superimposed flowfield for rotor Z/D=1.2 and longitudinal measurement plane Y/D=0.3

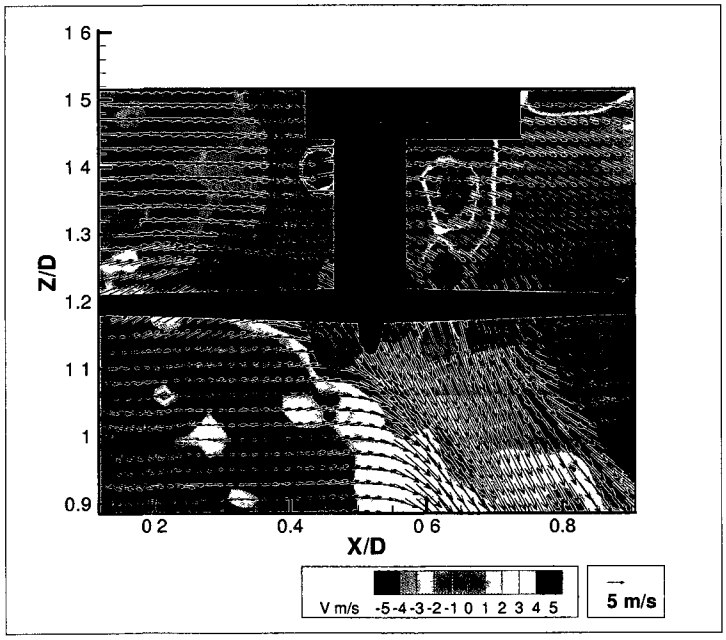

Figure 211: Generated superimposed flowfield for rotor Z/D=1.2 and longitudinal measurement plane Y/D=0.4

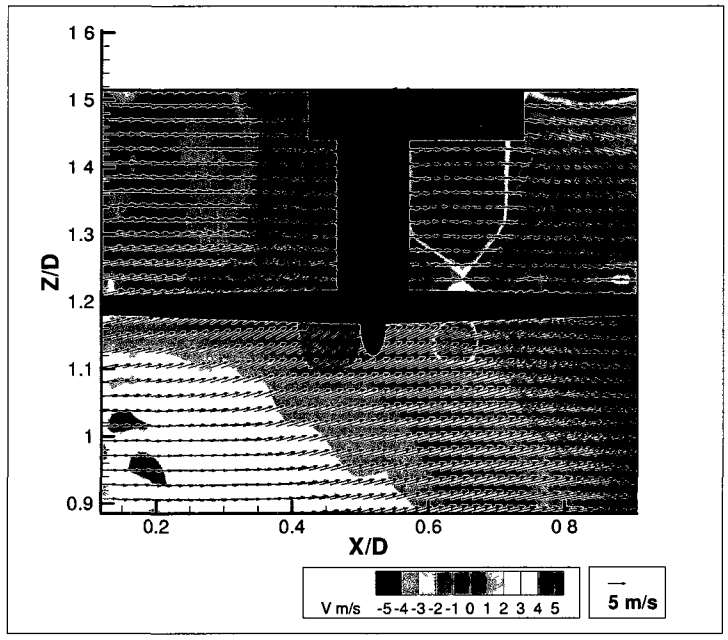

Figure 212: Generated superimposed flowfield for rotor Z/D=1.2 and longitudinal measurement plane Y/D=0.5

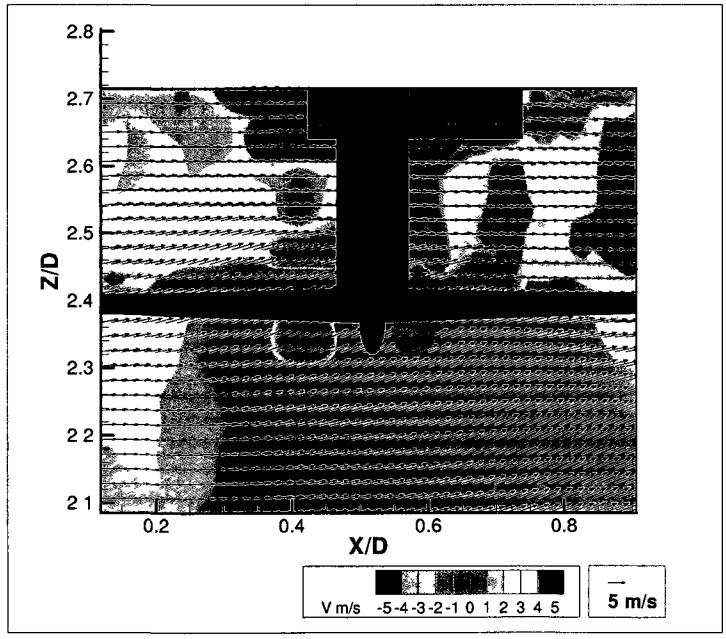

Figure 213: Generated superimposed flowfield for rotor Z/D=2.4 and longitudinal measurement plane Y/D=-0.5

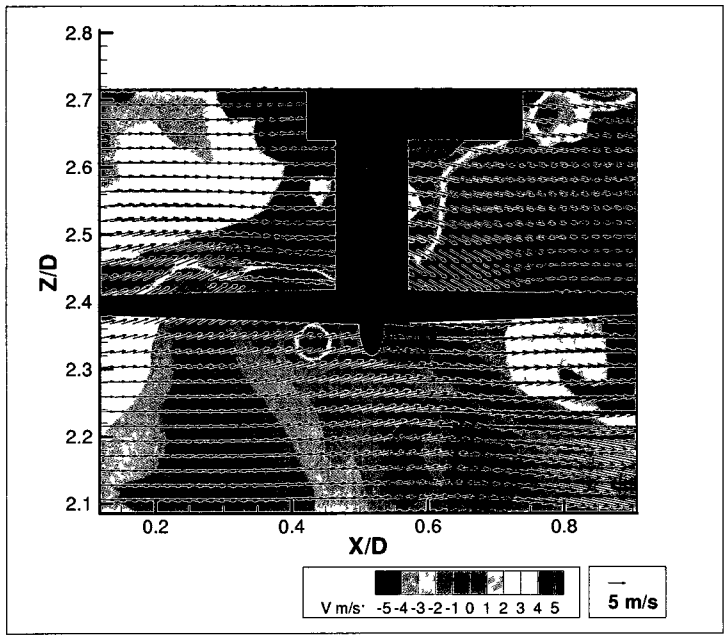

Figure 214: Generated superimposed flowfield for rotor Z/D=2.4 and longitudinal measurement plane Y/D=-0.4

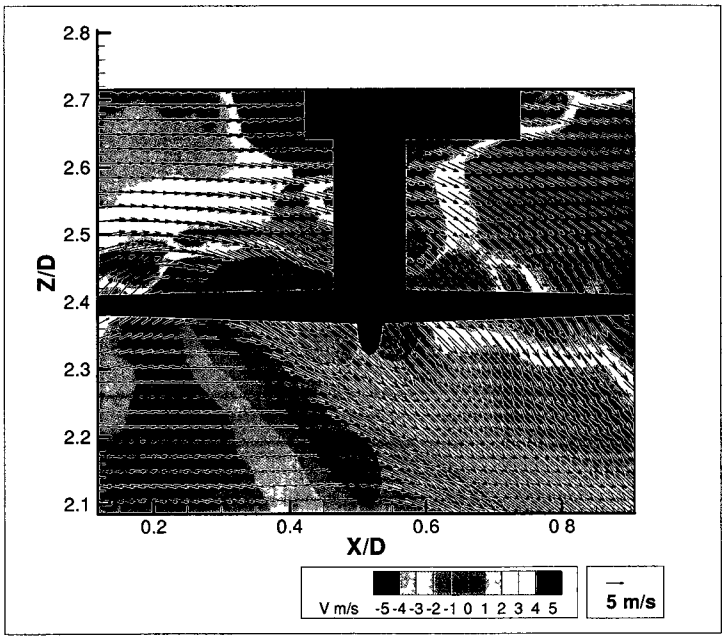

Figure 215: Generated superimposed flowfield for rotor Z/D=2.4 and longitudinal measurement plane Y/D=-0.3

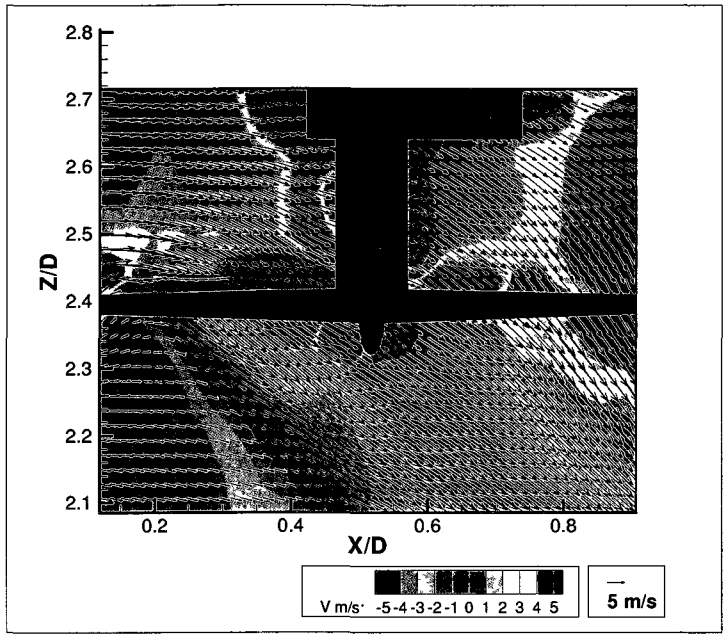

Figure 216: Generated superimposed flowfield for rotor Z/D=2.4 and longitudinal measurement plane Y/D=-0.2

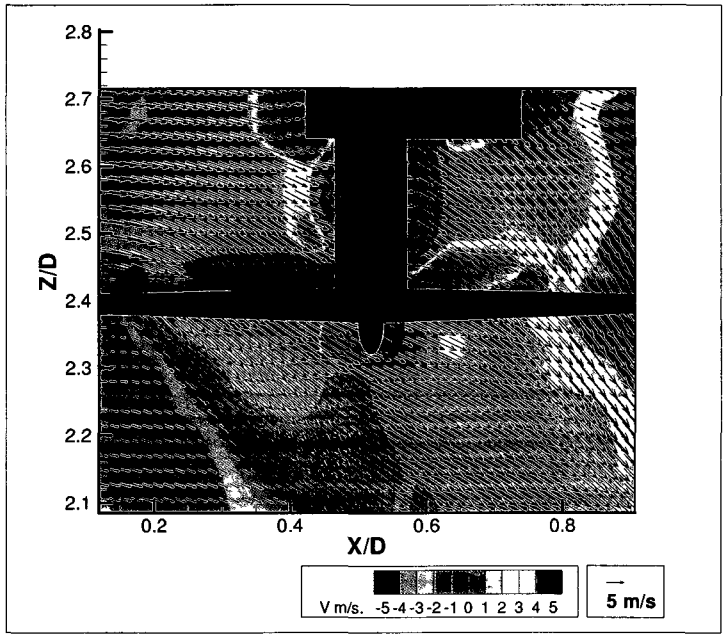

Figure 217: Generated superimposed flowfield for rotor Z/D=2.4 and longitudinal measurement plane Y/D=-0.1

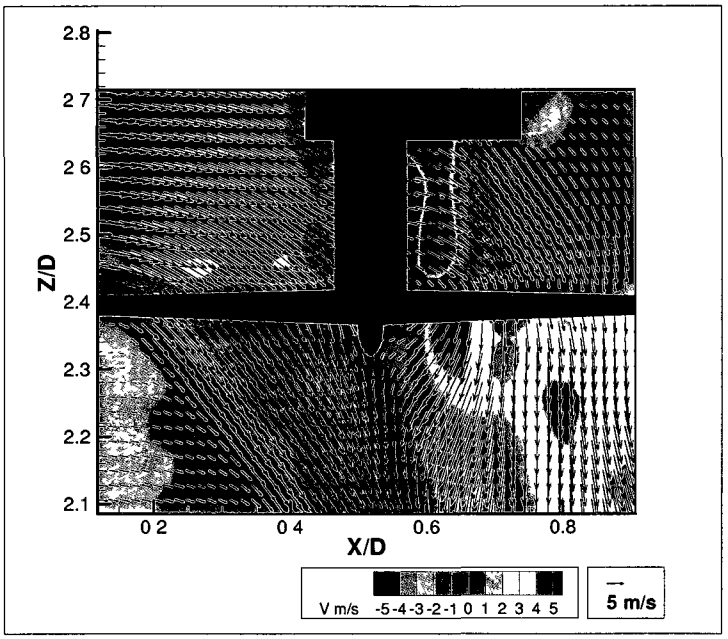

Figure 218: Generated superimposed flowfield for rotor Z/D=2.4 and longitudinal measurement plane Y/D=0.1

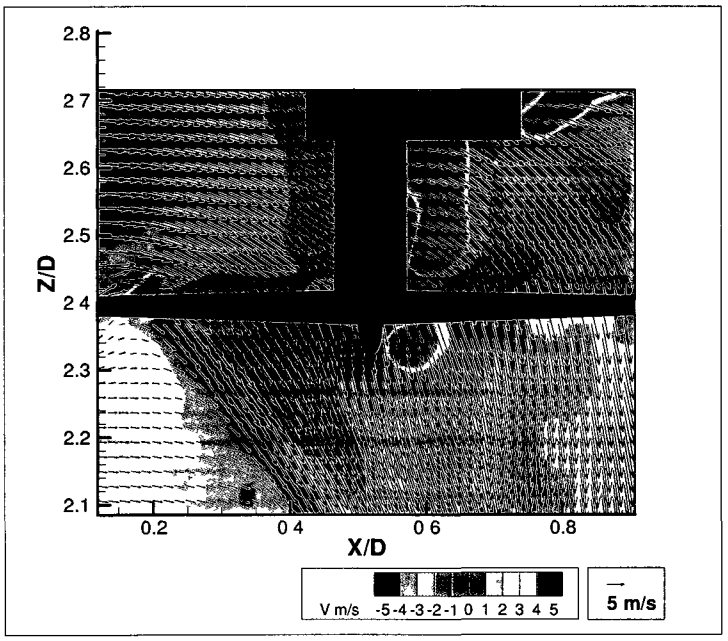

Figure 219: Generated superimposed flowfield for rotor Z/D=2.4 and longitudinal measurement plane Y/D=0.2

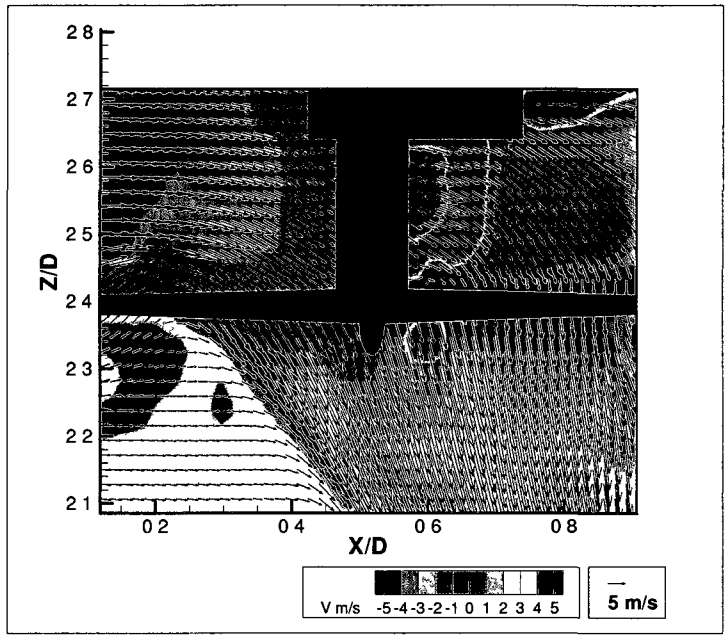

Figure 220: Generated superimposed flowfield for rotor Z/D=2.4 and longitudinal measurement plane Y/D=0.3

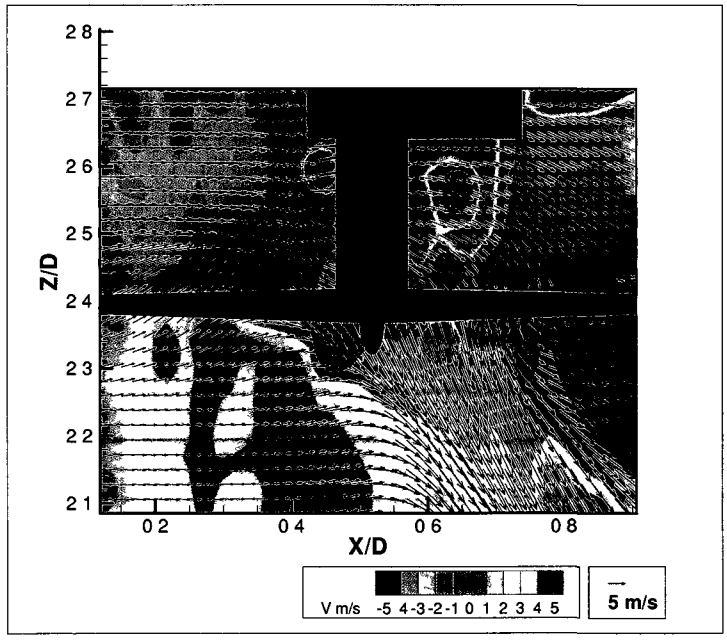

Figure 221: Generated superimposed flowfield for rotor Z/D=2.4 and longitudinal measurement plane Y/D=0.4

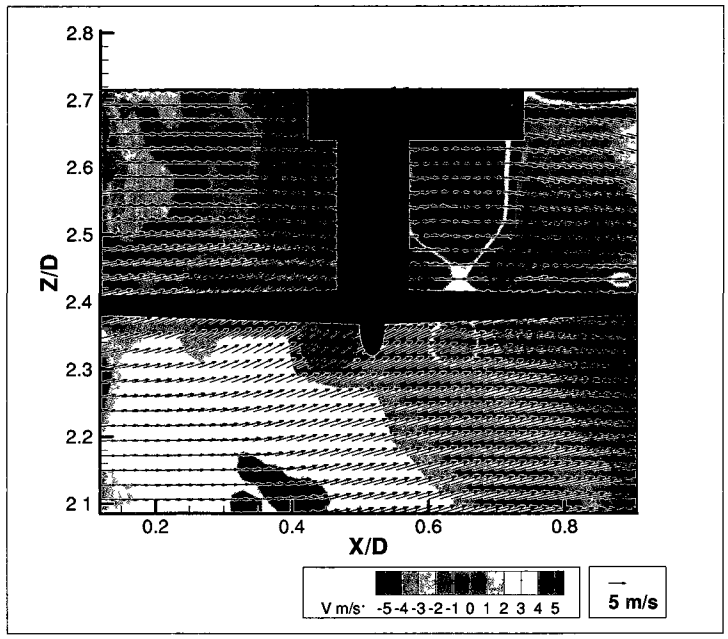

Figure 222: Generated superimposed flowfield for rotor Z/D=2.4 and longitudinal measurement plane Y/D=0.5

APPENDIX L: U-Velocity Component Discrepancies for a Longitudinal Rotor Location of X/D=0.5125

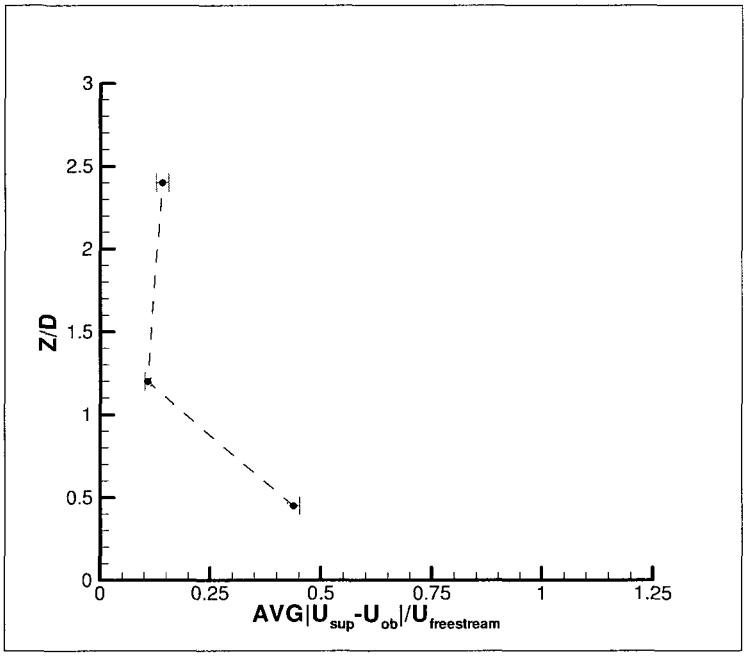

Figure 223: U-Velocity discrepancy versus rotor height above deck for rotor location X/D=0.5125 and Y/D=-0.5

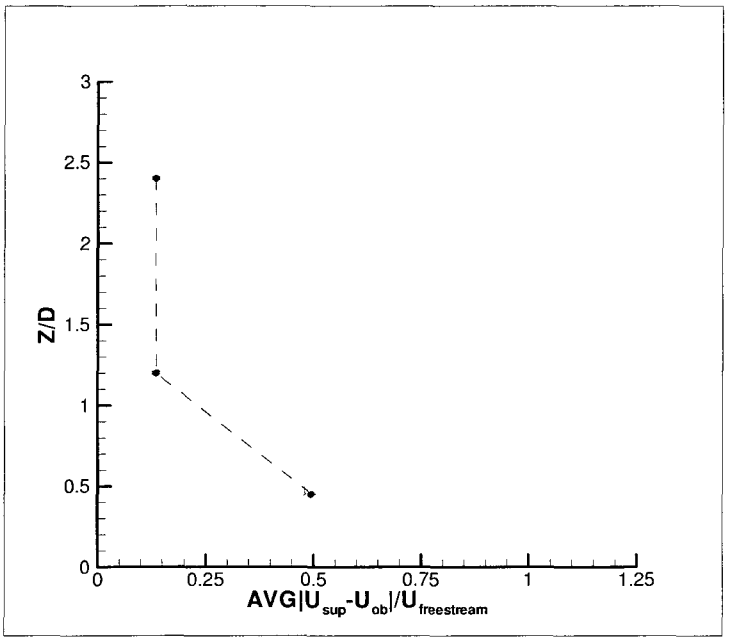

Figure 224: U-Velocity discrepancy versus rotor height above deck for rotor location X/D=0.5125 and Y/D=-0.4

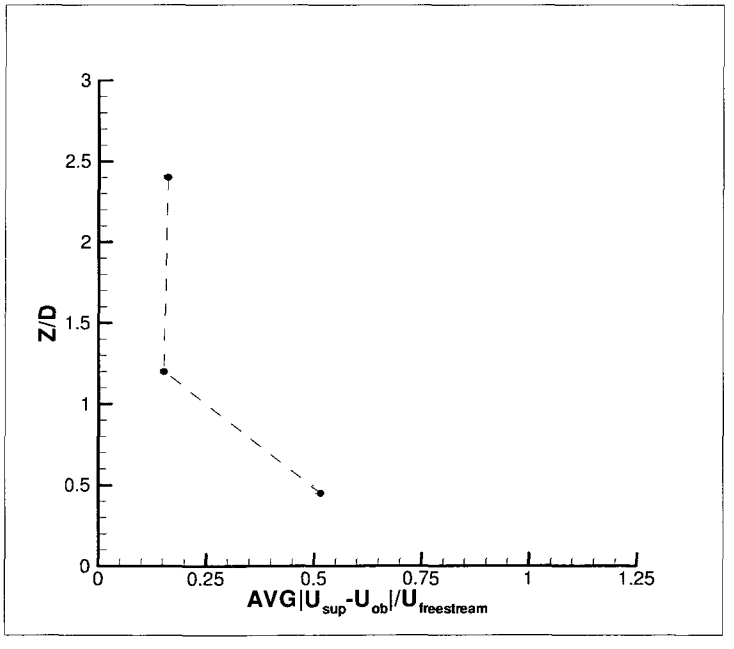

Figure 225: U-Velocity discrepancy versus rotor height above deck for rotor location X/D=0.5125 and Y/D=-0.3

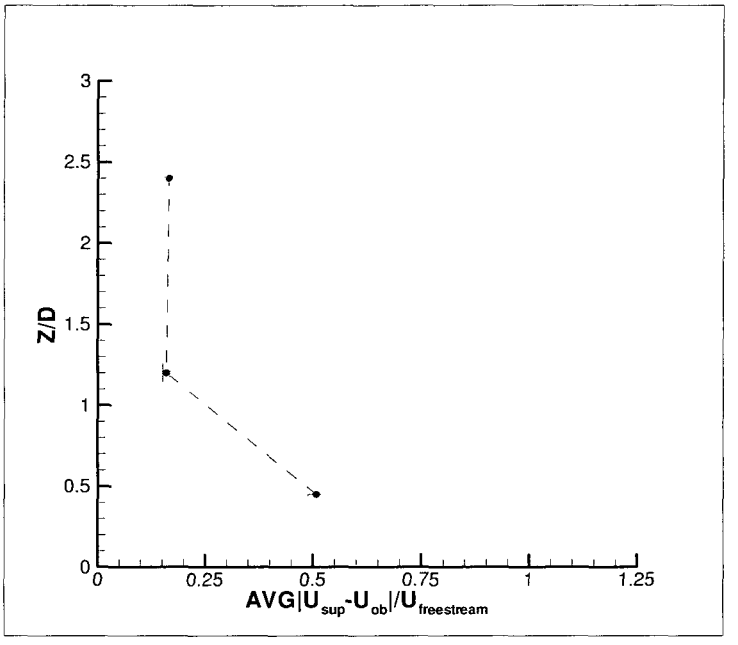

Figure 226: U-Velocity discrepancy versus rotor height above deck for rotor location X/D=0.5125 and Y/D=-0.2

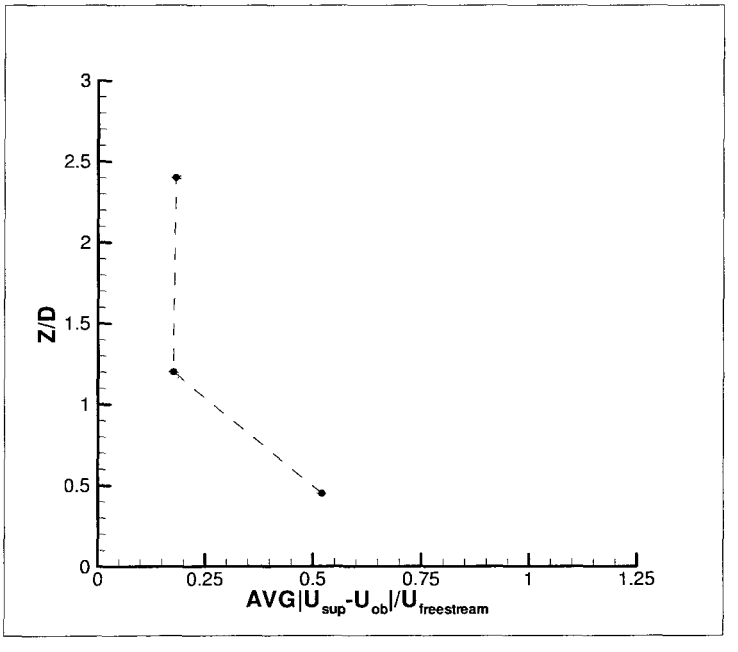

Figure 227: U-Velocity discrepancy versus rotor height above deck for rotor location X/D=0.5125 and Y/D=-0.1

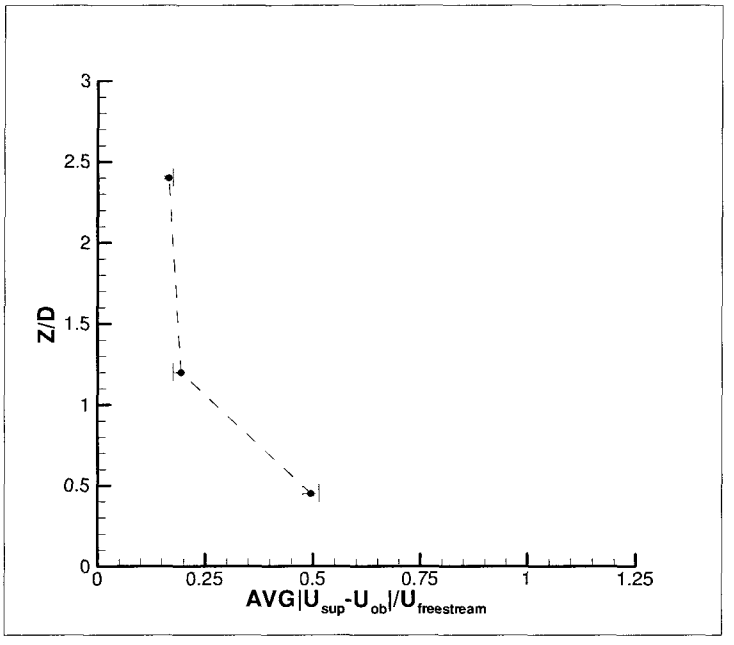

Figure 228: U-Velocity discrepancy versus rotor height above deck for rotor location X/D=0.5125 and Y/D=0.0

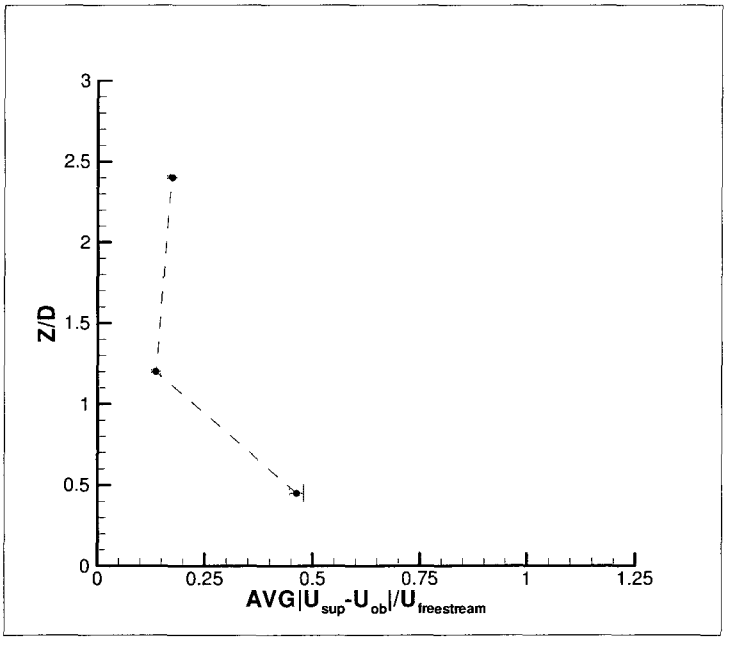

Figure 229: U-Velocity discrepancy versus rotor height above deck for rotor location X/D=0.5125 and Y/D=0.1

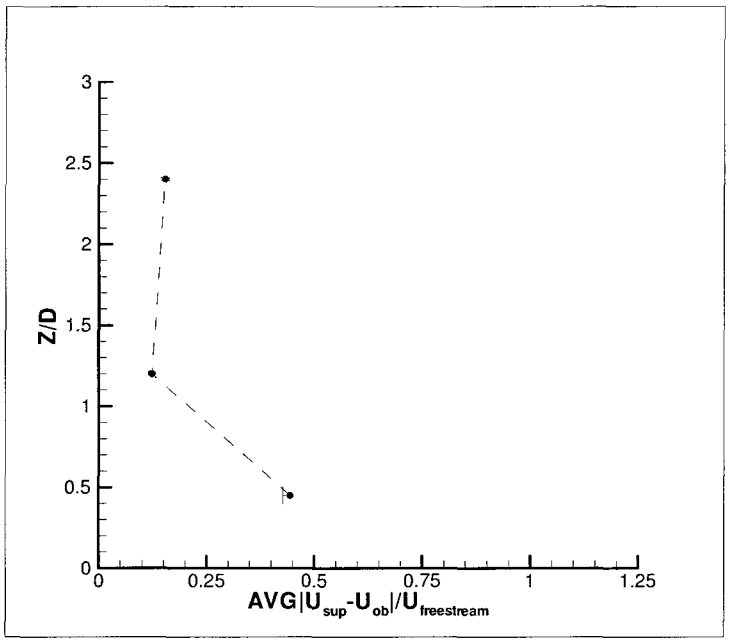

Figure 230: U-Velocity discrepancy versus rotor height above deck for rotor location X/D=0.5125 and Y/D=0.2

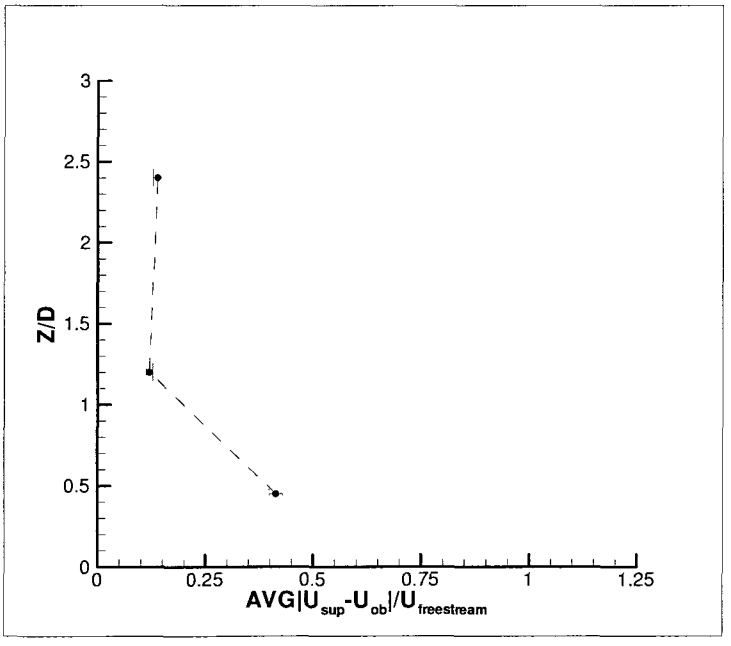

Figure 231: U-Velocity discrepancy versus rotor height above deck for rotor location X/D=0.5125 and Y/D=0.3

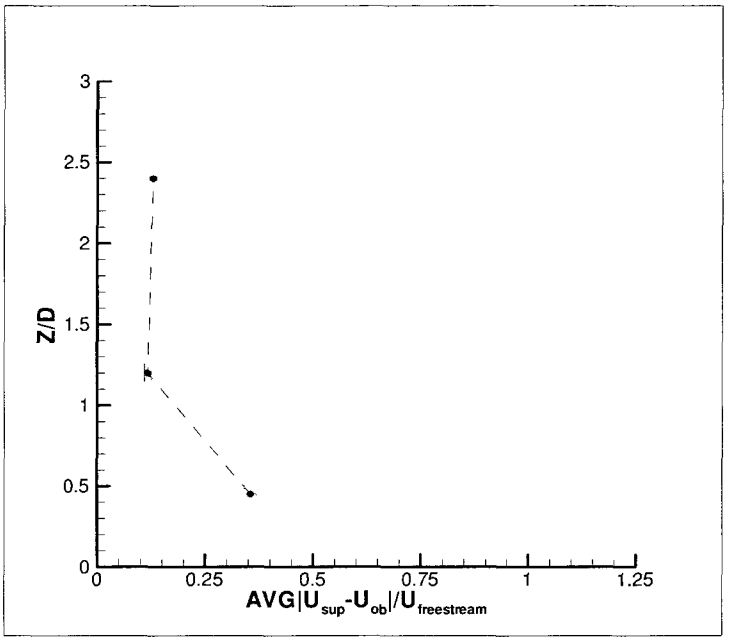

Figure 232: U-Velocity discrepancy versus rotor height above deck for rotor location X/D=0.5125 and Y/D=0.4

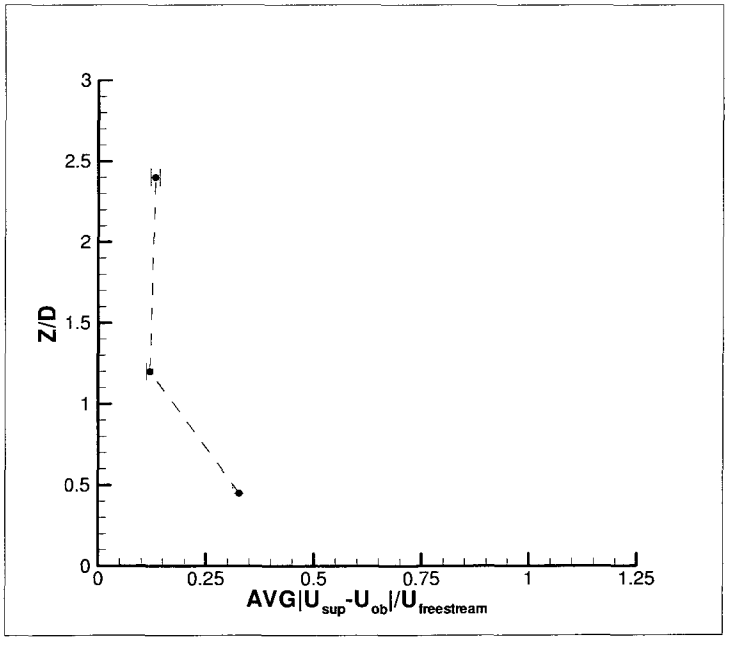

Figure 233: U-Velocity discrepancy versus rotor height above deck for rotor location X/D=0.5125 and Y/D=0.5

APPENDIX M: V-Velocity Component Discrepancies for a Longitudinal Rotor Location of X/D=0.5125

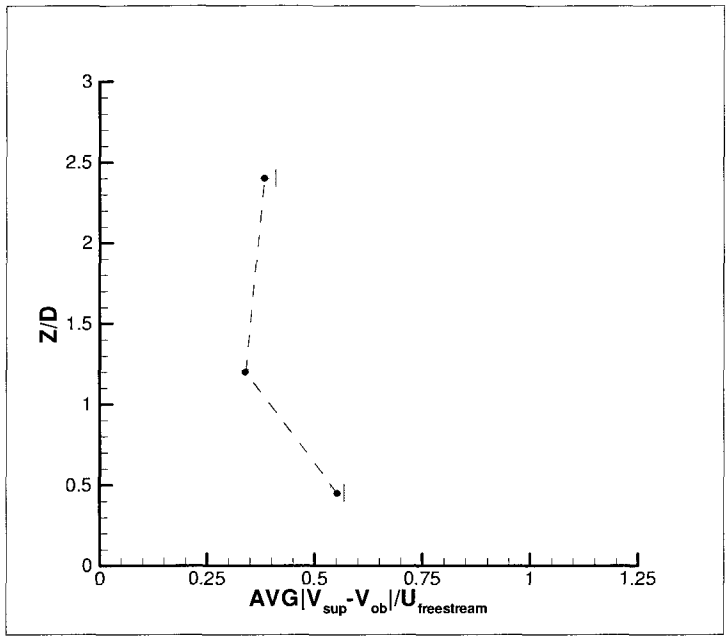

Figure 234: V-Velocity discrepancy versus rotor height above deck for rotor location X/D=0.5125 and Y/D=-0.5

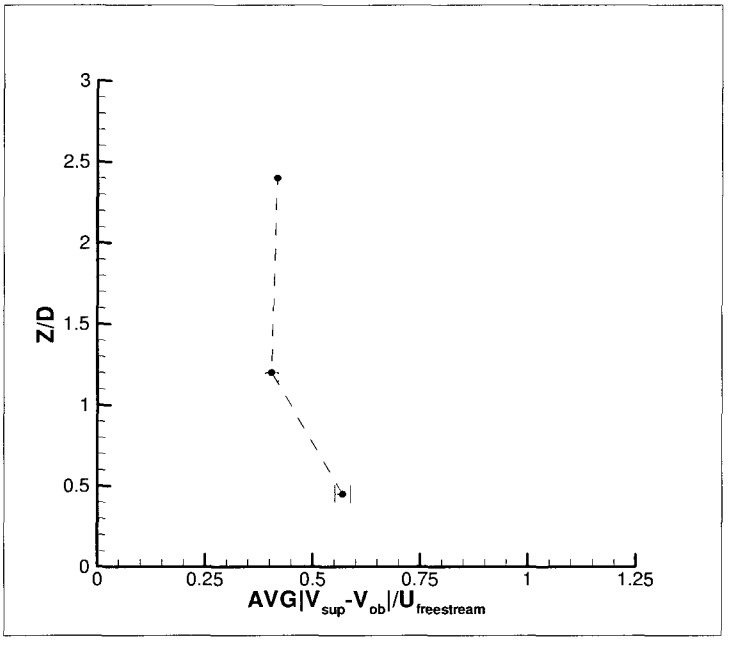

Figure 235: V-Velocity discrepancy versus rotor height above deck for rotor location X/D=0.5125 and Y/D=-0.4

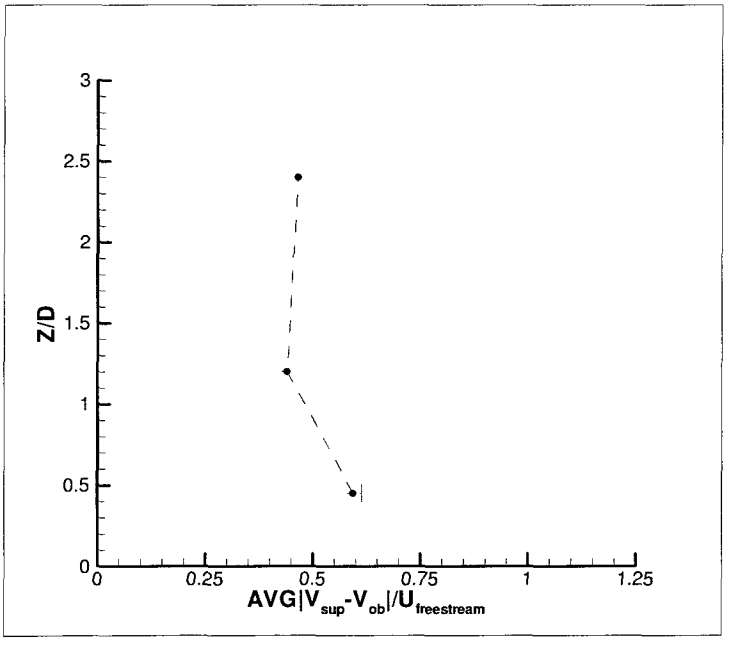

Figure 236: V-Velocity discrepancy versus rotor height above deck for rotor location X/D=0.5125 and Y/D=-0.3

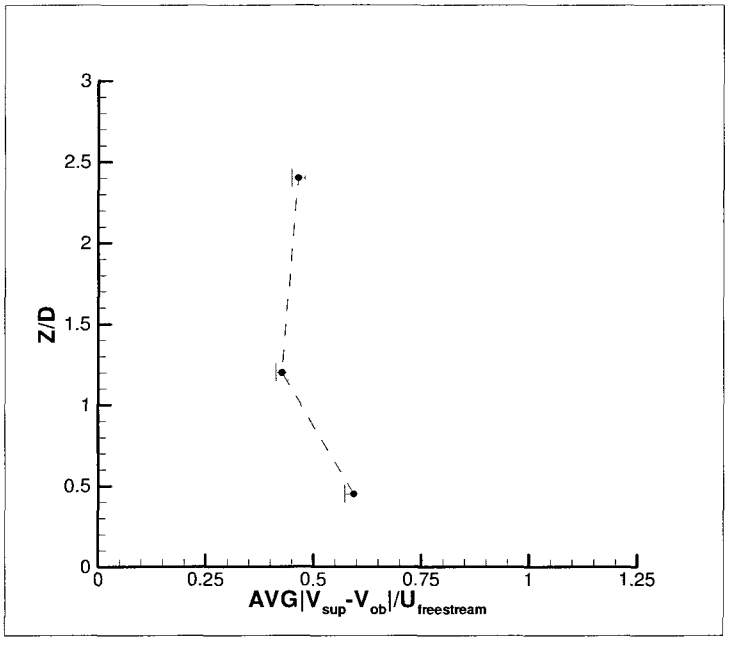

Figure 237: V-Velocity discrepancy versus rotor height above deck for rotor location X/D=0.5125 and Y/D=-0.2

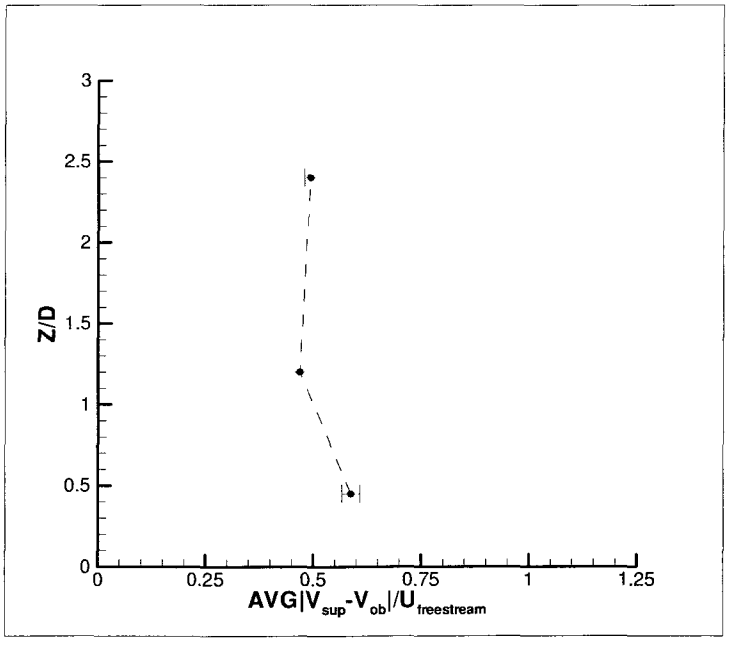

Figure 238: V-Velocity discrepancy versus rotor height above deck for rotor location X/D=0.5125 and Y/D=-0.1

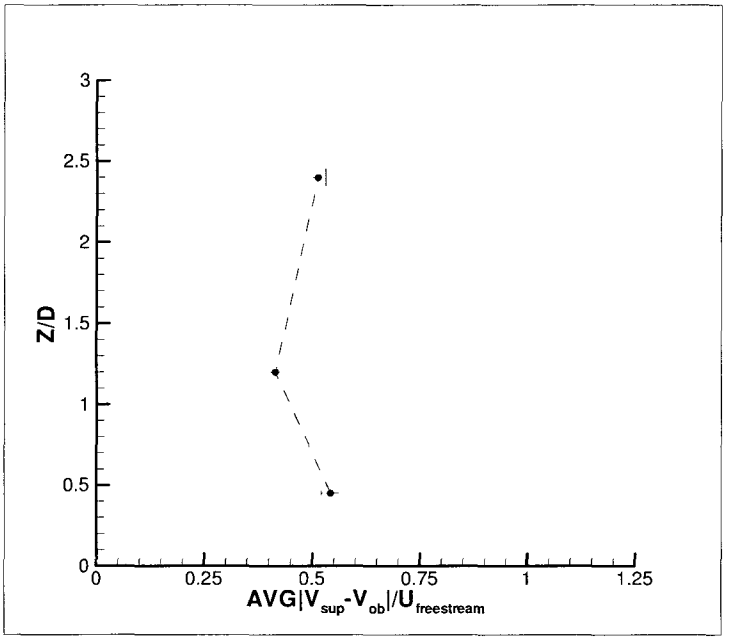

Figure 239: V-Velocity discrepancy versus rotor height above deck for rotor location X/D=0.5125 and Y/D=0.0

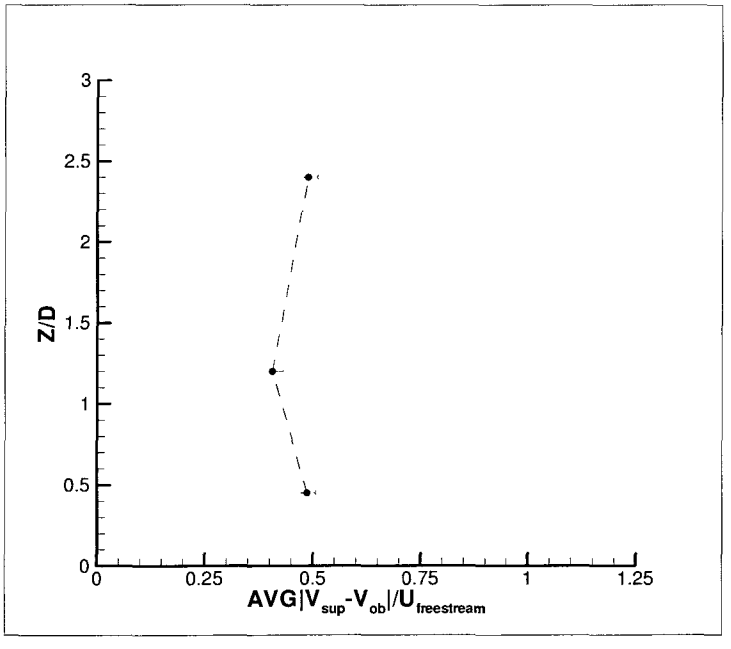

Figure 240: V-Velocity discrepancy versus rotor height above deck for rotor location X/D=0.5125 and Y/D=0.1

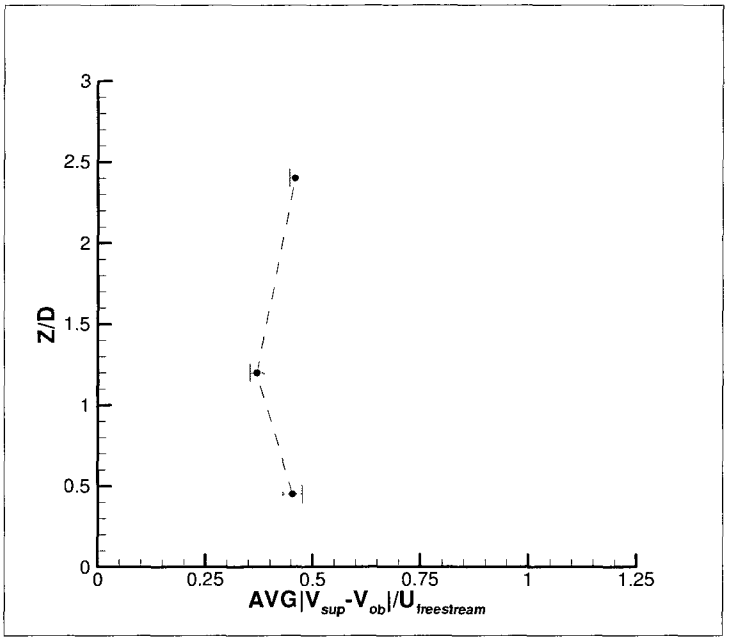

Figure 241: V-Velocity discrepancy versus rotor height above deck for rotor location X/D=0.5125 and Y/D=0.2

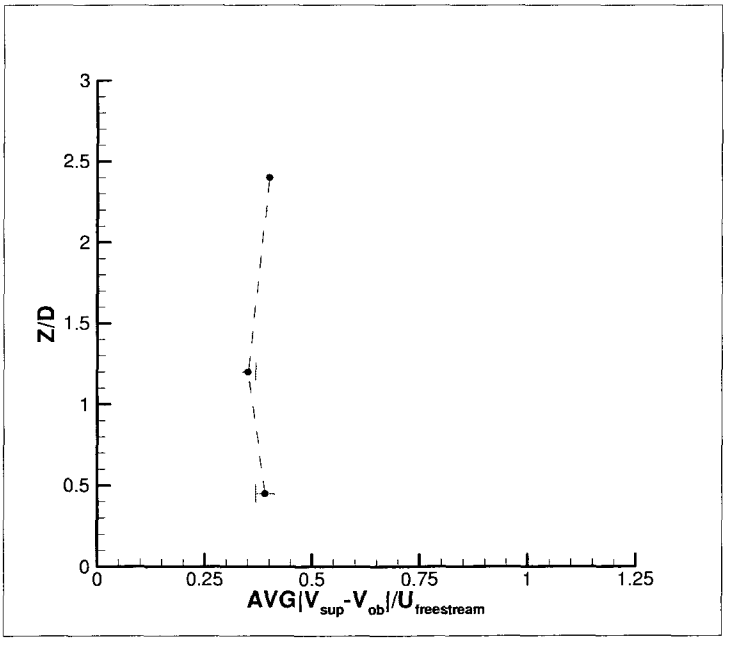

Figure 242: V-Velocity discrepancy versus rotor height above deck for rotor location X/D=0.5125 and Y/D=0.3

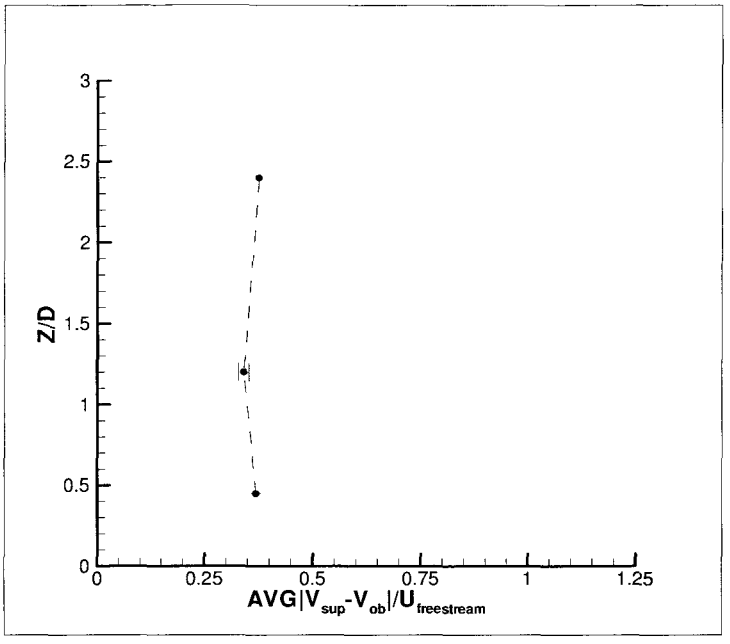

Figure 243: V-Velocity discrepancy versus rotor height above deck for rotor location X/D=0.5125 and Y/D=0.4

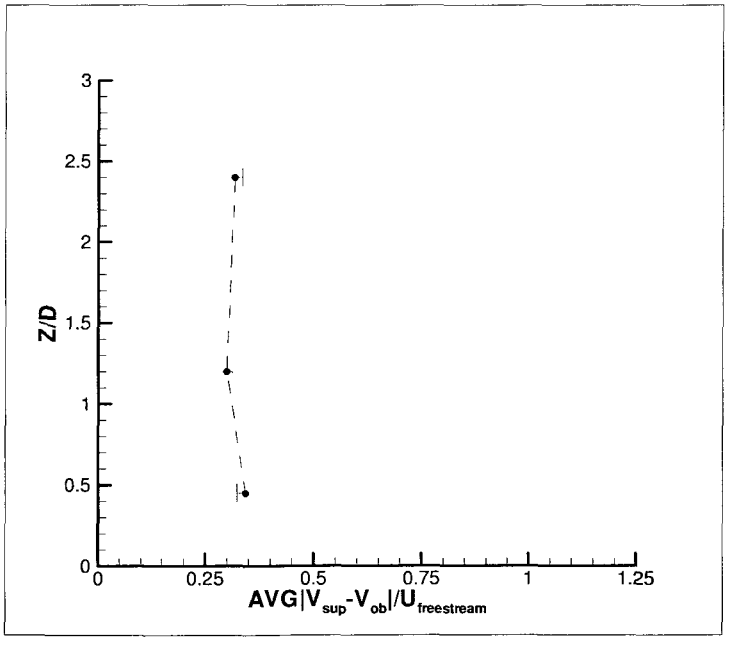

Figure 244: V-Velocity discrepancy versus rotor height above deck for rotor location X/D=0.5125 and Y/D=0.5

APPENDIX N: W-Velocity Component Discrepancies for a Longitudinal Rotor Location of X/D=0.5125

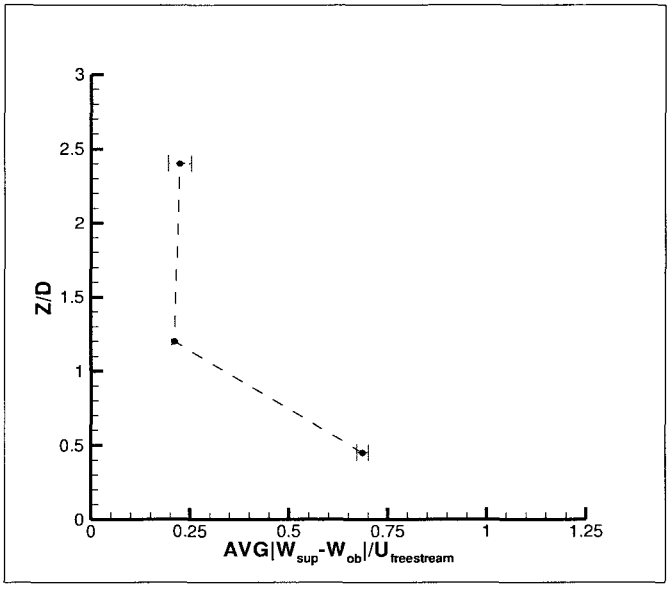

Figure 245: W-Velocity discrepancy versus rotor height above deck for rotor location X/D=0.5125 and Y/D=-0.5

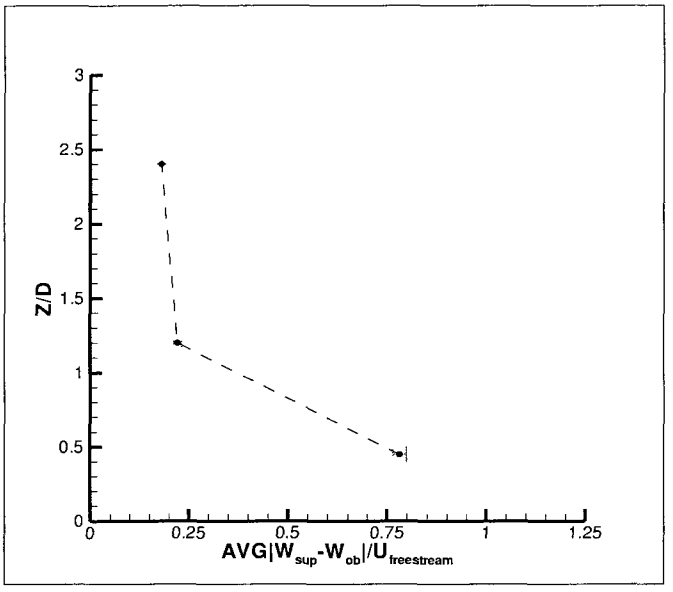

Figure 246: W-Velocity discrepancy versus rotor height above deck for rotor location X/D=0.5125 and Y/D=-0.4

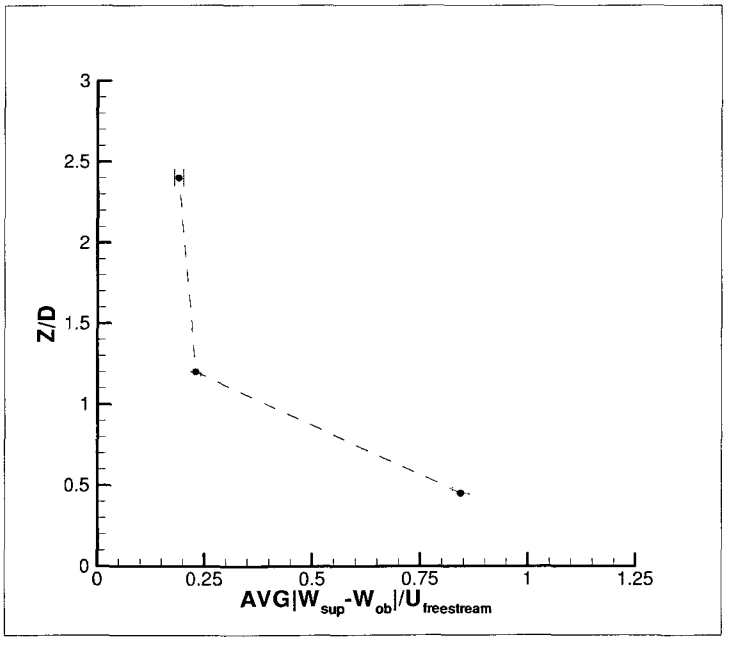

Figure 247: W-Velocity discrepancy versus rotor height above deck for rotor location X/D=0.5125 and Y/D=-0.3

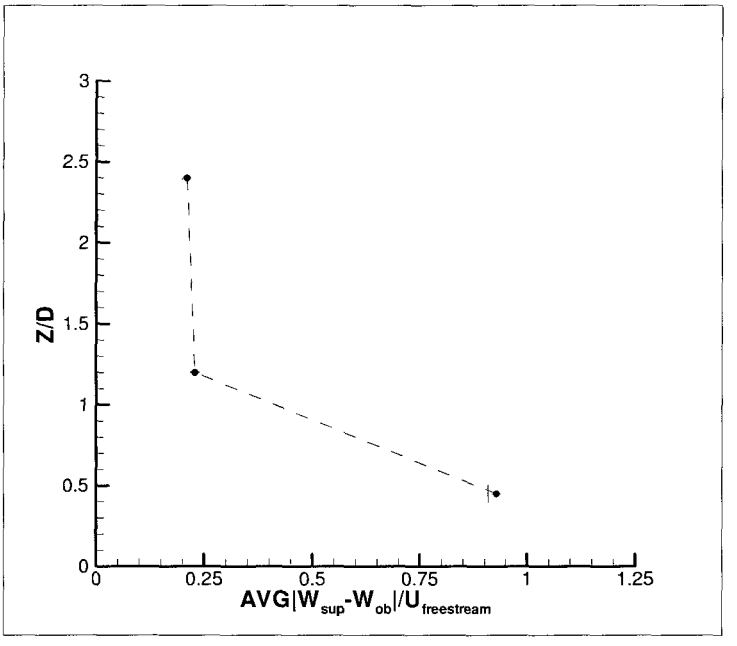

Figure 248: W-Velocity discrepancy versus rotor height above deck for rotor location X/D=0.5125 and Y/D=-0.2

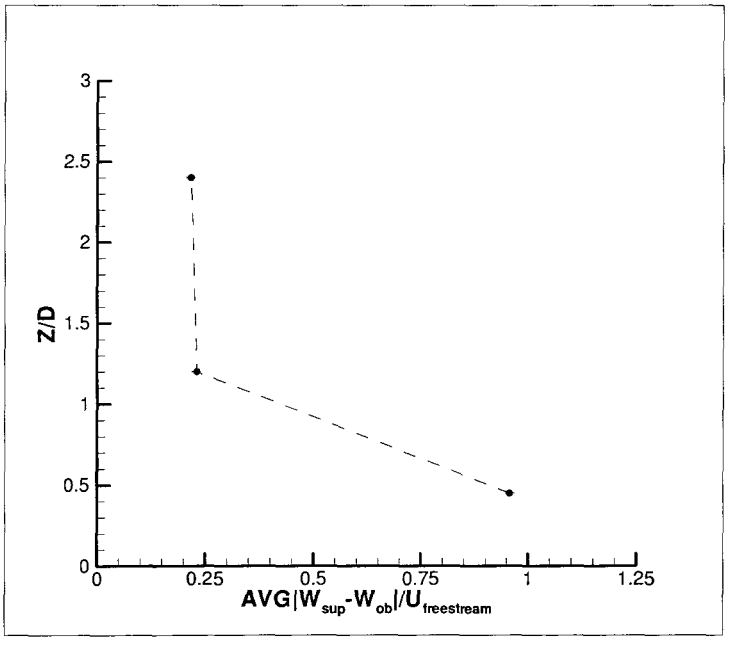

Figure 249: W-Velocity discrepancy versus rotor height above deck for rotor location X/D=0.5125 and Y/D=-0.1

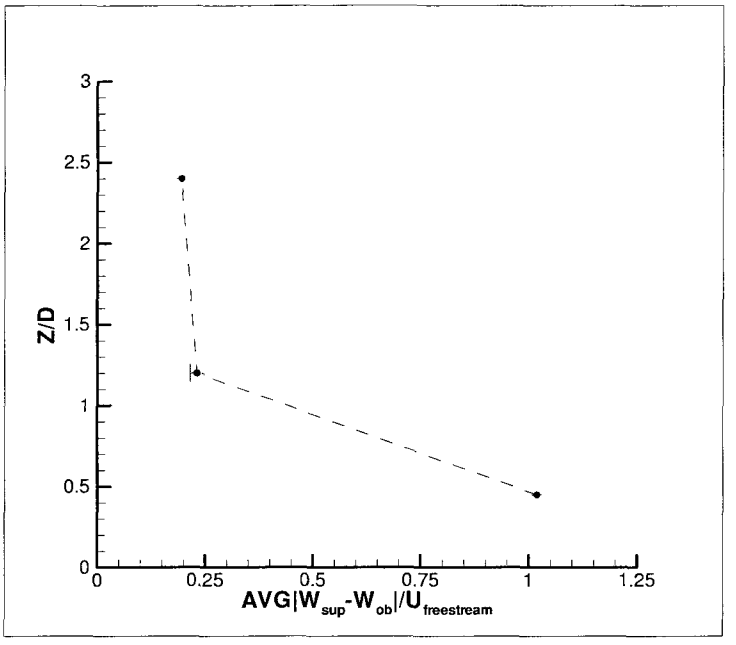

Figure 250: W-Velocity discrepancy versus rotor height above deck for rotor location X/D=0.5125 and Y/D=0.0

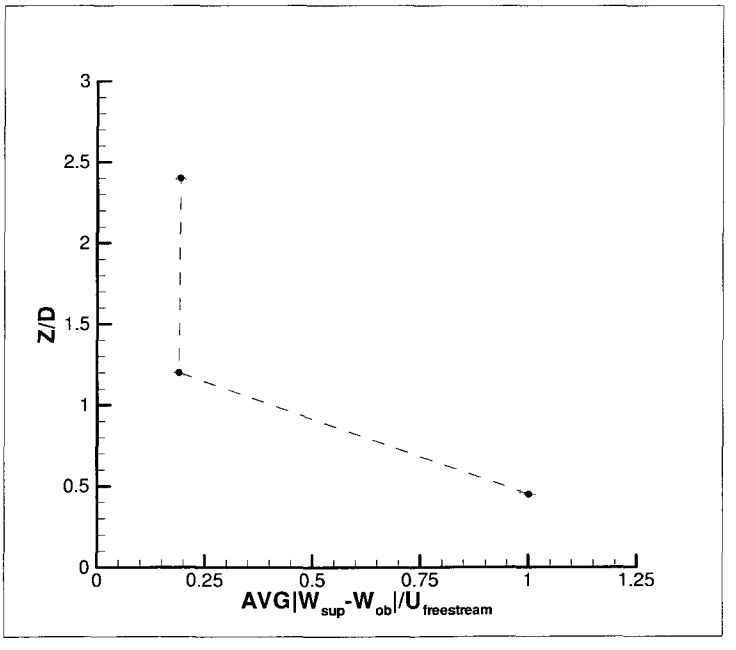

Figure 251: W-Velocity discrepancy versus rotor height above deck for rotor location X/D=0.5125 and Y/D=0.1

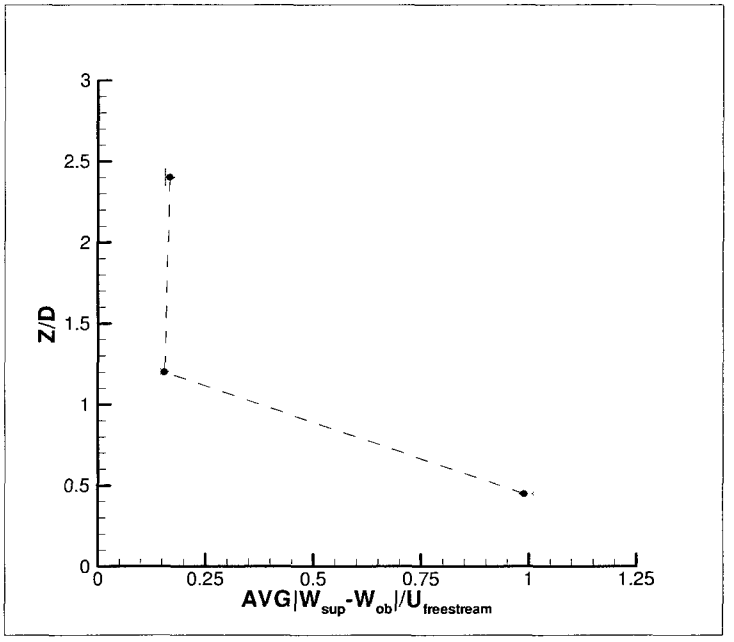

Figure 252: W-Velocity discrepancy versus rotor height above deck for rotor location X/D=0.5125 and Y/D=0.2

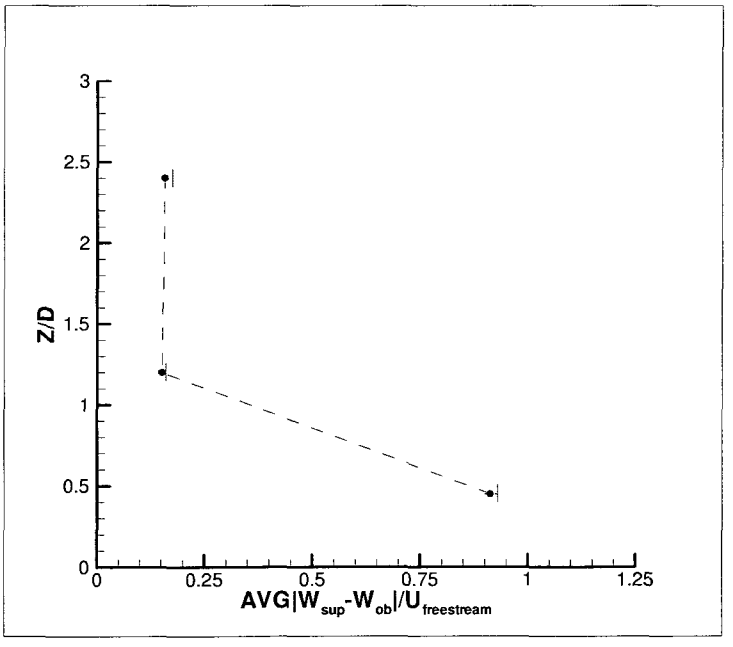

Figure 253: W-Velocity discrepancy versus rotor height above deck for rotor location X/D=0.5125 and Y/D=0.3

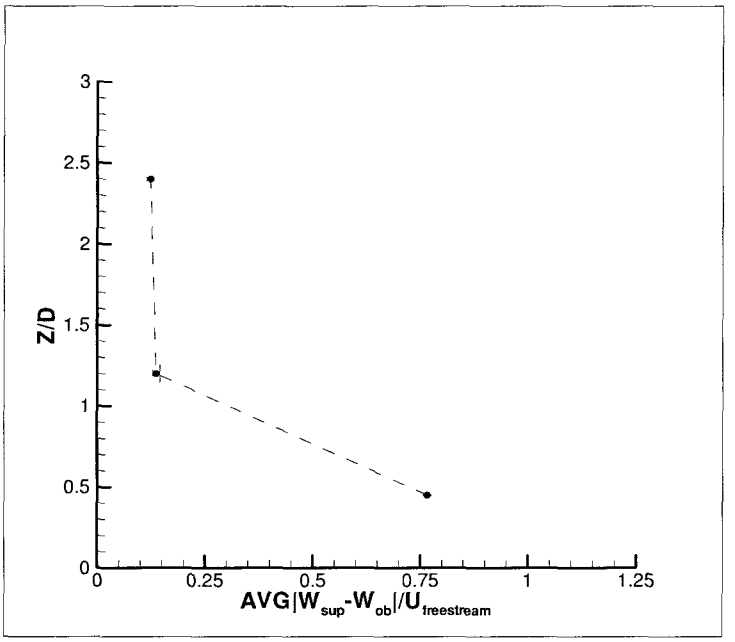

Figure 254: W-Velocity discrepancy versus rotor height above deck for rotor location X/D=0.5125 and Y/D=0.4

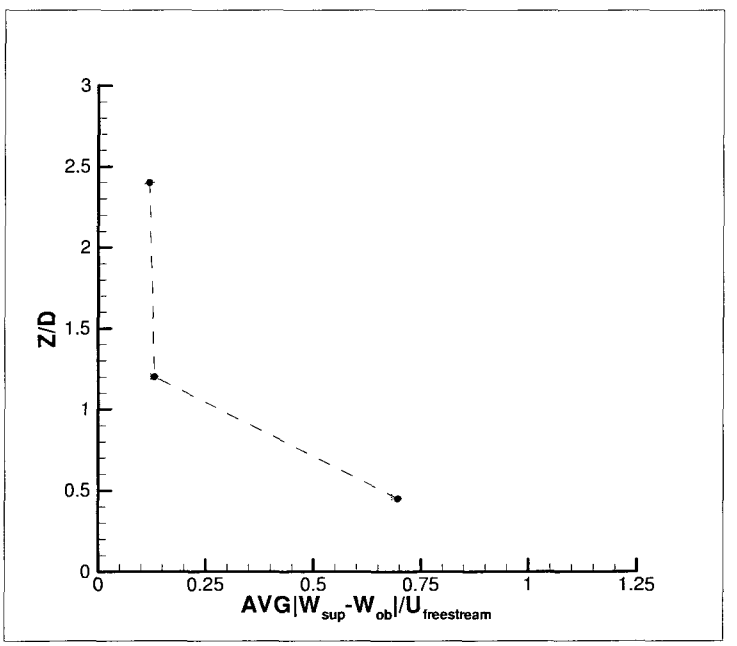

Figure 255: W-Velocity discrepancy versus rotor height above deck for rotor location X/D=0.5125 and Y/D=0.5

APPENDIX O: U-Velocity Component Discrepancies for a Rotor Location of X/D=1.3

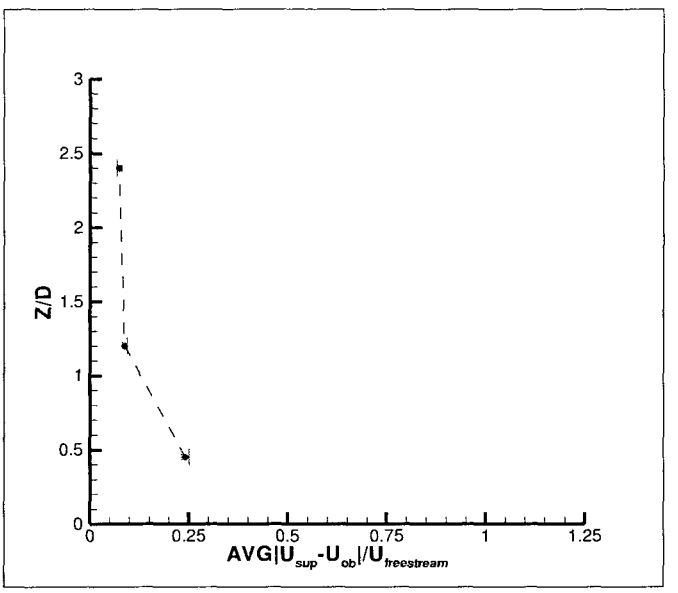

Figure 256: U-Velocity discrepancy versus rotor height above deck for rotor location X/D=1.3 and Y/D=-0.5

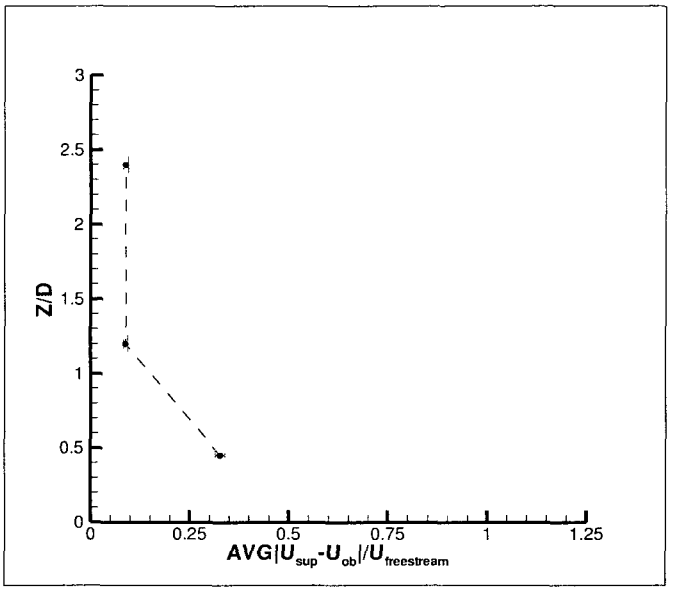

Figure 257: U-Velocity discrepancy versus rotor height above deck for rotor location X/D=1.3 and Y/D=-0.4

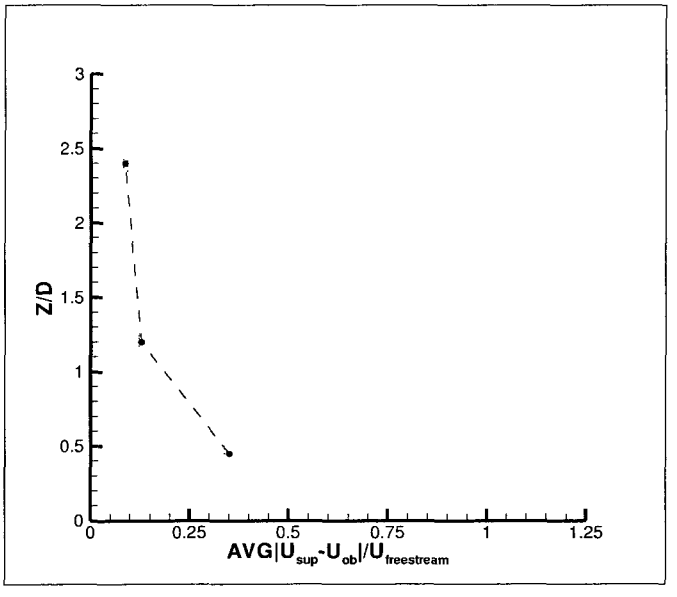

Figure 258: U-Velocity discrepancy versus rotor height above deck for rotor location X/D=1.3 and Y/D=-0.3

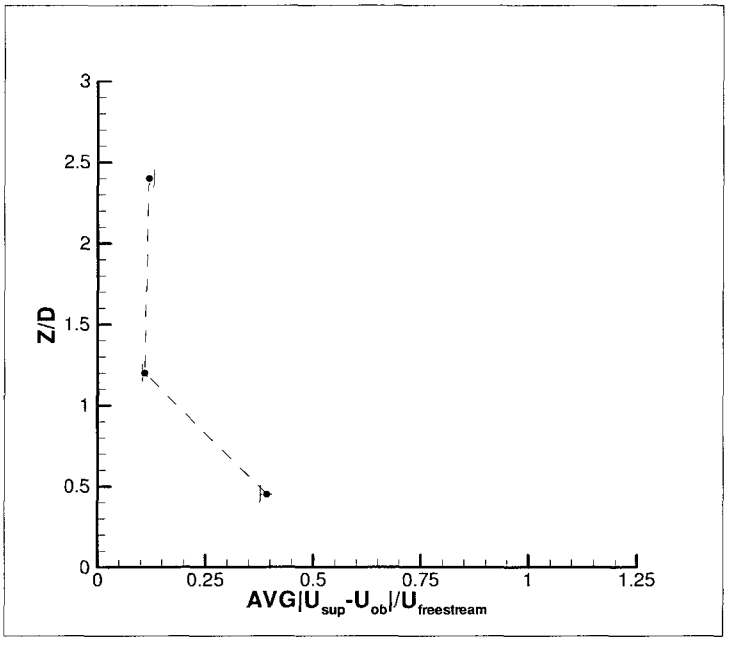

Figure 259: U-Velocity discrepancy versus rotor height above deck for rotor location X/D=1.3 and Y/D=-0.2

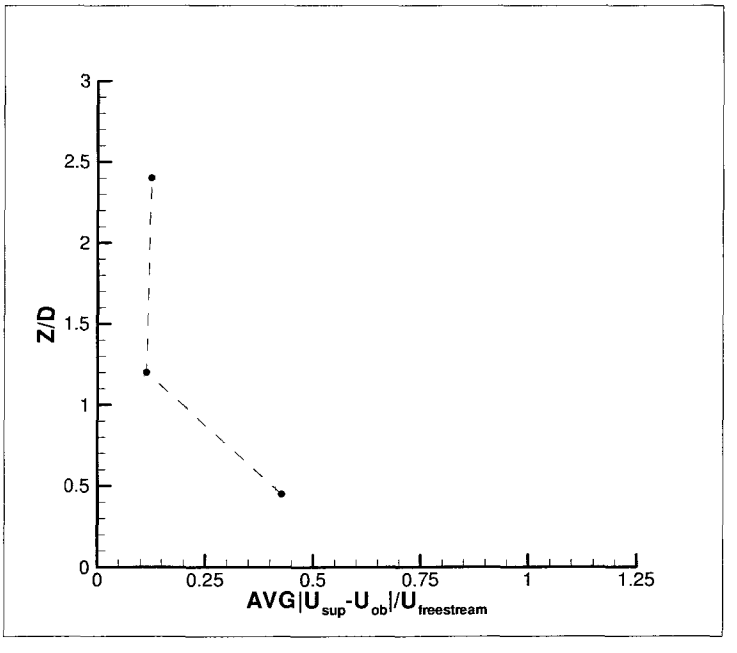

Figure 260: U-Velocity discrepancy versus rotor height above deck for rotor location X/D=1.3 and Y/D=-0.1

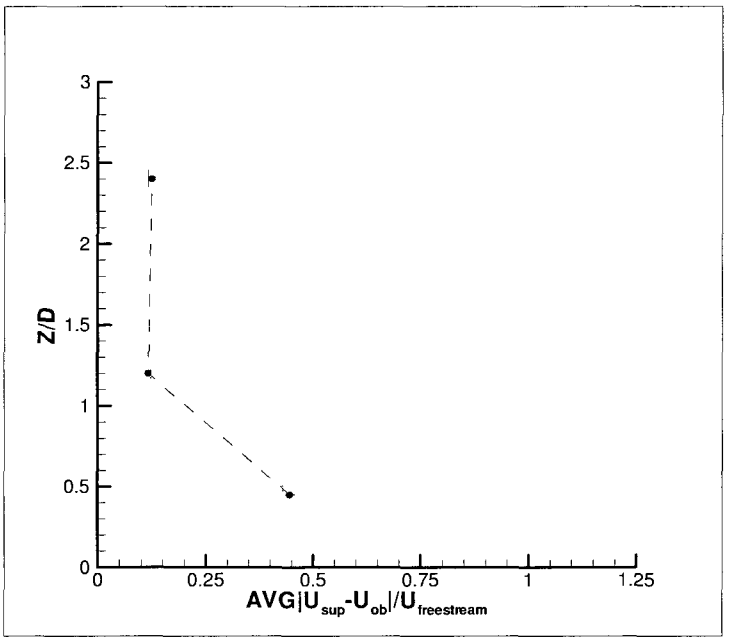

Figure 261: U-Velocity discrepancy versus rotor height above deck for rotor location X/D=1.3 and Y/D=0.0

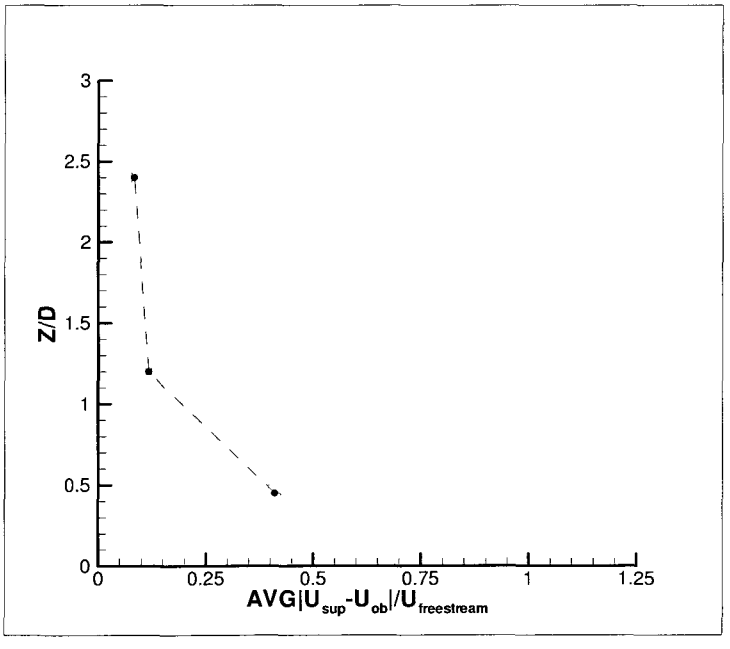

Figure 262: U-Velocity discrepancy versus rotor height above deck for rotor location X/D=1.3 and Y/D=0.1

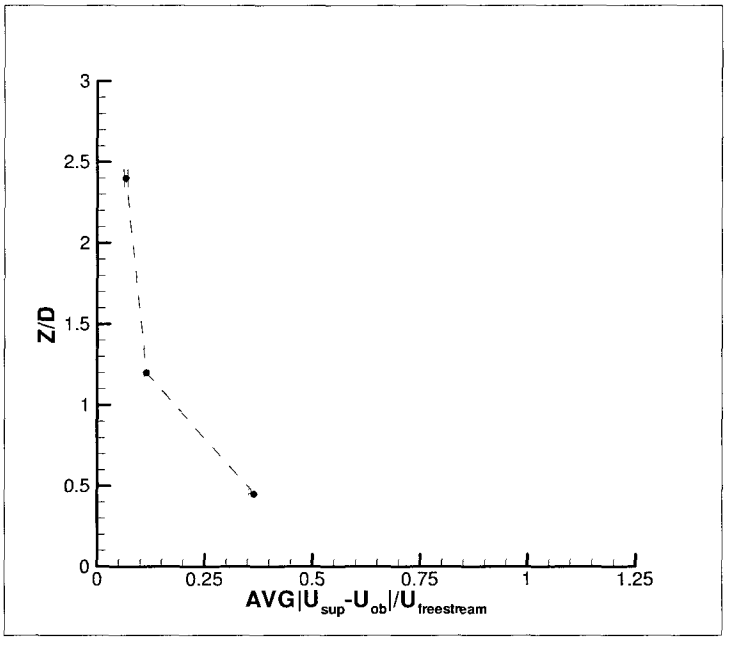

Figure 263: U-Velocity discrepancy versus rotor height above deck for rotor location X/D=1.3 and Y/D=0.2

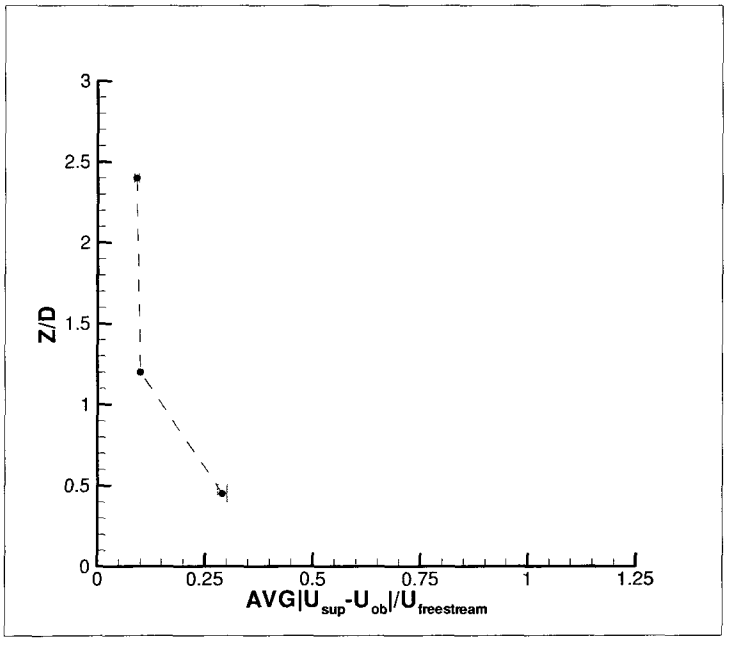

Figure 264: U-Velocity discrepancy versus rotor height above deck for rotor location X/D=1.3 and Y/D=0.3

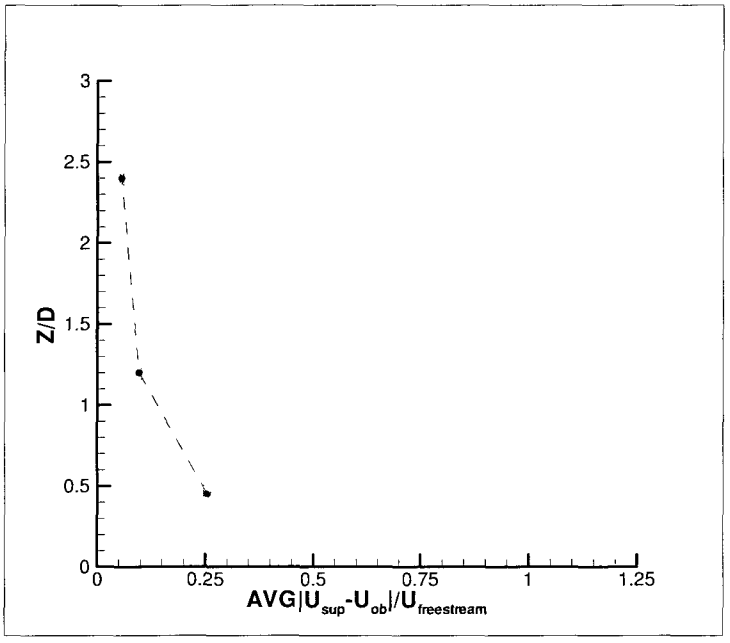

Figure 265: U-Velocity discrepancy versus rotor height above deck for rotor location X/D=1.3 and Y/D=0.4

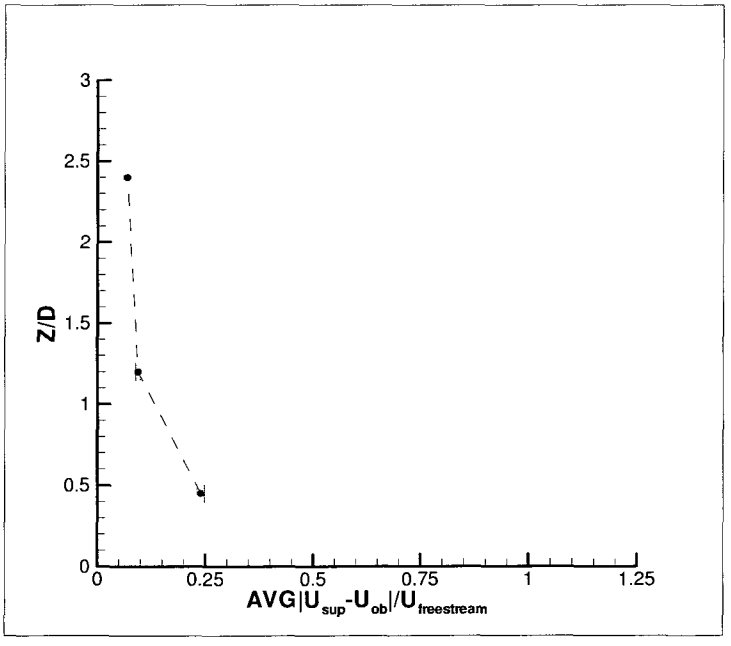

Figure 266: U-Velocity discrepancy versus rotor height above deck for rotor location X/D=1.3 and Y/D=0.5

APPENDIX P: W-Velocity Component Discrepancies for a Rotor Location of X/D=1.3

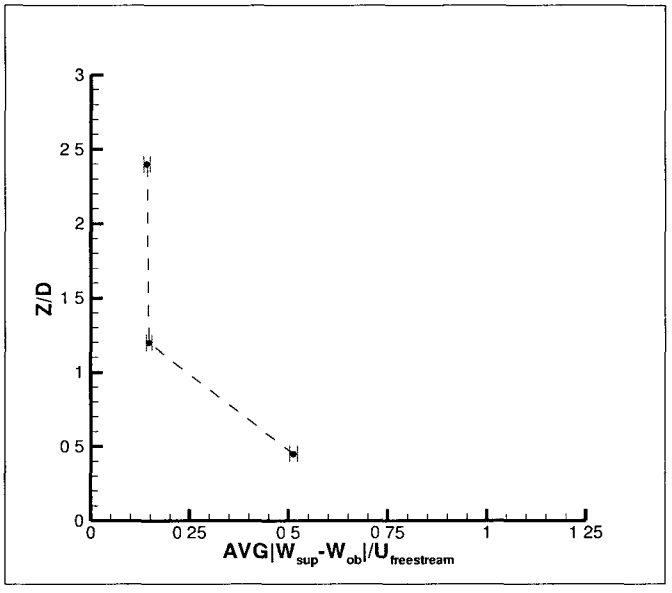

Figure 267: W-Velocity discrepancy versus rotor height above deck for rotor location X/D=1.3 and Y/D=-0.5

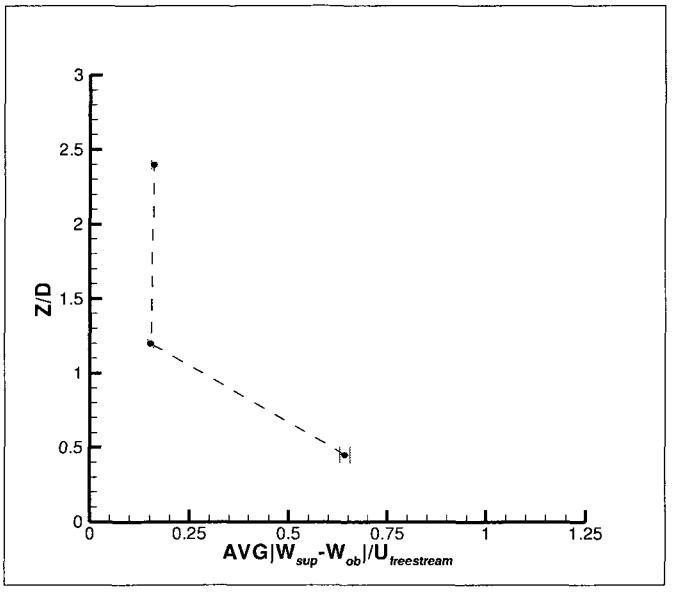

Figure 268: W-Velocity discrepancy versus rotor height above deck for rotor location X/D=1.3 and Y/D=-0.4

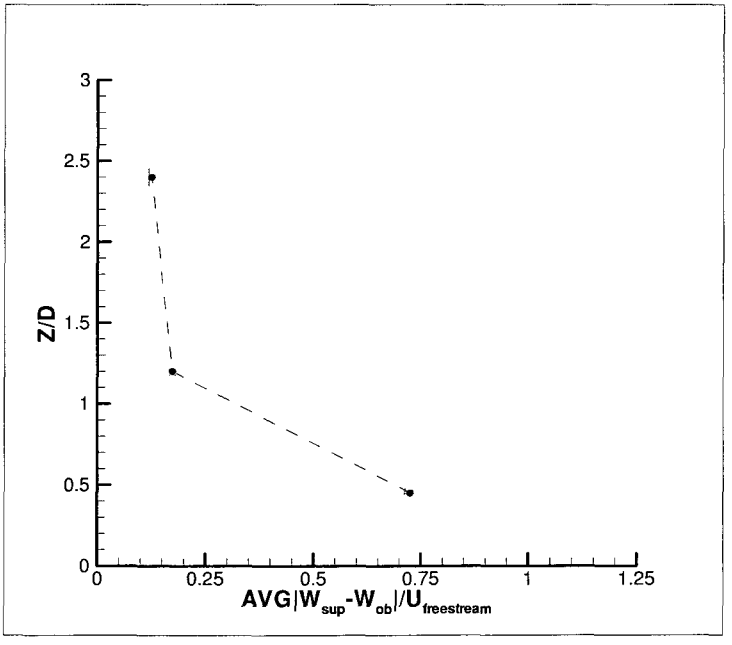

Figure 269: W-Velocity discrepancy versus rotor height above deck for rotor location X/D=1.3 and Y/D=-0.3

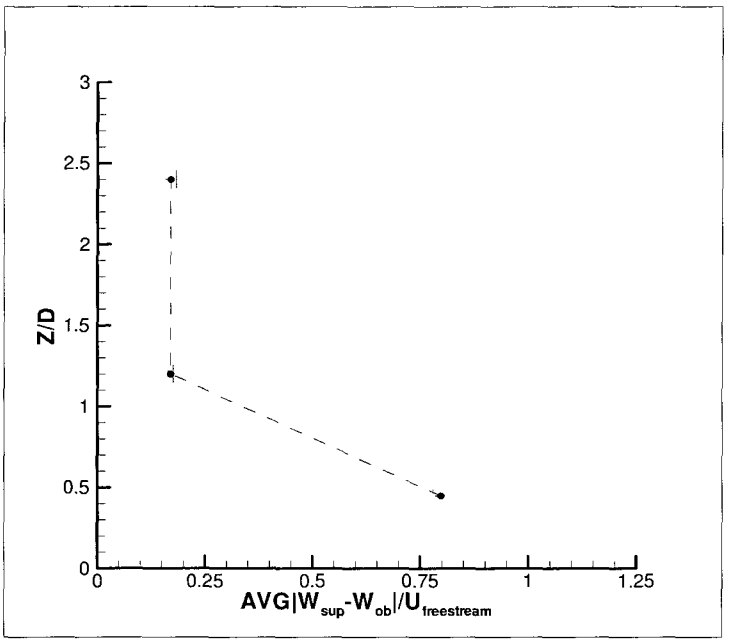

Figure 270: W-Velocity discrepancy versus rotor height above deck for rotor location X/D=1.3 and Y/D=-0.2

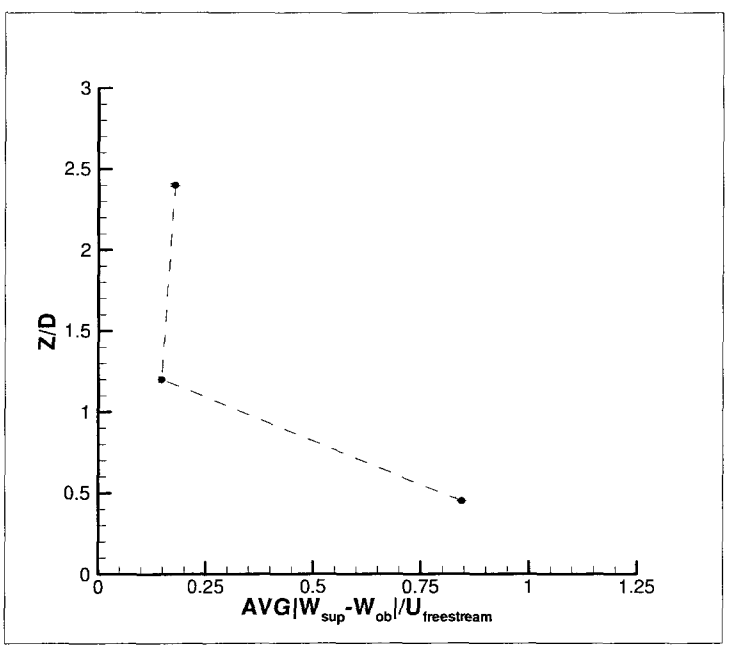

Figure 271: W-Velocity discrepancy versus rotor height above deck for rotor location X/D=1.3 and Y/D=-0.1

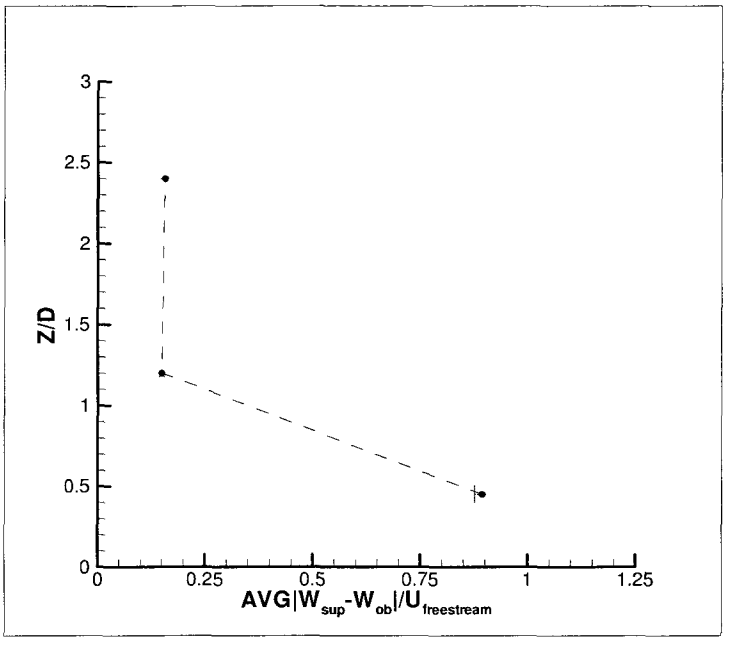

Figure 272: W-Velocity discrepancy versus rotor height above deck for rotor location X/D=1.3 and Y/D=0.0

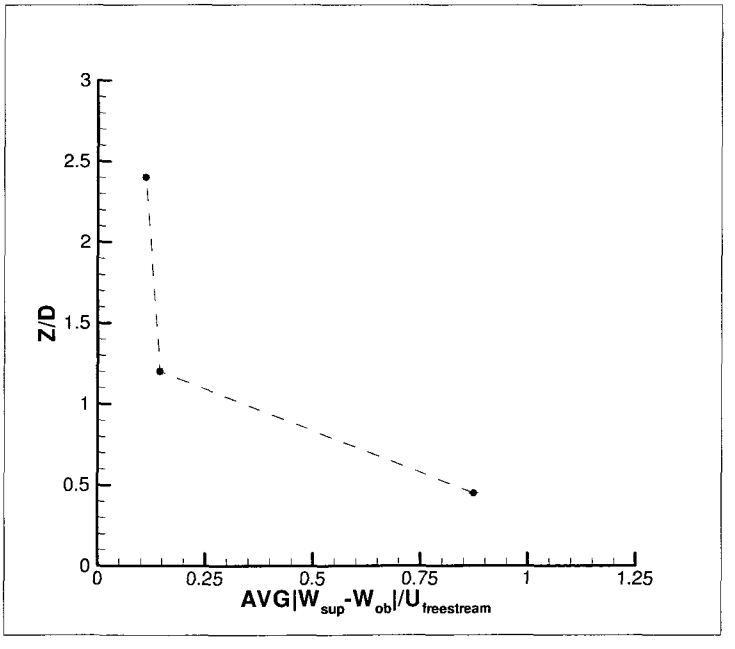

Figure 273: W-Velocity discrepancy versus rotor height above deck for rotor location X/D=1.3 and Y/D=0.1

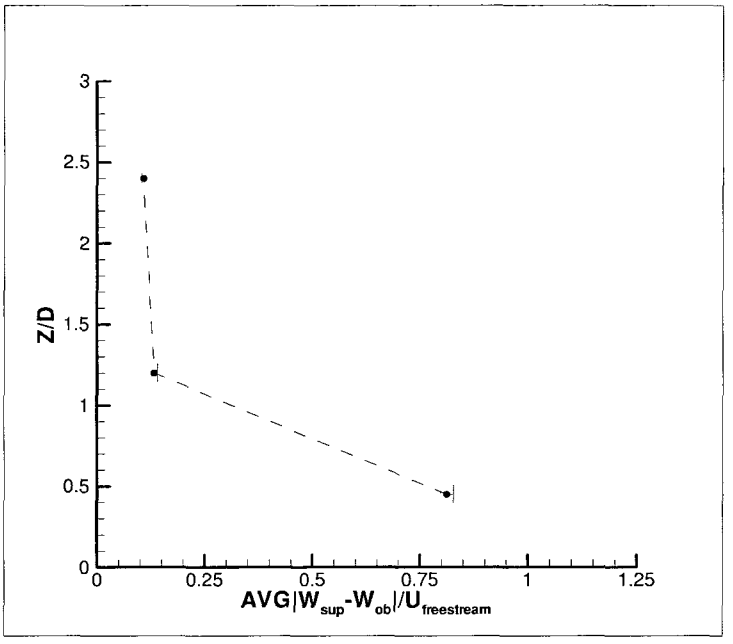

Figure 274: W-Velocity discrepancy versus rotor height above deck for rotor location X/D=1.3 and Y/D=0.2

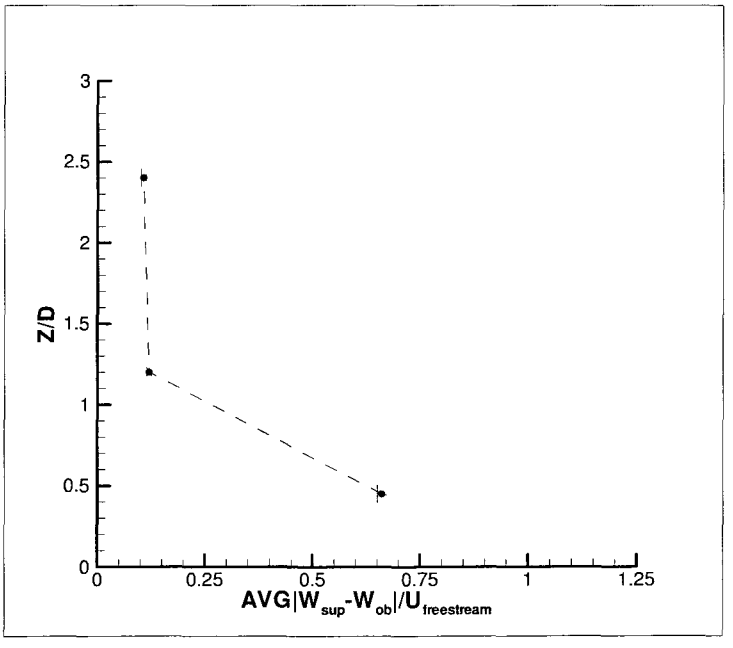

Figure 275: W-Velocity discrepancy versus rotor height above deck for rotor location X/D=1.3 and Y/D=0.3

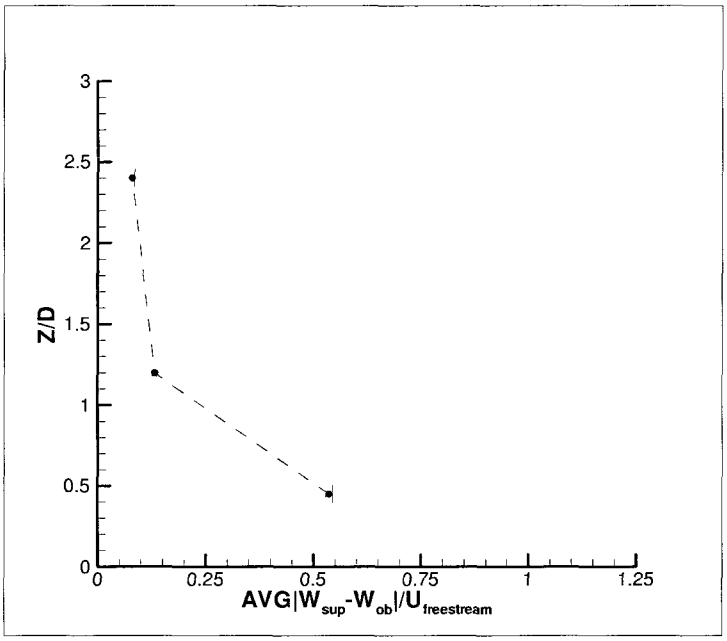

Figure 276: W-Velocity discrepancy versus rotor height above deck for rotor location X/D=1.3 and Y/D=0.4

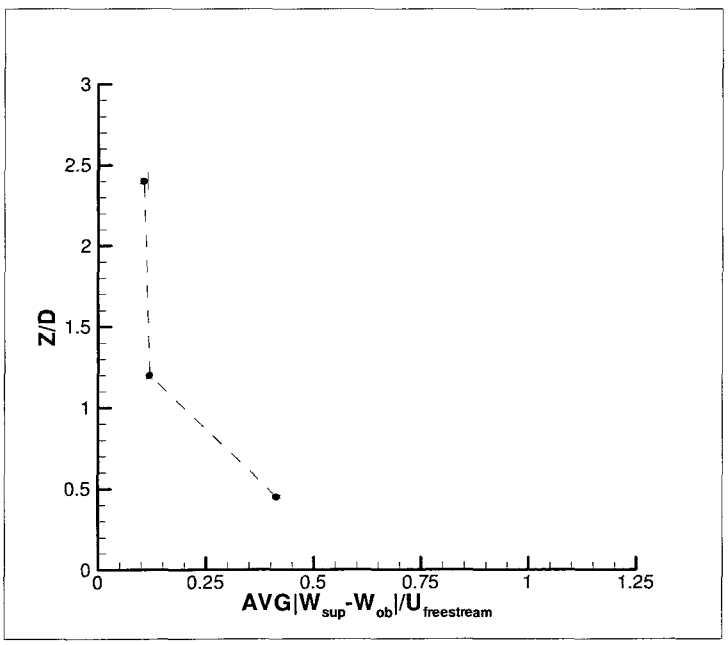

Figure 277: W-Velocity discrepancy versus rotor height above deck for rotor location X/D=1.3 and Y/D=0.5

APPENDIX Q: Rotor Thrust Coefficients for a Rotor Location of X/D=0.5125 and Z/D=0.45, 1.2, and 2.4

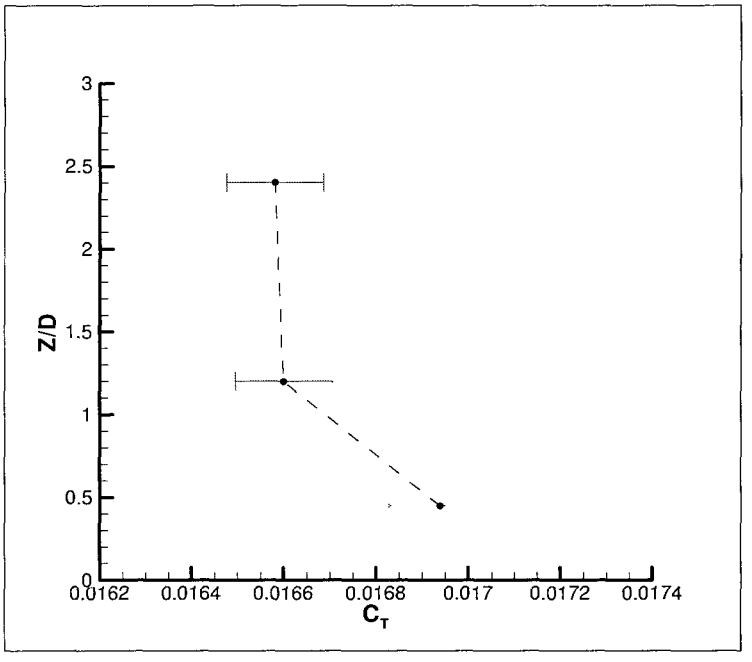

Figure 278: Rotor thrust coefficient for Y/D=-0.5

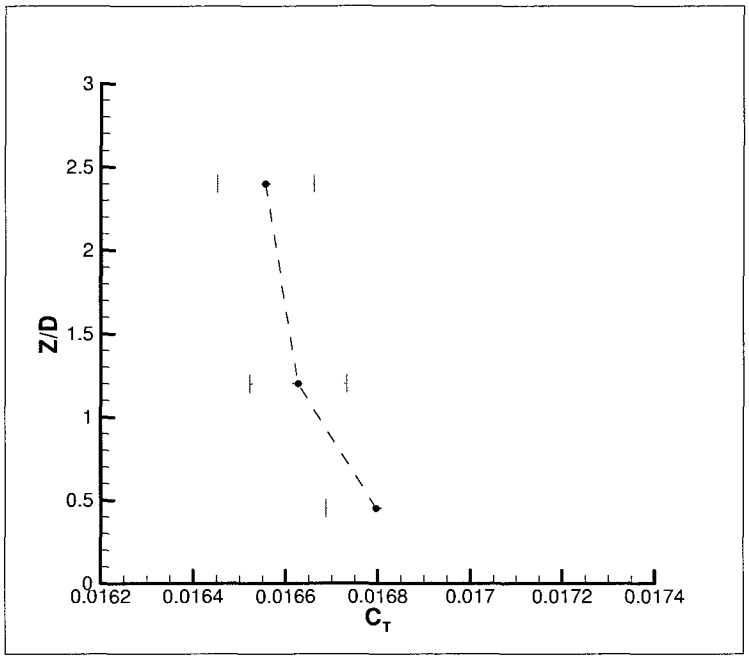

Figure 279: Rotor thrust coefficient for Y/D=-0.4

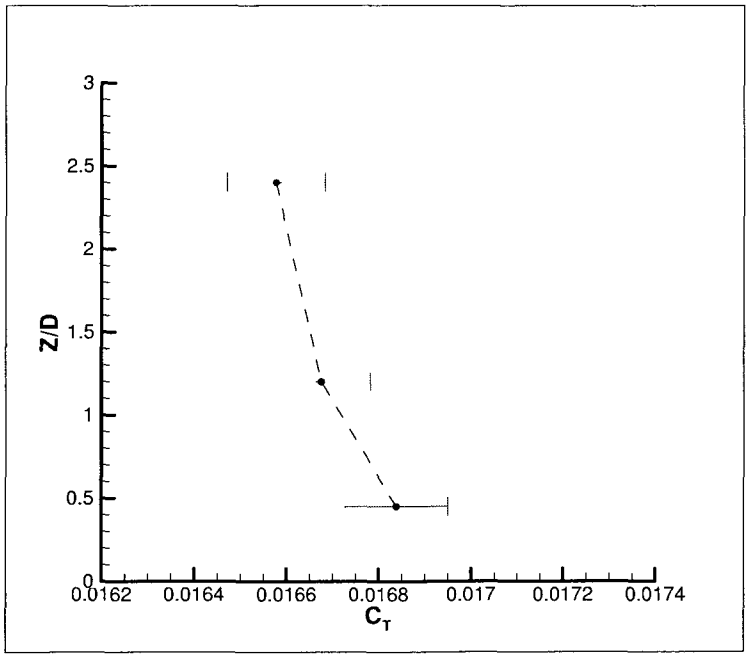

Figure 280: Rotor thrust coefficient for Y/D=-0.3

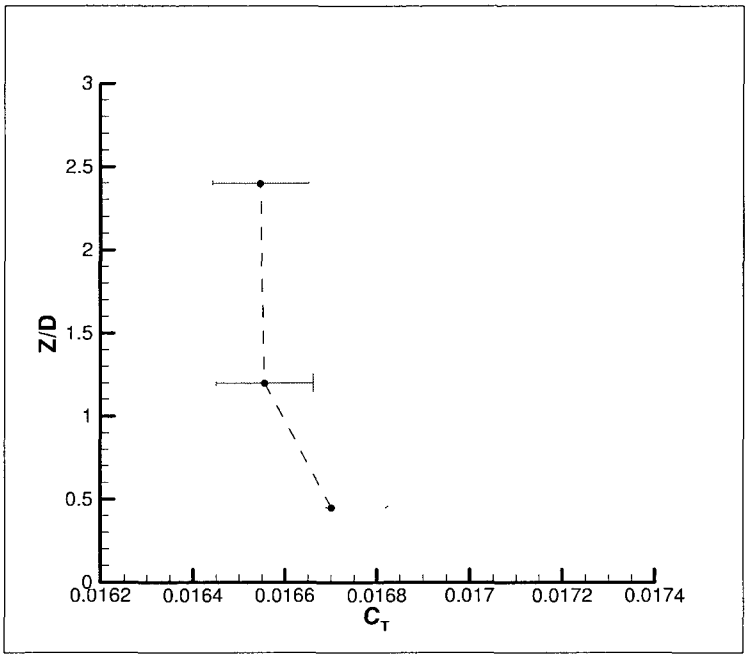

Figure 281: Rotor thrust coefficient for Y/D=-0.2

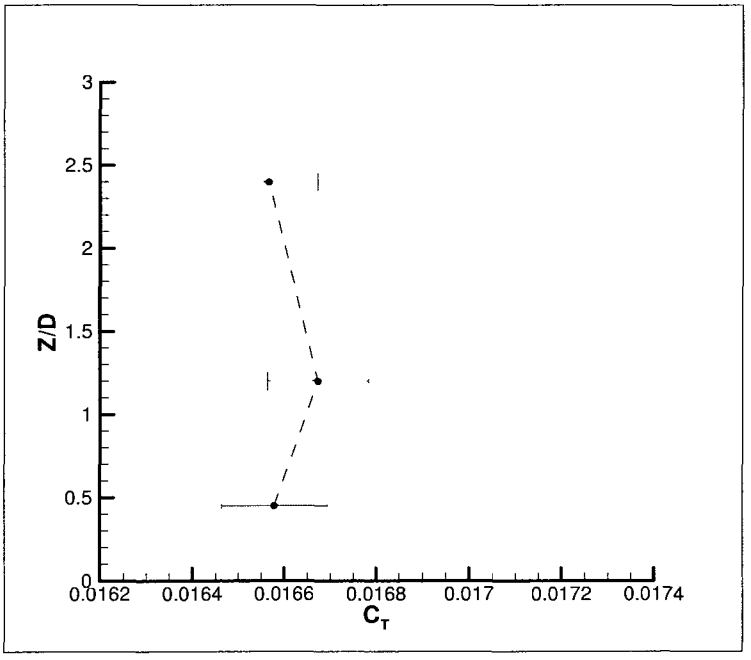

Figure 282: Rotor thrust coefficient for Y/D=-0.1

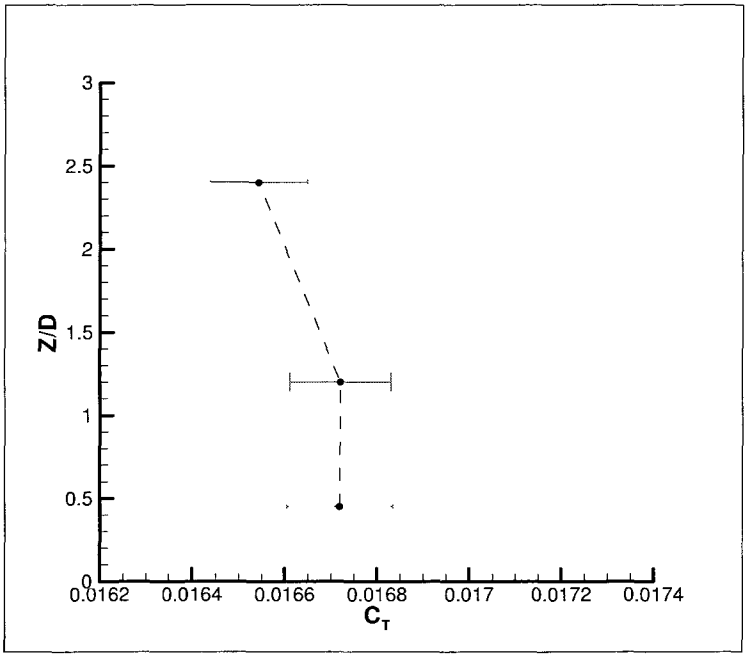

Figure 283: Rotor thrust coefficient for Y/D=0.0

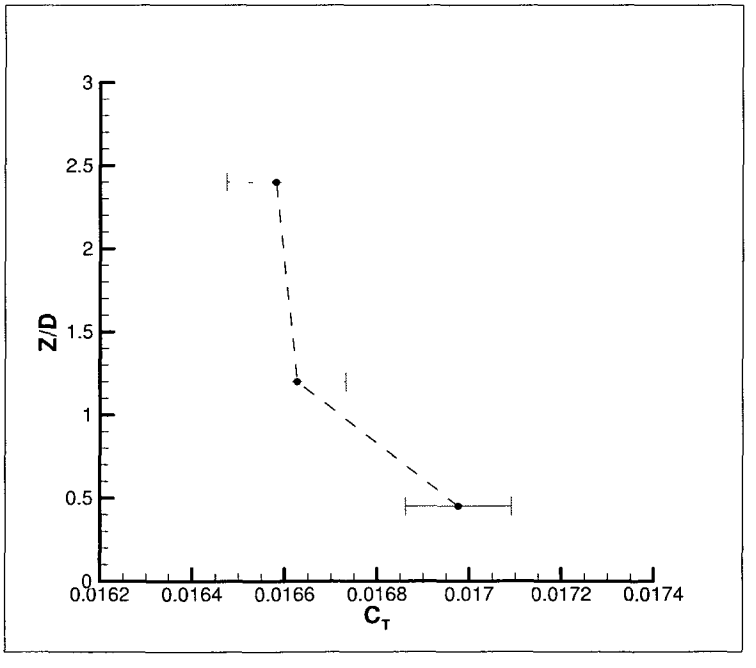

Figure 284: Rotor thrust coefficient for Y/D=0.1

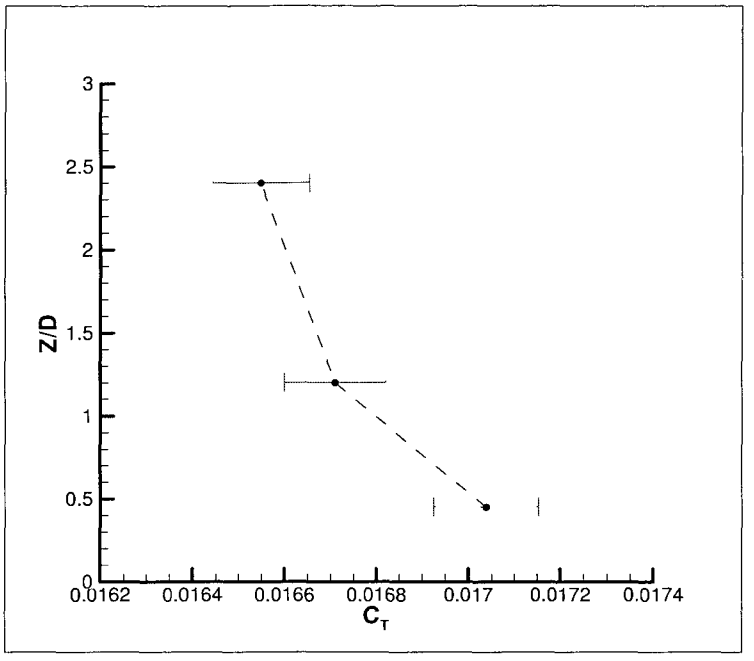

Figure 285: Rotor thrust coefficient for Y/D=0.2

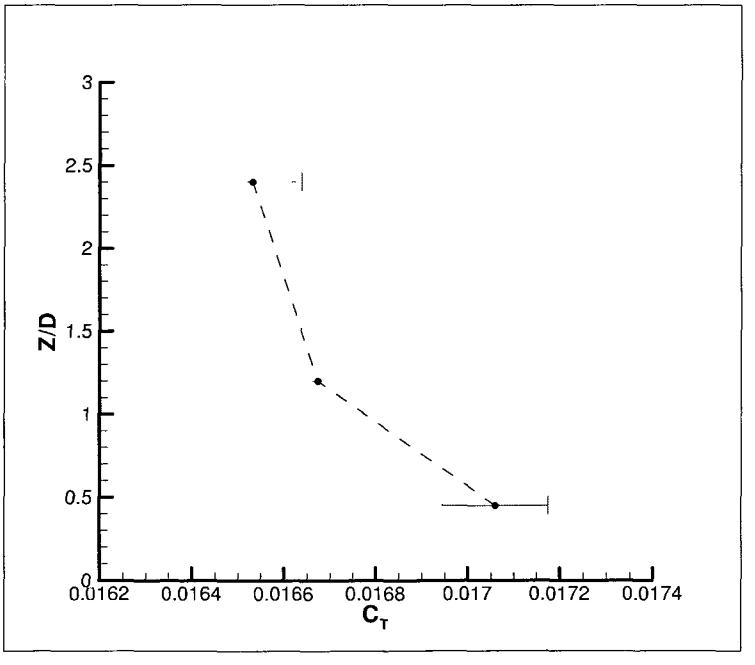

Figure 286: Rotor thrust coefficient for Y/D=0.3

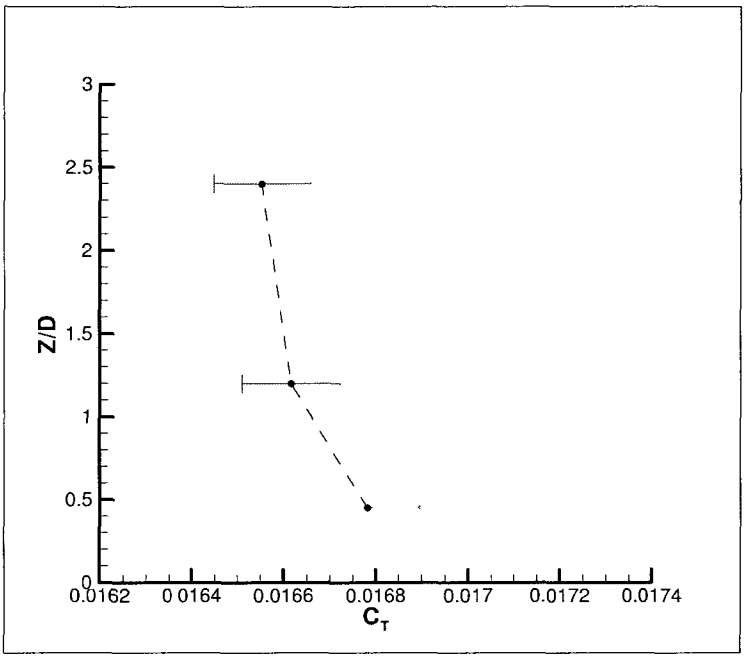

Figure 287: Rotor thrust coefficient for Y/D=0.4

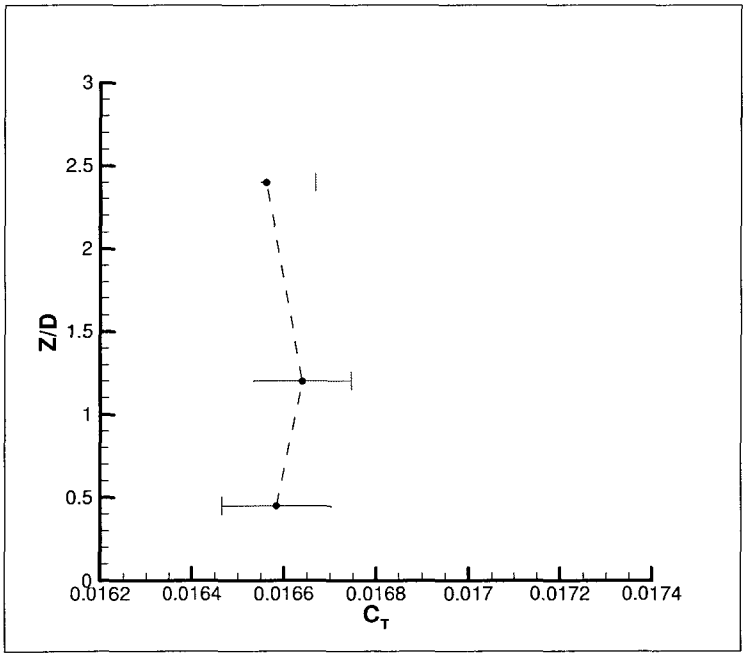

Figure 288: Rotor thrust coefficient for Y/D=0.5

APPENDIX R: Rotor Thrust Coefficients Reported for a Rotor Locations of X/D=1.3 and Z/D=0.45, 1.2, and 2.4

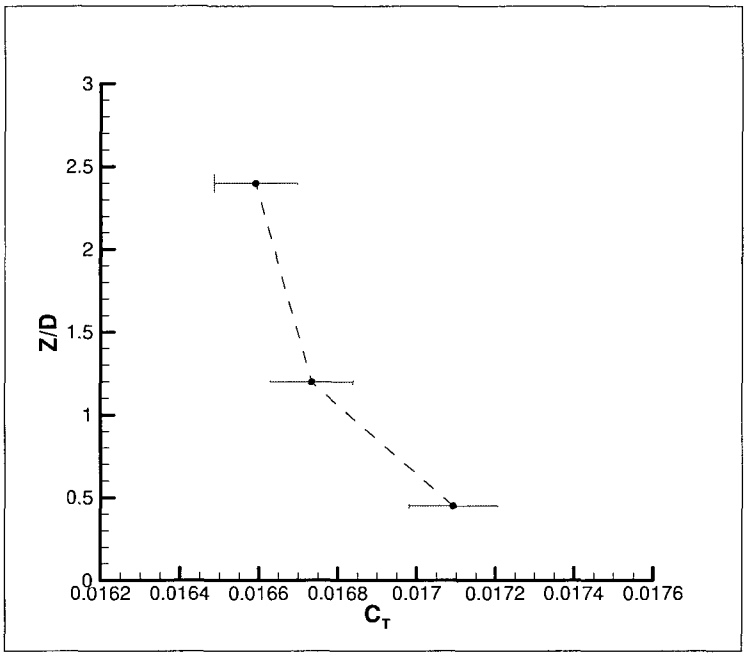

Figure 289: Rotor thrust coefficient for Y/D=-0.5

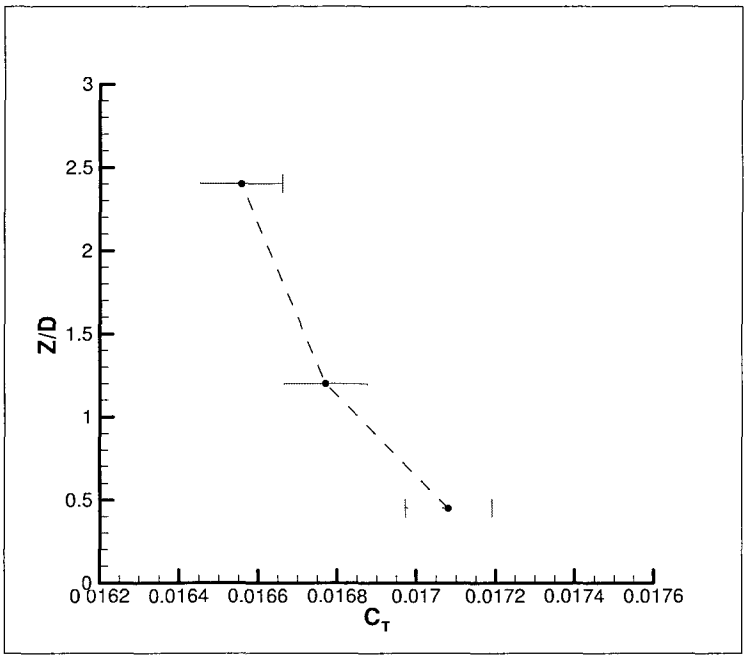

Figure 290: Rotor thrust coefficient for Y/D=-0.4

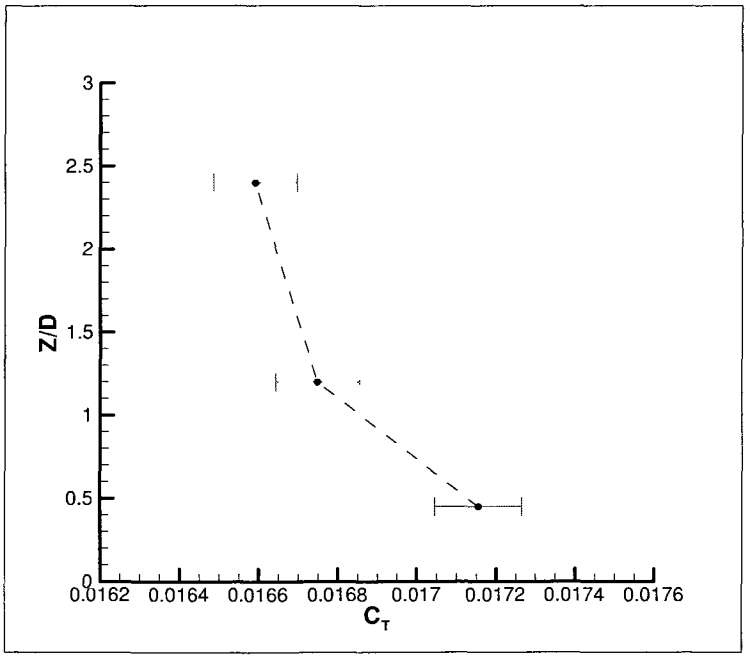

Figure 291: Rotor thrust coefficient for Y/D=-0.3

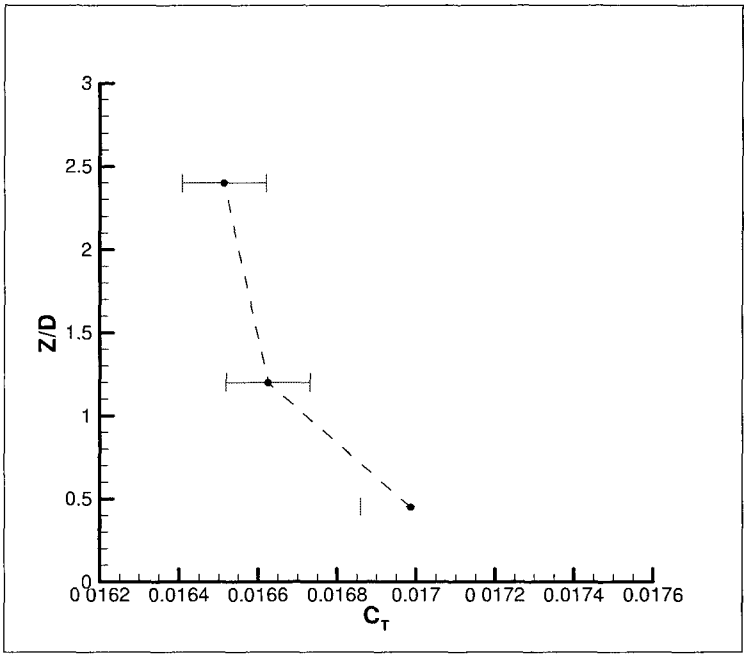

Figure 292: Rotor thrust coefficient for Y/D=-0.2

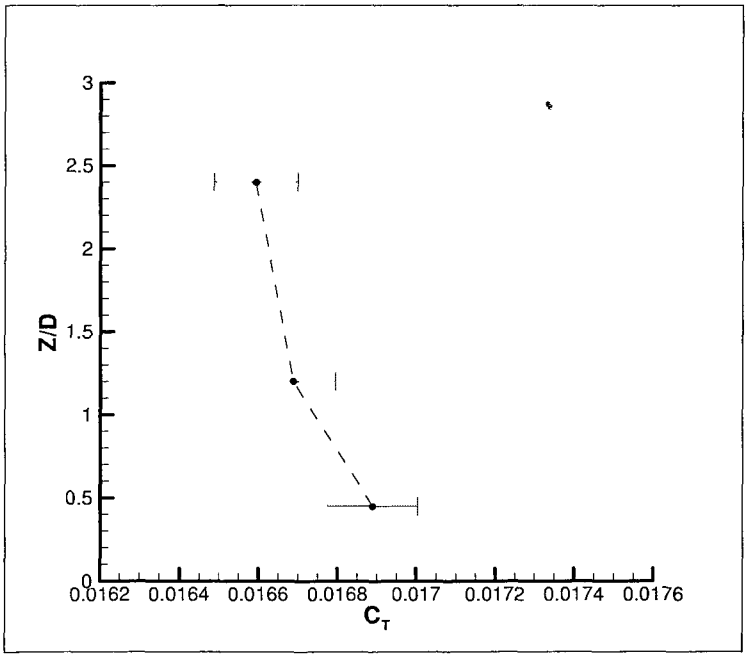

Figure 293: Rotor thrust coefficient for Y/D=-0.1

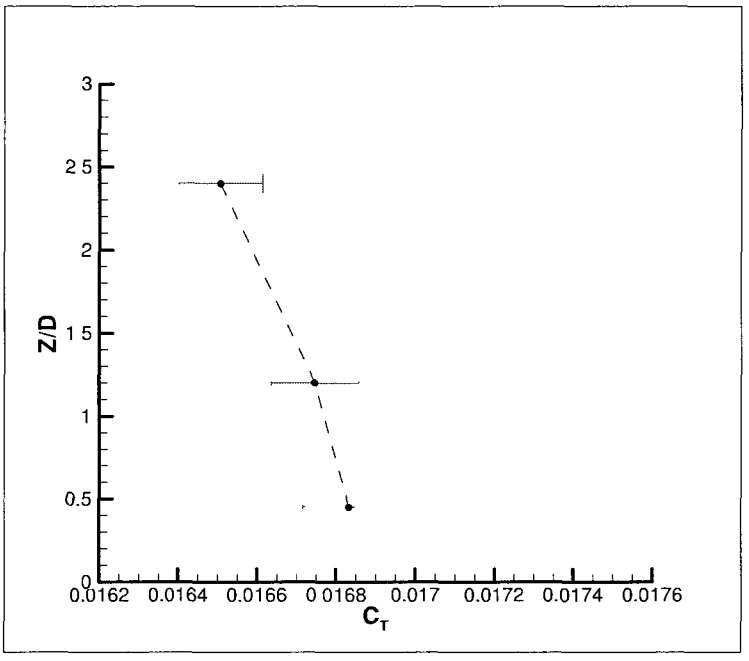

Figure 294: Rotor thrust coefficient for Y/D=0.0

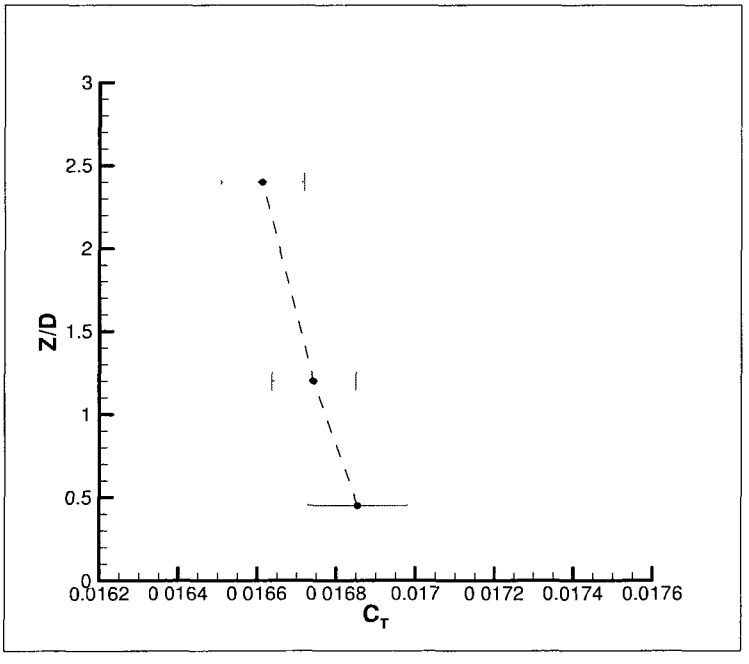

Figure 295: Rotor thrust coefficient for Y/D=0.1

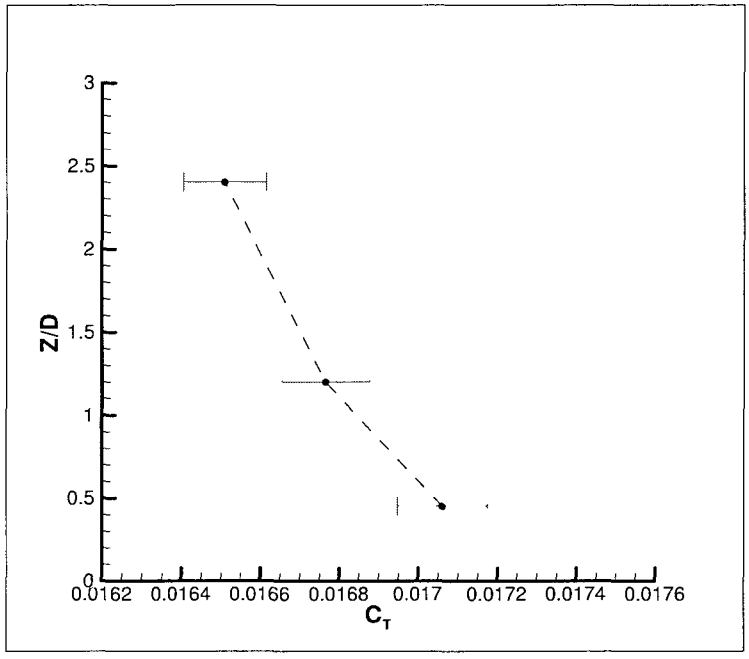

Figure 296: Rotor thrust coefficient for Y/D=0.2

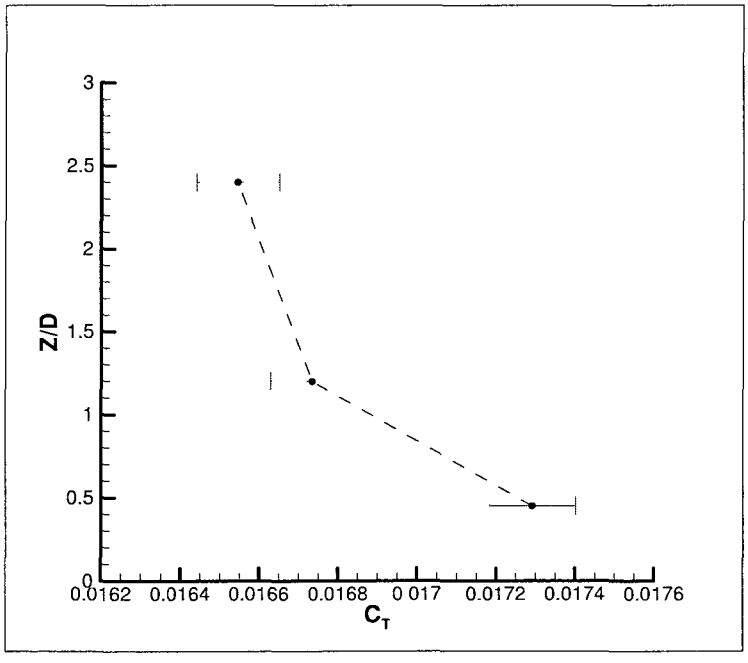

Figure 297: Rotor thrust coefficient for Y/D=0.3

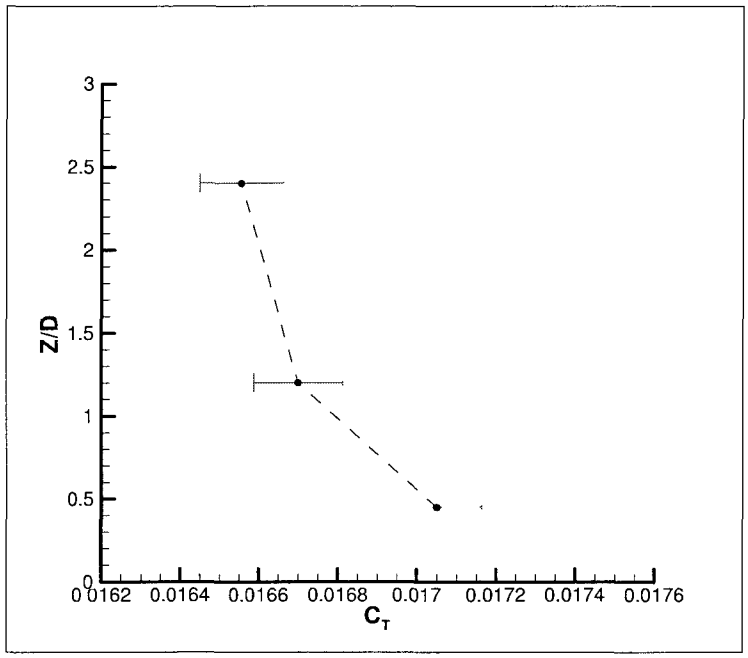

Figure 298: Rotor thrust coefficient for Y/D=0.4

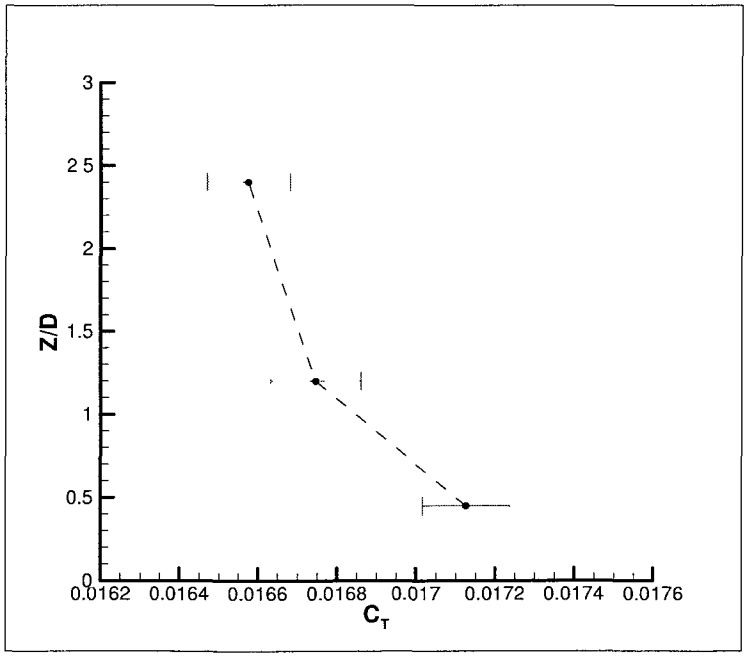

Figure 299: Rotor thrust coefficient for Y/D=0.5

VITA

Stargel R. Doane
Department of Mechanical and Aerospace Engineering
Old Dominion University
Norfolk, VA 23529-0267

Education

B.S. in Mechanical Engineering
May 2006
Minor: Mathematics
Concentration: Aerodynamics
Old Dominion University
Magna Cum Laude

Publications

Doane, S.R., Landman, D., & Wood, R.M., "A Computer Simulation of the Effect of Wind on Heavy Truck Fuel Consumption Testing," *SAE Technical Paper, 2010-01-2039, 2010.*

Ahonsi, M.O., Banko, T.J., **Doane, S.R.**, Demuren, A.O., Copes, W. E., & Hong, C., "Effects of Hydrostatic Pressure, Agitation and CO2 Stress on Phytophthora Nicotianae Zoospore Survival," *Pest Management Science*, Vol. *66*, No.7, 2010, pp. 696-704.

Accepted Publications

Nacakli, Y., Landman, D., and **Doane, S. R.**, "Investigation of Backward Facing Step Flowfield for Dynamic Interface Application," *Journal of the American Helicopter Society*, Accepted for publication.

Recent Presentations

Doane, S. R., and Landman, D. "Development of Wind Tunnel Measurement Techniques for the Identification of Ship Airwake/Rotor Downwash Coupling," *Presented to NAVAIR Applied Aerodynamics and Store Separation Branch*, Patuxent River, MD, February 28, 2011.

Doane, S. R., Landman, D., and Wood, R. M., "A Computer Simulation of the Effect of Wind on Heavy Truck Fuel Consumption Testing," *Presented at the SAE Commercial Vehicle Congress,* Rosemont, IL, October 5^{th}-6^{th}, 2010.